NO_2 Profile Retrieval using Airborne Multiaxis Differential Optical Absorption Spectrometer (AMAXDOAS) data

Vom Fachbereich für Physik und Elektrotechnik
der Universität Bremen

Zur Erlangung des akademisches Grades eines
Doktor der Naturwissenschaften (Dr. rer. nat.)
genehmigte Dissertation

von
Dipl. Phys. Marco Bruns
aus Langwedel

1. Gutachter:	Prof. Dr. John P. Burrows
2. Gutachter:	Prof. Dr. Otto Schrems
Eingereicht am:	02.11.2004
Tag des Promotionskolloquims:	21.12.2004

Contents

Chapter 1

Introduction

Since the early 1970's ground-based measurements of the ultraviolet (UV) and visible light scattered from the zenith sky have been used to determine the absorptions and thereby the atmospheric column densities of various trace gases (e.g. O_3, NO_2, BrO, OClO, ...) by several research groups e.g. [Brewer and Kerr, 1973; Noxon, 1975; McKenzie and Johnston, 1982; Solomon *et al.*, 1987b; Pommereau and Goutail, 1988]. These measurements identify specific absorption features using the well known Differential Optical Absorption Spectroscopy (DOAS) method [Platt and Hausmann, 1994]. The typical quantity derived from such measurements is a differential slant column density. That is the difference of the integrated column of molecules along the different light paths through the atmosphere. This is converted to a vertical column by a so-called air mass factor (AMF).

A more relevant quantity is the atmospheric profile of a trace gas. Noxon was the first to estimate the profile information contained in slant column measurements [Noxon, 1979]. Later McKenzie *et al.* used the weighted Chahine inversion, an iterative method that requires a convergence constraint to retrieve vertical NO_2 profiles [McKenzie *et al.*, 1991]. The Optimal Estimation method was used to retrieve NO_2 profiles from ground-based UV/visible zenith skylight absorption measurements at different SZA [Preston, 1995; Preston *et al.*, 1997]. The vertical resolution of such profiles is relatively low, and up to now profile retrievals were only attempted for NO_2. Vertically resolved measurements would also be of interest for BrO to investigate the presence of BrO in the boundary layer and in the free troposphere and its role in catalytic cycles removing O_3 [Barrie *et al.*, 1988; Richter *et al.*, 1998; Wagner and Platt, 1998].

Airborne UV/visible zenith sky absorption measurements have been performed since the 1980's [Wahner *et al.*, 1989b,a, 1990b,a; Schiller *et al.*, 1990; Brandtjen *et al.*, 1994; Pfeilsticker and Platt, 1994; Erle *et al.*, 1998; McElroy *et al.*, 1999]. The experimental setups in these works apply zenith sky absorption measurements to retrieve trace gas columns. Petritoli *et al.* have demonstrated that by using a horizon pointing (off-axis) measurement, the retrieval of in-situ information near flight altitude is possible [Petritoli *et al.*, 2002]. More recently, Melamed *et al.* have used zenith and nadir lines of sight to show the possibility of the separation of the total column in columns below and above the aircraft [Melamed *et al.*, 2003].

For the validation of measurements from the Scanning Imaging Absorption Spectrometer for Atmospheric Chartography (SCIAMACHY) [Bovensmann *et al.*, 1999] instru-

ment on board of ENVISAT, the Airborne MultiAxis DOAS instrument (AMAX-DOAS) [Wagner *et al.*, 2001] was developed, that takes simultaneous measurements of UV/visible sky absorptions at different lines of sight (LOS) pointing above and below the aircraft. The main focus of the AMAXDOAS measurements is the retrieval of stratospheric and tropospheric columns by using the zenith-sky and nadir viewing directions at a flight altitude close to the tropopause. However, the additional viewing directions are included to investigate the possibility to derive information on the vertical distribution of the absorbers. This is similar to the approach used in ground-based multiaxis measurements[Hönninger and Platt, 2002; Wittrock *et al.*, 2004], which resolve the lower troposphere. More independent pieces of information are expected for AMAXDOAS as compared to the ground-based multiaxis DOAS, as a result of the viewing geometry observed from an aircraft.

In this work, the information content of airborne multiaxis measurements is evaluated, and sensitivity studies are performed to assess the impact of different parameters on the retrieved profiles. A best case scenario with cloudless clear skies and simplified measurement errors is used. The results of this study provide an upper estimate of profile information, which can be retrieved from real measurements. This study analyzes the Airborne MultiAXis Differential Optical Absorption Spectrometer (AMAXDOAS) measurements quantitatively. The results are also qualitatively valid for other airborne DOAS measurements.

This work includes the development of the AMAXDOAS Profile Retrieval Algorithm (APROVAL). During this process it was discovered that the ideal setup of lines of sight (LOS) is including four LOS (0° [nadir], 88°, 92°, and 180° [zenith]) and using three wavelength regions (center wavelengths at 362.5 nm, 437.5 nm, and 485.0 nm). APROVAL was used to retrieve profiles from real AMAXDOAS measurements gathered during two major campaigns in 2002 and 2003.

1.1 Motivation

The motivation for this work is to retrieve profile information for the trace gas NO_2 from differential slant column densities measured by airborne UV/visible absorption spectroscopy in different directions. NO_2 is an important trace gas in the tropospheric boundary layer due to the fact that it is involved in the production of tropospheric Ozone, which plays a major role in smog situations, and NO_2 is very hazardous to the biosphere. NO_2 is also an important trace gas in the upper troposphere/lower stratosphere (UTLS) region because the increasing commercial air traffic induces large emissions of NO_2 into the UTLS region. This region is a dynamically very active region, which is important for the troposphere/stratosphere exchange enabling the transport of NO_2 emitted by air traffic into the stratosphere.

Using airborne skylight absorption measurements is an excellent tool to determine the geographical location of the sources of NO_2. The advantage of airborne measurements compared to ground-based measurements is the ability to cover large latitudinal and longitudinal cross sections.

1.2 Structure of this work

Chapters 2 and 3 are an introduction to atmospheric physics and atmospheric chemistry necessary to understand the investigation presented in this work. Chapter 4 deals with the experimental setup of the instrument used in this work as well as a brief discussion of the Differential Optical Absorption Spectroscopy (DOAS) method. Chapter 4 also discusses the important issue of the measurement geometry of airborne UV/visible skylight absorption measurements. Last but not least this chapter explains the two satellite experiments scanning imaging absorption spectrometer for atmospheric chartography (SCIAMACHY) and Meteosat, since it is shown in this work that the profile retrieval algorithm developed in this work is in theory applicable to space-based UV/visible absorption measurements. The Meteosat system is discussed because in the interpretation of retrieved profiles from the airborne instrument Meteosat data will be used.
Chapter 5 deals with profile retrieval theory necessary for the development of the AMAXDOAS profile retrieval algorithm (APROVAL) presented in this work. The structure of APROVAL is discussed, too. Chapter 6 presents an error analysis of the profile retrieval. Sensitivity Studies investigating the topic of airborne UV/visible skylight measurements containing profile information are presented in chapter 7. These sensitivity studies investigate the influence of different parameters like surface spectral reflectance (albedo), two flight altitudes, number and specific directions of the lines of sight, different solar zenith angles, two wavelength regions, two step-sizes of the retrieval grid, since the retrieved profile is discrete rather than a continuous function.
Chapter 8 presents retrieved profiles using simulated AMAXDOAS data showing the potential of the profile retrieval algorithm developed in this work. In chapter 9 the retrieved profiles using real AMAXDOAS data of two major campaigns in September 2002 and February/March 2003 are presented. These results are interpreted in chapter 10 concluding that the AMAXDOAS instrument is able to detect boundary layer NO_2 as well as NO_2 in the UTLS region. The latter is interpreted as NO_2 emitted by air traffic. Chapter 11 contains a conclusion of this whole work and an outlook for future investigations.

Chapter 2

Physics of the Atmosphere

This chapter contains a brief introduction into the physics of the earth's atmosphere. The physical concepts responsible for the structure of the earth's atmosphere are discussed. The different parts (troposphere, tropopause, stratosphere, stratopause, mesosphere, and mesopause) of the atmosphere are introduced. Further the atmospheric temperature and pressure structure are explained. Also the important term 'potential temperature' are introduced. The second part of this chapter describes aspects of radiation being important to this work. This chapter is based primarily on [Roedel, 1992; Houghton, 1986; Brasseur and Solomon, 1986].

2.1 Structure of the Atmosphere

Dividing the earth's atmosphere into different parts is a result of the hydrostatic equation and Thermodynamics. The gravitational influence of the earth is the reason for the characteristics of the earth's atmospheric pressure profile, which demonstrates an exponential decay. The basic features of the atmospheric temperature profile are influenced by the sun's radiation. The actual shape of the temperature profile with a temperature minimum at the tropopause and the temperature maximum at the stratopause originate from the emissivity of the earth' surface and the absorption features of the trace gas Ozone described below.
First the pressure profile of the atmosphere will be discussed. The hydrostatic equation describes the pressure profile of the atmosphere.

$$\frac{\mathrm{d}p}{\mathrm{d}z} = -\varrho \cdot g, \qquad \varrho = \frac{M \cdot p}{R \cdot T} \tag{2.1}$$

$$\Rightarrow \qquad p = p_0 \cdot exp\Big(-\frac{z}{H}\Big), \qquad H = \frac{R \cdot T^*}{M \cdot g} \tag{2.2}$$

where p is the atmospheric pressure, p_0 is the pressure at the surface, z is the altitude, ρ is the air density, g the gravitational acceleration, M is the molecular weight, R is the gas constant, T is the atmospheric temperature, T^* is the so-called harmonic mean of the atmospheric temperature. In eq. 2.2 a new atmospheric quantity is introduced: the atmospheric scale height H. The scale height marks the specific altitude where

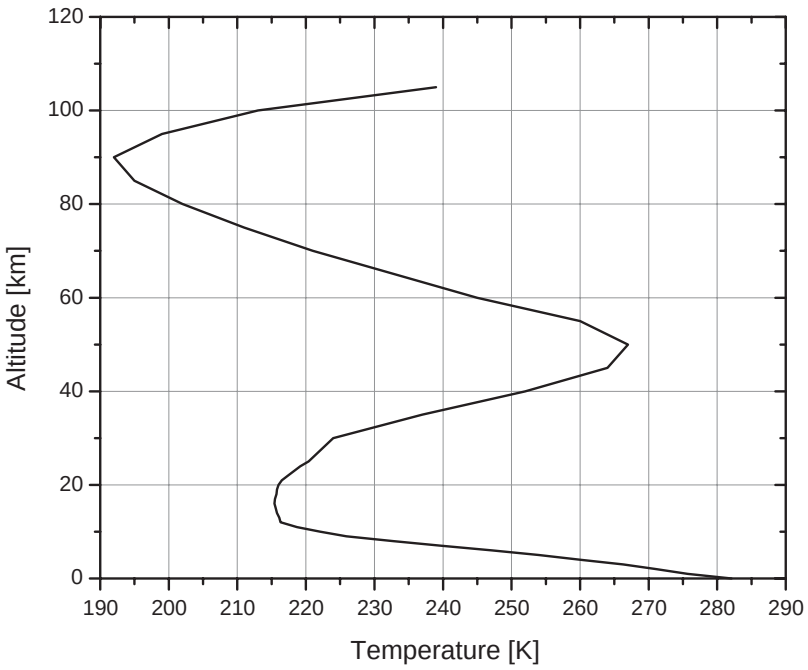

Figure 2.1: Temperature profile of the atmosphere. The data was taken from [Houghton, 1986].

the pressure has been reduced by a factor of e. For the standard atmosphere the scale height is about 8 km.
To understand the behavior of the atmospheric temperature profile in the lower atmosphere (see Fig. 2.1) the first law of thermodynamics has to be considered:

$$\mathrm{d}U = \delta Q + \delta W = \delta Q - p \cdot V; \qquad \mathrm{d}U = C_V \cdot \mathrm{d}T \tag{2.3}$$

$$\Rightarrow \qquad \delta Q = p \cdot \mathrm{d}V + C_V \cdot \mathrm{d}T; \qquad p \cdot \mathrm{d}V + V \cdot \mathrm{d}p = R \cdot \mathrm{d}T \tag{2.4}$$

where C_V is the specific heat at constant volume, U is the free energy, δQ is a certain quantity of heat, δW is a certain quantity of work, and V is the volume. The equations are valid for one mol of a gas. The equation on the right hand side of eq. 2.4 is the ideal gas law in its differential form. This law transforms the equation on the left hand side of eq. 2.4 into:

$$\delta Q = -V \cdot \mathrm{d}p + (R + C_V) \cdot \mathrm{d}T = -V \cdot \mathrm{d}p + C_p \cdot \mathrm{d}T \tag{2.5}$$

where C_p is the specific heat at constant pressure. Using $V = R \cdot T/p, \delta Q = 0$ (for adiabatic processes) and eq. 2.2 in its differential form the change in pressure can be substituted by the change in altitude:

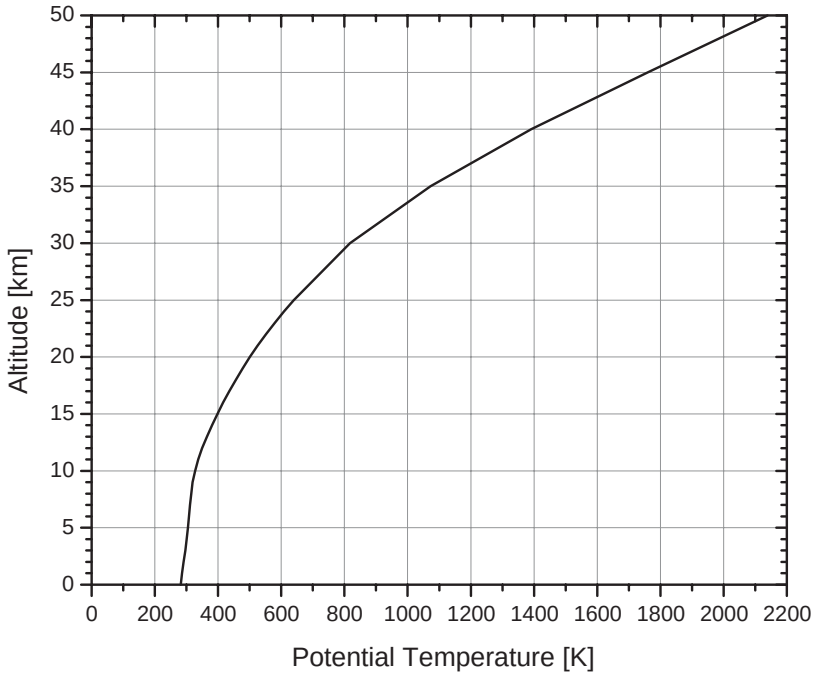

Figure 2.2: Potential temperature profile of the atmosphere. The data was taken from [Houghton, 1986].

$$C_p \cdot \mathrm{d}T = -M \cdot g \cdot \mathrm{d}z \tag{2.6}$$

$$\Rightarrow \qquad \frac{\mathrm{d}T}{\mathrm{d}z} = -\frac{M \cdot g}{C_p} \tag{2.7}$$

Eq. 2.7 is the so called dry adiabatic temperature lapse rate. Considering atmospheric values for C_p, M, and g this lapse rate has a value of the order of:

$$\frac{\mathrm{d}T}{\mathrm{d}z} = -0,00981\frac{K}{m} \approx -\frac{1K}{100m} \tag{2.8}$$

Considering a diabatic change of air containing water vapor nothing will change this value in first approximation unless condensation occurs. The lowermost 10 km of the temperature profile shown in Fig. 2.1 are explained by eq. 2.8. A description of the characteristics of the atmosphere can also be found in Tab. 2.1. To understand the physical relevance of eq. 2.6 and 2.7 more precisely, one has to go into detail. The sum of the left hand side (thermal energy) and the right hand side (potential energy) of eq. 2.6 is obeying the law of conservation of energy, meaning in an adiabatic ascent of an air parcel the thermal energy will be converted into potential energy. This results in a decrease of temperature as it is observed in the temperature profile. To be able to

atmospheric region	temperature gradient	temperature	convection
troposphere	-5 to $-10K/km$	-	yes
tropopause	-	$210K$	-
stratosphere	approx. $+1,5$ to $+2K/km$	-	no
stratopause	-	approx. $273K$	-
mesosphere	$-3,75K/km$	-	yes
mesopause	-	$< 200K$	-
thermosphere	-	-	yes

Table 2.1: Regions and characteristics of the atmosphere.

compare air parcels on different altitude levels the term 'potential temperature' is introduced. The potential temperature is defined as the temperature an air parcel would have if it was transferred adiabatically to the pressure level at the surface (1013 hPa). The potential temperature Θ and the actual temperature T are linked by the Poisson equation for adiabatic changes:

$$\frac{T^x}{p^{x-1}} = const; \qquad x = \frac{c_p}{c_V} \tag{2.9}$$

$$\frac{T^x}{p^{x-1}} = \frac{\theta^x}{p_0^{x-1}} \tag{2.10}$$

$$\Rightarrow \qquad \theta = T \cdot \left(\frac{p_0}{p}\right)^{\frac{x-1}{x}} \tag{2.11}$$

where c_p and c_V are the specific heat constants normalized to the molecular weight M. For air $(x-1)/x$ has a value of 0.286. Using eq. 2.2 and the temperature profile of Fig. 2.1 every potential temperature can now be associated with an altitude level (see Fig: 2.2).

Eq. 2.7 is valid for adiabatic processes but up to an altitude of 10 km the influence of solar radiation has to be taken into account. An air parcel near the earth's surface is heated due to solar radiation and ascends. At an altitude of about 10 km the air parcel loses heat due to the emission of the thermal radiation of the water vapor, which is contained in the air parcel. The cooling process leads to a descent of the air parcel. This convective region of the atmosphere from 0 to about 10 km altitude (the upper boundary depends on the latitude) is called 'troposphere'. The convection induces a well mixed troposphere. The temperature minimum above the troposphere is called 'tropopause'.

Above the tropopause the behavior of the temperature is different due to the missing of a large heat source (earth's surface) and the significantly decreased water vapor at 50 km altitude. Thus no convection is observed in this part of the atmosphere which is called 'stratosphere'. The temperature gradient is positive in contrast to the troposphere because the trace gas Ozone with a maximum at about 25 km altitude absorbs large fractions of the solar radiation between 200 and 300 nm. Virtually all absorbed energy goes into the kinetic energy of the molecules heating up the atmosphere. The temperature minimum at about 50 km altitude is called 'stratopause'.

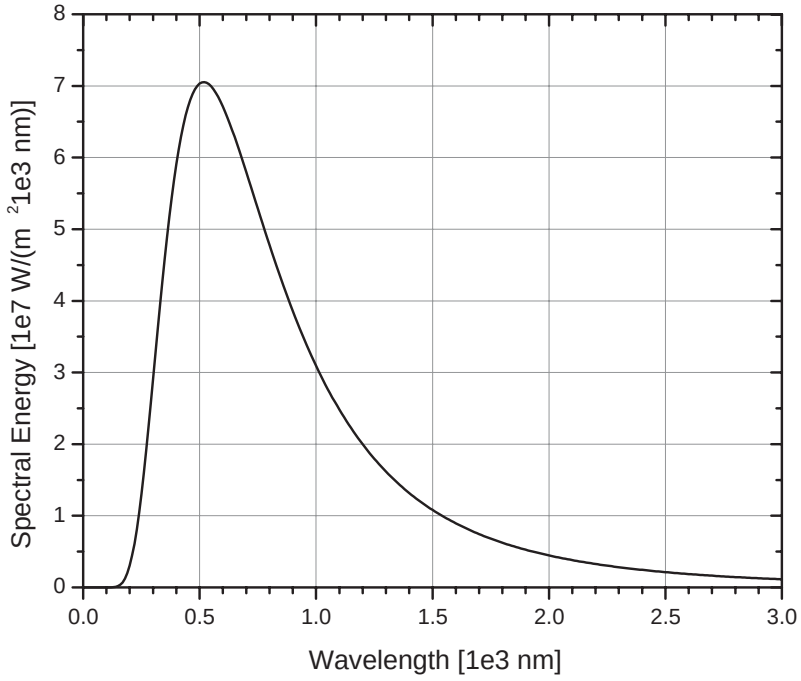

Figure 2.3: Black body spectrum at a temperature of 5800 K according to Planck's law.

Above the stratopause there is the mesosphere, which has a negative temperature gradient due to similar reasons as the troposphere. A dry-adiabatic temperature gradient of $dT/dz = -3.75K \cdot km^{-1}$ can be derived considering the warm upper stratosphere as heat source. Thus the mesosphere is subject to strong convection. At 85-90 km altitude, a region with the lowest temperature is observed in the earth's atmosphere is called 'mesopause'. Above the latter the atmosphere is called the 'thermosphere' due to high temperature of more than 1000 K. Nitrogen and oxygen atoms are responsible for such high temperatures through the absorption of solar radiation at very short wavelengths.

2.2 Radiation in the Atmosphere

The sun is responsible for the radiation being observed in the earth's atmosphere. Understanding of the various physical processes occurring in the atmosphere demands the consideration of atmospheric radiative transfer. Solar radiation is absorbed and scattered by molecules and aerosols and solar radiation is the source of thermal heating of the surface. Even the emission of terrestrial thermal radiation is caused by solar radiation.
The parameter to characterize the total radiative energy flux outside the earth's at-

mosphere is the solar constant. The latter has a value of 1367 W/m^2 at a distance of 1 AU[1] from the sun.
To get an idea of the spectral distribution of the energy arriving at the top of atmosphere, it can be assumed that the sun is a black body. Using Planck's law the solar spectral energy density E looks like Fig. 2.3:

$$E_\lambda = \frac{dE}{d\lambda} = \frac{2\pi hc^2}{\lambda^5} \cdot \frac{1}{e^{hc/kT\lambda} - 1} \tag{2.12}$$

where k is the Boltzmann constant ($1.38 \cdot 10^{-23} JK^{-1}$), and h is Planck's constant ($6.63 \cdot 10^{-34} Js$), c is the speed of light ($3 \cdot 10^8 ms^{-1}$), λ is the wavelength, and T is the sun surface temperature.
However the sun's spectrum does not look so smooth due to a variety of chemical elements in the solar atmosphere causing absorption lines. These lines in the solar spectrum are called Fraunhofer lines.

[1] An Astronomical Unit (AU) is the mean distance from earth to sun.

Chapter 3

Chemistry of the Atmosphere

This chapter contains a brief introduction of the Ozone chemistry. The chemistry described here plays an important role as a framework to understand the contents of this work. This chapter is divided into four parts. The first three parts deal with the most important trace gases the Differential Optical Absorption Spectroscopy (DOAS) method is able to detect. The last part describes the role each of these three trace gases is playing in forming the Ozone hole. The description of this chemistry is mainly based on the work of [Brasseur and Solomon, 1986; Wayne, 1991; Roedel, 1992; Finlayson-Pitts and Pitts, 2000].

3.1 Ozone

Ozone has different effects on different parts of the atmosphere. In the stratosphere Ozone is considered to be "healthy" due to its absorption of dangerous ultraviolet (UV) radiation whereas it is considered to be "unhealthy" in the troposphere because Ozone is a poisonous gas. A natural amount of Ozone in the stratosphere is able to remove virtually all UV radiation between 230 and 290 nm. Even the UV-B radiation between 290 and 320 nm, which causes skin cancer, is reduced dramatically. In the troposphere Ozone is responsible for smog situations. As will be shown below Ozone is produced after significant emissions of NO_x.

3.1.1 Stratospheric Ozone

As already stated above stratospheric Ozone is important because of its absorption in the UV. The absorption spectrum of Ozone shows three main absorption bands:

1. the Hartley-band from 220 to 310 nm
2. the Huggins-band from 310 to 350 nm
3. the Chappuis-band in the visible (green).

First research activities regarding Ozone in the atmosphere were performed by W. N. Hartley back in 1881. He analyzed the absorption behavior of Ozone [Hartley, 1881]. The most important absorption band was named after him - the Hartley-band. In 1930

Chapman published a theory about Ozone stating that Ozone is located in a layer in the atmosphere with peak values at 30 km altitude [Chapman, 1930]. Chapman's static photochemical model considered Ozone and Oxygen only:

$$\mathrm{O_2} + h\nu\ (\lambda < 242\ nm) \rightarrow \mathrm{O} + \mathrm{O(^3P)} \qquad +2 \qquad \text{(R1)}$$
$$\mathrm{O(^3P)} + \mathrm{O_2} + \mathrm{M} \rightarrow \mathrm{O_3} + \mathrm{M} \qquad \pm 0 \qquad \text{(R2)}$$
$$\mathrm{O_3} + \mathrm{O(^3P)} \rightarrow 2\mathrm{O_2} \qquad -2 \qquad \text{(R3)}$$
$$\mathrm{O_3} + h\nu\ (\lambda < 310\ nm) \rightarrow \mathrm{O_2} + \mathrm{O(^1D)} \qquad \pm 0 \qquad \text{(R4)}$$
$$\mathrm{O_3} + h\nu\ (\lambda < 1180\ nm) \rightarrow \mathrm{O_2} + \mathrm{O(^3P)} \qquad \pm 0 \qquad \text{(R5)}$$
$$\mathrm{O(^1D)} + \mathrm{O(^1D)} + \mathrm{M} \rightarrow \mathrm{O_2} + \mathrm{M} \qquad -2 \qquad \text{(R6)}$$

This is the updated Chapman cycle being the total knowledge of the atmospheric Ozone chemistry until 1970. The numbers on the right side of (R1) to (R5) represent the variation in Odd Oxygen like Ozone and atomic Oxygen. Odd Oxygen is potential Ozone because due to reaction (R2) atomic Oxygen can be converted to Ozone easily. Changes in Odd Oxygen indicate changes in Ozone. Until the 1960's it was accepted that the Chapman cycle could explain the Ozone concentration in the stratosphere. But it turned out that reaction (R6) was by orders slower than assumed (the latest measurements indicate a rate constant of $10^{-34} \cdot \mathrm{cm^6} \cdot \mathrm{molecules^{-1}} \cdot \mathrm{s^{-1}}$ for reaction (R6)). A comparison of first model results and measurements for stratospheric Ozone [Crutzen, 1970; Johnston, 1971] showed an amount of Ozone only half the size in the stratosphere as expected using the updated rate constant for reaction (R6).
In 1950 the concept of the catalytic cycle was introduced. This concept was able to explain the lower Ozone concentrations observed [Bates and Nicolet, 1950]. In the early 1970's this concept was applied to the NO_x family [Stolarski and Cicerone, 1974; Molina and Rowland, 1974]. This led to other Ozone depletion processes than the one in the Chapman cycle. The other Ozone depletion processes are:

$$\mathrm{X} + \mathrm{O_3} \rightarrow \mathrm{XO} + \mathrm{O_2} \qquad \text{(R7)}$$
$$\mathrm{XO} + \mathrm{O} \rightarrow \mathrm{X} + \mathrm{O_2} \qquad \text{(R8)}$$
$$\text{Net}: \quad \mathrm{O_3} + \mathrm{O} \rightarrow 2\ \mathrm{O_2}$$

where X is not only a variable for NO but also for one of these radicals: H, OH, Cl, or Br. The catalytic cycles are named after the specific radical involved: HO_x (H and OH), NO_x (NO and $\mathrm{NO_2}$), ClO_x. Sometimes there are different cycles of one radical family. For example $\mathrm{NO_3}$ is not a member of the NO_x family. In case $\mathrm{NO_3}$ is involved the following catalytic cycle is also possible:

$$\mathrm{NO} + \mathrm{O_3} \rightarrow \mathrm{NO_2} + \mathrm{O_2} \qquad \text{(R9)}$$
$$\mathrm{NO_2} + \mathrm{O_3} \rightarrow \mathrm{NO_3} + \mathrm{O_2} \qquad \text{(R10)}$$
$$\mathrm{NO_3} + h\nu \rightarrow \mathrm{NO} + \mathrm{O_2} \qquad \text{(R11)}$$
$$\text{Net}: \quad 2\ \mathrm{O_3} + h\nu \rightarrow 3\ \mathrm{O_2}$$

The catalytic cycle involving reaction (R9) is only one example for the many cycles involving reaction (R7) not discussed here.
Catalytic cycles like cycle (R9)-(R11) are able to deplete Ozone constantly unless the chain reaction is aborted by removing one of the catalytic agents. This is possible by linking different cycles through specific reactions producing so called reservoirs. These reservoirs are species, which are not very reactive and do not destroy Ozone. Catalytic agents are caught up in these reservoirs. The HO_x-, NO_x-, and ClO_x-cycles are linked through the following reactions:

$$OH + NO_2 + M \rightarrow HNO_3 + M \quad \text{(R12)}$$
$$ClO + NO_2 + M \rightarrow ClONO_2 + M \quad \text{(R13)}$$

All catalytic agents of the families (HO_x, NO_x, and ClO_x) are present in the unpolluted atmosphere. Natural source of OH and H is the photolysis of water. NO is a product of the photolysis of N_2O, which originates from the biosphere and due to its very long lifetime (years) can be transported into the stratosphere. ClO is a product of the CH_3Cl photolysis. The sources of CH_3Cl are biomass burning and metabolism of algae.

3.1.2 Tropospheric Ozone

Compared to the stratosphere the chemistry of Ozone in the troposphere is more complicated. This is due to the vast number of species having their sources in the biosphere. The large number of species leads to a great number of possible reactions in the troposphere. So this section is a brief overview concerning the most important reactions only. In case of the tropospheric Ozone chemistry three scenarios must be taken into consideration. The first scenario is the remote boundary layer, the second scenario is the anthropogenic influenced boundary layer[1], and last but not least the free troposphere.

Remote Boundary Layer

The difference of the remote boundary layer compared to the anthropogenic influenced boundary layer is low NO_x [Crutzen, 1995]. These conditions lead to production of OH by photolysis of Ozone (R4) and the reaction of atomic Oxygen and water.

$$O(^1D) + H_2O \rightarrow 2OH \quad \text{(R14)}$$

The largest sink for OH in the remote marine boundary layer where there are no significant sources of biogenic VOCs (volatile organic compounds) is the reaction with CO and CH_4.

[1]The boundary layer is the part of the atmosphere closest to the earth's surface. This part of the atmosphere is influenced by the surface (turbulence). Above the boundary layer the troposphere is not influenced by the surface. Usually the boundary layer is up to 2 km thick, but it depends on the meteorological conditions.

$$OH + CO \rightarrow H + CO_2 \quad \text{(R15)}$$
$$OH + CH_4 \rightarrow CH_3 + H_2O \quad \text{(R16)}$$

OH and HO_2 can also be sinks for Ozone:

$$HO_2 + O_3 \rightarrow OH + 2O_2 \quad \text{(R17)}$$
$$OH + O_3 \rightarrow HO_2 + O_2 \quad \text{(R18)}$$

Considering the last two reactions it is interesting to note that OH and HO_2 act as catalytic agents.

Anthropogenically Polluted Boundary Layer

In the anthropogenically influenced boundary layer NO_x is present in large concentrations. Most anthropogenic NO_x is emitted in the form of NO as it is typical for combustion systems [Schulte *et al.*, 1997] and NO is converted to NO_2 by Ozone:

$$NO + O_3 \rightarrow NO_2 + O_2 \quad \text{(R19)}$$

In case the troposphere is also polluted with peroxy radicals (HO_2 and RO_2[2]) reactions with NO can also reduce NO concentrations in the troposphere.

$$NO + HO_2 \rightarrow NO_2 + OH \quad \text{(R20)}$$
$$NO + CH_3O_2 \rightarrow NO_2 + CH_3O \quad \text{(R21)}$$

Reactions (R20) and (R21) are involved in an Ozone production cycle in NO_x and HO_2/RO_2 polluted areas [Wayne, 1991].

$$NO_2 + h\nu\ (\lambda < 420\ nm) \rightarrow NO + O(^3P) \quad \text{(R22)}$$
$$O(^3P) + O_2 + M \rightarrow O_3 + M \quad \text{see (R2)}$$
$$OH + CO \rightarrow H + CO_2 \quad \text{(R23)}$$
$$H + O_2 + M \rightarrow HO_2 + M \quad \text{(R24)}$$
$$NO + HO_2 \rightarrow NO_2 + OH \quad \text{see (R20)}$$

$$\text{Net :} \quad CO + 2O_2 + h\nu \rightarrow CO_2 + O_3$$

In case of high HO_2/RO_2 pollution and low NO_x concentrations in the boundary layer the large HO_2/RO_2 abundance is reducing Ozone due this sequence:

[2]R is a substitute for hydrocarbons such as CH_3 as in (R21).

$$\begin{aligned} HO_2 + O_3 &\rightarrow OH + 2O_2 && \text{(R25)} \\ OH + CO &\rightarrow H + CO_2 && \text{see (R23)} \\ H + O_2 + M &\rightarrow HO_2 + M && \text{see (R24)} \end{aligned}$$

$$\text{Net :} \quad CO + O_3 \rightarrow CO_2 + O_2$$

Current models suggest the Ozone production via the cycle including oxidation of NO is exceeding the Ozone loss via the cycle including (R25) for atmospheric mixing ratios of NO $\geq 3 \cdot 10^{-11}$. As long NO_x is available in the troposphere the Ozone production is limited only by the supply of CO and HO_2/RO_2. For both cycles introduced above there are versions including RO_2 instead of HO_2.

The Free Troposphere

While there has been a lot of research activity dealing with the boundary layer and the stratosphere, there is much less known about the layer in between - the free or upper troposphere. It became more of a topic in the recent years because of the potential impact of the increasing commercial aircraft traffic. Model predictions based on the simple O_3-H_2O-OH-CO-CH_4 chemistry described above, have shown much more OH than measured. These measurements indicate an additional source of OH and other free radicals producing OH [Wennberg *et al.*, 1998]. To reach the free troposphere, a trace gas must have a long enough life time. In some special scenarios like a thunderstorm with strong convection even very reactive substances can reach the free troposphere.
Photolysis has been proposed to be the additional source of species like CH_3COCH_3, HCHO, CH_3OOH, and H_2O_2 [Chatfield and Crutzen, 1984; Singh *et al.*, 1995; Prather and Jacob, 1997; Lee *et al.*, 1998].
Another significant uncertainty in the chemistry of the free troposphere is the NO_x/NO_y ratio. The observed ratio is higher than expected based on model calculations [Jaegle *et al.*, 1998]. An unrecognized chemistry leading NO_y back to NO_x was proposed [Chatfield, 1994]. Other studies propose NO_x production by lightning [McKeen *et al.*, 1997; Prather and Jacob, 1997; Jaegle *et al.*, 1998].
Under certain conditions injection of stratospheric air into the troposphere is very important too. Measurements of Ozone and NO_x have shown that higher concentrations from the stratosphere were injected into the troposphere [Suhre *et al.*, 1997; Dias-Lalcaca *et al.*, 1998].

3.2 NO_2

NO_2 has proven to be a major player in atmospheric chemistry [Crutzen, 1970, 1971]. This section describes the chemistry involving NO_2 and its influences on the Ozone chemistry. This section is divided into two parts. The first part considers the stratospheric chemistry and the second part describes the NO_2 chemistry in the troposphere.

3.2.1 Stratospheric NO_2

To be able to discuss the chemistry of the nitrogen oxides (especially NO_2) in the stratosphere it is important to identify the sources of NO_x in the stratosphere first. The only relevant nitrogen containing species living long enough to reach the stratosphere is nitrous oxide (N_2O). This was first shown by Bates and Hays [Bates and Hays, 1967]. After N_2O has reached the stratosphere it is photolysed during daylight:

$$N_2O + h\nu \rightarrow N_2 + O(^1D) \quad \text{(R26)}$$
$$N_2O + h\nu \rightarrow NO + N(^4S) \quad \text{(R27)}$$

The quantum yield of reaction (R27) was first believed to be 0.2. Later measurements [Greenblatt and Ravishankara, 1990] revealed a quantum yield of less than 0.01. N_2O is still the major source of nitrogen oxides in the stratosphere because of the minor loss reaction (since photolysis is the major loss of N_2O) with excited oxygen atoms.

$$N_2O + O(^1D) \rightarrow N_2 + O_2 \quad \text{(R28)}$$
$$N_2O + O(^1D) \rightarrow 2NO \quad \text{(R29)}$$

The channel of reaction R29 is the most important with a fraction of 60%. The product NO of the N_2O photolysis is involved in a catalytic cycle consisting of the following two reactions depleting Ozone. The third reaction is the NO_2 photolysis [Burrows *et al.*, 1998]:

$$NO + O_3 \rightarrow NO_2 + O_2 \quad \text{see (R9)}$$
$$NO_2 + O \rightarrow NO + O_2 \quad \text{(R30)}$$
$$NO_2 + h\nu \rightarrow NO + O \quad \text{(R31)}$$

After having discussed the sources of NO_2 the sinks of NO_2 have to be identified. In general it can be stated that the sinks of NO_2 are reservoirs. The chemical character of the these species has already been discussed in section 3.1. NO_2 is transferred into the following major reservoirs:

$$NO_2 + NO_3 + M \rightarrow N_2O_5 + M \quad \text{(R32)}$$
$$NO_2 + OH + M \rightarrow HNO_3 + M \quad \text{(R33)}$$
$$NO_2 + HO_2 + M \rightarrow HO_2NO_2 + M \quad \text{(R34)}$$

N_2O_5 is one of the most important NO_x reservoirs because it is involved in the diurnal variation of NO_2. After sunset the NO_2 is increasing rapidly due to the missing NO_2 photolysis (R31). The missing photolysis has the effect of transferring all NO to NO_2. During the night NO_2 is converted slowly to N_2O_5 (R32). This conversion results in decreasing NO_2 concentrations at night. In the morning after sunrise the NO_2 concentrations drop down rapidly due to the beginning photolysis of NO_2. During the

day the NO_2 is rising slowly again while N_2O_5 is photolyzed slowly [see (R35)]. Another important stratospheric reservoir is HNO_3 (R33). This reservoir is easily accumulated by droplets, which start to descend in case they are large enough leading to a flux from the stratosphere to the troposphere. HNO_3 is therefore a large sink of nitrogen compounds in the stratosphere. The reservoir HO_2NO_2 (R34) is formed in the lower stratosphere only because HO_2 has a peak concentration near 30 km altitude ([Brasseur and Solomon, 1986] p. 246).
Even though reservoirs are considered to be quite stable, there are loss processes for reservoirs, too:

$$N_2O_5 + h\nu \rightarrow NO_2 + NO_3 \quad \text{(R35)}$$
$$N_2O_5 + M \rightarrow NO_2 + NO_3 + M \quad \text{(R36)}$$
$$HNO_3 + h\nu \rightarrow NO_2 + OH \quad \text{(R37)}$$
$$HNO_3 + OH \rightarrow NO_3 + H_2O \quad \text{(R38)}$$
$$HO_2NO_2 + h\nu \rightarrow NO_3 + H_2O \quad \text{(R39)}$$
$$HO_2NO_2 + OH \rightarrow H_2O + NO_2 + O_2 \quad \text{(R40)}$$

The most important reactions of this group are the photolytic reactions due to the fact that there is a lot of radiation present in the stratosphere. The thermal decomposition of N_2O_5 is only important at high temperatures (approx. 300 K).

3.2.2 Tropospheric NO_2

All the reactions discussed in section 3.2.1 are also important in the troposphere with a few exceptions (see below). The accumulation of HNO_3 by rain drops is a very important effect in the troposphere, because the troposphere contains more water than the stratosphere. The hydrolysis of N_2O_5 looks like this:

$$N_2O_{5(g)} + H_2O_{(l)} \rightarrow 2\ HNO_{3(aq)} \quad \text{(R41)}$$

This reaction reduces the tropospheric lifetime of N_2O_5 from 4.5 h to 1.5 h assuming 50% relative humidity and a temperature of 291 K [Wahner *et al.*, 1998]. It is also well known that the hydrolysis is catalyzed by surfaces. The hydrolysis of N_2O_5 is believed to be the major source of HNO_3 in the troposphere.
Reaction (R41) can also take place in the gas phase. In this case HNO_3 is subject to dry deposition. It was shown that in dry areas like Los Angeles a large fraction (40%) of the nitrogen flux towards the surface is in form of dry deposition [Russell *et al.*, 1993].
The photolysis of HNO_3 (R37) is not as important in the troposphere as it is in the stratosphere due to the reduced UV radiation in the troposphere, since the HNO_3 molecules have the largest absorption cross section below 200 nm [DeMore *et al.*, 1997].

3.2.3 NO_2 Emissions by Aircraft

As shown in the previous sections NO_2 and NO_x in general play an important role in the chemistry of the earth's atmosphere. Aircraft emissions contribute only a small fraction

of 3% to the total NO_x emissions, but aircraft emission is the only man-made source of NO_x in the upper troposphere and lower stratosphere (UTLS) region. The influence of the air traffic NO_x depends strongly on the residence time in the atmosphere, and the residence time is depending strongly on whether the NO_x was emitted below or above the tropopause. Subsonic aircraft flying in the troposphere are increasing the tropospheric ozone but have no significant effect on stratospheric Ozone and vice versa.

In 1977 Hidalgo and Crutzen were the first to estimate to total global emission of NO_x from aircraft being 2.1 Mt/a [Hidalgo and Crutzen, 1977]. Other estimates by different groups followed but all with different results, which is mostly due to different times and a varying fleet of aircrafts. Other model studies followed such as [Johnston *et al.*, 1989; McInnes and Walker, 1992]. These studies all focussed on the pollutant emissions of the global commercial aircraft fleet. For this work model studies of the evolution of a single exhaust plume covering the first twelve hours after emission is more interesting, because the knowledge of the behavior of such a plume is important for the interpretation of the retrieved profiles as one will see later. Tsai *et al.* have modeled the evolution of an aircraft exhaust plume assuming an initial diameter of 400 m and an initial volume mixing ratio (VMR) of NO_x of 130 ppbv 1000 s after emission [Tsai *et al.*, 2001]. The study of Tsai *et al.* shows the temporal evolution of the plume diameter and the NO_x VMR. The main focus of the work of Tsai *et al.* is the evolution of a plume covering days.

The first airborne NO_x measurements were reported in 1988 regarding NASA's GTE/CITE 2 project [Hübler, 1988], but these measurement did not focus on aircraft emissions rather than on NO_x chemistry linked to the Ozone chemistry.

First airborne measurements concentrating on aircraft emission plumes were reported by Arnold *et al.*. The studies presented in [Arnold *et al.*, 1992] focussed on measurements of plumes emitted by a DC-9 jetliner. The DC-9 jetliner was trailed by another aircraft the FALCON 20 of the German Aerospace Center (the same aircraft was used in this work as instrument platform) in about 2 km distance at an altitude of 9.5 km. This distance is equivalent to 9 sec time difference meaning the exhaust fumes were measured 9 sec after emission. A mass spectrometer was used as an in-situ instrument to measure the plume compounds of NO, NO_2, HNO_2, and HNO_3. The abundance of NO and NO_2 were 780 and 150 ppbv respectively.

In 1995 Fahey *et al.* report NO_2 levels in aircraft exhaust plumes of up to 0.8 ppbv [Fahey *et al.*, 1995]. These measurements were done using NASA's ER-2 high altitude research aircraft as instrument platform flying at 19 km altitude. During this experiment a large variety of trace gases were measured by in-situ instruments including NO and NO_2. NO was measured using NO/O_3 chemoluminescence, and NO_2 was measured using UV-photolysis to create NO, and the NO was again detected by indexNO/O_3 chemoluminescence NO/O_3 chemoluminescence. In this experiment the ER-2's own exhaust plume was used as object of interest by flying in loop patterns to encounter the plume again about 500 to 700 sec after emission. In the plume peak values of 0.8 ppbv NO_2 were measured with the plumes being 1 to 2 km wide.

Schumann *et al.* report NO measurements of commercial airliners by identifying each aircraft using video records from the air traffic control radar display of the flight control station in Prestwick in 1995 [Schumann *et al.*, 1995]. The NO is measured using NO/O_3 chemoluminescence too. In ten plume encounters NO VMR of up to 2.4 ppbv were

measured. These measurements are only partly useful for this work because additional information on the NO/NO_x ratio is used to derive information on NO_2. NO/NO_x ratios in different altitudes were measured by Ziereis *et al.* during the POLINAT 2 campaign in 1997 [Ziereis *et al.*, 2000]. The NO/NO_x ratios for 9, 10, and 11 km altitude in [Ziereis *et al.*, 2000] are 0.71, 0.57, and 0.60 respectively.

The chemistry of NO_x production in fuel combustors is described briefly. Due to very high temperatures in the fuel combustion process in aircraft jet engines (above 600°) the production of NO_x (mainly NO) is the result of the production of atomic Nitrogen via the Zeldovich mechanism:

$$N_2 + O \rightarrow NO + N \quad \text{(R42)}$$
$$N + O_2 \rightarrow NO + O \quad \text{(R43)}$$
$$N + OH \rightarrow NO + H \quad \text{(R44)}$$

where reaction (R42) is the primary production pathway [Blazowski and Saywer, 1975]. The production of NO_2 is occurring outside the jet engine due to reaction (R9).

3.3 The Ozone Hole

In 1985 Farman *et al.* reported a dramatic reduction of the Ozone column in the Antarctic from 1975 to 1985 [Farman *et al.*, 1985]. Today it is generally accepted that the observed Ozone loss is due to active chlorine from chlorofluorocarbons (CFCs) and heterogeneous chemistry on polar stratospheric cloud (PSC) particles. The chemistry in this area is the result of a unique meteorology. Schoeberl and Hartmann described the development of a polar vortex in the stratosphere during polar winter [Schoeberl and Hartmann, 1991]. When the sun sets in fall over the polar regions, radiative cooling of air in the upper stratosphere occurs. These cooler air masses begin to sink causing adiabatic heating, which compensates the radiative cooling partly. Finally radiative equilibrium is reached at 30 km altitude. This results in a temperature gradient in the stratosphere leading to a thermal wind surrounding the cold air mass - the polar .

The temperatures in the stratosphere can be as low as 185 K. At these temperatures PSCs are forming. The formation of PSCs is quite complex (for more details see [Finlayson-Pitts and Pitts, 2000]). It is believed that PSC particles consist of crystalline nitric acid trihydrate (NAT) and tenary solutions of HNO_3, H_2SO_4, and water. The PSC particles play an important role in providing surface area for heterogeneous reactions.

The first step in the formation of the Ozone hole is the so called preconditioning chemistry. This chemistry involves heterogeneous chemistry of rather inactive reservoirs like $ClONO_2$, N_2O_5, and HCl.

$$N_2O_{5(g)} + HCl_{(l)} \rightarrow ClNO_{2(g)} + HNO_{3(l)} \quad \text{(R45)}$$
$$N_2O_{5(g)} + H_2O_{(l)} \rightarrow 2\ HNO_{3(l)} \quad \text{(R46)}$$
$$ClONO_{2(g)} + H_2O_{(l)} \rightarrow HOCl_{(g)} + HNO_{3(l)} \quad \text{(R47)}$$
$$ClONO_{2(g)} + HCl_{(l)} \rightarrow Cl_{2(g)} + HNO_{3(l)} \quad \text{(R48)}$$
$$HOCl_{(g)} + HCl_{(l)} \rightarrow Cl_{2(g)} + H_2O_{(l)} \quad \text{(R49)}$$

The preconditioning chemistry transfers the chlorine in reservoirs into photochemically active species like Cl_2 or $ClNO_2$.
After sunrise in the polar regions the preconditioned halogen species are photolysed to form very reactive radicals. These radicals are involved in catalytic cycles such as the ClO_x cycle (see reactions (R7) and (R8)). A major difference in chemistry of the polar stratosphere compared to the chemistry in mid-latitudes is the formation of the ClO dimer [Molina and Molina, 1987]. The formation of the ClO dimer is possible in the polar stratosphere due to the large amounts of ClO present and the low temperatures. The low temperatures are critical because the bond between both ClO molecules is very weak, so large vibrations in the molecule due to high temperatures will break the bond.

$$ClO + ClO + M \rightarrow (ClO)_2 + M \quad \text{(R50)}$$
$$(ClO)_2 + h\nu \rightarrow Cl + ClOO \quad \text{(R51)}$$
$$ClOO + M \rightarrow Cl + O_2 + M \quad \text{(R52)}$$
$$Cl + O_3 \rightarrow ClO + O_2$$
$$Cl + O_3 \rightarrow ClO + O_2$$

Net : $2\ O_3 + h\nu \rightarrow 3\ O_2$

In case of high BrO levels in the polar stratosphere ClO-BrO cycle proposed by [Yung *et al.*, 1980] is important.

$$ClO + BrO + M \rightarrow Br + OClO + M + h\nu \rightarrow Br + Cl + O_2 \quad \text{(R53)}$$
$$\rightarrow Br + ClOO + h\nu \rightarrow Br + Cl + O_2 \quad \text{(R54)}$$
$$\rightarrow BrCl + O_2 + h\nu \rightarrow Br + Cl + O_2 \quad \text{(R55)}$$
$$3\ (BrO + O_3 \rightarrow Br + O_2)$$
$$3\ (ClO + O_3 \rightarrow Cl + O_2)$$
$$BrO + O_3 \rightarrow Br + O_2$$
$$ClO + O_3 \rightarrow Cl + O_2$$

Net : $6\ O_3 + h\nu \rightarrow 9\ O_2$

Evidence for the ClO-BrO cycle can be detected by measurements of OClO using the DOAS technique (see below). OClO can be measured quite easy with this technique due to the characteristic absorption features in the UV region [Solomon *et al.*, 1987a]. The performance of all three catalytic cycles mentioned above leads to a dramatic reduction of Ozone in the polar stratosphere between 15 and 20 km altitude.
The Ozone concentrations in the polar stratosphere recover after the sun has increased the stratospheric temperatures substantially leading to a collapse of the polar vortex. The breaking up of the vortex is transferring stratospheric air masses from the mid latitudes into the polar regions and vice versa. These air masses contain much larger amounts of NO_x and Ozone. The NO_x will transfer large parts of the active chlorine species to their reservoirs again stopping the Ozone destruction.

Chapter 4

The Experimental Setup

DOAS instruments in general use scattered sky light to measure the abundance of atmospheric constituents by means of its absorption spectral features. Using airborne DOAS instruments altitude dependent abundance of atmospheric constituents can be retrieved from those measurements. This vertical sensitivity is the result of measurements in different directions simultaneously compared to most ground-based DOAS measurements pointing at the zenith only. This is not true for ground-based measurements performed at the Institute of Environmental Physics. These instruments are able to measure in multiple viewing directions, too. The simplest case of these vertical profiles is the separation of the tropospheric and stratospheric trace gas abundance, while the aircraft is flying near the tropopause. The main advantage of airborne DOAS measurements is the flexibility to measure trace gas abundance at different geolocations in contrast to fixed ground-based DOAS instruments. Another advantage of airborne DOAS measurements is the ability the retrieve vertical information on trace gases near flight altitude down to the lower troposphere. In contrast multi axis ground-based DOAS measurements are able to retrieve vertical trace gas information in the planetary boundary layer only.
This chapter is containing the description of the AMAXDOAS instrument in detail. This description comprehends the telescopes, the quartzfiber, the spectrometers, the detectors, and the wavelength calibration. Further this chapter covers the topic of data analysis. A brief introduction of the DOAS method is given as well as the specifications of the radiative transfer model SCIATRAN. The measurement geometry of the AMAXDOAS instrument is characterized as well. Last but not least the Meteosat system is described briefly because the Meteosat data is used later to interpret the retrieved profiles.

4.1 The AMAXDOAS Instrument

The Airborne MultiAXis Differential Optical Absorption Spectrometer is a joint venture of the University of Heidelberg and the University of Bremen. To ensure high spectral resolution of the AMAXDOAS measurements the instrument consists of two spectrometers; one in the visible and one in the UV wavelength region. This instrument is able to measure up to ten lines of sight (LOS) simultaneously using one telescope for each LOS and spectrometer. The light of each telescope is directed into the spec-

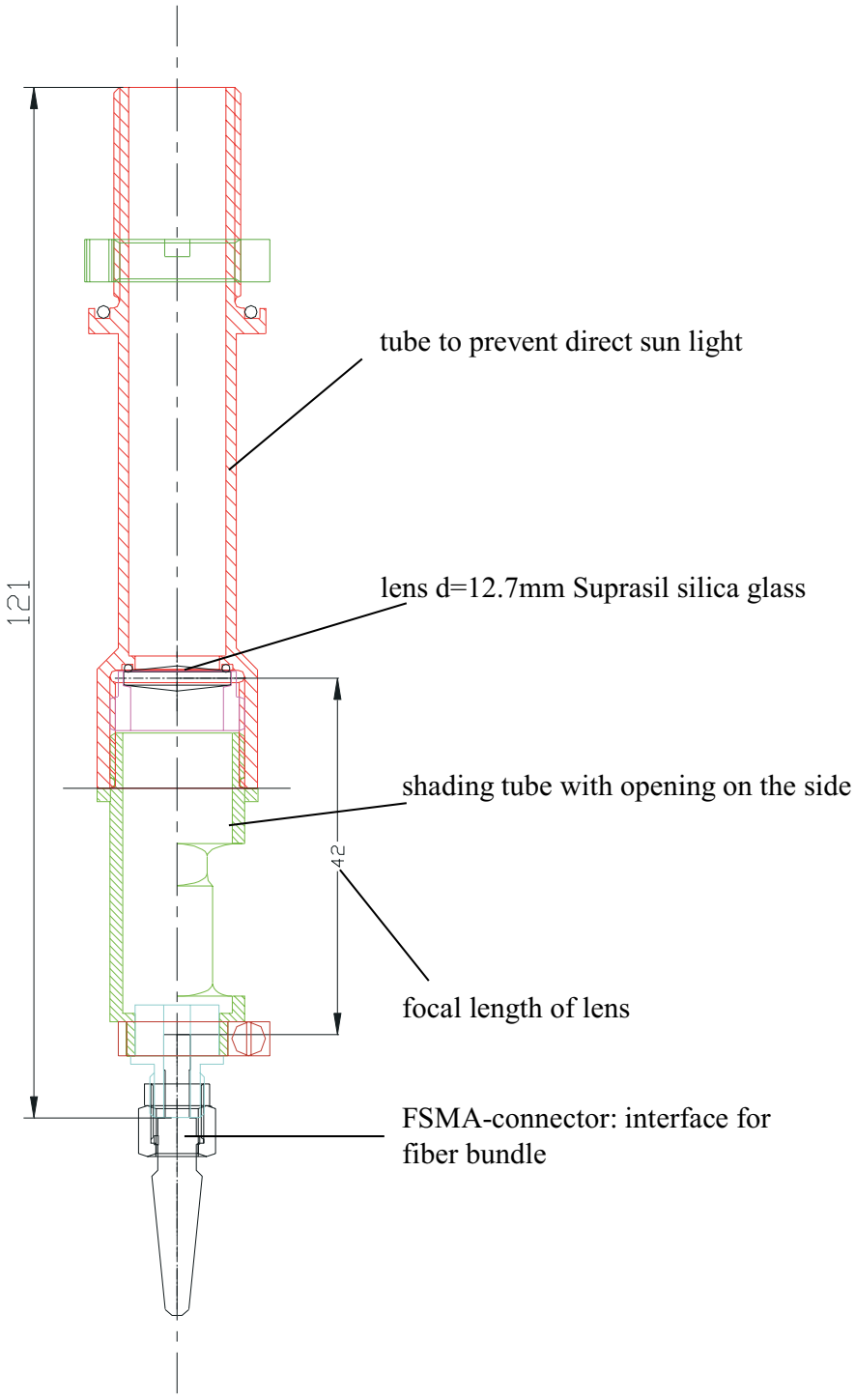

Figure 4.1: Schematic of one telescope of the AMAXDOAS instrument [Heue, 2004].

trometers using a custom made quartzfiber bundle. The spectrometers are designed to image the entrance slit to the focal plane. Therefore all LOS can be distinguished from one another. CCD cameras act as data acquisition devices.

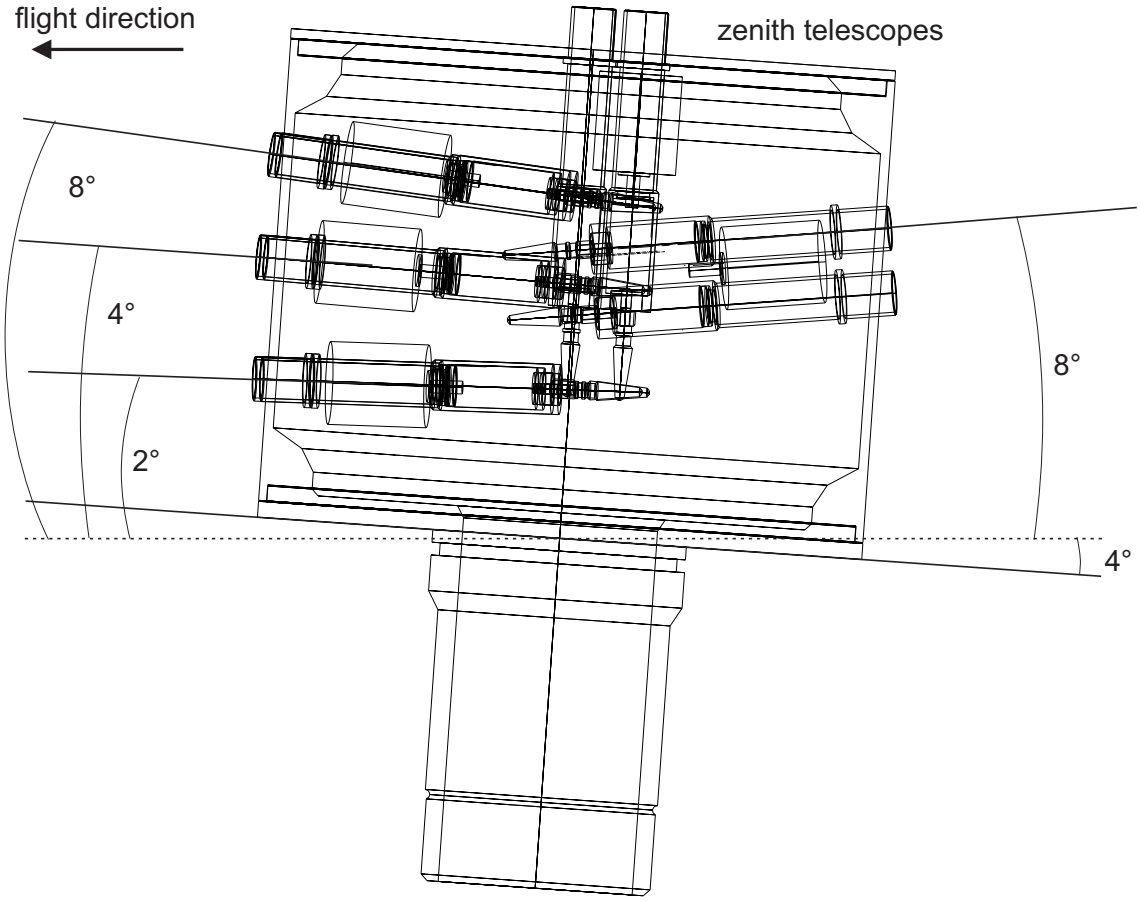

Figure 4.2: Schematic of the telescopes mounted inside the upper dome. The telescopes of the lower dome point 2°, 5°, and 8° below the horizon in flight direction, 8° below the horizon against flight direction, and towards the nadir [Heue, 2004].

4.1.1 The Telescopes

Two different concepts for the design of the telescopes had to be considered. The first concept comprehends one telescope per LOS and spectrometer. The advantage of this concept is the ability to measure all LOS simultaneously. The downside of this approach is the reduced Signal-to-Noise Ratio (SNR) (see below) of the measurements because all LOS have to be recorded simultaneously on the CCD chip. The second concept is to use one telescope per spectrometer and to inject the sky light from different LOS using a turnable mirror. The advantage of this concept is the significant improvement of the SNR, because the CCD chip is able to co add[1] over a large number of pixels. The disadvantages of this concept are the asynchronous recording of all LOS and moving parts in the experiment setup.
For the AMAXDOAS instrument the first concept using one telescope per LOS and spectrometer was adopted. In Fig. 4.1 the design of an individual telescope is presented [Heue, 2004]. It consists of an aluminum tube 12 mm in diameter, a lens 12.7 mm in

[1]Co adding is a feature of the CCD camera, which can add up defined clusters of pixel to be read out at once to reduce the readout noise (see section 4.1.4 'The CCD detector').

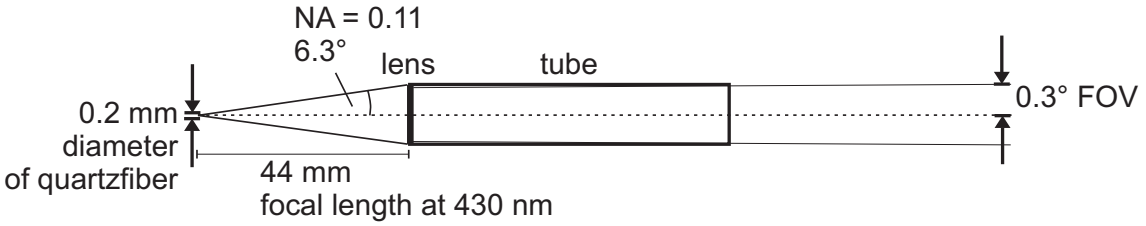

Figure 4.3: Schematic of the total FOV of an AMAXDOAS telescope [Heue, 2004].

diameter and a focal length of 44 mm at a wavelength of 430 nm, and a connector to attach the quartzfiber. The hole system of the telescope (diameter of quartzfiber, focal length and diameter of the lens, and the diameter and length of the tube[67.9 mm]) limits the field-of-view (FOV) to restrict light entering the telescope to the observed LOS. The telescope has an effective FOV of 0.6°, which translates to a width of the measurement of 100 m at a flight altitude of 10 km. The tube also protects the telescope against direct sun light in case an observed LOS is near the sun. The lower part of the telescope between the lens, and the connector of the quartzfiber has an opening to engage a shutter if necessary. The shutter is controlled by a photodiode right next to the telescope pointing towards the same LOS as the telescope acting as a sun sensor. In case the photodiode is illuminated by direct sunlight the shutter is closed to avoid direct sunlight from entering the quartzfiber and possibly damaging the latter. Another reason to avoid direct sunlight is that it is so much brighter than scattered sunlight it would make the CCD chip insensitive to the other LOS observing only scattered sunlight. The determination of the exposure time of the CCD-chip (controlled by the data acquisition software 'AMAXOMA' [Richter, 2003a]) is done by taking into account the pixel with the largest signal.
The design of the upper dome (the lower dome looks very similar) containing the telescopes mounted on top of the aircraft using a special opening in the aircraft's fuselage is presented in Fig. 4.2 [Heue, 2004]. The pairs of telescopes are mounted in the upper dome to achieve LOS angles of 262° (8° above the horizon backwards), 180° (zenith), 98°, 95°, and 92°. In the lower dome the LOS translate to 0° (nadir), 82°, 85°, 88°, and 278° (8° below the horizon backwards). As temperatures at flight altitudes (up to 39000 ft) are low, the domes are heated from the inside.

4.1.2 The quartzfiber Bundle

The AMAXDOAS instrument was flown in different setups. Therefore different quartzfiber bundles were designed. These quartzfiber bundles were custom made by Ceram-Optik (Bonn, Germany) and use circular shaped step-index fibers with a diameter of 150 μm. Step-index fibers are characterized by the large change of the refraction index at the boundary of the core and the cladding. To ensure the phenomenon of total reflection at the core/cladding boundary the refraction index of the cladding must be smaller than the refraction index of the cladding. The used fibers have a Numeric Aperture (N.A.) of 0.11. The Numeric Aperture can be converted to an aperture angle (θ) using following equation:

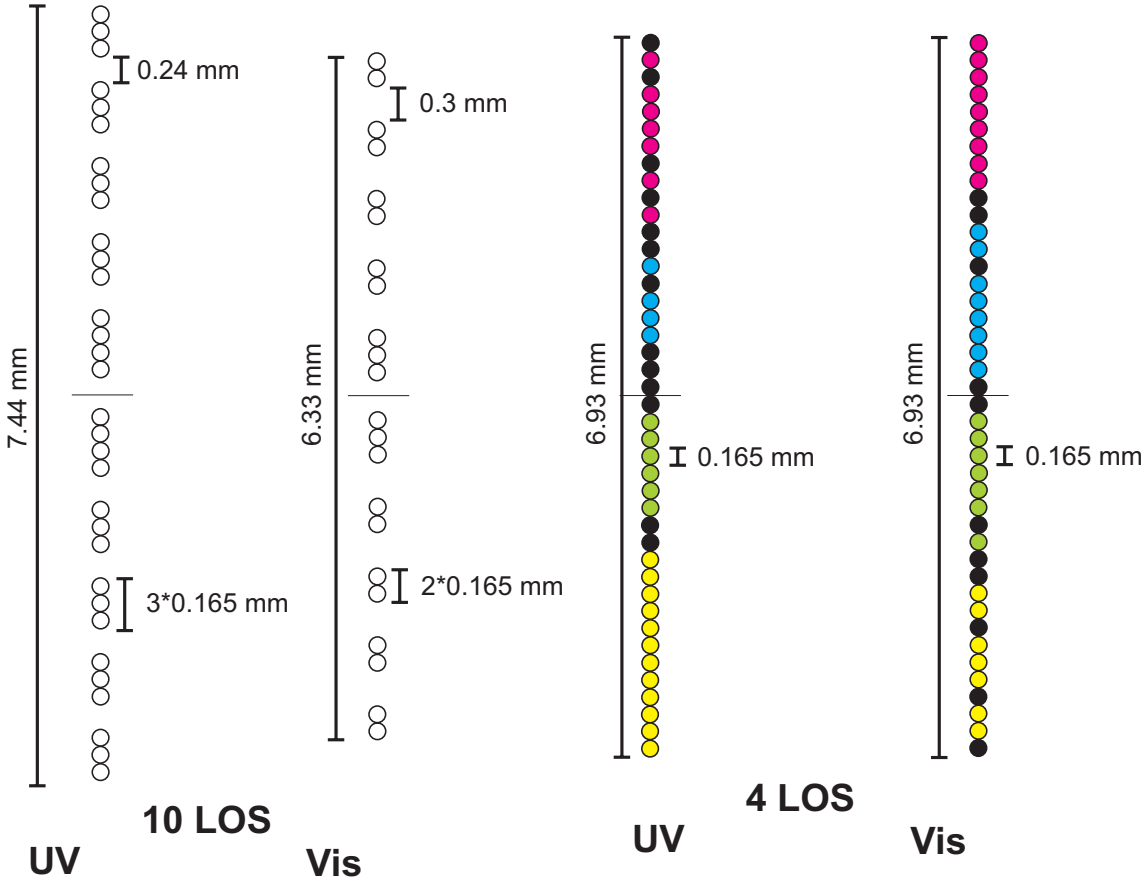

Figure 4.4: Schematic of the configuration of the individual fibers within the bundle for the ten and four LOS setups. Each fiber configuration is embedded into a metal adapter to fit into the entrance slit of the spectrometer. The diameter of one fiber is 150μm (core) plus two times 7.5μm (cladding). The colors indicate the allocation of the fibers to the LOS in the four LOS setup. The horizontal lines mark the position the adapter can be separated into parts coming from the upper and lower domes (see text).

$$N.A. \equiv \sqrt{n_1^2 - n_2^2} = n_0 sin(\theta) \tag{4.1}$$

where n_1 is the refraction index of the fiber core, n_2 is the refraction index of the cladding, and n_0 is the refraction index the medium surrounding the fiber. Since the AMAXDOAS instrument is operated in a dry environment, the enfolding medium is air with a refraction index of approximately 1. Using eq. 4.1 and the value of 0.11 as N.A. an aperture angle of 12.6° is calculated.

Originally the AMAXDOAS instrument was designed to have ten different LOS (five upward and five downward looking). The configuration of the individual fibers is represented in Fig. 4.4. Each LOS consists of three fibers for the UV and two fibers for the visible instrument except for two LOS of the UV bundle containing four fibers and two LOS of the vis bundle containing three fibers. The reason for the two LOS having one additional fiber is that the nadir and the zenith LOS proved to have a very low intensity. The nadir LOS usually experiences low intensities when flying over areas with

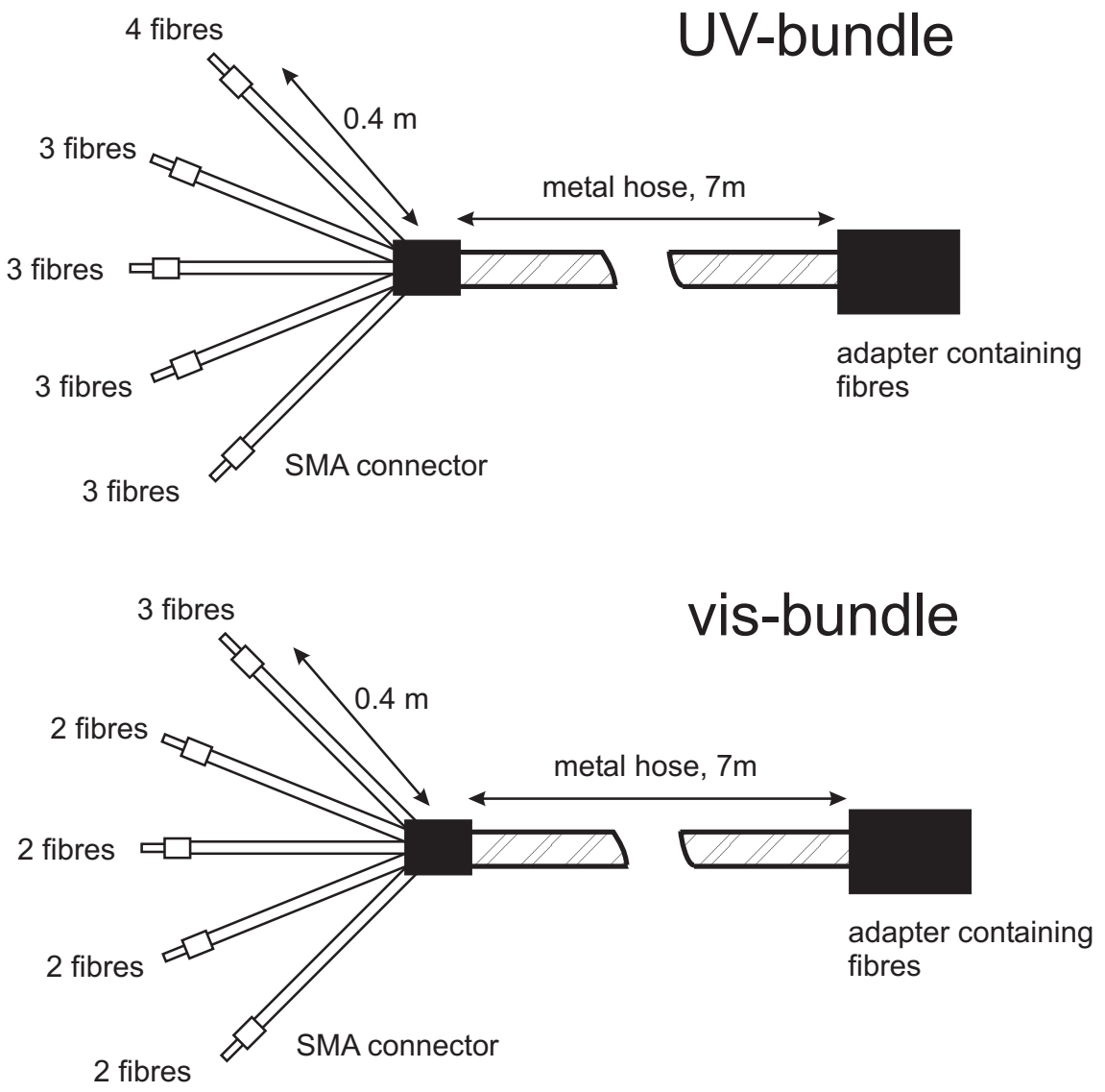

Figure 4.5: Schematic of the configuration of the two bundles for the ten LOS setup. The two bundles of the four LOS setup look the same, but they have only two SMA connectors each.

a low albedo, which is mostly the case except in high latitudes with an snow covered surface. The zenith LOS is experiencing low intensities due to the thin atmosphere above the aircraft. As can be seen in Fig. 4.4 the fiber bundle configurations for the UV and the visible instrument have different dimensions due to different sizes of the CCD chips for the two instruments.

To assure a clear separation of each LOS 'dark' fibers are used between the LOS to keep a certain distance. These 'dark' fibers were included to reduce the influence of stray light on the CCD chip from other LOS on a specific LOS. Each fiber configuration is embedded into a metal adapter (19 mm by 6.4 mm) using a rectangular to circular (25 mm diameter) converter to fit into the entrance slit mounting of the spectrometer.

The analysis of the data of the second test flight campaign has shown that the SNR of measurements using ten LOS is much smaller compared to those using a setup with

two LOS (nadir and zenith), which was flown in the first test flight campaign. For the two main campaigns it was decided to use a compromise setup containing four LOS (nadir, 2° below the horizon, 2° above the horizon, and zenith) to enhance the SNR. The fiber configuration of the four LOS setup is presented in Fig. 4.4 on the right hand side. The allocation of the individual fibers to its LOS is not as clear as for the ten LOS setup. This is because of the reuse of an existing quartzfiber bundle that has been used in the first test flight campaign already. This bundle suffered from broken fibers, so each fiber in the schematic was color coded to allocate it to a LOS.

The design of the whole quartzfiber bundle is shown in Fig. 4.5. The individual fibers of each LOS shown in Fig. 4.4 are separated from the bundle and equipped with an SMA connector to be connected to the corresponding telescope (see Fig. 4.1 and 4.2). A UV and vis quartzfiber bundle is needed for each dome adding up to four quartzfiber bundles in total to connect the telescopes of each of the two AMAXDOAS domes to the two spectrometers. Because of this design two parts (one coming from the lower and one coming from the upper dome for each spectrometer) of the adapters shown on the right of Fig. 4.5 have to be connected to fit into the entrance slit mounting of the spectrometers. The adapters had to be made separable because the SMA connectors for all LOS had to be connected to the telescopes before installing the domes on the aircraft.

4.1.3 The Spectrometer

For the spectral decomposition of light the AMAXDOAS instrument is using two grating spectrometers made by Acton Research Corp. with a focal length of 300 mm. This type of spectrometer (see Fig. 4.6) is characterized by two parabolic mirrors. The first one is focused on the entrance slit providing the grating with parallel light. The second parabolic mirror is focused on the image plane where the CCD camera is located.
The main characteristic is the resolution of the spectrometer. The resolution is influenced by the choice of the grating, the width of the entrance slit, and the focal length of the parabolic mirrors. Considering a given grating consisting of N grooves the resolution is calculated by:

$$\frac{\lambda}{\delta\lambda} = mN \tag{4.2}$$

where m is the order of diffraction, which is used for operation of the spectrometer, λ is the wavelength, and $\delta\lambda$ is the limit in the difference of wavelengths the s pectrometer can resolve. Considering the given size of the grating (68 mm × 68 mm) and a grating with 600 lines/mm the spectrometer has a total number of 40800 grooves. Assuming a wavelength of 350 nm in the UV $\delta\lambda$ is 0.009 nm and a wavelength of 450 nm in the visible $\delta\lambda$ is 0.011 nm. This is the theoretical resolution of the grating. To get the theoretical resolution of the spectrometer/detector system it is crucial to know the linear dispersion $dx/d\lambda$ in the focal plane:

$$\frac{dx}{d\lambda} = fcos\Theta\frac{d\Theta}{d\lambda} = \frac{fm}{g} \tag{4.3}$$

where f is the focal length, $d\Theta/d\lambda$ is the angular dispersion, and g is the grating

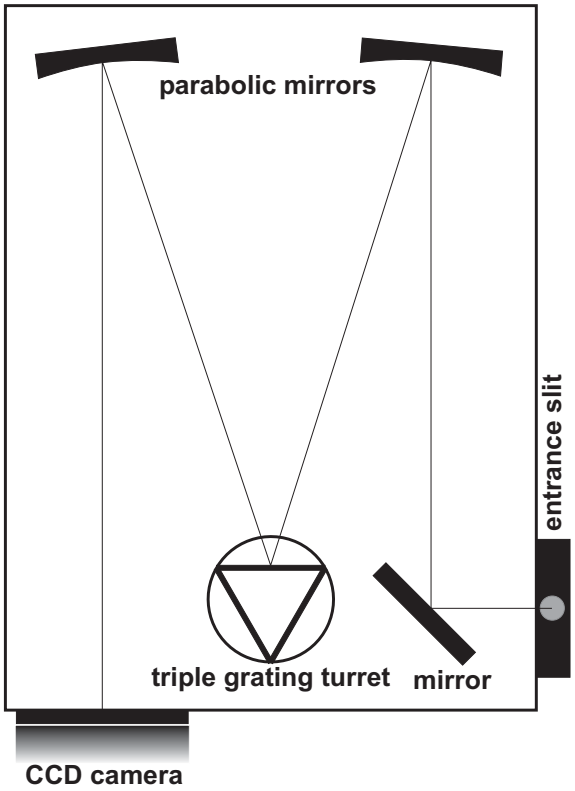

Figure 4.6: Schematic of a Czerny-Turner spectrometer.

constant. Assuming perpendicular incoming light ($\Theta \approx 0$) the inverse linear dispersion is 5.56 nm/mm. With a pixel size of 20 μm the spectral resolution of the spectrometer/CCD-camera combination is 0.11 nm. Thus the spectral resolution of the spectrometer is about an order of magnitude lower than the spectral resolution of the grating. To calculate the real resolution of the instrument the slit function has to be considered. The mathematical treatment of this subject will be omitted in this thesis [Richter, 1997].

Both spectrometers of the AMAXDOAS instrument (see Tab. 4.1) are equipped with turrets holding several gratings. The turret enables the operator to choose between different gratings by turning the desired grating into position. To achieve a high stability of the wavelength calibration, the turret was not turned during the measurement campaigns. A high stability of the wavelength calibration enables the comparison of measurements taken at different times. For the same reason it is important to prevent temperature drifts of the spectrometer because differences in spectrometer temperatures will affect wavelength calibration due to thermal expansion of the spectrometer. To avoid temperature drifts both spectrometers are heated using adhesive heating foils. The heating is controlled by a thermostat minimizing the temperature drifts to 0.1° K. Since the spectrometers are heated only, the thermostat fails in case the surrounding temperature exceeds the target value of 35° C of the thermostat. This was occasionally the case in the tropics on both SCIA-VALUE campaigns in 2002/2003. Thus the thermostat was set to 40°C.

Table 4.1: Characteristics of the AMAXDOAS spectrometers.

	UV	vis
grating [lines/mm]	600.0	300.0
blaze wavelength [nm]	300.0	500.0
resolution of grating [nm]	0.009	0.022
resolution of spectrometer [nm]	0.11	0.15
real resolution of instrument [nm]	0.7	1.0
focal length [mm]	300.0	300.0
slit width [μm]	150.0	150.0

4.1.4 The CCD Detector

The AMAXDOAS instrument uses two CCD detectors (see Tab. 4.2) as data acquisition devices one in the UV and one in the visible wavelength range. The information on CCD cameras presented in this section was taken from [Pfanhauser, 2004].
In the pure crystalline form, each silicon atom has a covalent bond with each neighbor. Only energy greater than the band gap energy is able to break such a bond and create an electron-hole pair. Usually light enters a CCD chip through gates of the parallel register of front-illuminated CCD chips. These gates are made of very thin layers of polysilicon. At longer wavelength above 400 nm these gates are reasonably transparent, but they become opaque at shorter wavelength below 400 nm. Hence gate structures attenuate incoming UV light. Sophisticated acid-etching techniques are able to uniformly reduce the thickness of a CCD to approximately 10 μm. Now the image can be focused on the back side of the CCD register (back-illuminated CCD, see Fig. 4.7). This technique increases the sensitivity (quantum efficiency) of a CCD chip in the blue and

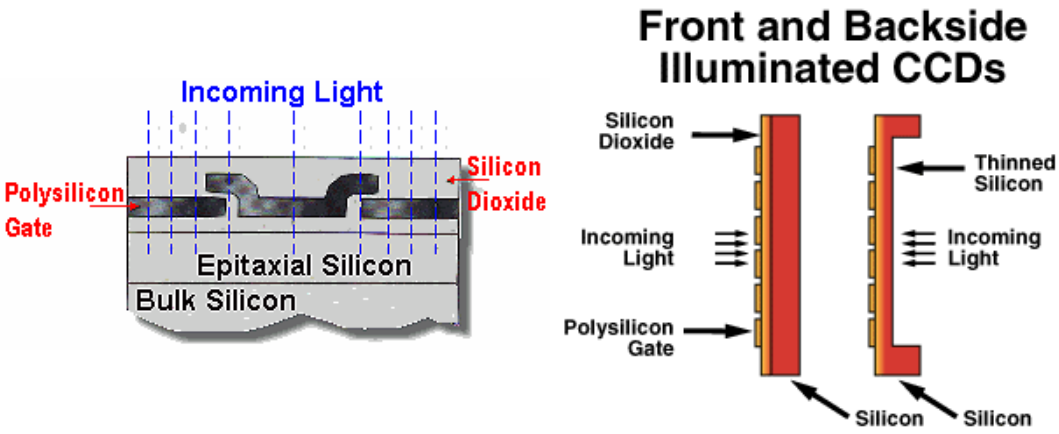

Figure 4.7: Schematic of the mode of operation of a CCD chip [Pfanhauser, 2004].

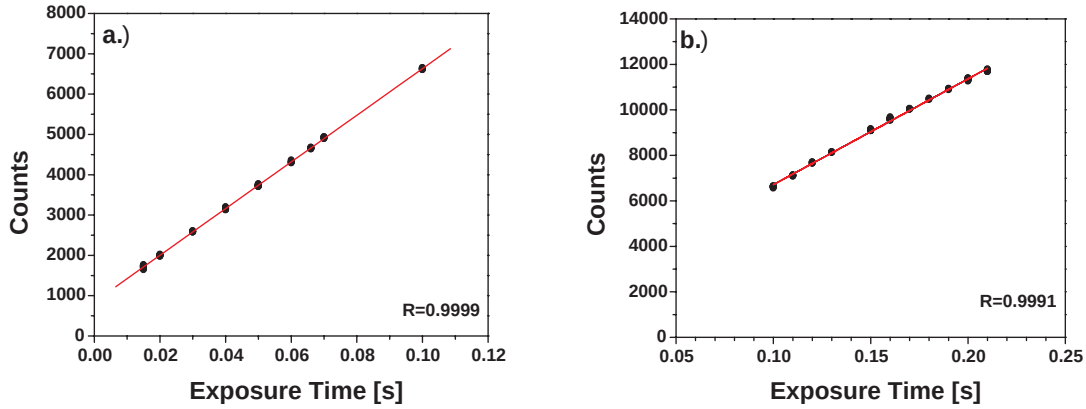

Figure 4.8: Linearity plots of the Roper CCD taken from [Wang, 2004].

UV wavelength regions.
CCD chips are specified by a large number of characteristics. The quantum efficiency is the effectiveness of a CCD chip to produce electron-hole pairs from incident photons. There is the Full Well Capacity (FWC). The FWC indicates the amount of electron-hole pairs a single pixel[2] can hold. The FWC is depending on the pixel size because larger pixels can hold more electron-hole pairs. The FWCs of the CCD detectors used in the AMAXDOAS instrument can be found in Tab. 4.2. When the FWC of a chip's pixel is reached, then the pixel is saturated. This has to be avoided by setting the exposure time accordingly, because saturation of a single pixel is also effecting the linear behavior of the chip and pixels in the vicinity of the saturated pixel. This effect is called 'blooming'.
Another characteristic is the linearity of the CCD chip. The linearity is strongly related to the physical process of converting the photonic input to electronic output. Incoming photons will be converted to electron-hole pairs and the electrons will be captured beneath the gate electrodes. An amplifier converts these electrons to a voltage output signal ready to be digitized. The transfer function between the incoming photonic signal and the digitized output should be linear:

$$Digital\ Signal = constant \times amount\ of\ incoming\ light \tag{4.4}$$

CCDs used for quantitative imaging are required to have a very good linearity. There is no standard method for measuring linearity. One method is to plot the mean signal value versus the exposure time. A linear least square fit can be used to calculate the deviation in each data point. The sum of the maximum and minimum deviation divided by maximum signal in percentage is a measure for the non-linearity of the CCD.

$$nonlinearity(\%) \equiv \frac{(\sigma_{pos} + \sigma_{neg})}{S_{max}} \cdot 100 \tag{4.5}$$

[2]The term 'pixel' is an abbreviation for the term 'picture element' and refers to the smallest component of an image.

Table 4.2: Characteristics of the AMAXDOAS CCD detectors.

	UV	vis
chip size [mm^2]	26.8×8.0	27.6×6.9
pixel size [μm]	20.0	13.5
quantum yield	0.47 @ 350 nm	0.1 @ 450 nm
linearity [%]	0.0	1.0
system read noise @ 1 MHz		
digitization [e$^-$/pixel]	8.0	10.0
dark current @ -40° C [e$^-$/pixel/s]	0.1	<0.1
Full Well Capacity [e$^-$/pixel]	250000.0	500000.0

where σ_{pos} is the maximum positive deviation, σ_{neg} is the maximum negative deviation, and S_{max} is the maximum signal. Fig. 4.8 shows the two linearity plots for the Roper CCD [Wang, 2004] used in the AMAXDOAS UV instrument at two exposure time ranges. Using eq. 4.5 the nonlinearity for this CCD can be calculated to be 1,7% for Fig. 4.8a and 2.7% for Fig. 4.8b.

Electronic circuits in general generate undesirable noise. There are different noise sources in the CCD camera. First there is the so-called photon noise. It is a fundamental characteristic due to the quantum nature of light. The total number a steady source is emitting over a random time interval is changing according to the Poisson distribution. The Poisson distribution describes processes in general, which are independently distributed (i.e. temporal or spatial). For Poisson distributions the noise is equal to the square root of the signal. In other words photon noise is simply the uncertainty of the data:

$$n_{photon} = \sqrt{I\phi t} \tag{4.6}$$

where n_{photon} is the photon noise, I is the photon flux in [photons/pixel/sec], ϕ is the quantum yield, which is the efficiency of the semiconductor material to convert photons to electrons in [electrons/photon], and t is the exposure time in [sec]. In addition to the photon noise there is the readout noise generated by the on-chip output amplifier. This noise source can be reduced by binning several pixels of the CCD chip into a super pixel. Because readout noise occurs only during readout, the readout process of the super pixel is only one event compared the x readout events of the x individual pixels forming the super pixel. The last noise component is coming from the dark current. The dark current is a thermally generated charge that cannot be distinguished from charges generated by photons. The dark current can only be measured, when taking a measurement in complete darkness. Thus it is called dark current. Therefore the total noise of the CCD chip is:

$$n = \sqrt{I\phi t + n_{dark}t + n_{read}^2} \tag{4.7}$$

where n_{dark} is the dark current noise in [electrons/pixel/sec] and n_{read} is the readout noise in [electrons/pixel]. Having introduced the noise of the CCD the next important characteristic of the CCD is the (SNR). SNR describes the quality of the measurements.

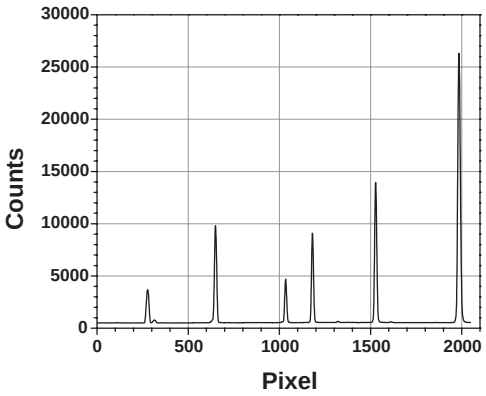

Figure 4.9: HgCd spectrum for wavelength calibration taken on March 17 2003 using the visible spectrometer of the AMAXDOAS instrument.

It refers to the relative magnitude of the signal compared to the noise of the CCD. As shown above the noise is the uncertainty of the signal on a per-pixel basis. High values of the SNR indicate a measurement of high quality. When calculating the noise of a CCD, all noise sources have to be considered as discussed above. Using eq. 4.7 the SNR is:

$$SNR \equiv \frac{I\phi t}{\sqrt{I\phi t + n_{dark}t + n_{read}^2}} \tag{4.8}$$

where $I\phi t$ is the measured signal.
Considering the noise issue it has to be noted that the noise due to dark current is corrected by subtracting a dark current signal from the measurements. The dark current signal is recorded after touch down of the aircraft.
During digitization of the analog signal of the CCD camera another noise component called 'digitization noise' is occurring, but it can be neglected.

4.1.5 Wavelength Calibration

To ensure a high data quality it is necessary to perform a precise wavelength calibration. For this process the light of a HgCd line lamp is used. These calibration measurements were performed after each flight and each LOS was calibrated separately. Therefore a tube was attached to the case of the lamp. This tube had a diameter slightly larger than the tubes of the telescopes for those to fit in. To enable a uniformly illuminated field of view of the telescopes a diffuser plate made of Teflon was engaged between the lamp and the telescopes.
The line positions have to be known very accurately (small fractions of a detector pixel). To guarantee such an accuracy the positions of the lines have to be calculated very precisely [Richter, 1997]. There are two methods to calculate these positions:

1. determination of the line maximum using interpolation. This method uses cubic

spline interpolation [Press *et al.*, 1989] or Akima interpolation [Hilberg, 1989]. The maximum of the interpolated line is considered to be the center of the line.

2. determination of the center of mass [Falk, 1984]. This method calculates the first momentum of the spectral line:

$$\bar{x} = \frac{\sum_{i=-p}^{p} x_i y_i}{\sum_{i=-p}^{p} y_i} \tag{4.9}$$

where x_i represents the pixel number, y_i is the measured intensity at x_i. The line width $2p$ has to be chosen carefully so the line is acquired in total. Further no other line is allowed to influence the center of mass of the considered line.

Since the line positions are known very accurately from laboratory measurements, these wavelengths are fitted to the calculated line positions using a linear least square fit. Fig. 4.9 shows a measured line spectrum of the AMADOAS instrument.

4.2 The SCIAMACHY Instrument

In this chapter a brief description of the satellite instrument SCanning Imaging Absorption spectroMeter for Atmospheric CHartographY (SCIAMACHY) [Burrows and Chance, 1992] will be presented. For a more detailed description see [Bovensmann *et al.*, 1999] and references therein. In March 2002 ESA's ENVISAT was launched. One experiment onboard ENVISAT called SCIAMACHY is a space-based spectrometer covering almost completely the UV-VIS-NIR spectral range from 240 up to 2380 nm. Using measurements of the extraterrestrial solar irradiance and the earthshine radiance, i. e.

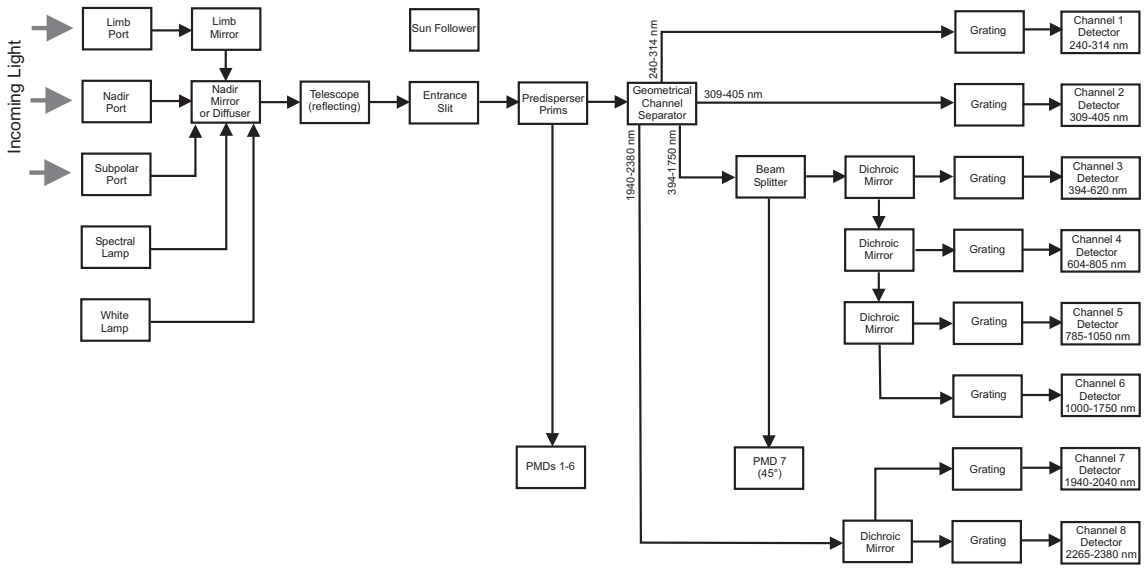

Figure 4.10: Schematic view of the optical layout of the SCIAMACHY instrument. All imaging components such as mirrors, prisms, and lenses are omitted.

sunlight, which is transmitted, reflected, and scattered by the earth's atmosphere or surface, SCIAMACHY is able to detect the amounts of several trace gases (O_3, O_2, O_4, BrO, OClO, SO_2, H_2CO, NO, NO_2, CO, CO_2, CH_4, H_2O, N_2O). Further SCIAMACHY is measuring the amounts of clouds and aerosols. The SCIAMACHY spectrometer has a moderate resolution of 0.21 to 1.56 nm depending on the considered channel. SCIAMACHY comprehends a mirror system, a telescope, a spectrometer, several detectors, and thermal and electronic subsystems (see Fig. 4.10). Radiation enters the instrument using one of three ports:

1. the earthshine radiation used for nadir measurements is directed into the spectrometer by a nadir mirror, which is pointed at the telescope focusing on the entrance slit of the spectrometer.

2. the radiation (earthshine, direct sun, or moonshine) used for limb and solar/lunar occultation is reflected by the limb mirror to the nadir mirror, which directs the radiation into the telescope. The telescope focuses the radiation onto the entrance slit of the spectrometer.

3. the radiation (line lamps and solar) used for internal and sub solar calibration measurements is directed by the nadir mirror into the telescope.

To enhance the lifetime of SCIAMACHY there are few movable parts. The only movable parts are the scan mirrors and a shutter. It is very important to minimize stray light as the measured intensities differ by several orders of magnitude in different spectral regions. This is achieved by combining predispersing prisms and gratings. Light coming from the entrance slit is collimated and directed onto the predispersing prism. This design forms a spectrum in the middle of the instrument. A reflective optical system splits the spectrum into four parts:

1. the shorter wavelengths of the spectrum are directed into channel 1 (240-340 nm).

2. radiation containing wavelengths between 314 and 405 nm are directed into channel 2.

3. the main part of the beam (405-1750 nm) passes without reflection to channels 3 to 6.

4. the infrared part of the spectrum (1940-2380 nm) is reflected to channels 7 and 8.

Dichroic[3] mirrors are used to separate the wavelength ranges for channels 3,4,5,6,7, and 8. Each individual channel comprehends a grating, transmission optics, and a 1024 pixel diode array as a detector. To reduce detector noise and dark current the detectors are cooled: the detectors of channel 1 and 2 are cooled to 200 K, channels 3-5 to 235 K, channel 6 to 200 K, and channel 7 and 8 to 150 K. The whole system is cooled to 235 K to minimize infrared emissions that influences the detectors of channels 6-8.

[3]Dichroism is the selective absorption of one polarization component using specific birefringent materials. The simplest dichroic system is a metal grating with a grating constant in the order of the wavelength of the considered radiation. This grating is transmittant perpendicular to the alignment of the grating. Parallel aligned waves are dissipated due to friction caused by the oscillation of the electrons.

4.3 Data Analysis

The data measured with the AMAXDOAS or SCIAMACHY instruments are analyzed using the Differential Optical Absorption Spectroscopy (DOAS) method. In this chapter a brief overview of the DOAS method will be given. Important terms such as vertical column, slant column, solar zenith angle (SZA), and air mass factor (AMF) will be discussed. A more detailed description of this method can be found at [Noxon, 1975; Perner and Platt, 1979; Platt and Perner, 1980; Solomon *et al.*, 1987a; Perliski and Solomon, 1993]. This chapter also deals with the description of the radiative transfer model SCIATRAN, which is necessary to calculate the AMFs.

4.3.1 The DOAS Method

The DOAS method is based on the identification of atmospheric trace gases by the features of its absorption spectra in the UV and visible spectral range. This method is applied to spectra of scattered skylight measurements. The abundance of the absorber in the atmosphere is proportional to the absorption along the light path through the atmosphere. These slant columns[4] are converted into vertical columns by radiative transfer model calculations (see below). The vertical column is the vertical integral of the absorber density from the earth's surface to the top of atmosphere.
According to Beer's Law the intensity I of a light beam in a homogenous absorbing medium is decreasing exponentially with increasing light path s:

$$I(\lambda) = I_0(\lambda)\exp(-s\rho\sigma(\lambda)) \tag{4.10}$$

where I_0 is the intensity in absence of the absorbing medium, λ is the wavelength, ρ is the absorber density, and $\sigma(\lambda)$ is the absorption cross section of the absorber. In the real atmosphere there are several absorbers present, therefore an ensemble of absorbers have to be considered during data analysis. For J absorbers eq. 4.10 becomes:

$$I(\lambda) = I_0(\lambda) \cdot \exp\left(-\sum_{i=1}^{J}\left[\sigma_i(\lambda) \cdot \int_s \rho_i(s)\mathrm{d}s\right]\right); \quad SC_i(\theta) \equiv \int_s \rho_i(s(\theta))\mathrm{d}s \tag{4.11}$$

The integral is calculated along the light path, so the defined slant column depends on the solar zenith angle (SZA) θ and the wavelength λ.
In addition to absorption scattering on molecules and aerosols also occurs in the atmosphere. This phenomenon is treated in approximation as attenuation of the light beam according to Beer's Law. In this case the scattering cross sections are used as absorption cross sections. Rayleigh scattering, Mie scattering, and Raman scattering is taken into account. The Raman scattering is responsible for the so-called 'Ring-Effect' [Grainger and Ring, 1962; Solomon *et al.*, 1987a; Vountas *et al.*, 1998].
Eq. 4.11 is not useful for the calculation of the slant columns because the contributions of each single process (absorption, scattering) are inseparable due to large variations in the intensity (clouds, twilight). The solution to this problem is the separation of the

[4]To be more precise a slant column is rather a slant column density, but both terms are used synonymously. This is true for the vertical column as well.

absorption cross section in two components. The first component takes into account the smooth variations of the cross sections only whereas the second component includes the rapid variations of the spectral features of the cross sections. This separation is achieved by the subtraction of a fitted polynomial of lower order.

$$\ln I_0(\lambda) - \ln I(\lambda) = \sum_p [a_p \cdot \lambda^p] + \sum_i \sigma_i'(\lambda) \cdot SC_i \tag{4.12}$$

where a_p are the polynomial coefficients, p is the index of the order of the polynomial, and SC_i are the slant column of the absorbers. These are the quantities searched for by the fitting process. σ_i' are the differential absorption cross sections, which are calculated using the cross sections measured in the laboratory and subtract a fitted polynomial.

When dealing with atmospheric sky light measurements, an appropriate reference spectrum I_0 has to be chosen. The ideal choice would be an extraterrestrial spectrum, but this is only available for space-based instruments. For airborne and ground-based instruments a reference spectrum I_0^M recorded at high sun (lowest SZA possible) is used. In this case eq. 4.12 is becoming:

$$\ln I_0^M(\lambda) - \ln I(\lambda) = \sum_p [a_p \cdot \lambda^p] + \sum_i \sigma_i'(\lambda) \cdot \underbrace{(SC_i - SC_i^M)}_{\Delta SC_i} \tag{4.13}$$

ΔSC_i are the differential slant columns because a reference spectrum recorded within the atmosphere was used. This reference spectrum is containing an absorption caused by a specific abundance of the trace gas present at the time, when the reference spectrum was recorded. After having determined the differential slant columns the AMF are needed to convert the differential slant columns into vertical columns. The AMF is defined as:

$$\mathrm{AMF}_j(\lambda, \theta) \equiv \frac{\mathrm{SC}_j(\lambda, \theta)}{\mathrm{VC}_j} \tag{4.14}$$

$$\underbrace{AMF(\lambda, \theta) - AMF(\lambda, \theta_M)}_{\Delta \mathrm{AMF}_j(\lambda, \theta, \theta_M)} = \frac{\overbrace{\mathrm{SC}_j(\lambda, \theta) - \mathrm{SC}_j(\lambda, \theta_M)}^{\Delta \mathrm{SC}_j(\lambda, \theta, \theta_M)}}{\mathrm{VC}_j} \tag{4.15}$$

where θ is the SZA and θ_M is the SZA of the reference spectrum. Thus the AMF represents the enhancement of the slant column compared to the vertical column. The AMF are calculated using a radiative transfer model, which simulates the light path through the atmosphere. It has to be noted that for this work the conversion of the AMAXDOAS slant columns into vertical columns is not necessary, since the profile retrieval is based on using slant columns as can be seen later.

4.3.2 Data Analysis of AMAXDOAS Data

The DOAS method described in the previous section was used to analyze the AMAX-DOAS raw data. After wavelength calibration (described above in this chapter) the

data were corrected for stray light. This correction is necessary, because every optical component of the instrument is causing stray light, has imperfections, and may be a little bit unclean.
The stray light correction performed on the data was different for the two spectrometers of the AMAXDOAS instrument. For the visible spectrometer a CCD line showing no spectral features was used to subtract the value of each pixel of this line from the corresponding pixels of all other CCD lines containing atmospheric spectral data. This process was done for each measured CCD image separately containing the data of all LOS of the instrument. For each measured CCD image its own line containing the stray light correction data was determined and subtracted from all other CCD lines containing atmospheric spectral data.
For the UV spectrometer the stray light correction was done a little bit differently, because no line existed that contained any spectral features. Instead the averaged value of the first 20 pixels of the end of the spectrum containing the shortest wavelengths (approx. at 305 nm) was subtracted from the whole spectrum. Again this process was repeated for every single spectrum. The reason for this type of stray light correction assumption that no light at 305 nm is able to reach the detector, because the intensities at this wavelength are very small. Further it is assumed that stray light is independent of wavelength, which in reality is not the case. The stray light correction of the AMAXDOAS data was done by Wang [2004].
The exposure times used by the CCD camera usually is about one to two seconds, but the data are intregrated (averaged) over certain time intervals. For the UV spectrometer this time interval is ten seconds and for the visible spectromter the integration time is about 32 seconds.
The description the fitting process of the AMAXDOAS data is described in chapter 9 'Profile Retrieval using real AMAXDOAS data'.

4.3.3 The Radiative Transfer Model SCIATRAN

The radiative transfer model SCIATRAN[5] [Rozanov *et al.*, 1997; Kurosu *et al.*, 1997; Rozanov *et al.*, 2000, 2001, 2002] is calculating a numerical solution of the radiative transfer equation. For nonlimb-viewing geometry the integral form of the radiative transfer equation can be written as [Chandrasekhar, 1960]:

$$\begin{aligned} I_{\mathrm{dif}}(\mathbf{r},\mathbf{s}) =& I_{\mathrm{dif}}(\mathbf{r}_0,\mathbf{s})e^{-\tau(\mathbf{r}_0,\mathbf{r})} \\ &+ \int_r^{r_0} B_{ms}(\tilde{\mathbf{r}},\tilde{\mathbf{s}})\alpha(\tilde{r})e^{-\tau(\tilde{\mathbf{r}},\mathbf{r})}J(\tilde{\mathbf{r}},\tilde{\mathbf{s}})d\tilde{r} \\ &+ \int_r^{r_0} B_{ss}(\tilde{\mathbf{r}},\tilde{\mathbf{s}})\alpha(\tilde{r})e^{-\tau(\tilde{\mathbf{r}},\mathbf{r})}J(\tilde{\mathbf{r}},\tilde{\mathbf{s}})d\tilde{r} \end{aligned} \tag{4.16}$$

where $\mathbf{r}$ is the point[6] in the atmosphere where the radiance will be calculated, $I_{\mathrm{dif}}(\mathbf{r}_0,\mathbf{s})$ is the diffuse radiance at the atmospheric boundary $\mathbf{r}_0$ (i.e. top or bottom) in direction[7] $\mathbf{s}$, α is the total extinction coefficient, $B_{ms}(\tilde{\mathbf{r}},\tilde{\mathbf{s}})$ and $B_{ss}(\tilde{\mathbf{r}},\tilde{\mathbf{s}})$ are the multiple

[5]The ancestor of SCIATRAN is the GOMETRAN radiative transfer model
[6]The vector $\mathbf{r}$ is characterized by the three coordinates r, Ψ, and Φ.
[7]The direction $\mathbf{s}$ is defined by the two angles Θ and φ.

and single scattering source functions, and $J(\tilde{\mathbf{r}}, \tilde{\mathbf{s}})$ is the Jacobian, which is responsible for the transformation of the coordinates. τ is the optical depth between two arbitrary points $\mathbf{r}_1$ and $\mathbf{r}_2$ in the atmosphere.

$$\tau(\mathbf{r}_1, \mathbf{r}_2) = \int_{r_1}^{r_2} \alpha(\tilde{r}) J(\tilde{\mathbf{r}}, \tilde{\mathbf{s}}) d\tilde{r} \tag{4.17}$$

The multiple-scattering source function depends on the diffuse radiance $I_{\text{dif}}(\mathbf{r}, \mathbf{s})$:

$$B_{ms}(r, \Psi, \Theta, \gamma_0) = \frac{\omega(r)}{4\pi} \int_0^{2\pi} d\tilde{\varphi} \int_0^{\pi} d\tilde{\Theta} p(r, \gamma) I_{\text{dif}}(r, \Psi, \tilde{\Theta}, \tilde{\varphi}) \tag{4.18}$$

where $\omega(r)$ is the single-scattering albedo, $p(r, \gamma)$ is the scattering phase function considering a scattering angle γ depending on $\Theta, \varphi, \tilde{\Theta}, \tilde{\varphi}$. The single-scattering source function is given by:

$$B_{ss}(r, \Psi, \gamma_0) = \frac{\omega(r)}{4} \mathrm{F}_0 p(r, \gamma_0) \exp\left(- \int_r^{r_t} \alpha(\tilde{r}) J(\tilde{\mathbf{r}}, \tilde{\mathbf{s}}_\mathbf{0}) d\tilde{r} \right) \tag{4.19}$$

where $\tilde{\mathbf{s}}_\mathbf{0}$ is the direction of the solar beam at location $\tilde{\mathbf{r}}$, $\pi \cdot F_0$ is the incoming solar flux, r_t represents the top of atmosphere, and γ_0 is the scattering angle between the direct solar beam and the LOS. Thus γ_0 is a constant along the line of integration in an atmospheric model neglecting refraction.
The simplest way to solve eq. 4.16, 4.18, and 4.19 is a plane parallel approximation. Assuming a plane-parallel atmosphere means the angle variables Ψ, Θ, and φ do not change along the LOS. Thus B_{ms} and B_{ss} depend only on r. The Jacobians can be written like this:

$$J(\mathbf{r}, \mathbf{s}) = -\frac{1}{\cos\Theta}, \qquad J(\mathbf{r}, \mathbf{s}_0) = \frac{1}{\cos\Psi} \tag{4.20}$$

Combining eq. 4.16 with eq. 4.18 the following integro-differential-equation for diffuse radiation in a plane-parallel atmosphere is obtained:

$$\begin{aligned} &+ \cos\Theta \frac{dI_{\text{dif}}(r, \Psi, \Theta, \varphi)}{dr} + \alpha(r) I_{\text{dif}}(r, \Psi, \Theta, \varphi) \\ &- \alpha(r) \frac{\omega(r)}{4\pi} \int_0^{2\pi} d\tilde{\varphi} \int_0^{2\pi} d\tilde{\Theta} p(r, \gamma) I_{\text{dif}}(r, \Psi, \Theta, \varphi) \\ &= \alpha(r) B_{ss}(r, \Psi, \Theta, \varphi) \end{aligned} \tag{4.21}$$

In pseudospherical radiative transfer models (GOMETRAN [Rozanov *et al.*, 1997]) the radiative transfer equation eq. 4.16 is solved in a pseudospherical atmosphere meaning a plane parallel atmosphere is homogenously illuminated horizontally by direct solar radiance. The latter is being attenuated as in a spherical atmosphere. Thus the integral

in eq. 4.19 for the single-scattering source function is calculated using the spherical Jacobian:

$$J(\mathbf{r}, \mathbf{s}_0) = \frac{r}{\sqrt{r^2 - (r_0 \sin\Psi_0)^2}} \tag{4.22}$$

where r_0 and Ψ_0 are parameters for the model input. The integral term containing the multiple-scattering source function is calculated using the plane-parallel Jacobian. In summary the pseudospherical approximation includes single-scattering treated in full spherical approximation and multiple-scattering treated in plane-parallel approximation. This means that in pseudosherical approximation the left hand side of the integro-differential equation for plane-parallel approximation (eq. 4.21) remains unchanged. The single-scattering source function on the right hand side therefore is calculated in full spherical approximation. Rozanov *et al.* [2000] called this the Combined Differential-Integral (CDI) approach for radiation field computation on the spherical shell atmosphere.
For limb-viewing geometry eq. 4.16 looks almost the same except that the first term on the right hand side of eq. 4.16 is missing. The CDI approach [Rozanov *et al.*, 2000] is not accurate enough to calculate limb-viewing geometries for certain scenarios. The relative difference between the CDI model and the spherical model is as large as 10% for the tangent heights of 45 km and a wavelength of 800 nm [Rozanov *et al.*, 2002]. Thus the Combined Differential-Integral approach involving the Picard Iterative approximation (CDIPI) was introduced [Rozanov *et al.*, 2001]. It has to be noted that the AMAXDOAS profile retrieval is based entirely on the CDI approach due to the fact that tangent heights are below 10 km and the wavelengths are below 550 nm. In these cases the CDI approach for limb-viewing geometry has a relative difference compared to the spherical model of below 1% [Rozanov *et al.*, 2001].

4.4 Measurement Geometry

In this chapter the viewing geometries of the (AMAXDOAS) and the SCIAMACHY instruments will be described. It will help to understand the geometry of the measurements, and it emphasizes the concepts of both instruments being important to this work.

4.4.1 AMAXDOAS

Before discussing the retrieval theory and the sensitivity studies, a qualitative discussion of the viewing geometry highlights and explains the concept to be exploited by the multiaxis measurements. Fig. 4.11a shows the measurement geometry of AMAXDOAS measurements assuming single-scattering. The ray coming directly from the sun penetrates the atmosphere and is scattered at a specific altitude. As can be seen in this plot, the light paths after scattering are different, and depend on the LOS. The LOS are defined as angle between the axis pointing towards the nadir and the viewing direction in flight direction (see Fig. 4.12). The LOS pointing close to the horizon are weighting

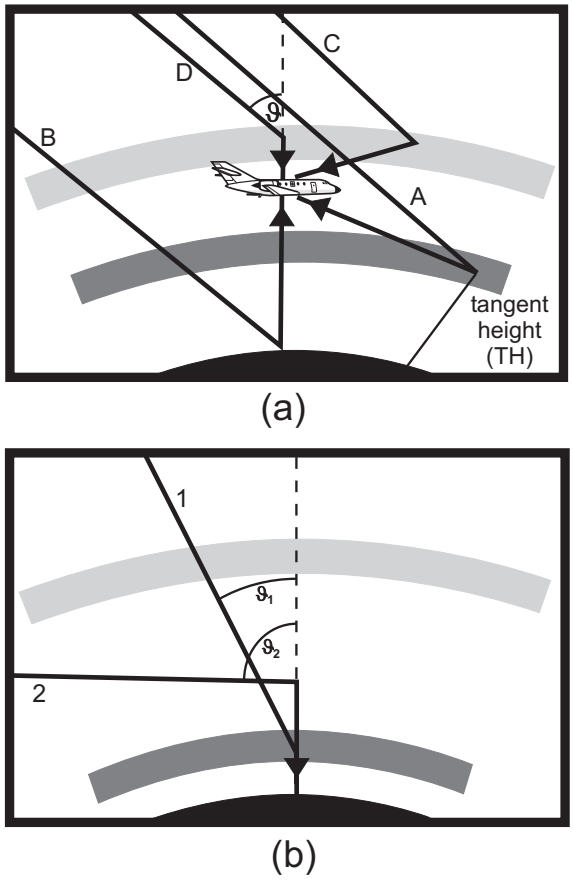

Figure 4.11: This plot shows the light paths observed by an airborne UV/vis skylight absorption spectrometer (a) compared to the light paths observed by a ground-based UV/vis zenith sky absorption spectrometer (b). The displayed light paths indicate the most probable light paths. In reality the light observed at a specific LOS originates from a variety of different light paths as a result of multiple scattering.

strongly the altitudes containing the trace gas indicated by the longer path inside the gray layers (see Fig. 4.11a). This feature is used by the method described below to retrieve profile information by combining simultaneous measurements in different directions. The distance of the point of scattering from the aircraft is determined by the visibility. The visibility depends on the wavelength, the density of the atmosphere, the aerosol loading, and in the case of nadir view also the distance to the surface.

The upward looking LOS all see the atmosphere above the aircraft, but in the single-scattering approximation are not influenced by the atmosphere below flight altitude. The height (which produces most of the measurement signal) depends strongly on the length it travels through denser areas of the atmosphere close to the aircraft. Therefore LOS pointing near the horizon will retrieve a relatively larger signal from the altitudes near flight altitude than LOS pointing more to the zenith.

All downward looking LOS do see the atmosphere above the aircraft too, but in addition also probe the atmosphere below flight altitude. These LOS can be divided into two categories. The first category is for those LOS where radiation is scattered above the

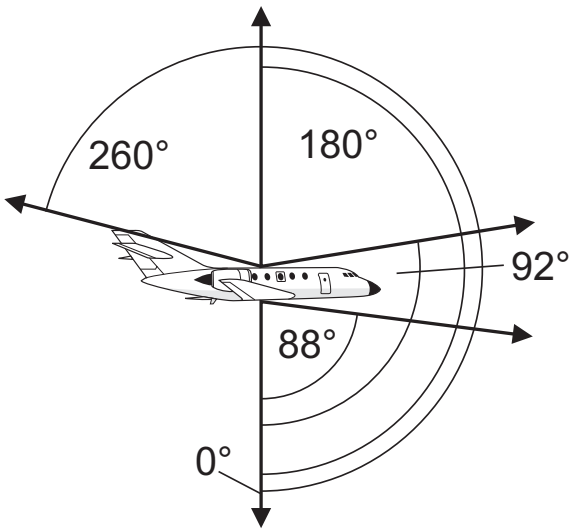

Figure 4.12: The definition of the lines of sight.

earth's surface. We call these LOS the limb mode of the AMAXDOAS instrument. For such LOS the largest part of the measurement signal is coming from the tangent height. The different tangent heights for different LOS yield the profile information in the measurements. Due to the spherical shape of the earth there is a shortest distance between the LOS and the earth's surface. This distance is called tangent height (see Fig. 4.13). For the single scattering approximation such LOS do not see the atmosphere below that altitude. The second category of LOS include those viewing directions where radiation is scattered close to or at the earth's surface. We call these LOS the nadir mode of the AMAXDOAS instrument. As all these LOS probe all altitudes below the aircraft, the information content of the profile is small and only based on different amounts of scattering depending on the viewing angle. In general these explanations are valid for both the visible and the UV wavelength regions. In the UV the larger

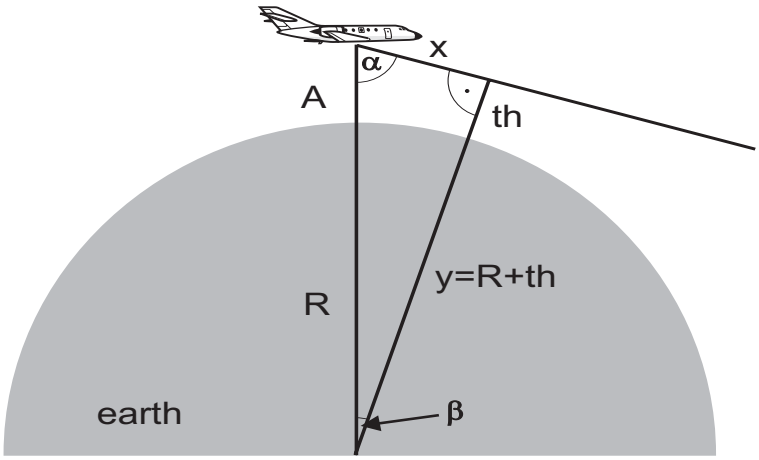

Figure 4.13: The calculation of the tangent height.

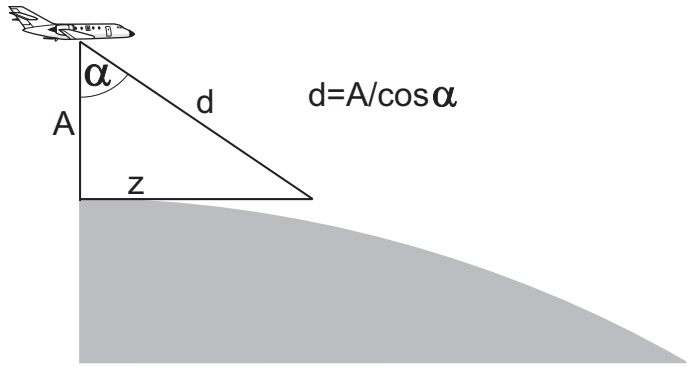

Figure 4.14: The calculation of the distance from aircraft the surface for a specific LOS. It has to be noted that this calculation is only an approximation due to the spherical nature of the earth.

extinction by Rayleigh scattering reduces the visibility. More LOS will then act as limb LOS and potentially add profile information below the aircraft.
The radiative modeling used in the quantitative studies reported below includes full multiple scattering, and it is not limited to the simple assumptions made here. Tab. 4.3 presents the tangent heights and distances d from the aircraft to the surface for several LOS. This table sheds light on the issue from what altitude range the most information for the individual LOS comes from. Fig. 4.14 presents a scheme to calculate the distances from the aircraft to the surface for those LOS that do not have a tangent height. The results of these calculations are again presented in Tab. 4.3. It has to be noted that Fig. 4.14 is a first approximation of the problem because of the spherical nature of the earth, but this figure is only meant as an indication.
To demonstrate the influence of the tangent heights on the profile retrieval the treatment of the weighting functions is foreclosed although the detailed description of these are given in chapter 5 'Profile Retrieval Method'. Here the only important characteristic of weighting functions is the dependence of the measurements on the vertical profile for each LOS meaning the weighting functions represent the sensitivity of each

Table 4.3: List of tangent heights and distances from aircraft to surface.

flight altitude [km]	LOS [°]	x [km]	th [km]	d [km]
10	89	111.4	9.0	-
10	88	222.7	6.1	-
10	87	334.0	1.3	-
10	85	-	-	114.7
10	80	-	-	57.6
10	60	-	-	20.0

x is the distance from aircraft to tangent point, th is the tangent height, and d is the distance from aircraft to surface in first approximation.

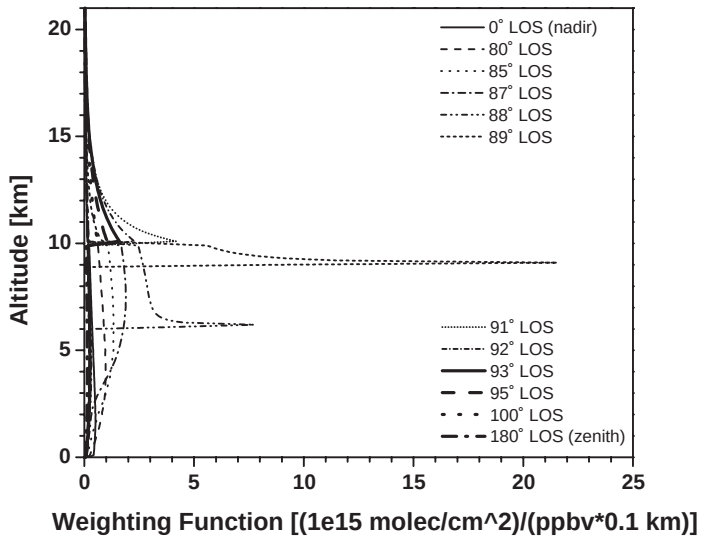

Figure 4.15: Weighting Functions calculated on a 100 m grid for scenario 32 (see Tab. 7.1 in chapter 7 'Sensitivity Studies') to demonstrate the influence of the tangent height.

measurement (LOS) to different altitudes. Fig. 4.15 presents the weighting functions calculated on a 100 m grid for twelve LOS (0° (nadir), 80°, 85°, 87°, 88°, 89°, 91°, 92°, 93°, 95°, 100°, and 180° (zenith)) at a wavelength of 500 nm. It can be seen the LOSs of 88° and 89° show very distinct peaks at 6.1 km and 9.0 km altitude respectively. These altitudes are exactly the tangent heights of these LOSs as already presented Tab. 4.3. The fact that the peak at 6.1 km is smaller depends on the larger distance from the tangent point to the aircraft, which is responsible for more photons being absorbed or scattered. It is noticeable that the 87° LOS does not show a distinctive peak at 1.3 km altitude as proclaimed by Tab. 4.3. It can be argued that the distance of 330 km from tangent point to the aircraft is to large for any photons to reach the instrument.

4.4.2 SCIAMACHY

In the last section the viewing geometry of the AMAXDOAS instrument was discussed. In some points the viewing geometry of the SCIAMACHY instrument is similar. Like the AMAXDOAS instrument the SCIAMACHY instrument has a nadir and a limb mode (see Fig. 4.16). In addition to these two modes the SCIAMACHY instrument has also an occultation mode for direct solar and lunar measurements. This mode will not be discussed here, but for further information see [Bovensmann *et al.*, 1999].
As AMAXDOAS SCIAMACHY is looking straight down towards the earth's surface using its nadir measurement mode. Since the swath path of the nadir mode is 960 km wide[8] and SCIAMACHY is flying at an altitude of 800 km, the edge of this swath

[8]The surface covered with each swath is 960 x 30 km. The spatial resolution depends on the

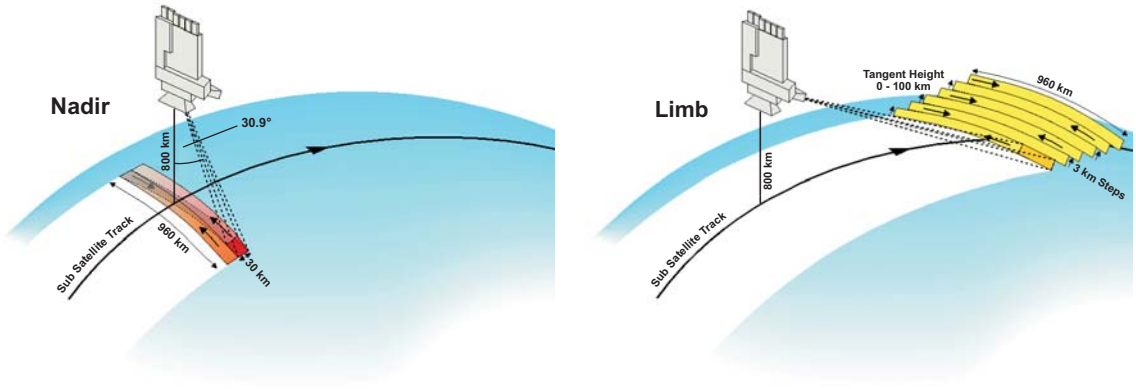

Figure 4.16: Viewing geometry of the SCIAMACHY instrument. The left schematic shows the SCIAMACHY nadir mode and the right schematic shows the SCIAMACHY limb mode [SOST, 2004].

path has a LOS of 30.9° assuming the LOS definition given in the description of the AMAXDOAS instrument (see Fig. 4.16 left schematic). Comparing SCIAMACHY's range of LOS in the nadir mode (0° - 30.9° across track) to the LOS used in nadir mode of the AMAXDOAS instrument (0°, 60°, 80°, and 85°) it shows that the LOS are very different due to the very different flight altitude. The 80° and 85° LOS in AMAXDOAS nadir mode are SCIAMACHY LOS in limb mode (see below).

In limb mode SCIAMACHY looks ahead along a LOS that penetrates the earth's atmosphere some 3000 km ahead of the sub satellite nadir point (see Fig. 4.16). The limb scan mirror scans through different tangent heights from 0 to 100 km, whereas the nadir scan mirror scans the different azimuth direction as it does in nadir mode. The step size of the elevation scan is about 3 km. A complete limb scan consists of 34 elevation steps. During each elevation step the azimuth mirror scans in azimuth directions resulting in a swath width of 960 km as in nadir mode. One elevation step scan takes 1.5 seconds. The typical limb integration time is 0.375 seconds giving a horizontal resolution of 240 km. The tangent heights of the LOS can be transferred to the angle notation of the LOS used in the description of the AMAXDOAS viewing geometry. A tangent height of 0 km translates to a LOS of 81.88° and a tangent height of 60 km translates to 87.86°. The profile retrieval discussed in this work does not take into account tangent heights larger than 60 km.

The unique feature of the SCIAMACHY instrument is the ability to observe the same atmospheric volumes in limb and nadir modes within a short time interval (only eight minutes apart). This feature enables so-called limb-nadir-matching. Thus it is possible to derive a tropospheric trace gas column by subtracting stratospheric columns derived from stratospheric profiles (limb measurements) from the total nadir columns. This is possible for a number of trace gases (O_3, BrO, SO_2, H_2CO, NO_2, CO, CH_4, H_2O, N_2O).

wavelength and the ground pixel size is 30 x 30 km at best [Noel *et al.*, 2000].

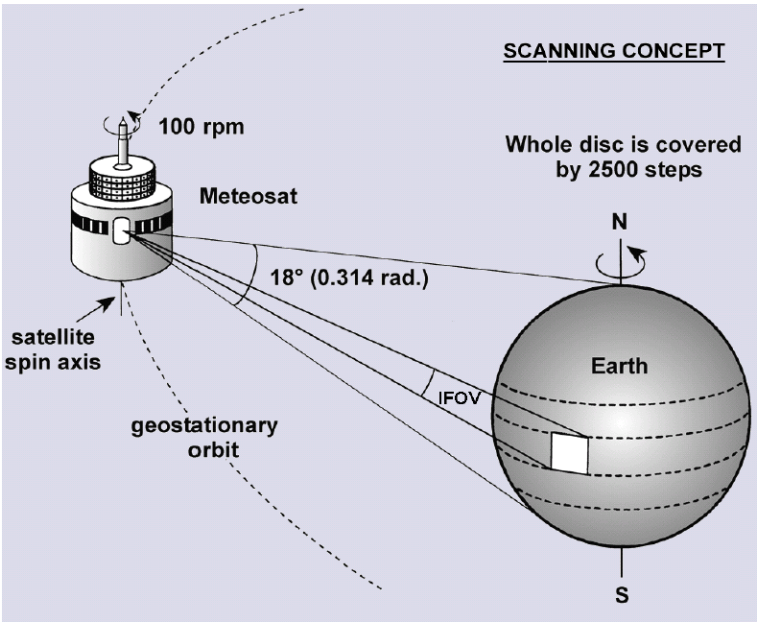

Figure 4.17: The scanning concept of the Meteosat satellite. 'IFOV' is the instrument's field of view [Eumetsat, 2000].

4.5 Meteosat

In this section the Meteosat system is described briefly because the data is used in the process of data analysis during interpretation of the retrieved profiles of the AMAX-DOAS instrument. The Meteosat system was designed to provide data at frequent intervals covering large areas. Therefore the Meteosat system is an essential data acquisition device for meteorological and climtological data. Precise weather forecasts have become very important to society in the last decades for a variety of industries such as agricultural to schedule activities dependant on the weather, the retail industry to plan the sales of weather dependant products (food, clothes, and air condition units), and the energy industry to name just a few. The need of climate data has become important as well due to changing weather patterns in the last decades.
The Meteosat system is important to this work due to the system's ability to acquire satellite images of cloud patterns as well as meteorological cloud analysis data including cloud top pressure, cloud coverage, and winds derived from cloud motion.
The main payload of the Meteosat satellites is a radiometer operating in three spectral bands. The first spectral band is in the visible to near-infrared wavelength region from 0.45 μm to 1.0 μm. This spectral region is used for imaging the earth during daylight. The second spectral band is the water vapor absorption band from 5.7 μm to 7.1 μm. This band is used to determine the amount of water vapor in the middle atmosphere. The last band is the thermal infrared band from 10.5 μm to 12.5 μm used for imaging by day and nighttime and for cloud temperature determination.
The scanning concept of the Meteosat satellite is shown in Fig. 4.17. The satellite scans the whole visible earth disc in 30 minutes. The earth is scanned from east to west using the satellites own rotation. The scanning from south to north is done in

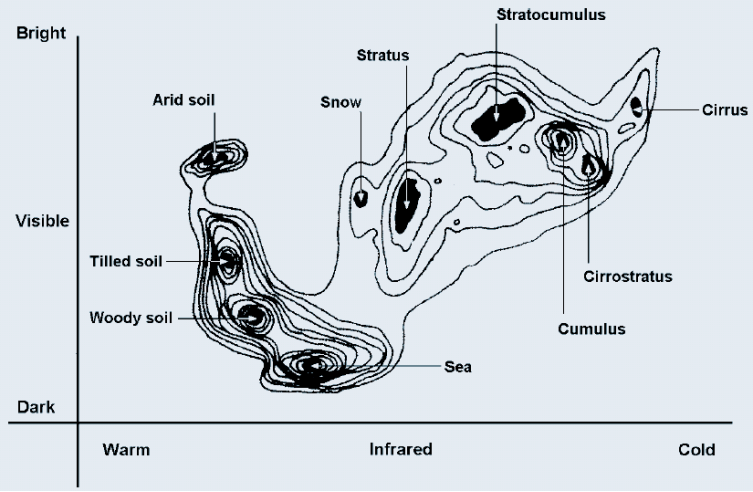

Figure 4.18: Two-dimensional image histogram of the Meteosat segments processing [Eumetsat, 2000].

2500 steps achieved by small increments in the direction of the telescope. With each rotation of the satellite one line of the earth's disk is sampled. Within one line the data is sampled electronically 2500 times resulting in a resolution of 2500 times 2500 pixels per water vapor and infrared image. Thus one pixel has a footprint of 5 km times 5 km at the sub satellite point. In the visible one line is sampled by two detectors at once leading to a resolution of 5000 times 5000 pixels with a footprint of 2.5 km times 2.5 km.

The meteorological products of the Meteosat system are based on the analysis of the water vapor and infrared data. These products are analyzed on a lower resolution than the image data. One segment contains an array of 32 x 32 infrared pixels and is centered over a fixed geolocation. The segments overlap slightly and create an array of 80 x 80 segments covering the entire field of view of Meteosat. The meteorological products are obtained by the systematic data processing of each image segment. The systematic data processing is limited to 64 x 64 segments within 60° of great circle arc from the sub-satellite point. Each segment has a footprint of 150 x 150 km^2 at the sub-satellite point. At the edge of the visible earth's disk the footprint increases to 250 x 250 km^2 due to the spherical shape of the earth.

Before segment processing of each individual segment is performed some background information on the specific segment has to be gathered. This information includes the physical characteristics (presence of land or sea), meteorological characteristics (expected state of the atmosphere such as temperature and pressure), and information on clouds. The information on the latter two is taken from model predictions. The first step of segment processing is the multispectral analysis of the radiance data for each segment. The purpose of this analysis is to assign each pixel to a characteristic cluster of radiances (see Fig. 4.18). A particular source of radiation can be identified for each cluster of radiances. The second step in segment processing is the interpretation stage. This stage assigns each cluster a specific source of radiation knowing in advance the expected range of radiances for each source (see Fig. 4.19).

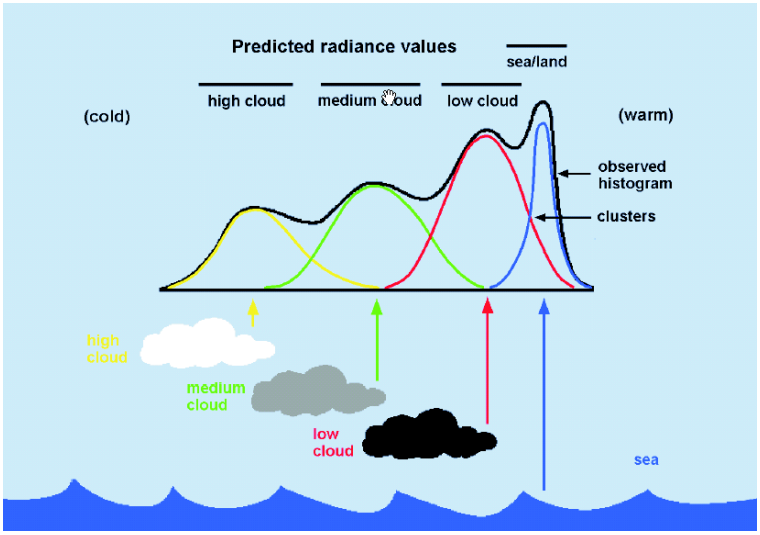

Figure 4.19: Interpretation of the two-dimensional image histogram of the Meteosat segments processing [Eumetsat, 2000].

This technique is able to identify up to three cloud layers and the surface. This output of the segment processing is the starting point of the calculation of the individual meteorological products. The cloud motion wind (CMW) analysis is able to deduce the apparent wind speed and direction from one image to the next. Features in the water vapor channel are used as tracers. This enables the algorithm to create wind vectors even for cloud free segments. The automatic processing interval is 90 minutes. The cloud analysis (CLA) product is a direct derivative of the segment processing. This analysis identifies pixels with up to three cloud layers. The product provides the percentage of cloud cover and cloud top temperature for each layer present. This analysis is done in a six hour interval. There are more meteorological data products available, but only these two are used during interpretation of the retrieved profiles in this work. A more detailed description of the Meteosat system can be found in [Eumetsat, 2000].

Chapter 5

Profile Retrieval Method

This chapter is discussing the theoretical background necessary to understand the profile retrieval method used in this work. The subject of 'resolution' is also addressed here as well as the forward model that is used to simulate the physical processes in the atmosphere. Last but not least the profile retrieval algorithm will be described.

5.1 Profile Retrieval Theory

A set of differential slant columns at a certain SZA using different LOS contains information about the vertical distribution of a specific trace gas in the atmosphere. To analyze the quality of the information for profile retrieval the characterization of a retrieval method from Rodgers [1976, 1990, 2000] is used. This characterization includes a formal treatment of errors. A set of measurements $\mathbf{y}$ can be related to a vertical profile $\mathbf{x}$ by a forward model F [Rodgers, 1990]:

$$\mathbf{y} = F(\mathbf{x},\mathbf{b}) + \epsilon \tag{5.1}$$

where $\mathbf{b}$ is the vector of the forward model parameters, and ϵ is the sum of the different error components including the measurement error and the model error. These error components will be discussed later in chapter 6 'Error Analysis'. Here, $\mathbf{y}$ is a vector of slant columns as a function of LOS, and $\mathbf{x}$ is the vertical profile of the trace gas of interest. The profile $\mathbf{x}$ - a continuous function in the real atmosphere - has to be sampled discretely by the retrieval algorithm, and it is therefore presented as a vector. Eq. 5.1 can be rewritten in a linearized form ([Rodgers, 1976]; chapter 2.2):

$$\mathbf{y} = \mathbf{K}\mathbf{x} \tag{5.2}$$

where

$$\mathbf{K} = \frac{d\mathbf{y}}{d\mathbf{x}} \tag{5.3}$$

The rows of the $\mathbf{K}$ matrix represent the weighting functions, and each row corresponds to a different measurement. Each LOS is considered as a single measurement. The weighting functions describing this problem contain the dependence of the slant columns on the vertical profile for each LOS. In other words: the weighting functions

give the change of the slant column, when varying the VMR of the profile by a certain amount at a certain altitude.
There is no unique solution to the inversion of eq. 5.2, because the problem is ill-posed with a condition-number κ. The latter is calculated by doing a singular value decomposition of matrix $\mathbf{K}$. κ is the ratio of the largest and the smallest singular values. If κ is of the order of 10^6 or larger the problem is generally considered to be ill-posed. In the case of scenario 1 (see Tab. 7.1 in chapter 7 'Sensitivity Studies') κ is of the order of 10^{29}. To reduce the amount of possible solutions the Optimal Estimation Method described by Rodgers [1976, 1990, 2000] adds a priori information. A requirement for the Optimal Estimation method to be used is linearity or moderate non-linearity of the problem. The retrieval problem for trace gas skylight absorption measurements is nearly linear because most trace gases (e.g. NO_2) are optically thin (i.e. absorptions smaller than 2%). In this study the Maximum a Posteriori (MAP) solution is chosen [Rodgers, 2000]. This method calculates the retrieved profile $\hat{\mathbf{x}}$ as follows:

$$\hat{\mathbf{x}} = \left(\mathbf{K}^T\mathbf{S}_\epsilon^{-1}\mathbf{K} + \mathbf{S}_a^{-1}\right)^{-1}\left(\mathbf{K}^T\mathbf{S}_\epsilon^{-1}\mathbf{y} + \mathbf{S}_a^{-1}\mathbf{x}_a\right) \tag{5.4}$$

where $\mathbf{K}$ is the weighting function matrix, $\mathbf{K}^T$ is the transposed weighting function matrix $\mathbf{K}$, $\mathbf{S}_\epsilon$ is the measurement error covariance matrix, $\mathbf{S}_a$ is the error covariance matrix of the a priori vector, $\mathbf{y}$ is the measurement vector, and $\mathbf{x}_a$ is the a priori profile information.
To characterize the retrieved profile more precisely, the contribution function matrix $\mathbf{D}$ is introduced. It represents the sensitivity of the retrieved profile to the changes of the slant columns:

$$\mathbf{D} = \frac{\partial\hat{\mathbf{x}}}{\partial\mathbf{y}} = \mathbf{S}_a\mathbf{K}^T\left(\mathbf{K}\mathbf{S}_a\mathbf{K}^T + \mathbf{S}_\epsilon\right)^{-1} \tag{5.5}$$

The contribution functions indicate the variation of the retrieved profile, when changing the slant column at a given LOS by a certain amount of molecules per cm^2. The retrieved profile can be thought of as a weighted average of the true and the a priori profiles. The averaging kernel matrix $\mathbf{A}$ supplies the weights for the true profile.

$$\mathbf{A} = \mathbf{D}\mathbf{K} \tag{5.6}$$

A change in the real atmospheric profile by a certain amount of molecules per cm^3 in a specific altitude causes a change of a certain amount of molecules per cm^3 in the retrieved profile at all altitudes represented by a function, the averaging kernel for this specific altitude.

5.1.1 Resolution

First it has to be defined what is meant by 'resolution' in the context of profile retrieval. In spectroscopy the resolution is a measure of the instrument's ability to distinguish between two δ-peaked point sources. This is not very useful in profile retrieval, since it is dealing with atmospheric states rather than δ-function perturbations. A more useful measure would be how well one can see structures that might be present in the

atmospheric profile. Rodgers [2000] proposed to use the 'full width at half maximum' (FWHM) of the averaging kernels as characteristic of the resolution. Even though the FWHM could cause problems in case the FWHM is to be used in algebraic equations or the averaging kernels have lobes of some kind, the FWHM is satisfactory for the purpose in this work as a measure of resolution. A more detailed description of the resolution in profile retrieval can be found in [Rodgers, 2000]. The algorithm to calculate the actual FWHM values is described below in section 5.3 'The AMAXDOAS Profile Retrieval Algorithm (APROVAL)'.

5.2 The Forward Model

The radiative transfer model SCIATRAN [Rozanov *et al.*, 1997, 2000, 2001, 2002] is used as forward model. The radiative transfer part of the forward model was already discussed in the chapter 4 'The Experimental Setup'. SCIATRAN is used to calculate the weighting functions in this work.
The radiative transfer model SCIATRAN [Rozanov *et al.*, 2001] was used in the this retrieval method. SCIATRAN is a full spherical radiative transfer model considering refraction that is able to calculate the radiance in specific lines of sight for a specific flight altitude.
In principle the calculation of weighting functions is done by perturbing each layer of the a priori trace gas profile consecutively. Using these perturbed profiles the "perturbed" radiances have to be calculated, so that the elements of the weighting functions matrix can be approximated as follows:

$$K_{i,j} = \frac{dy_i}{dx_j} \approx \frac{\Delta I_i}{\Delta x_j} = \frac{I_i - I_i^p}{x_j - x_j^p} \tag{5.7}$$

i represents the index over all measurements and j represents the index over all perturbed layers, I_i is the intensity of the radiance calculated with the unperturbed NO_2 profile, I_i^p is the intensity of the radiance calculated with the perturbed profile, x_j is the unperturbed profile at layer j, and x_j^p is the perturbed profile at layer j.
This method of calculating weighting functions unfortunately is very time consuming. Thus SCIATRAN calculates the weighting functions by solving the linearized radiative transfer equation. For a more detailed description of how SCIATRAN is actually calculating weighting functions see [Rozanov *et al.*, 1998]. The latter give the absolute change in intensity for a relative change of 100% of a parameter, for example NO_2 in a specific layer. However, for AMAXDOAS one is more interested in a weighting function that indicates the change in slant column for a change in say NO_2 at a specific layer. Fortunately, for an optically thin atmosphere, the weighting functions as calculated by SCIATRAN can easily be converted into weighting functions regarding the change in slant columns [Richter, 2003b].

$$WF_{SC}(h,\lambda) = \frac{-WF_I(h,\lambda) \cdot \Delta VMR}{I_0(\lambda) \cdot \sigma(\lambda) \cdot VMR(h)}, \tag{5.8}$$

where WF_{SC} are the weighting functions regarding the change in slant columns, h is the altitude, λ is the wavelength, WF_I are the weighting functions regarding the

change in intensity (output of the SCIATRAN model), ΔVMR is the difference in volume mixing ratio in each layer, I_0 is the absolute intensity at the top of atmosphere, σ is the wavelength dependent absorption cross section of the considered trace gas, and VMR is the profile of the considered trace gas in volume mixing ratio. The units of WF_{SC} depend on the units of ΔVMR and step size in the retrieval grid used in the profile retrieval run. E.g. ΔVMR has the unit of 1 ppbv, and the step size of the retrieval grid is 2 km. Thus the unit of WF_{SC} is $molec \cdot cm^{-2} \cdot ppbv^{-1} \cdot 2km^{-1}$. After calculating the contribution functions using eq. 5.5 the averaging kernels can be calculated using eq. 5.6 with **K** representing the weighting functions. This method of calculation of the weighting functions is based on the assumption of an optically thin atmosphere concerning the considered trace gas.

5.3 The AMAXDOAS Profile Retrieval Algorithm (APROVAL)

This section is dealing with a description of the AMAXDOAS profile retrieval algorithm (APROVAL) developed in this work in order to analyze measured slant columns with the AMAXDOAS instrument. APROVAL was implemented as a MATLAB script in combination with the use of SCIATRAN. In principle this algorithm is able to retrieve vertical profiles for various trace gases (NO_2, O_3, BrO, SO_2, HCHO) from slant columns that were measured using the DOAS method (see chapter 4 'The Experimental Setup'). This work is focused on NO_2 only because the main part of this work comprehends the development of a profile retrieval algorithm based on slant column measurements.

5.3.1 Algorithm Structure

In the beginning the MATLAB script of APROVAL reads all necessary files needed during the profile retrieval process beginning with the weighting functions calculated by SCIATRAN as described in the previous section. SCIATRAN calculates the weighting functions on a fine grid with 100 m step size. This is to avoid problems with the weighting functions in the lowest layer, which is even in a equally spaced retrieval grid always narrower than all other layers due to the surface in case the grid point represents the center of the layer. For the actual retrieval the weighting functions will be transformed to the retrieval grid (e.g. 0 km, 1 km, 3 km, ..., 39 km) by adding up weighing functions within the layers created by the grid. For example: to calculate the weighting function value of the retrieval grid at 0 km altitude the values of the fine grid weighting function from 0 km to 0.5 km are added up; to get the 1 km value (assuming the next grid point is at 3 km) the fine grid values from 0.6 km to 2.0 km are added up, and so on. Besides SCIATRAN's weighting functions the profile interpolated to SCIATRAN's retrieval grid is also read by the MATLAB script as well as the intensities and absorption cross sections needed in eq. 5.8. Last but not least the measured slant columns, the a priori profile information, the a priori errors, and the measurement errors are read. It has to be noted that the measured slant columns are differential slant columns because the DOAS analysis is using a reference spectrum near the lowest SZA. This retrieval algorithm on the other hand is using absolute slant columns. This

is achieved by adding the slant column of the reference spectrum to all measured slant columns. The slant column of the reference spectrum is calculated using the a priori profile and SZA of the reference spectrum.
The second step is the calculation of the weighing function matrix **K** as described in eq. 5.8. Having calculated the **K**-matrix the calculation of the retrieved profiles is next (see eq. 5.4). To characterize the retrieved profiles the contribution function matrix **D** (see eq. 5.5) and the averaging kernels are calculated according to eq. 5.6.
The third step is the calculation of the resolution using the FWHM of the averaging kernels as discussed in section 5.1.1 'Resolution'. A more detailed description of the FWHM calculation can be found in the next section.
The retrieval errors are calculated in the fourth step. The theoretical background on the error analysis including the calculation of the total retrieval error and the individual error components contributing to the total retrieval error can be found in chapter 6 'Error Analysis'.
The fifth step deals with the conversion of the retrieved profile to concentration in molecules per cm^3. During the actual retrieval process the algorithm uses volume mixing ratio in ppbv as unit.
The final step is writing the results to files and plotting the results like averaging kernels, weighting functions, error, retrieved profiles in VMR and concentration, and the resolution.

5.3.2 Calculation of the Vertical Resolution

To calculate the resolution the FWHM of each averaging kernel has to be determined. Therefore the averaging kernels are interpolated on a much finer grid with a step size of 20 m. Now the peak values and peak altitudes of each averaging kernel is determined searching for the maximum value of the averaging kernels and storing the maximum value's altitude. Starting from the peak altitude the altitudes for the half maximum values below and above the peak altitude are determined. By calculating the difference of these two altitudes the FWHM value of the averaging kernel is determined.
The lowest averaging kernels could raise problems using the FWHM algorithm described above in case the lower flank does not exist at all (e.q. the 0-km averaging kernel has its maximum value at 0 km peak altitude) or lower flank hits the surface at value between maximum value and half of the maximum value. In this case a different method is used to determine the half maximum value below the peak altitude. The slope of the upper flank is determined between the peak altitude and the altitude above the peak altitude where the averaging kernels are zero. Using this slope the lower flank is extrapolated. Using these extrapolated values of the averaging kernel the altitude of the half maximum value below the peak altitude is determined. Again the difference between the upper altitude and lower altitude of the half maximum values the FWHM value is calculated.

Chapter 6

Error Analysis

The total error ϵ of the retrieved profile in eq. 5.1 of the previous chapter can be calculated. According to [Rodgers, 2000] the total error of the profile retrieval is the difference between the retrieved and the true profile:

$$\epsilon = \hat{\mathbf{x}} - \mathbf{x} = (\mathbf{A} - \mathbf{I})(\hat{\mathbf{x}} - \mathbf{x}_a) + \mathbf{D}\epsilon_y + \mathbf{D}\Delta_b \tag{6.1}$$

where $\hat{\mathbf{x}}$ is the retrieved profile, $\mathbf{x}$ is the true profile of the atmosphere, $\mathbf{x}_a$ is the a priori profile, $\mathbf{A}$ is the averaging kernel matrix, $\mathbf{I}$ is the identity matrix, $\mathbf{D}$ is the contribution function matrix, ϵ_y is the measurement error vector, and Δ_b is the forward model error vector. The total error of the retrieved profile can be separated into three components. Due to error propagation the error covariance matrix of the total error can be written as:

$$\mathbf{S}_{tot} = \mathbf{S}_s + \mathbf{S}_m + \mathbf{S}_f \tag{6.2}$$

$\mathbf{S}_s$ is the smoothing error covariance matrix, $\mathbf{S}_m$ is the retrieval noise covariance matrix, and $\mathbf{S}_f$ is the forward model error covariance matrix. Since the total retrieval error covariance matrix $\mathbf{S}_{tot}$ introduced in eq. 6.2 is representing the total retrieval error in the profile space[1], the three components on the right hand side of eq. 6.2 are represented in the profile space as well. One task of this chapter is to translate the error covariance matrices $\mathbf{S}_a$ and $\mathbf{S}_\epsilon$ of the previous chapter into the profile space. It has to be noted that the a priori error covariance matrix $\mathbf{S}_a$ is already in the profile space but the measurement error covariance matrix $\mathbf{S}_\epsilon$ is not. Since this matrix contains the measurement errors, it exists in the measurement space[2].
The last error component $\mathbf{S}_f$ will not be treated analytically. Instead sensitivity studies are presented to estimate the magnitude of this error component.
In this retrieval algorithm the errors are treated as covariance matrices meaning the square root of all diagonal elements create the error vector ($\epsilon_y = \sqrt{\mathbf{S}_\epsilon \cdot \mathbf{I}}$ for example, where $\mathbf{I}$ is the unity matrix). All other elements of the covariance matrix contain

[1]The profile space (or state space) according to Rodgers [2000] is a vector space of dimension n, within each conceivable state is represented by a point. These points refer to the grid points of the retrieval grid in this case.

[2]According to Rodgers [2000] the measurement space (or data space) is a vector space of dimension m, in which each conceivable measurement is likewise represented by a point or vector. The act of measurement is then mapping from profile space (or state space) into the measurement space

Table 6.1: Systematic errors in measured NO_2 slant columns taken from Richter [1997].

error component	error value
error in absorption cross sections	3%
neglecting of wavelength dependent AMF	1-2%
error in AMF	5%
error in wavelength of the reference spectrum	$< 5\%$
error in wavelength of the absorption cross sections	$< 5\%$
uncertainty due to choice of fitting window	6%

zeros, which indicates complete independence of all single errors due to the fact that the eigenvector transformation of a diagonal matrix produces the diagonal elements as eigenvalues. In case of the measurement error this is true in first approximation, since the measurements in different viewing directions are independent. In case of the a priori error this is not true even in first approximation in the stratosphere, because the NO_2 profile has a distinct shape, so a specific value at 25 km altitude predicts a higher value above and a lower value below 25 km. But in the troposphere one can assume that the tropospheric NO_2 depends mainly on the sources at the surface, which are quite randomly distributed and absolute independent of the profile above the source. Since this retrieval is insensitive to the stratosphere, one can assume independent errors of the a priori profile.

6.1 Error Sources of the AMAXDOAS instrument

Before achieving to solve the task proposed in the introduction of this chapter one has to take a look at the sources of the measurement error ($\mathbf{S}_\epsilon$) of the AMAXDOAS instrument introduced in the previous chapter. First the sources of the components of the measurement error will be discussed. The data analysis of DOAS measurements as presented in chapter 4 'The Experimental Setup' involves a non-linear fit, which introduces a statistical error, the so-called fitting error. This represents the measurement errors of the instrument such as drifts in wavelength, noise due to digitization, and noise due to amplifying. Besides the statistical component the measurement error has a systematic error component. The systematic error includes uncertainties due to error in absorption cross sections, neglecting wavelength dependent AMF, error in AMF, error in wavelength of reference spectrum, error in wavelength of the absorption cross sections, and the choice of the fitting window. The systematic errors summarized in Tab. 6.1 are taken from Richter [1997] and will be taken into account as approximation during profile retrieval as discussed later (see chapter 9 'Profile Retrieval using Real AMAXDOAS Data').
As shown in eq. 6.2 the profile retrieval itself induces systematic errors. One of those is the uncertainty of the a priori profile ($\mathbf{S}_a$). The reason for this uncertainty is the use of a climatological trace gas profile that might not represent the actual trace gas abundance in the atmosphere very well during the measurement. To estimate the magnitude of the a priori error one has to consider the possible deviation from the

a priori profile. The deviation can vary depending on the specific altitude. For the profile retrieval using real data a deviation of 3 ppbv at 1 km altitude, 1 ppbv at 4 km altitude, and 0.7 ppbv above 4 km altitude was chosen, because the deviation in the boundary layer is the largest due to expected tropospheric NO_2. This topic will be discussed later (see chapter 9 'Profile Retrieval using Real AMAXDOAS Data').

6.2 Smoothing Error

The error covariance matrix $\mathbf{S}_s$ can be calculated as:

$$\mathbf{S}_s = \Big(\mathbf{A} - \mathbf{I}\Big)\mathbf{S}_a\Big(\mathbf{A} - \mathbf{I}\Big)^T \tag{6.3}$$

where $\mathbf{S}_a$ is the error covariance matrix of the a priori profile. Rodgers [2000] refers to $\mathbf{S}_s$ as smoothing error, as this covariance matrix corresponds to portions of the profile space the measurements cannot see due to smoothing. In our case those portions are the altitudes in the stratosphere, and small scale variations obscured by the limited altitude resolution of the profile retrieval. The smoothing error covariance matrix $\mathbf{S}_s$ is the weighted a priori covariance matrix $\mathbf{S}_a$ using $(\mathbf{A} - \mathbf{I})$ as weights.
Another source of error in real applications is the pointing accuracy of the LOS. A high pointing accuracy is difficult to achieve because of the intrinsic pitch and roll of an aircraft in flight. The matter of pointing accuracy will be dealt with in the sensitivity studies below.

6.3 Retrieval Noise

The error covariance matrix $\mathbf{S}_m$ can be calculated as:

$$\mathbf{S}_m = \mathbf{D}\mathbf{S}_\epsilon\mathbf{D}^T \tag{6.4}$$

where $\mathbf{S}_\epsilon$ is the covariance matrix of the measurement error and $\mathbf{D}$ is the contribution function matrix. The measurement error is due to noise in the measurements propagating into the retrieval. The contribution function matrix maps the measurement error covariance matrix $\mathbf{S}_\epsilon$ into the profile space. Rodgers [2000] refers to this error covariance matrix as retrieval noise. This error component is usually the easiest one to calculate. The measurement error has to be assumed to be random, unbiased, and uncorrelated between measurement channels due to missing information.
In case of UV/vis spectroscopy there are three main error sources of the measurement error. First there are instrumental errors including stray light in the spectrometer, flaws in the grating and other optical components, readout noise of the detector, and the photon noise (see eq. 4.9). The second error source is the absorption cross section which are measured too. Some trace gases have temperature and pressure dependent absorption cross sections leading to measurement errors when neglected. In this work errors due to absorption cross sections will be considered a forward model error (see below). The third measurement error source is the data analysis.

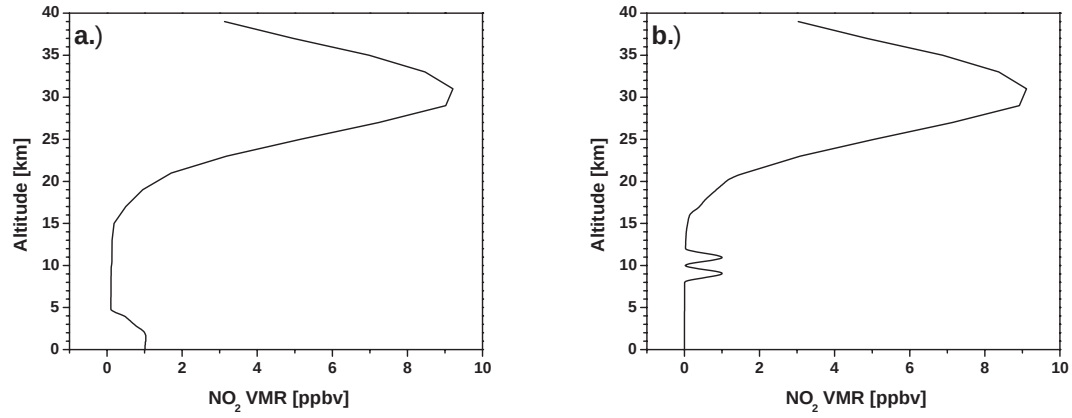

Figure 6.1: NO_2 profiles used in the error analysis. Plot a shows the NO_2 profile used in the studies dealing with the influences of temperature, pressure, aerosol loading, albedo, absorption cross sections, and Center Wavelength Approximation. Plot b shows the NO_2 used in the study dealing with the pointing accuracy.

6.4 The Forward Model Error

The third term in eq. 6.1 $\mathbf{D}\Delta_b$ is the propagation of forward model errors into the retrieval. Those errors arise from use of incorrect physics such as neglecting multiple scattering and refraction, ignoring cloud effects, or using temperature, pressure, aerosol profiles that are different from the true atmosphere. In this work fortunately a very good forward model was at hand. Thus some of the proposed forward model error components need no consideration such as multiple scattering and refraction, since the forward model already takes those into account. Unfortunately the cloud effect on the forward model error could not be investigated, since the used version of the forward model does not support calculation of weighting functions for cloudy scenarios. In this study every forward model error component was calculated separately. Therefore the left hand side of eq. 6.1 was used. All studies except the center-wavelength-approcimation were calculated as described below using the NO_2 profile shown in Fig 6.1a. The calculation of the Center-Wavelength-Approximation will be described separately in the section 6.4.6. Three model runs were performed. The first model run acted as reference since no error was introduced. The second model run was calculated for 'parameter - error' and a third model run was calculated for 'parameter + error'. Finally two profile retrieval runs have to be performed. The first run uses the weighting functions of the reference model run and the simulated slant columns of the 'parameter - error' model run. The second retrieval uses again the weighting functions of the reference model run and the simulated slant columns of the 'parameter + error' model run. The retrieved profiles of these two runs are subtracted from the retrieved profile of the reference run. The result is the absolute error of the profile caused by the variation of the model parameter.

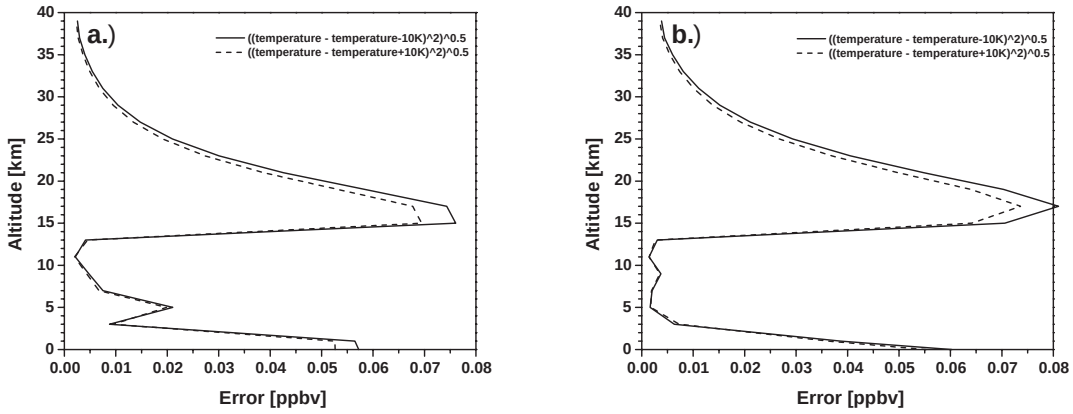

Figure 6.2: Magnitude of the error in case the temperature is changed by ±10 K. Plot a shows the forward model error due to temperature changes at 350 nm and plot b shows this forward model error component at 500 nm. These plots represent the absolute values of the this error component.

6.4.1 Influence of Temperature on the Forward Model Error

This investigation deals with the impact of temperature variations on the forward model error, and it is necessary due to uncertainties in the temperature profile of the a priori information because the latter is based on climatological data. In order to analyze this impact profile retrievals for varying temperatures of ±10 K were performed. Changing the temperature in the atmospheric profile is affecting the density of the considered trace gas according to the ideal gas law (see eq. 2.4 on the right hand side). Reducing the temperature is increasing the density of the trace gas and vice versa. Fig. 6.2a shows the error of the retrieved profile in case the whole temperature profile has an error of ±10 K at 350 nm. This figure shows the absolute value of the error against altitude for both cases 'temperature - 10 K' and 'temperature + 10 K'. As can be seen in Fig. 6.2a the influence of a change of ±10 K is nonlinear considering the profile's covered range of altitude. The largest errors occur at 15 to 17 km altitude. This fact seems to be peculiar at first, because the profile retrieval is not able to retrieve values at this altitude as can be seen in chapter 7 dealing with the sensitivity studies. The reason why this large errors occur at these altitudes will be explained in chapter 8 'Profile Retrieval using Simulated Data'. A second error maximum can be found at 0 to 1 km altitude. The maximum value of 0.06 ppbv is as well small compared to retrieval error values of 0.7 ppbv observed in the same altitude of the reference profile retrieval run (see Fig. 7.1e).

At 500 nm, the result of the forward model error component does not look very different from the result at 350 nm. Even the magnitude of the forward model error is quite the same as the comparison of Fig. 6.2a and b is showing. In this case the maximum value of 0.06 ppbv is small compared to a retrieval error value of 0.4 ppbv observed in 0 km altitude of the reference profile retrieval run (see Fig. 7.1f). The result of this

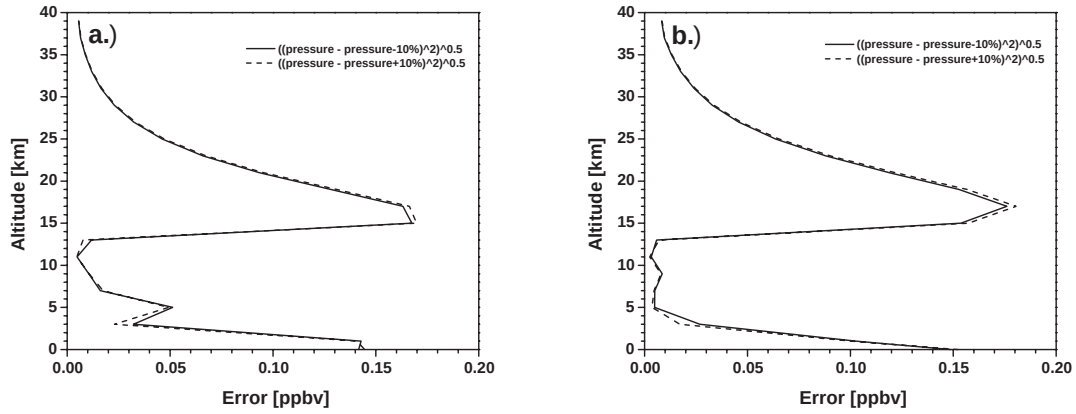

Figure 6.3: Magnitude of the error in case the pressure is changed by ±10 %. Plot a shows the forward model error due to pressure changes at 350 nm and plot b shows this forward model error component at 500 nm. These plots represent the absolute values of the this error component.

investigation is that the profile retrieval is quite invariant to temperature changes of ±10 K, so this error is negligible.

6.4.2 Influence of Pressure on the Forward Model Error

This study deals with the influence of pressure variations on the forward model error. This investigation is necessary due to the same reason as stated in the previous section. In order to analyze this influence profile retrievals for varying pressures of ±10 % were performed. In this investigation a relative change in the parameter was chosen compared to an absolute change of temperature in the previous section because the order of magnitude in the pressure profile is changing dramatically depending on altitude. On the other hand the order of magnitude in the temperature is the same below 60 km altitude. Changing the pressure in the atmospheric profile is affecting the density of the considered trace gas according to the ideal gas law (see eq. 2.4 on the right hand side). Reducing the pressure is also reducing the trace gas concentration and vice versa. Fig. 6.3a shows the error of the retrieved profile in case the whole pressure profile has an error of ±10 % at 350 nm. This figure shows the absolute value of the error against altitude for both cases 'pressure - 10 %' and 'pressure + 10 %'. As can be seen in Fig. 6.3a the influence of a change of ±10 % again is nonlinear considering the profile's covered range of altitude. The largest errors occur at 15 to 17 km altitude. As already explained in the previous section this phenomenon will be explained in chapter 8 'Profile Retrieval using Simulated Data'. A second error maximum again could be found at 0 to 1 km altitude. This maximum value of 0.14 ppbv corresponds to 20% of the retrieval error value of 0.7 ppbv observed in the same altitude of the reference profile retrieval run (see Fig. 7.1e).
At 500 nm, the result of the forward model error component looks almost the same as the result at 350 nm. Even the magnitude of the forward model error is quite the same

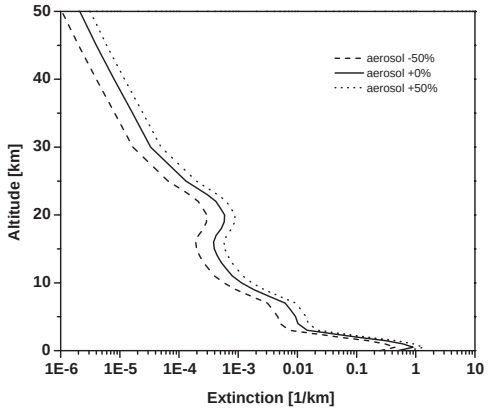

Figure 6.4: Extinction profiles used in the investigation on the influence of aerosols on the forward model error.

as the comparison of Fig. 6.3a and b is showing. In this case the maximum value of 0.15 ppbv corresponds to 38% of the retrieval error value of 0.4 ppbv observed in 0 km altitude of the reference profile retrieval run (see Fig. 7.1f). The main result of this investigation is that the profile retrieval is quite invariant to pressure changes in large parts of the altitude range covered by this retrieval keeping in mind that uncertainties in pressure of ±10% are large considering the largest and lowest atmospheric pressures ever observed on earth. The highest atmospheric pressure ever observed occurred in Siberia (1083.8 hPa, 31 Dec. 1968)[3]. The lowest atmospheric pressure ever observed occurred in typhoon 'Tip' over the Pacific west of Guam (870 hPa, 12 Oct. 1979)[4]. The largest atmospheric pressure ever observed is well within the ±10% considering 1013 hPa as the mean value. The lowest pressure ever observed on the other hand is outside the ±10% but this value was observed under very extreme conditions, and it is not an every day situation for airborne campaigns. The conclusion of this investigation is that an uncertainty of ±10% in atmospheric pressure is a conservative assumption for the uncertainty of the atmospheric pressure. Thus errors due to changes of ±10% in atmospheric pressure are an conservative estimate.

6.4.3 Influence of Aerosols on the Forward Model Error

Fig. 6.4 shows the aerosol profiles, which consist of four different layers containing a different mixture of aerosol particles. The description of this aerosol scenario is based on Kauss [1998]. Tab. 6.2 shows all the details concerning the aerosol scenario used in this investigation. The lowest layer with an upper boundary of 2 km altitude (the boundary layer) has a relative humidity of 80% and contains three different aerosol components. The major aerosol component in this layer is soot that has a large absorption potential. The optical properties of soot particles are depending strongly on

[3]Source:http://www.dwd.de/de/wir/Interessantes/Rekorde/Luftdruck/welt.html
[4]Source:http://www.dwd.de/de/wir/Interessantes/Rekorde/Luftdruck/welt.html

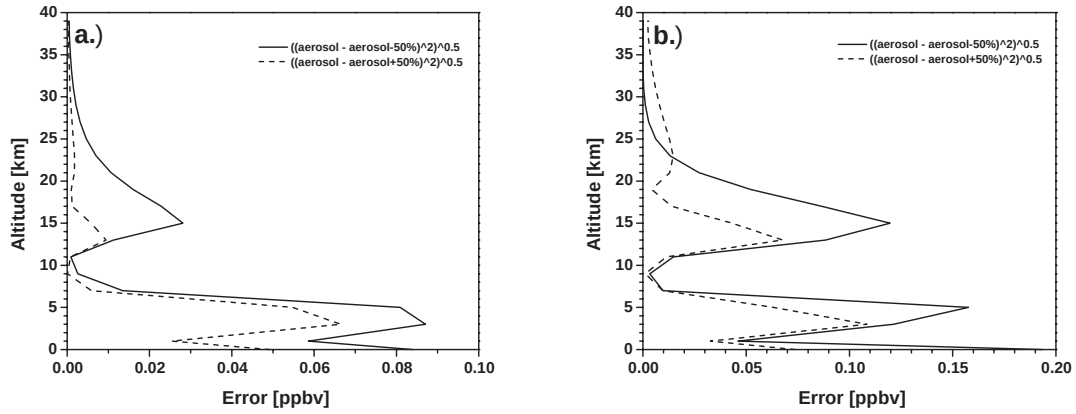

Figure 6.5: Magnitude of the error in case the extinction is changed by ± 50 %. Plot a shows the forward model error due to changes in aerosol concentration at 350 nm and plot b shows this forward model error component at 500 nm. These plots represent the absolute values of the this error component.

the process of particle formation. The second largest aerosol component is water soluble particles consisting mostly of sulfates, nitrates and other water soluble substances. This category contains anthropogenic sulfates, too. The smallest aerosol component in this layer is insoluble particles like dust. These particles are dispersed into the troposphere in mid-latitudes. The next layer encloses the free troposphere up to 10 km altitude. This layer contains the same aerosol components as the boundary layer but in different fractions (see Tab. 6.2). The third layer up to an altitude of 30 km contains only one aerosol component - sulfates. These particles originate mostly from biologic and volcanic processes and form the stratospheric background aerosol. The last layer up to an altitude of 100 km contains only meteoric dust particles originating from meteoric storms. These particles enter the stratosphere mostly over polar regions, but the abundance is very small compared to the other aerosol components (see Fig. **??**). This study deals with the influence of variations in aerosol concentration on the forward

Table 6.2: Aerosol Scenario.

upper boundary [km]	rel. humidity [%]	aerosol component	relative mixing ratio
2	80	water soluble	0.31399
		insoluble (dust)	0.00001
		soot	0.68600
10	70	water soluble	0.45790
		insoluble (dust)	0.00010
		soot	0.54200
30	0	sulfate	1.00000
100	0	meteoric dust	1.00000

model error is important for the profile retrieval because the real aerosol loading of the atmosphere is sometimes not known. In order to analyze this influence profile retrievals for varying extinction profiles of ±50 % were performed. The choice of relative change of the parameter was made in this investigation because of the same reason as stated in the previous section. Fig. 6.5a shows the error of the retrieved profile in case the whole aerosol profile has an error of ±50 % at 350 nm. This figure shows the absolute value of the error against altitude for both cases 'aerosol - 50 %' and 'aerosol + 50 %'. As can be seen in Fig. 6.5a the influence of a change of ±50 % again is nonlinear considering the profile's covered range of altitude. A large error occurs at 15 km altitude. As already explained in the previous section this phenomenon will be explained in the chapter 8 'Profile Retrieval using Simulated Data'. Two but much larger error maxima could be found at 0 km altitude and at 3 to 5 km altitude in this study. These maximum values of approximately 0.09 ppbv correspond to 13% of the retrieval error value of 0.7 ppbv at 0 km, to 23% of the retrieval error value of 0.4 ppbv at 3 km altitude, and to 15% of the retrieval error value of 0.6 ppbv at 5 km altitude observed in the same altitudes of the reference profile retrieval run (not shown here).
At 500 nm, the results are quite different as can be seen in Fig. 6.5b. In this case all error maxima are much larger. The error maxima values of 0.2 ppbv (0 km), 0.16 ppbv (5 km), and 0.12 ppbv (15 km) shown in Fig. 6.5b are large in some occasions compared to retrieval error values of 0.28 ppbv at 0 km (0.08 ppbv at 5 km) altitude and 0.83 ppbv at 15 km altitude observed in the same altitudes of the reference profile retrieval run (not shown here). The main result of this investigation is that the profile retrieval is dependent on aerosol changes of ±50 % in some altitudes and some wavelength regions. The reason why the two observed wavelength regions display a different behavior when changing the aerosol loading is the fact that the same extinction profile (Fig. 6.4) was used for the two wavelength regions. In reality one aerosol concentration profile has a different extinction at different wavelengths due to the wavelength dependent extinction coefficient.

6.4.4 Influence of Albedo on the Forward Model Error

This study deals with the influence of variations of albedo on the forward model error. This analysis is important because the albedo is set to a fixed value in the forward model, and it is performed to estimate the influence of minor changes in surface albedo on the profile retrieval. Large changes due to snow covered or snow free surfaces are investigated in chapter 7. In order to analyze this influence profile retrievals for varying albedo of ±0.15 were performed. An albedo of 0.3 was assumed as reference. Fig. 6.6a shows the error of the retrieved profile in case the albedo has an error of ±0.15 at 350 nm. This figure shows the absolute value of the error against altitude for both cases 'albedo - 0.15' and 'albedo + 0.15'. As can be seen in Fig. 6.6a the influence of a change of ±0.15 in albedo again is nonlinear considering the profile's covered range of altitude. A large error occurs at 17 km altitude. As already explained in the previous section this phenomenon will be explained in chapter 8 'Profile Retrieval using Simulated Data'. A larger error maximum can be found at 0 km altitude in this study. This maximum value of approximately 0.3 ppbv corresponds to 43% compared to the retrieval error value of 0.7 ppbv at 0 km in the same altitude of the reference

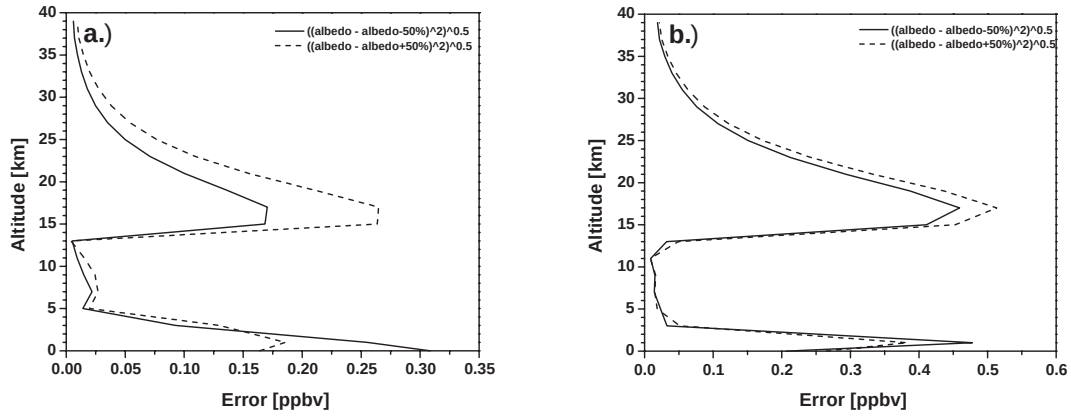

Figure 6.6: Magnitude of the error in case the albedo is changed by ±0.15. Plot a shows the forward model error due to albedo changes at 350 nm and plot b shows this forward model error component at 500 nm. These plots represent the absolute values of the this error component.

profile retrieval run (not shown here).
At 500 nm, the results are quite similar except the maximum error values are significantly larger. At 1 km altitude this error component has a value of almost 0.5 ppbv which is large compared to 0.46 ppbv total retrieval error of the reference retrieval run. The main result of this investigation is that the profile retrieval is very dependent on albedo changes of ±0.15. But it has to be noted that this estimate of this error component is conservative because the absolute change of 0.15 when considering snow free surfaces is very large.

6.4.5 Influence of Absorption Cross Sections on the Forward Model Error

This study deals with the influence of variations of the absorption cross sections for NO_2 on the forward model error. This investigation is important to estimate the uncertainties due to errors in the trace gas absorption cross section being used in the forward model. The reason for choosing a relative change in the parameter is the same as stated in section 6.4.2 dealing with the influence of pressure on the forward model error. In order to analyze this influence profile retrievals for varying cross sections of ±50 % were performed. Fig. 6.7a shows the error of the retrieved profile in case the cross sections have an error of ±50 % at 350 nm. This figure shows the absolute value of the error against altitude for both cases 'cross sections - 50 %' and 'cross sections + 50 %'. As can be seen in Fig. 6.7a the influence of a change of ±50 % in absorption cross section again is nonlinear considering the profile's covered range of altitude. Two error maxima can be observed at 3 and 15 km altitude. As already explained in the previous section the peak at 15 km altitude will be explained in chapter 8 'Profile Retrieval using Simulated Data'. At 500 nm the errors are even smaller. Compared to the previous error components the errors observed in this investigation are small.

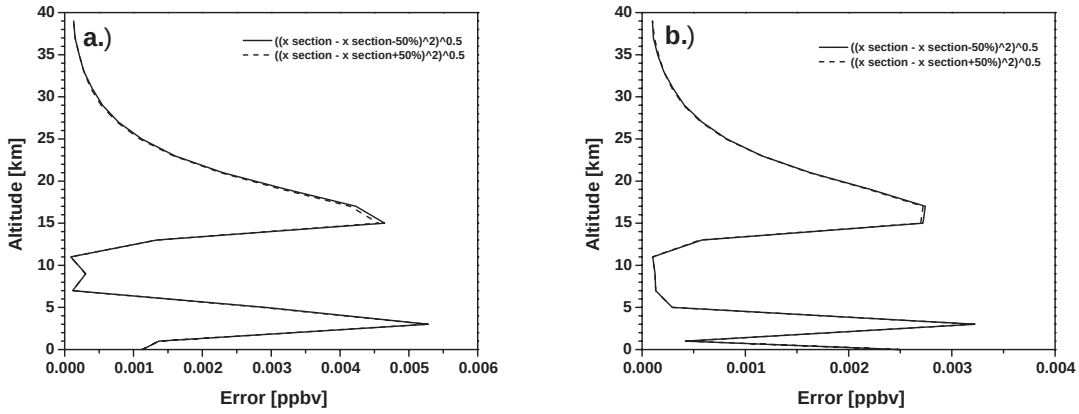

Figure 6.7: Magnitude of the error in case the absorption cross sections are changed by ± 50 %. Plot a shows the forward model error due to cross section changes at 350 nm and plot b shows this forward model error component at 500 nm. These plots represent the absolute values of the this error component.

The main result is that the profile retrieval is quite invariant to cross section changes of ± 50 %.

6.4.6 Influence of the Center-Wavelength-Approximation of the DOAS fitting window on the Forward Model Error

This investigation deals with the issue of approximating the DOAS fitting window by just one wavelength in the profile retrieval. This investigation is necessary to analyze

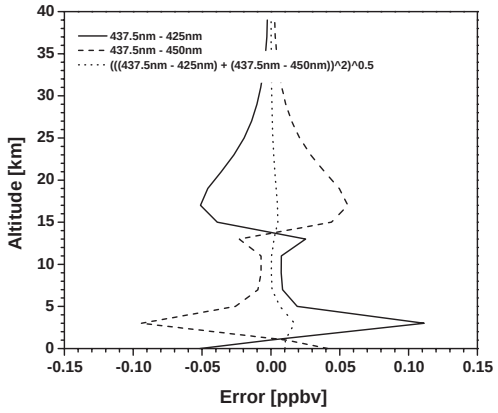

Figure 6.8: Investigation on the influence of the approximation a DOAS fitting window of 425 to 450 nm by the center wavelength (437.4 nm) on the forward model error.

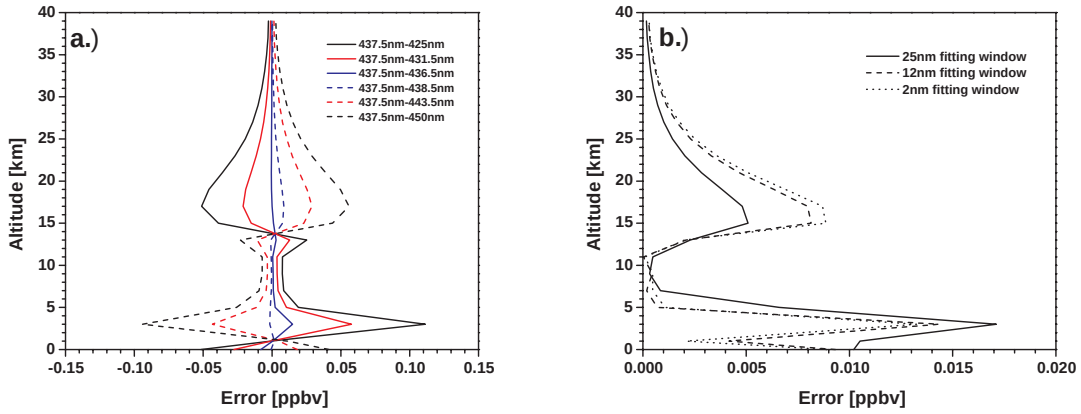

Figure 6.9: Magnitude of the error in case smaller DOAS fitting windows are used in the Center-Wavelength-Approximation at 437.5 nm. Plot a shows the results for a 2 nm, 12 nm, and 25 nm fitting window and plot b shows the total errors of all three fitting windows.

the approximation of a fitting by one wavelength. In the DOAS-analysis the measured spectra are fitted using a well defined fitting window e. g. for NO_2 a prominent fitting window encloses the wavelength region from 425 nm to 450 nm. The goal of this investigation is to estimate the error introduced by the approximation of this fitting window by its center wavelength (437.5 nm).
Before going into detail about this study a closer look on the DOAS data analysis seems to be necessary. Chapter 4 'The Experimental Setup' deals with the data analysis of measured DOAS spectra as well. Eq. 4.12 is the basic equation for analyzing DOAS data. Although in the DOAS data analysis this equation is not solved for just one wavelength but for a range of wavelengths. To reduce the residual[5] of the fit an ideal wavelength range (a so-called fitting window) is selected, where the correlation with other trace gases is small. APROVAL approximates the fitting window used by the DOAS analysis by treating the center wavelength of the fitting window only. This study estimates the error due to this Center-Wavelength-Approximation (CWA). The error is calculated by taking the differences of the retrieved profiles of the retrieval runs without and with ±error. These differences are referred to as partial errors from now on. Fig. 6.8 shows the partial errors and the total error due to CWA of the fitting window and as can be seen in these plots the partial errors are quite symmetric. This symmetry is expected because as approximation wavelength the center of the fitting was chosen. This choice already suggests a symmetry to occur in the partial errors. The total error due to the CWA of the fitting window can be calculated by simply adding the two partial errors. Another assumption made in this study is the linearity of the behavior of the partial errors meaning a broader fitting window leads to larger absolute valued partial errors. In case the assumption of this linearity is correct the result of this study would be a maximum partial error when taking into account the

[5]The residual of a DOAS fit is the difference between the modeled optical depth and the measured optical depth.

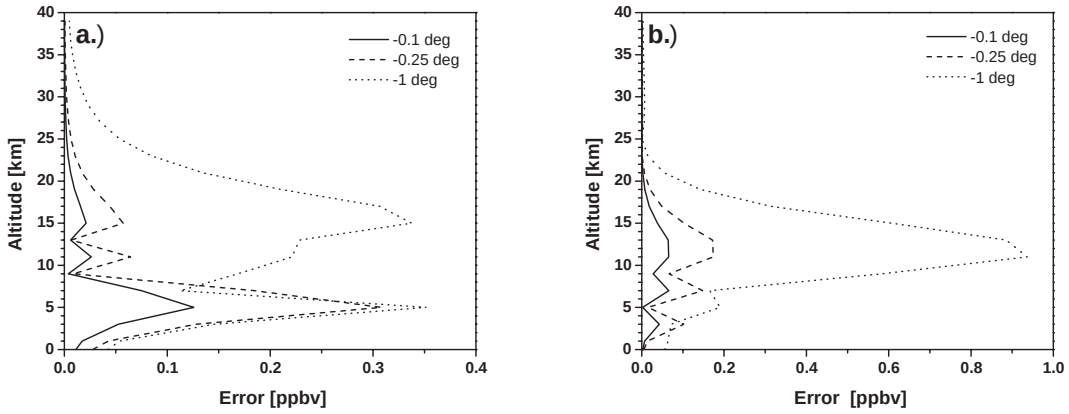

Figure 6.10: Magnitude of the error in case the LOS is changed by $-0.1°$, $-0.25°$, and $-1°$. Plot a shows the forward model error due to changes in LOS at 350 nm and plot b shows this forward model error component at 500 nm. These plots represent the absolute values of the this error component.

boundaries of the fitting windows to calculate the partial errors. The Comparison of Fig. 6.8b and Fig. 6.9a shows the linear behavior of the partial errors.
Unfortunately the total errors of the three considered fitting windows do not behave stringently linear as shown in Fig. 6.9b. The 12 nm fitting window has an approximately 20% larger total error than the 25 nm fitting window. So Fig. 6.9b represents the error of the CWA compared to a profile retrieval taking into account three wavelengths per fitting window (lower boundary of fitting window, center wavelength, and upper boundary of fitting window).

6.4.7 Influence of the LOS Pointing Accuracy on the Forward Model Error

This study deals with the influence of pointing accuracy of the LOS on the forward model error. In order to analyze this influence, profile retrievals for a change of $-1°$ in viewing direction were performed. Fig. 6.10a shows the error of the retrieved profile in case the LOS has an error of $-1°$ at 350 nm. This figure shows the absolute value of the error against altitude for the retrieval run 'LOS - 1°'. As can be seen in Fig. 6.10a the influence of a change of $-1°$ in LOS is nonlinear considering the profile's covered range of altitude. The largest error values of 0.35 ppbv occur at 5 and 15 km altitude. These values are quite large compared to the retrieval errors of 0.4 ppbv at 5 km and 0.9 ppbv at 15 km altitude as observed in scenario 31 (see Fig. 7.16e, chapter 7), which is the corresponding scenario with no change in the viewing directions. For a change of $-0.1°$ in LOS the error of this forward model error component is much smaller (error maximum of 0.15 ppbv at 5 km altitude).
At 500 nm, considering a change of $-1°$ in LOS the results are different because only one large maximum occurs. This error maximum has a value of 0.9 ppbv in 11 km

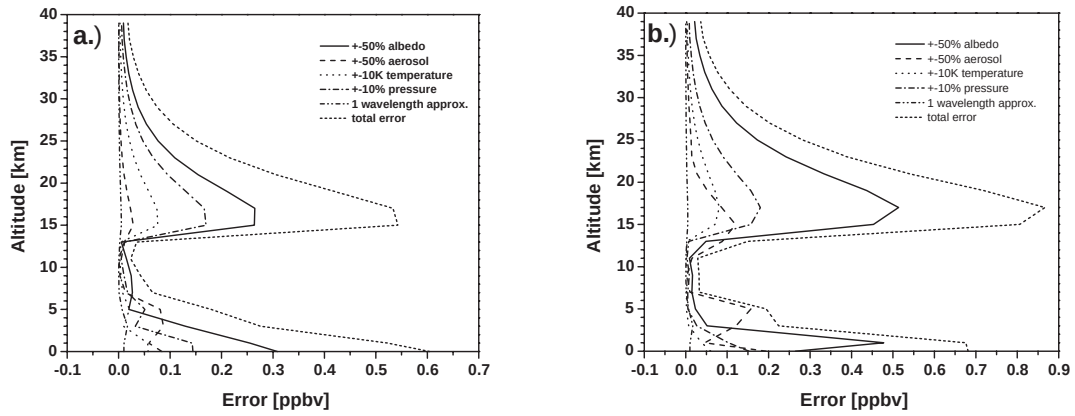

Figure 6.11: Magnitude of the forward model error components compared to each other. Plot a shows the results for 350 nm and plot b shows the results for 500 nm. Shown in these plots are the absolute values of the error components and the total forward model error.

altitude. Compared to the retrieval error of scenario 32 (see Fig. 7.16f, chapter 7) this value is large (0.2 ppbv in 11 km altitude). For a change of $-0.1°$ in LOS the error of this forward model error component is much smaller (errors < 0.1 ppbv), too. The main result of this investigation is that the profile retrieval is very sensitive to changes of $\pm 1°$ in LOS especially at 500 nm. For profile retrieval using real data an uncertainty in LOS of smaller than $0.1°$ is recommended. For the AMAXDOAS instrument the pointing accuracy is not an issue, since the recorded flight data have an uncertainty of $0.01°$ in pitch and roll of the aircraft. Thus the pointing accuracy of the AMAXDOAS LOS is $0.01°$.
Bruns *et al.* [2004] come to a similar result concerning the importance of pointing accuracy. It is claimed that a pointing accuracy of larger than $0.1°$ is strongly influencing the retrieved profiles at 500 nm. Bruns *et al.* have used a different criterion of quality concerning pointing accuracy. The pointing accuracy was analyzed by comparing the retrieval errors of both retrieval runs 'LOS' and 'LOS - 1°'. In this investigation another approach to the problem was used. According to Rodgers [2000] a more reasonable method of error calculation due to a specific parameter is the difference in retrieved profiles.

6.4.8 Total Forward Model Error

All forward model error components mentioned in the sections above are systematic errors. To calculate the total forward model error due to all error components involves the error propagation, which in theory could be calculated analytically because all physical phenomena causing those errors are well known. Unfortunately the radiative transfer model is based on integro-differential radiative transfer equations making the analytical calculation using the error propagation very difficult if not impossible. So an assumption has to be made to calculate the total forward model error. The assumption

is that all error components are independent, which is true for most parameters like pressure, temperature, pointing accuracy, aerosols, and albedo. The parameter of the absorption cross sections on the other hand depends on the temperature as discussed in its section above. This dependence has to be neglected when calculating the total forward model error. Due to the assumption of independence of all parameters the total forward model error can be calculated quite easily by adding up all forward model error components. Fig. 6.11 is showing the total forward model error and as can be seen the largest errors occur again at altitudes of 15 to 17 km. The difference between both considered wavelengths is small. A total forward model error of approximately 0.3 ppbv is small compared to the total retrieval error of more than 0.8 ppbv above 15 km altitude. A second error maximum occurs at 1 km altitude, but that is significantly smaller with an value of approximately 0.1 ppbv for both wavelengths. Fig. 6.11 does not account for the error due to changes in the absorption cross sections because this error is very small (< 0.003 ppbv). The error due to CWA is plotted for the 25 nm fitting windows, since it has one of the largest error values.

6.5 The Total Retrieval Error

The total error of the profile retrieval can be calculated using Eq. 6.2. Having discussed all necessary error components mentioned in eq. 6.2 it is a simple task to calculate S_{tot}. As mentioned in the section 6.4.8 'Total Forward Model Error' all error components included in the total forward model error are systematic. Thus the total forward model error is systematic as well. The Smoothing Error of eq. 6.3 is depending on the error of the a priori information which is taken from a model. Model errors are known to be systematic therefore the Smoothing Error is systematic as well. Last but not least there is the Retrieval Noise which depends on the measurement error according to eq. 6.4. Measurement errors are to some extend statistical errors. In this case the error of the measured slant columns densities are $\pm 1\sigma$. The systematic errors in Tab. 6.1 of the measured slant columns of NO_2 were estimated by Richter [1997].

6.6 Summary

The error analysis presented in this chapter has shown that:

- Two components of the total retrieval error (see eq. 6.2) can be calculated quite easily according to eq. 6.3 and 6.4.
- The third error component of the total retrieval error is more difficult to estimate. The forward model error component is estimated using sensitivity studies because of the non-linearity of the forward model. Thus error propagation calculations are very difficult to perform.
- A change of ± 10 K in temperature is not affecting the retrieved profiles significantly because the forward model error is always smaller than 0.1 ppbv at both wavelengths (350 and 500 nm).

- A change of ±10% in pressure results in an uncertainty of approx. 0.15 ppbv of the retrieved profiles at both wavelengths. This value is a maximum value which occurs near the surface and at 15 km altitude.

- The profile retrieval is dependent on the aerosol loading in the atmosphere at some altitudes specifically the lower troposphere.

- A change of ±50% (±0.15 absolute) in surface albedo results in an uncertainty of the retrieved profiles of up to 0.3 ppbv at 350 nm at 0 km altitude and up to 0.5 ppbv at 500 nm at 1 km altitude. The change of this parameter indicates the largest uncertainty observed in these sensitivity studies, but it has to be noted that an absolute change of ±0.15 in surface albedo is a very large change, which is not observed over land or ocean expect on boundaries to snow covered regions. But the changes in albedo of this order are analyzed in chapter 7.

- Uncertainties of retrieved profiles due to the center-wavelength-approximation proved to be very small (< 0.02 ppbv).

- A pointing accuracy of the LOS of smaller than 0.1° is necessary otherwise uncertainties of up to 0.9 ppbv are possible at 500 nm at 10 km altitude. This is not an issue considering the AMAXDOAS data, since the recording of the flight data included pitch and roll data of the aircraft with an uncertainty of 0.01°.

- The total error due to uncertainties of the forward model parameters adds up to 0.6 ppbv at 350 nm at 0 km altitude and 0.7 ppbv at 500 nm at 0 km altitude. But is has to be noted that this estimation is a worst case scenario as discussed partially the section for each forward model parameter. Thus the total forward model error is not taken into account in the profile retrieval using real AMAXDOAS data.

Chapter 7

Sensitivity Studies

The main question being addressed in these studies is: Do AMAXDOAS measurements contain any profile information at all? To assess the amount of profile information contained in AMAXDOAS measurements, slant columns are being simulated for a number of different scenarios and a retrieval performed using the method described in chapter 5. The work presented in this chapter was partially published in [Bruns *et al.*, 2004]. The results are discussed by evaluating the averaging kernels, weighting functions and retrieval errors. An overview of the different scenarios that are being studied is given in Tab. 7.1. Briefly, the influence of wavelength, surface spectral reflectance (from now on referred to as albedo), flight altitude, and also the choice of LOS is being investigated. While the choice of specific parameters (the standard LOS: 0°, 60°, 80°, 85°, 88°, 92°, 95°, 100°, 120°, 180°; a flight altitude of 10 km; and wavelengths of 350 and 500 nm) is based on the set-up and operation of the AMAXDOAS instrument, the results are valid in general and not restricted to this experiment. Also, the discussion is focused on the case of NO_2 retrieval but can readily be applied to other trace gases taking into account the differences in the absorption cross sections and wavelength used.

In this study different retrieval grids are used in order to take into account different vertical resolutions. The first retrieval grid is used for a flight altitude of 10 km and has 21 grid points at 0 km, 1 km, 3 km, ..., 39 km. A second retrieval grid with 19 points at 1 km, 4 km, 7 km, 9 km, 11 km, ..., 39 km is used for the combination of four LOS and three wavelengths. At a flight altitude of 2 km a third retrieval grid with 39 points at 0 km, 0.2 km, ..., 4 km, 5 km, 7 km, 9 km, ..., 39 km is used.

Unless stated otherwise a low aerosol scenario from LOWTRAN [Shettle and Fenn, 1979; Kneizys *et al.*, 1986] is chosen, using a visibility in the boundary layer (0 to 2 km) of 23 km, a maritime aerosol type, and 80% humidity. In the free troposphere (2 to 10 km) the visibility is set to 23 km and the humidity to 80%. In the stratosphere the aerosol loading is that of a background scenario. For all studies, a cloud free scenario is assumed.

The meteorological data used in the radiative transfer model are taken from the 3-dimensional chemical transport model SLIMCAT [Chipperfield, 1999]. A mid-latitude spring scenario and a fixed SZA of 51.6° is used. From the output of the radiative transfer model only data with a 90° relative azimuth angle with respect to the sun are taken into account. The investigation is based on the assumption that there are no

Table 7.1: Scenarios for the sensitivity studies.

scenario	albedo	λ [nm]	aerosol	SZA [°]	LOS [°]
1	0.1	350	LOWTRAN	51.6	0, 60, 80, 85, 88, 92, 95, 100, 120, 180
2	0.1	500	LOWTRAN	51.6	0, 60, 80, 85, 88, 92, 95, 100, 120, 180
3	0.9	350	LOWTRAN	51.6	0, 60, 80, 85, 88, 92, 95, 100, 120, 180
4	0.9	500	LOWTRAN	51.6	0, 60, 80, 85, 88, 92, 95, 100, 120, 180
5	0.1	350	no	51.6	0, 60, 80, 85, 88, 92, 95, 100, 120, 180
6	0.1	500	no	51.6	0, 60, 80, 85, 88, 92, 95, 100, 120, 180
7	0.1	350	clean continent	51.6	0, 60, 80, 85, 88, 92, 95, 100, 120, 180
8	0.1	500	clean continent	51.6	0, 60, 80, 85, 88, 92, 95, 100, 120, 180
9	0.1	350	urban	51.6	0, 60, 80, 85, 88, 92, 95, 100, 120, 180
10	0.1	500	urban	51.6	0, 60, 80, 85, 88, 92, 95, 100, 120, 180
11$^{\nabla}$	0.1	350	LOWTRAN	51.6	0, 60, 80, 85, 88, 92, 95, 100, 120, 180
12$^{\nabla}$	0.1	500	LOWTRAN	51.6	0, 60, 80, 85, 88, 92, 95, 100, 120, 180
13	0.1	350	LOWTRAN	20	0, 60, 80, 85, 88, 92, 95, 100, 120, 180
14	0.1	500	LOWTRAN	20	0, 60, 80, 85, 88, 92, 95, 100, 120, 180
15	0.1	350	LOWTRAN	80	0, 60, 80, 85, 88, 92, 95, 100, 120, 180
16	0.1	500	LOWTRAN	80	0, 60, 80, 85, 88, 92, 95, 100, 120, 180
17	0.1	350	LOWTRAN	90	0, 60, 80, 85, 88, 92, 95, 100, 120, 180
18	0.1	500	LOWTRAN	90	0, 60, 80, 85, 88, 92, 95, 100, 120, 180
19$^{\clubsuit}$	0.1	362.5 437.5 485.0	LOWTRAN	51.6	0, 60, 80, 85, 88, 92, 95, 100, 120, 180
20$^{\clubsuit}$	0.9	362.5 437.5 485.0	LOWTRAN	51.6	0, 60, 80, 85, 88, 92, 95, 100, 120, 180
21	0.1	350	LOWTRAN	51.6	0, 88, 92, 180
22	0.1	500	LOWTRAN	51.6	0, 88, 92, 180
23	0.1	350	LOWTRAN	51.6	0, 82, 85, 88, 92, 95, 102, 180
24	0.1	500	LOWTRAN	51.6	0, 82, 85, 88, 92, 95, 102, 180
25	0.1	350	LOWTRAN	51.6	0, 80, 85, 88, 89, 91, 92, 95, 100, 180
26	0.1	500	LOWTRAN	51.6	0, 80, 85, 88, 89, 91, 92, 95, 100, 180
27	0.1	350	LOWTRAN	51.6	86.8, 87.0, 87.3, 87.7, 88.2, 89.0 91.0, 91.8, 92.3, 92.7, 93.0, 93.2
28	0.1	500	LOWTRAN	51.6	see scenario 27
29	0.1	350	LOWTRAN	51.6	0, 80, 85, 95, 100, 180, 86.8, 87.0, 87.3, 87.7, 88.2, 89.0, 91.0, 91.8, 92.3, 92.7, 93.0, 93.2
30	0.1	500	LOWTRAN	51.6	see scenario 29
31	0.1	350	LOWTRAN	51.6	0, 80, 85, 87, 88, 89, 91, 92, 93, 95, 100, 180
32	0.1	500	LOWTRAN	51.6	see scenario 31
33$^{\spadesuit}$	0.1	350	LOWTRAN	51.6	see scenario 29
34$^{\spadesuit}$	0.1	500	LOWTRAN	51.6	see scenario 29
35$^{\triangle}$	0.1	350	LOWTRAN	51.6	see scenario 25
36$^{\triangle}$	0.1	500	LOWTRAN	51.6	see scenario 26

$^{\nabla}$ For these scenarios the flight altitude is 2 km and the retrieval grid is 0 km, 0.2 km, ..., 4 km, 5 km, 7 km, 9 km, ..., 39 km. $^{\clubsuit}$ For these scenarios the retrieval grid is 1 km, 4 km, 7 km, 9 km, 11 km, ..., 39 km. For all other scenarios the flight altitude is 10 km and the retrieval grid is: 0 km, 1 km, 3 km, ... , 39 km. $^{\spadesuit}$ For these scenarios the retrieval grid with 1 km step size from 0 km to 39 km altitude was used. $^{\triangle}$ For these scenarios the retrieval grid with 3 km step size from 0 km to 39 km altitude was used.

horizontal inhomogeneities in the trace gas abundance.
For APROVAL different LOS are crucial. The following ten different LOS are assumed: 0° (nadir), 60°, 80°, 85°, 88°, 92°, 95°, 100°, 120°, and 180° (zenith).
The sensitivity studies are done for NO_2. To perform the sensitivity studies, appropriate values for the a priori ($\mathbf{e}_a = \sqrt{\mathbf{S}_a} \cdot \mathbf{1}$)[1] and measurement error ($\mathbf{e}_\epsilon = \sqrt{\mathbf{S}_\epsilon} \cdot \mathbf{1}$)

[1]The error covariance matrix of the a priori error was defined in the previous chapter as a diagonal matrix with the diagonal elements containing the squares of the actual errors. Thus the square roots of the diagonal elements multiplied by the unity vector $\mathbf{1}$ of the same dimension as $\mathbf{S}_a$ represent the a priori (or any other error component) vector $\mathbf{e}_a$.

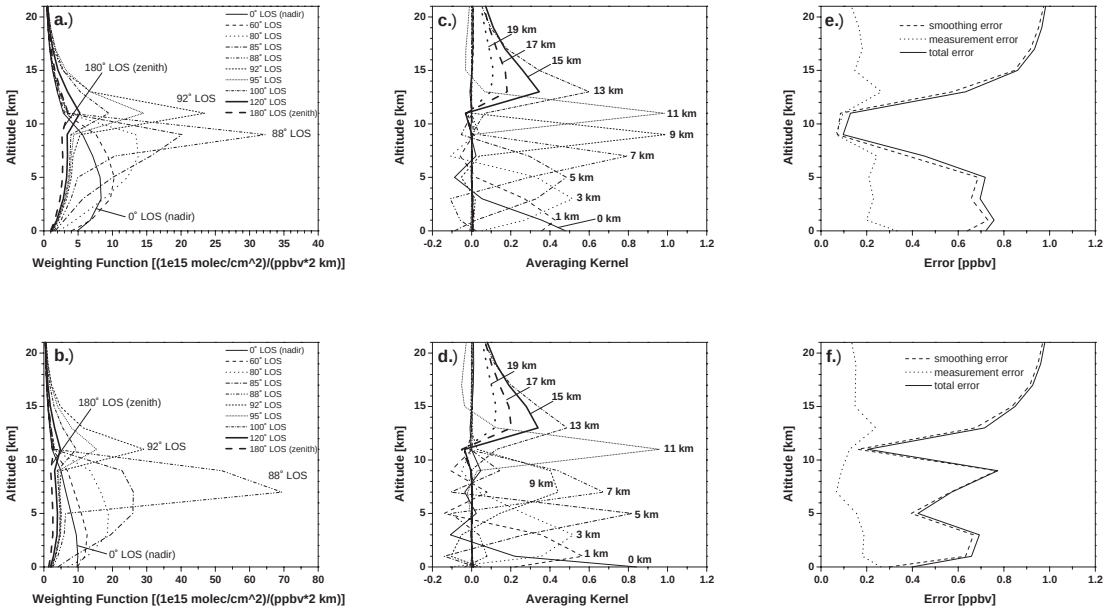

Figure 7.1: The weighting functions for the investigation dealing with the influence of wavelength on the retrieval are shown for 350 nm in plot a and for 500 nm in plot b, the corresponding averaging kernels are shown in plots c and d, and the retrieval errors are shown in plots e and f.

have to be assumed. Since the measured slant columns will be in the order of $1.0 \cdot 10^{16}$ molec/cm^2 to $1.5 \cdot 10^{16}$ molec/cm^2, a standard deviation of 10^{15} molec/cm^2 is a realistic measurement error. A good DOAS instrument is able to measure a differential optical depth as small as $3 \cdot 10^{-4}$ with a reasonable signal to noise ratio of 2. Using the differential cross section of NO_2 near 500 nm of $2.5 \cdot 10^{-19}$ cm^2/molecule the smallest slant column measurable with this instrument is calculated to be $1.2 \cdot 10^{15}$ molecules/cm^2.

The maximum mixing ratio of the NO_2 profile is in the order of 9 ppbv. In this case a standard deviation of 1 ppbv as a priori error seems to be reasonable.

In Fig. 7.1c the averaging kernels for scenario 1 are shown. This scenario assumes a flight altitude of 10 km, a wavelength of 350 nm, and an albedo of 0.1. A first look at the averaging kernels reveals a large sensitivity of the profile retrieval near flight altitude.

There are two distinctive averaging kernels (9 and 11 km) suggesting a very high sensitivity and a vertical resolution of 2.0 and 2.1 km near the flight altitude. Going further down towards the surface the averaging kernels broaden. In contrast to the 9 km averaging kernel the 1 km averaging kernel has a FWHM value of 4.9 km. The changing peak altitudes and FWHM values for the averaging kernels can be understood considering the limited visibility of the atmosphere in the UV at 350 nm. Good vertical resolution will be achieved if the average light paths through different altitude layers differ strongly. This is the case for the layer close to flight altitude, which is penetrated differently by the individual viewing directions. To understand this pattern of averaging kernels it is necessary to analyze the weighting functions. Chapter 5 dealing with the

retrieval theory described the weighting functions as sensitivity of the measurements as a function of altitude. The maximum of the weighting functions are indicators for the altitude from which most of the information for a given LOS is coming from. The weighting functions for scenario 1 are shown in Fig. 7.1a. The weighting functions for the downward looking LOS peak in different altitudes. This suggests, that different LOS are sensitive to different altitudes.
Above the aircraft the vertical resolution of the averaging kernels decreases. The FWHM of the 11 km averaging kernel is 2.1 km, whereas the FWHM value of the 13 km averaging kernel is 3.7 km. All averaging kernels above flight altitude peak at 13 km except for the 11 km averaging kernel. The weighting functions of Fig. 7.1a confirm the information given by the averaging kernels. The sensitivity of the upward looking LOS to altitudes above 13 km is small and does not contain profile information.
Fig. 7.1e shows the retrieval errors for scenario 1 resulting from the smoothing and measurement error described above. The total retrieval error ($\mathbf{e}_{ret} = \sqrt{(\mathbf{S}_s + \mathbf{S}_m)} \cdot \mathbf{1}$) is a measure of quality of the retrieval. A small total error indicates a retrieval of high quality.
A comparison with the retrieval error of a profile retrieval using a perturbation grid with 1 km step size (see section 7.7) reveals that the retrieval error decreases significantly when the perturbation grid step size is increased. There appears to be sufficient information in the measurements that a 2 km vertical resolution of the retrieved profile is appropriate.

7.1 Influence of the Wavelength on the Retrieval

The consideration of the wavelength is important for the profile retrieval because the absorbing potential of different trace gases in different wavelength regions is changing rapidly. In this investigation two wavelengths were used, one in the UV (350 nm) and one in the visible wavelength region (500 nm). The averaging kernels of scenario 1 (see Fig. 7.1c) and scenario 2 (see Fig. 7.1d) are compared. The overall behavior of the averaging kernels at 500 nm is basically the same as at 350 nm.
There are however a few exceptions. The first exception is that the vertical resolution of the 9 km averaging kernel decreases significantly (4.5 km instead of 2.0 km in scenario 1). The second exception is that the 0 km and 5 km averaging kernels have a significantly increased vertical resolution. Compared to scenario 1 the vertical resolution for the 0 km averaging kernel increases from 3.5 to 1.3 km. The vertical resolution for the 5 km averaging kernel increases from 4.9 to 2.4 km. The weighting functions for scenario 2 are plotted in Fig. 7.1b, and it can be seen that there are no two LOS, that can resolve the layer between flight altitude and 5 km explaining the significantly decreased vertical resolution at 9 km.
The third exception is, that the 0 km averaging kernel has a much larger value compared to the same averaging kernel at 350 nm. This feature suggests a higher sensitivity of the 500 nm measurements in the lower troposphere, as is expected as a result of the reduced importance of Rayleigh scattering at this wavelength.
As can be seen in Fig. 7.1d the vertical resolution at 500 nm is lower than at 350 nm between 7 and 9 km altitude, but it is higher at an altitude of 5 km. This result is

confirmed by the retrieval errors shown in Fig. 7.1f. For 500 nm, the retrieval error between 7 and 9 km is larger than at 350 nm but smaller than that at 350 nm at 5 km. The results of this investigation are very important for the profile retrieval using real AMAXDOAS data as can be seen in chapter 9. The wavelength dependent vertical resolution of the retrieved profiles resulting in different vertical resolutions in different altitudes observed in this investigation is very useful because for the profile retrieval using real AMAXDOAS data APROVAL applies the combination of four LOS at three wavelengths (362.5 nm, 437.5 nm, and 485.0 nm). Thus virtually twelve LOS are used in this specific LOS setup as will be discussed later in this chapter.

7.2 Influence of the Albedo on the Retrieval

The albedo or surface spectral reflectance might be important for the profile retrieval due to the strong influence on multiple scattering of radiation in the lowest parts of the troposphere and the influence of reflected light from the surface. This enhanced multiple scattering above surfaces with increased albedo is caused by the increased amount of reflected photons. To investigate the influence of albedo, the averaging kernels for albedos of 0.1 and 0.9 respectively are considered for the two wavelengths (350 and 500 nm). For scenario 4 at 500 nm (see Fig. 7.2d) and an albedo of 0.9, there is no significant change compared to scenario 2 at 500 nm and an albedo of 0.1. However, in the UV at 350 nm, the 1 km averaging kernel increases by 50% (see Fig. 7.2c). The averaging kernels for altitudes above 0 km do not change significantly

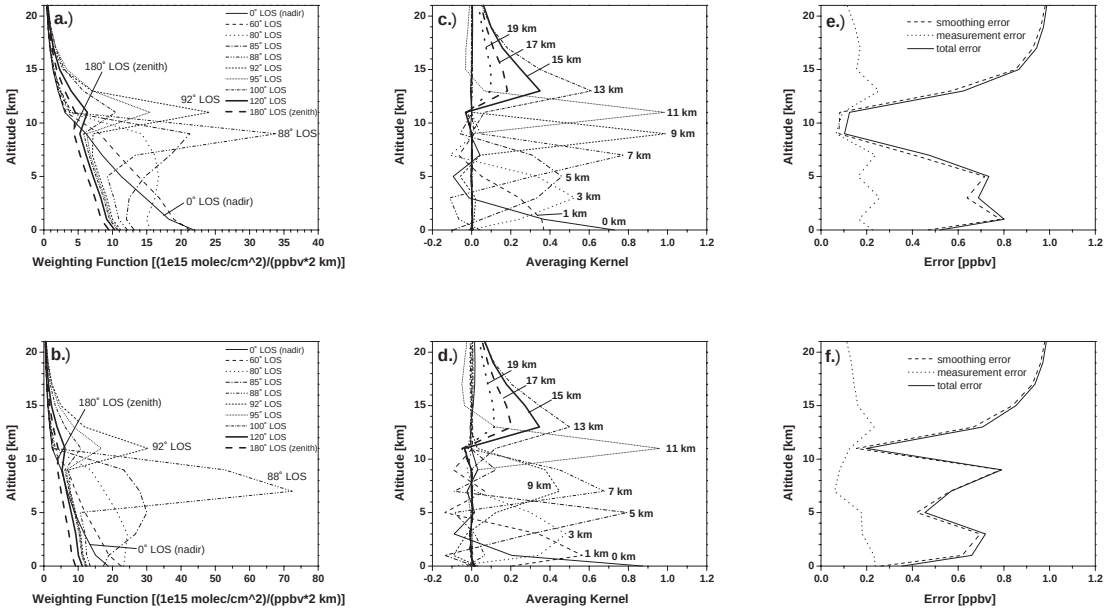

Figure 7.2: The weighting functions for the investigation dealing with the influence of albedo on the retrieval are shown for 350 nm in plot a and for 500 nm in plot b, the corresponding averaging kernels are shown in plots c and d, and the retrieval errors are shown in plots e and f.

when the albedo is changed from 0.1 to 0.9. The same holds for the averaging kernels above the aircraft. This can be explained by taking into account the enhancement of multiple scattering as a result of the larger number of reflected photons at the surface in the UV wavelength region. The enhanced multiple scattering is limited to the lower altitudes close to the surface, because multiple scattering is occurring most likely in parts of the atmosphere having a higher density. The overall result of this study is that large albedo will increase the sensitivity of UV measurements in the surface layer but apart from that, there is little influence on the profile information of the measurements. It has to be noted that in practice the measured signal for the downward looking LOS is much larger in case of albedo 0.9 compared to an albedo of 0.1. This behavior is shown by the weighting functions in Fig. 7.2a and b which have much larger values near the surface than the weighting functions calculated for an albedo of 0.1 as shown in Fig. 7.1a and b.

7.3 Influence of Aerosols on the Retrieval

Aerosols are important because of two reasons: The first reason is aerosols cause scattering of light, and the second reason is aerosols absorb radiation. The scattering of light due to aerosols can lead to an increased light path and therefore to an increased measured slant column due to multiple scattering depending on the aerosol's concentration. In case of high aerosol concentrations the absorption by aerosols is increased preventing the radiation from reaching the surface before being detected by an airborne spectrometer. This investigation is dealing with the influence of aerosols on the profile retrieval. Three aerosol scenarios (no aerosol, clean continental aerosol, and urban aerosol) will be compared to a reference scenario containing the aerosol profile from LOWTRAN described in the beginning of this chapter. The first aerosol scenario investigated contains no aerosol at all. This scenario was included to analyze the influence of total absence of aerosols on the profile retrieval. The clean continental

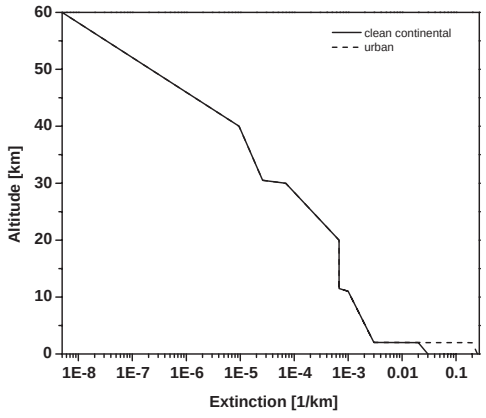

Figure 7.3: Extinction profiles of the aerosol scenarios taken from Kauss [1998].

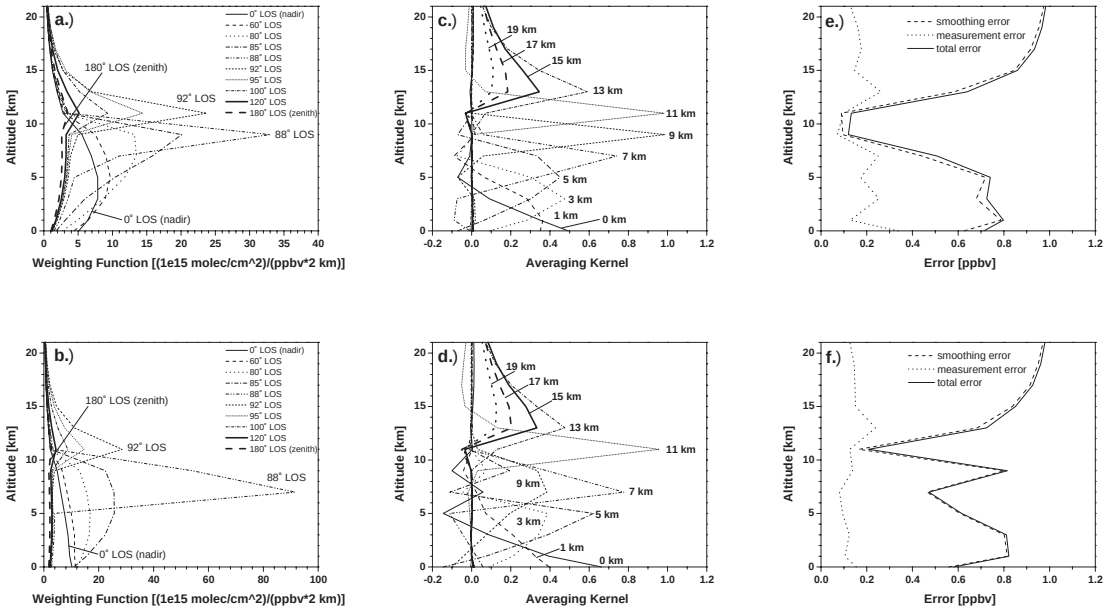

Figure 7.4: The weighting functions for the investigation dealing with the influence of missing aerosols on the retrieval are shown for 350 nm in plot a and for 500 nm in plot b, the corresponding averaging kernels are shown in plots c and d, and the retrieval errors are shown in plots e and f.

aerosol scenario contains an aerosol extinction profile shown in Fig. 7.3 and four layers containing different aerosol types (see section 7.3.2 'Clean Continental Aerosols' and Tab. 7.2). The last aerosol scenario contains urban aerosols and the extinction profile is shown in Fig. 7.3, too. This scenario contains four aerosol layers as well (see section 7.3.3 'Urban Pollution' and Tab. 7.3). These aerosol scenarios were taken from Kauss [1998].

7.3.1 No Aerosols

At 350 nm, the averaging kernels of the scenario containing no aerosol at all (scenario 5) show no significant differences to scenario 1 with an exception of the FWHM value at 1 km altitude. Scenario 1 has a FWHM value of 5.0 km whereas scenario 5 has a FWHM value of 6.2 km at 1 km altitude. This can be explained by less multiple scattering in the lower troposphere decreasing the light path of the measured slant column. The FWHM value at 0 km altitude of scenario 5 being virtually the same as the FWHM value of scenario 1 is a little bit peculiar. One would assume the influence of aerosols at 0 km altitude is the same as in 1 km altitude or even larger. Maybe this phenomenon is due to the approximation assumed in the calculation of the FWHM value in case only one half of the averaging kernel exists (see section 5.1.1 'Resolution').
At 500 nm, the results are quite different. The FWHM values of scenario 6 at 3 and 5 km altitude are 5.0 km and 3.3 km. On the contrary the FWHM values of scenario 2 at 3 and 5 km altitude are 4.3 km and 2.4 km. The increased FWHM values of scenario 6 at 3 and 5 km altitude show the aerosols are positively influencing the profile retrieval

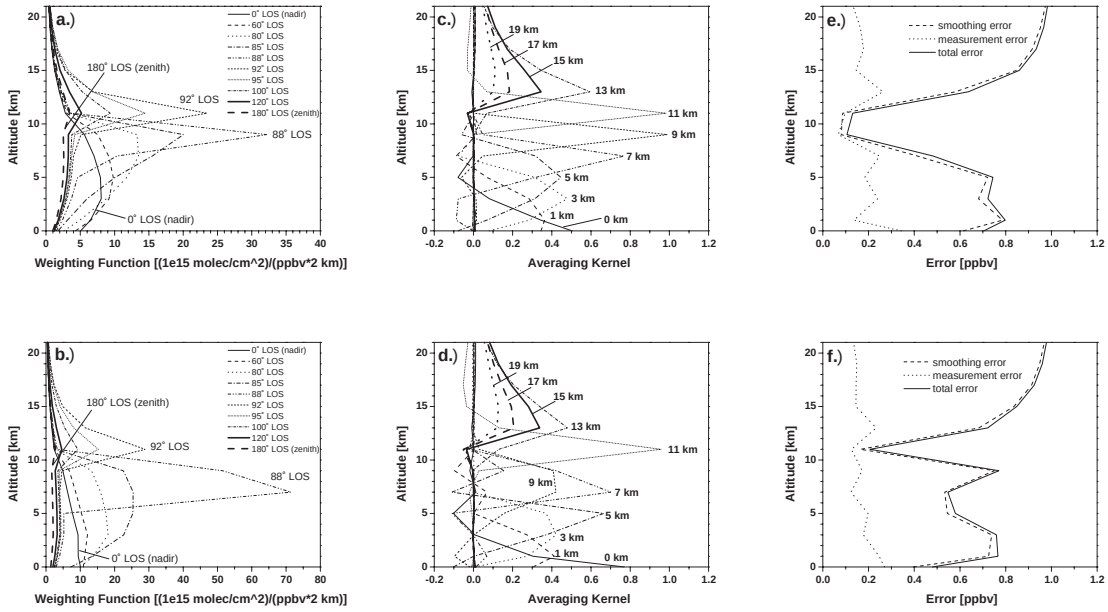

Figure 7.5: The weighting functions for the investigation dealing with the influence of clean continental aerosols on the retrieval are shown for 350 nm in plot a and for 500 nm in plot b, the corresponding averaging kernels are shown in plots c and d, and the retrieval errors are shown in plots e and f.

up to an altitude of 5 km due to enhanced multiple scattering. The FWHM values of scenario 6 at 0 and 1 km altitude are 2.8 km and 6.3 km in comparison to FWHM values (scenario 2) of 1.3 km and 3.1 km at 0 and 1 km altitude. Again this can be explained by enhanced multiple scattering in the lower troposphere.

7.3.2 Clean Continental Aerosols

The aerosol scenario used in this study was taken again from Kauss [1998]. This scenario consists of four aerosol layers. Tab. 7.2 contains all details concerning the aerosol types and relative aerosol concentration of each layer. The boundary layer up to 2 km altitude contains 80% relative humidity and two different aerosol types. Virtually

Table 7.2: Clean continental Aerosol Scenario.

upper boundary [km]	rel. humidity [%]	aerosol component	relative mixing ratio
2	80	water soluble	0.999942
		insoluble (dust)	0.000058
10	70	water soluble	0.999942
		insoluble (dust)	0.000058
30	0	sulfate	1.00000
60	0	meteoric dust	1.00000

Table 7.3: Urban Aerosol Scenario.

upper boundary [km]	rel. humidity [%]	aerosol component	relative mixing ratio
2	80	water soluble	0.177000
		insoluble (dust)	0.000009
		soot	0.822991
10	70	water soluble	0.457987
		insoluble (dust)	0.000026
		soot	0.541987
30	0	sulfate	1.00000
60	0	meteoric dust	1.00000

all aerosols in this layer are water soluble particles consisting mostly of sulfates, nitrates and other water soluble substances except for 58 ppmv insoluble particles such as dust. The second layer comprehends the free troposphere up to an altitude of 10 km containing 70% relative humidity. The composition of aerosol is the same as in the boundary layer. The third layer contains the stratosphere up to 30 km altitude. Since the stratosphere is very dry, this layer in this scenario contains no water vapor. The only aerosol particles are sulfates forming the stratospheric background aerosol. The last layer up to an altitude of 60 km contains no water vapor too and only meteoric dust as aerosols.

Fig. 7.5c shows the averaging kernels of the clean continental aerosol scenario at 350 nm (scenario 7). Compared to scenario 5 which contains no aerosols at all the averaging kernels show no significant differences. Thus the averaging kernels are very sensitive to a low aerosol abundance in the troposphere at 350 nm. At 500 nm the situation is quite different. As can be seen in Fig. 7.5d the averaging kernels below 5 km altitude behave differently compared to scenario 6 containing no aerosols. Each averaging kernel peaks at its altitude, and the FWHM values decrease while increasing the resolution. At 0 km altitude the FWHM value decreased from 2.8 km to 1.6 km, at 1 km altitude from 6.3 km to 5.1 km, and at 3 km the FWHM value does not change significantly. Above 3 km altitude the FWHM values do not change significantly either. The clean continental aerosol abundance seems to influence the lower troposphere only, due to the increased scattering that occurs on the aerosols present.

7.3.3 Urban Pollution

The aerosol scenario used in this study was also taken from Kauss [1998]. As the aerosol scenario in the previous section this scenario consists of four aerosol layers. Tab. 7.3 contains all details concerning the aerosol types and relative aerosol concentration of each layer. The boundary layer up to 2 km altitude contains 80% relative humidity and three different aerosol types. The most important type of aerosol in this layer is soot with over 80% in relative mixing ratio. The second largest abundance in this layer have water soluble particles with almost 18% in relative mixing ratio. The last aerosol type (insoluble particles) have a very small relative mixing ratio of 9 ppmv. The second layer comprehends the free troposphere up to an altitude of 10 km containing 70%

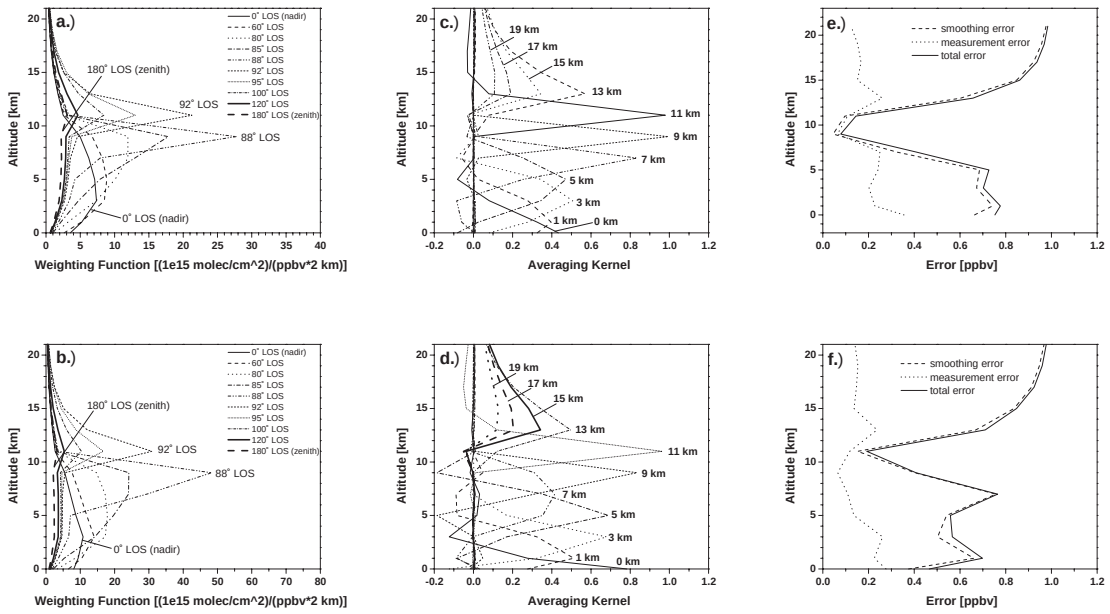

Figure 7.6: The weighting functions for the investigation dealing with the influence of urban aerosols on the retrieval are shown for 350 nm in plot a and for 500 nm in plot b, the corresponding averaging kernels are shown in plots c and d, and the retrieval errors are shown in plots e and f.

relative humidity. The composition of aerosol types is the same as in the boundary layer but with different relative mixing ratios. The third layer and fourth layer are the same as in the previous section.

At 350 nm, there is virtually no difference between scenarios 9 and 5. This is due to the fact that apparently the visibility is not influenced by aerosols in this wavelength region. At 500 nm the situation is again quite different. As can be seen in Fig. 7.6d the averaging kernels below 5 km altitude behave differently compared to scenario 6 containing no aerosols. Each averaging kernel peaks at its altitude, and the FWHM values decrease while increasing the resolution. At 0 km altitude the FWHM value decreases from 2.8 km to 1.5 km, at 1 km altitude from 6.3 km to 3.5 km, and at 3 km from 5.0 km to 3.4 km. This is again due to the increased scattering that occurs on the aerosols present in the lower troposphere. In this investigation there is also a difference in the averaging kernels above 3 km altitude. In scenario 6 the 9-km averaging kernel peaks in the same altitude as the 7-km averaging kernels due to the same reason as discussed in section 7.1 'Influence of the Wavelength on the Retrieval'. With increased aerosol abundance in the free troposphere the visibility is reduced even at 500 nm leading to more photons coming from areas closer to the aircraft along the light path. These photons enable the measurements to resolve the altitude range near 9 km. The downside of the reduced visibility is that there are much less photons coming from the altitudes near the tangent height, which deliver profile information on the altitude range above tangent height (approx. 5 km for the 88° LOS) below 9 km altitude. That is why the FWHM value of the 9 km averaging kernel in scenario 10 is decreased

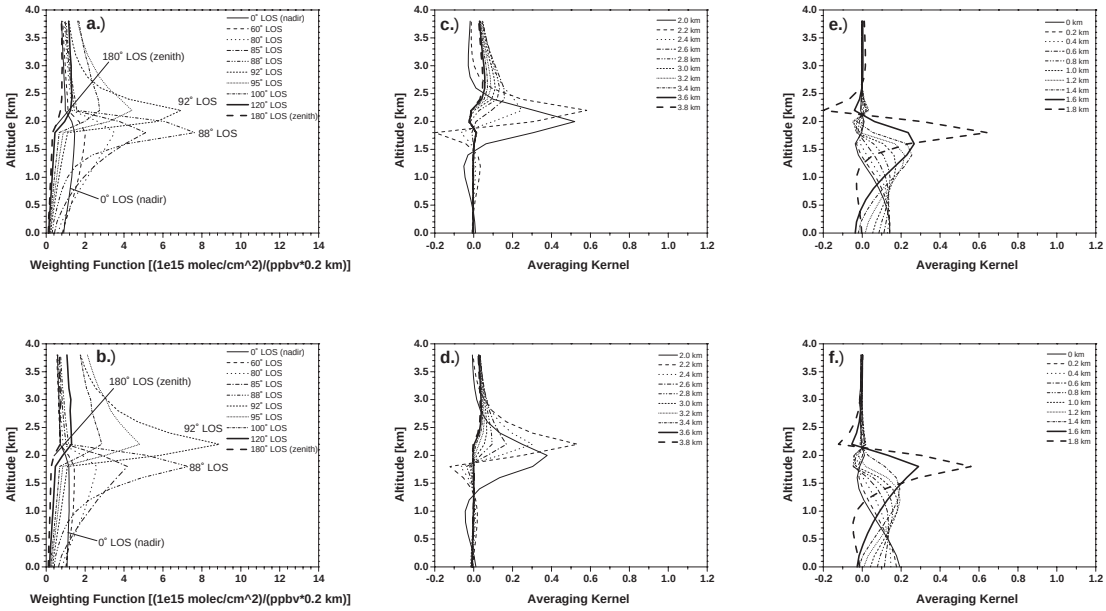

Figure 7.7: The weighting functions for the investigation dealing with the influence of the flight altitude on the retrieval are shown for 350 nm in plot a and for 500 nm in plot b, the corresponding averaging kernels above the aircraft are shown in plots and d, and the corresponding averaging kernels below the aircraft are shown in plots e and f.

(2.6 km compared to 5.0 km in scenario 6) increasing the resolution. The FWHM value of the 7-km averaging kernel is increased (5.5 km compared to 3.2 km in scenario 6) decreasing the resolution.

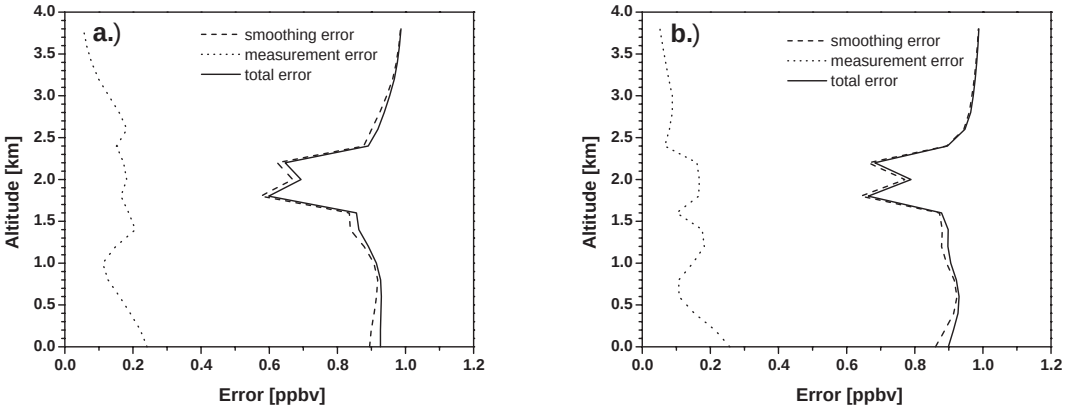

Figure 7.8: The retrieval errors for the investigation dealing with the influence of the flight altitude on the retrieval are shown for 350 nm in plot a and for 500 nm in plot b.

7.4 Influence of the Flight Altitude on the Retrieval

The flight altitude is crucial for the profile retrieval due to the changing geometry of each LOS as can be seen in section 4.4 dealing with the measurement geometry. In this part of the study calculations for a flight altitude of 2 km are compared to those for 10 km flight altitude. This investigation is interesting because the AMAXDOAS instrument was also flown on a smaller turboprop aircraft in lower altitudes of up to 2 km during the Formaldehyde as a tracer of oxidation in the troposhere (FORMAT) campaign. The goal of this investigation is to demonstrate whether it is possible to retrieve profile information from aircraft measurements [Pundt *et al.*, 2004a,b] performed at low altitudes.

Again, two cases have to be considered. The first case is the scenario 11 calculated for a wavelength of 350 nm, the second one is calculated for a wavelength of 500 nm. As can be seen in Fig. 7.7c and d for scenario 11, the averaging kernels calculated for this flight altitude do not peak as distinctively as they did for the 10 km flight altitude. This is to be expected given the vertical resolution of 2 km that could be achieved at 10 km. Above and below the flight altitude, the peak values of the averaging kernels are decreasing rapidly. This fact and a study of the retrieval error (see Fig. 7.8a and b) suggest that the measurement at 2 km flight altitude is not containing much profile information. In summary measurements at 2 km yield an in-situ measurement at flight altitude and the columns below and above the aircraft. The averaging kernels above the aircraft contain less profile information compared to measurements taken at 10 km

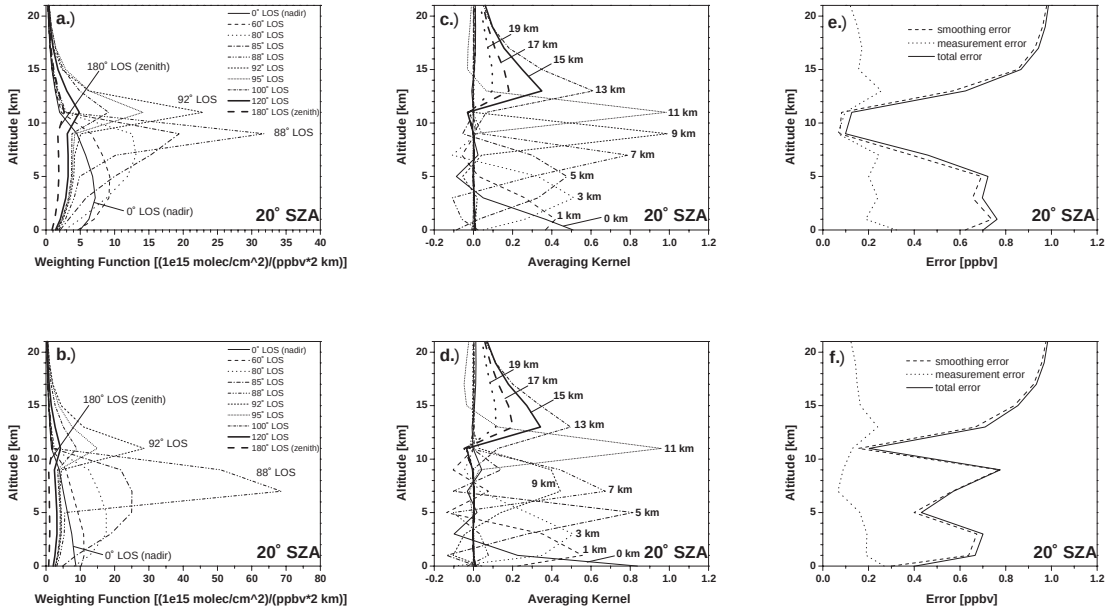

Figure 7.9: The weighting functions for the investigation dealing with the influence of the SZA (20°) on the retrieval are shown for 350 nm in plot a and for 500 nm in plot b, the corresponding averaging kernels are shown in plots c and d, and the retrieval errors are shown in plots e and f.

flight altitude in the UV.
The second case is the scenario 12 calculated for a wavelength of 500 nm. As can be seen in Fig. 7.7d and f, the averaging kernels are nearly identical to the UV case with the exception that the 0.2 km averaging kernel has larger values. Even the difference of averaging kernels between the two wavelengths is small. This is because the distances from the aircraft to the surface for almost all LOS at both wavelengths are within the visibility range of the model atmosphere. The main result of this study is that only a column above and beneath the aircraft can be retrieved.

7.5 Influence of the SZA on the Retrieval

This investigation to analyze the impact of different SZA on the profile retrieval is necessary because the altitude where most photons are scattered is strongly depending on the SZA. At low SZA the most photons are scattered in the lower troposphere. At high SZA ($\geq 90°$) most photons are scattered well within the stratosphere. This feature was used by Preston [1995]; Preston *et al.* [1997] to retrieve NO_2 profile information from zenith sky DOAS measurements. This study is interesting for the profile retrieval using real AMAXDOAS data in case twilight measurements have to be analyzed.
As stated above the SZA has a big impact on the light path. So, different SZA (20°, 51.6°, 80°, and 90°) have been investigated. At 350 nm, there is no significant change in the averaging kernels below the aircraft when the SZA increases from 20° to 90° (see Fig. 7.9c and Fig. 7.10i). Above the aircraft the averaging kernels peak values of 11 km, 13 km, and 15 km are getting smaller. On the other hand the averaging kernels of 17 km and 19 km are getting larger especially in the lower stratosphere above 15 km altitude. At 500 nm, the result is a totally different one: The peak values of the averaging kernels below the aircraft are not changing significantly comparing scenarios 14 (20° SZA) and 16 (80° SZA). There is the exception that the peak value of the 1 km averaging kernel is getting smaller, whereas the peak value of the 3 km averaging kernel is getting larger. Above the aircraft the behavior at 500 nm is comparable to the behavior of the averaging kernels at 350 nm. With increasing SZA above 80° the averaging kernels show a completely different behavior. Overall, the sensitivity near flight altitude gets worse, since the peak value of the 11 km averaging kernel decreases significantly. Another difference is the ability at 90° to get profile information from the altitudes between 7 and 9 km, since the averaging kernels peak in different altitudes compared to scenario 2 (see Fig. 7.1d and Fig. 7.10j).

7.6 What is the optimum LOS setup?

This question has two parts. The first is addressing the optimum number of LOS required when retrieving a profile with a certain resolution. Rodgers deals with this part of the question by the use of prior constraints. To make the inversion problem well-posed 'a discrete representation with fewer parameters than the number of degrees of freedom of the measurements', as required by the maximum a posteriori method is needed ([Rodgers, 2000], chapter 10). This translates to: If the retrieved profile below

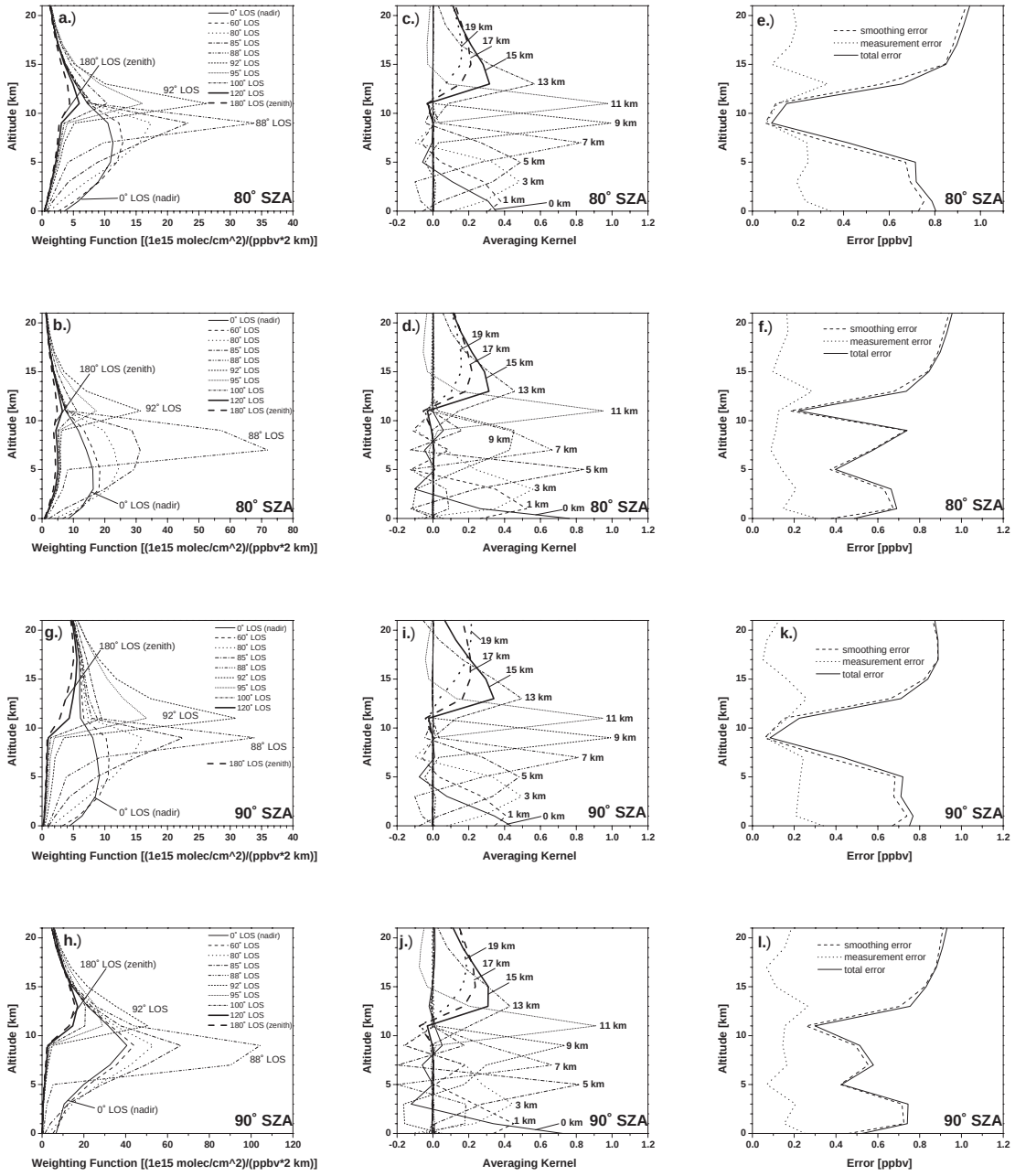

Figure 7.10: The weighting functions for the investigation dealing with the influence of the SZA (80°/90°) on the retrieval are shown for 350 nm in plot a&g and for 500 nm in plot b&h, the corresponding averaging kernels are shown in plots c&i and d&j, and the retrieval errors are shown in plots e&k and f&l.

the aircraft has five points, at least five measurements (downward looking LOS) are needed to make the problem well-posed.

The second part of the question is concerned with the selection of the LOS for a certain setup. This can be answered by selecting the LOS in such a way that for each layer

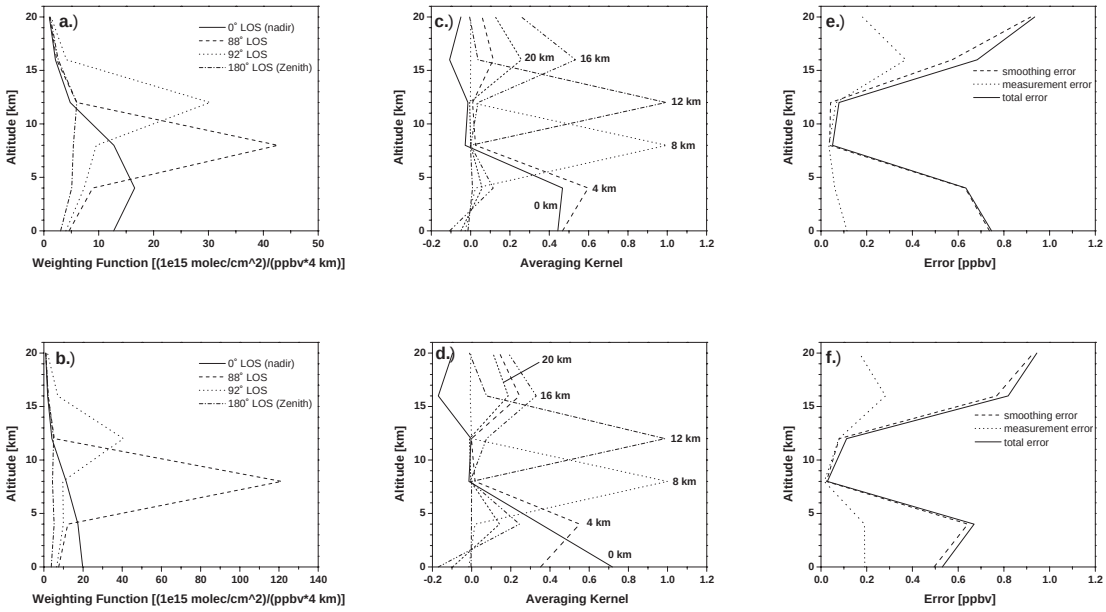

Figure 7.11: The weighting functions for the investigation dealing with four LOS are shown for 350 nm in plot a and for 500 nm in plot b, the corresponding averaging kernels are shown in plots c and d, and the retrieval errors are shown in plots e and f.

in the retrieval grid one limb measurement is taken that has the appropriate tangent height. For the retrieval grid of 0 km, 1 km, 3 km, ..., 9 km the according LOS would be: 86.8°, 87.0°, 87.3°, 87.7°, 88.2°, and 89.0°. Before investigating this LOS setup a few other LOS setups have to be discussed.

7.6.1 SCIA VALUE Setup: Four LOS

This LOS setup is important because it was used during both SCIA VALUE campaigns (see chapter 4 'The Experimental Setup'). In this setup the following LOS were used: 0° (nadir), 88°, 92°, and 180° (zenith). These LOS were selected from the setup used prior in the 2nd test flight campaign to improve the signal-to-noise ratio. The increase of the signal-to-noise ratio results from the larger area available for each LOS on the CCD chip due to averaging of more lines of the CCD chip per LOS. As a result of the reduced number of LOS used in this investigation, a different retrieval grid with an increased step size of 4 km had to be used.
At 350 nm, Fig. 7.11c is showing the averaging kernels for scenario 21. Compared to scenario 1 the vertical resolution is decreased (larger than 4 km, as a result of the FWHM values of the averaging kernels) due to the increased step size in the retrieval grid. The 0 km and 4 km averaging kernels are small indicating a limited sensitivity of the profile retrieval.
At 500 nm, the results are not significantly different (see Fig. 7.11d) except that the peak value of the 0 km averaging kernel is larger than that at 350 nm. This is confirmed by the weighting functions (see Fig. 7.11e and Fig. 7.11f).

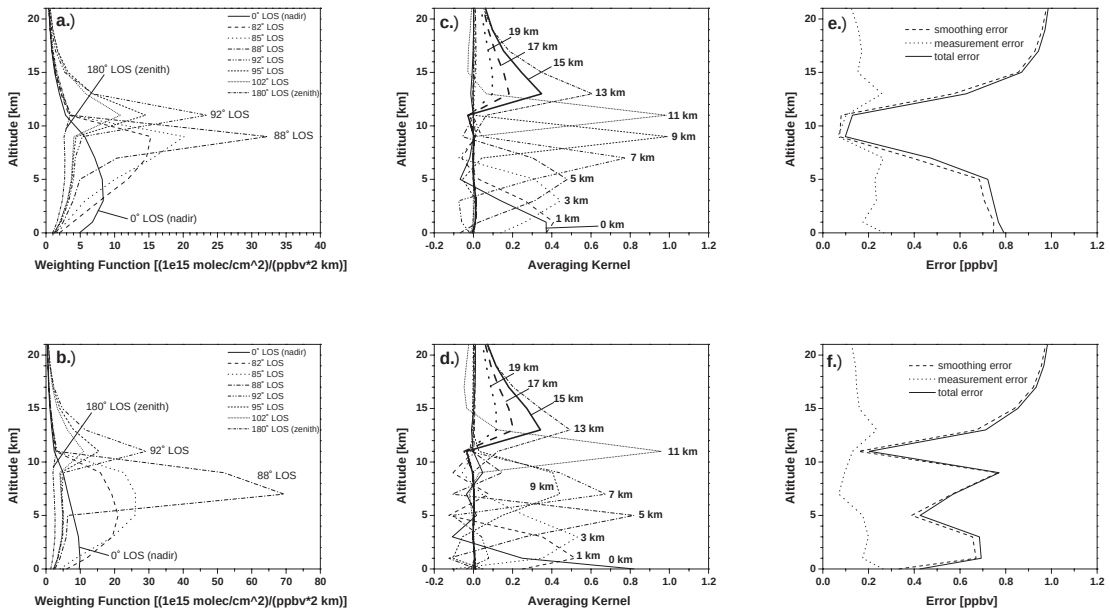

Figure 7.12: The weighting functions for the investigation dealing with eight LOS are shown for 350 nm in plot a and for 500 nm in plot b, the corresponding averaging kernels are shown in plots c and d, and the retrieval errors are shown in plots e and f.

The main result of this sensitivity study is the limited sensitivity of the four LOS setup in the lower troposphere.

Considering the profile retrieval using real data this is not very promising, since the highest tropospheric NO_2 abundance will be in the lower troposphere close to the surface.

7.6.2 Test Flight Setup: Eight LOS

During the second Test Flight campaign of the AMAXDOAS instrument this setup of LOS was used in order to test the ability to retrieve vertical profile information with as high a resolution as possible. This LOS setup was a trade-off between the number of LOS used and the area on the CCD-chip available for each LOS. Actually ten LOS (five downward and five upward looking LOS) were used in this setup: 0°, 82°, 85°, 88°, 92°, 95°, 98°, and 180°. These first eight LOS do all look in flight direction, whereas the last two LOS: 82° and 98° do look in the opposite direction. So two LOS do exist twice, but these do not contribute to the retrieval of vertical profile information.

Fig. 7.12c and d are showing the averaging kernels at 350 and 500 nm. Compared to scenarios 1 and 2 the averaging kernels do not change significantly even though the 60° and 120° LOS are missing. In other words these two LOS do not contribute any profile information to the retrieval.

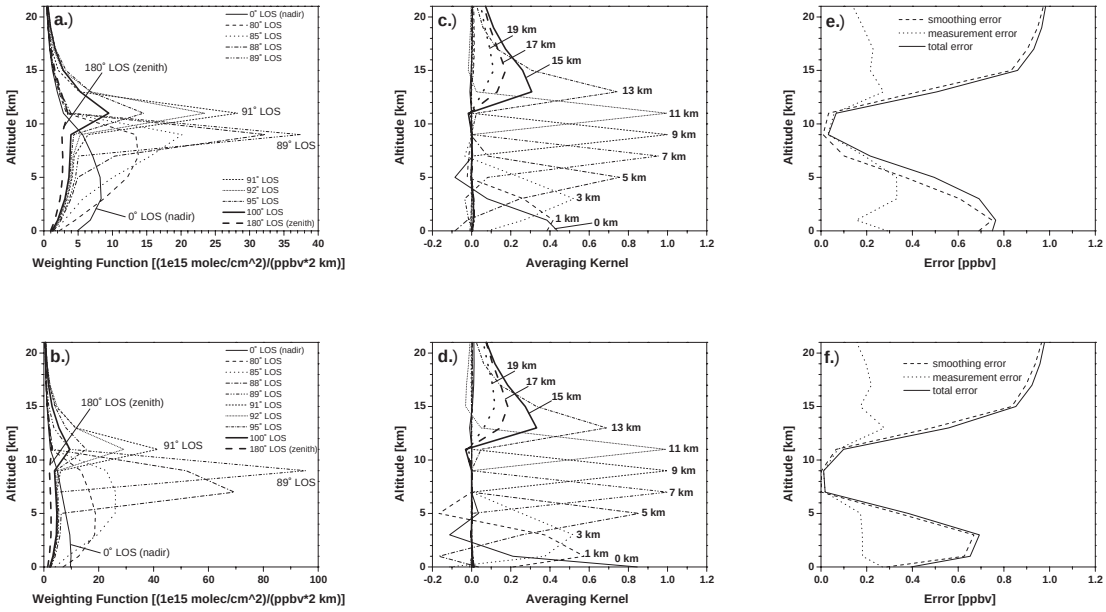

Figure 7.13: The weighting functions for the investigation dealing with the influence of additional LOS (89° and 91°) on the retrieval are shown for 350 nm in plot a and for 500 nm in plot b, the corresponding averaging kernels are shown in plots c and d, and the retrieval errors are shown in plots e and f.

7.6.3 Additional LOS Setup: Ten LOS

To investigate the usefulness of having LOS pointing more to horizon (see Fig. 7.13c and d; scenario 25 and 2) two additional LOS (89° and 91°) were included instead of the 60° and 120° LOS compared to scenarios 1 and 2 (see Fig. 7.1a and b). For scenario 26 the averaging kernels 7 and 9 km below the aircraft peak in different altitudes compared to those in scenario 2. The weighting functions for this scenario (Fig. 7.13b) explains this behavior. For the 89° LOS, the retrieval obtains information exclusively from the altitudes near 9 km, because the majority of the absorption signal originates from these altitudes. The 88° LOS weighting function is the same as in scenario 2. Therefore, as a result of the additional LOS, additional profile information about higher altitudes is gathered. For 350 nm (see. Fig. 7.13a; scenario 25) there is no difference in the weighting functions of the 88°, and the 89° LOS. Thus no increase in the vertical resolution is observed. The fact that the additional LOS do not increase the profile resolution at 350 nm results from the limited visibility at 350 nm. Above the aircraft the averaging kernels do not change compared to scenario 1.

Fig. 7.13b shows that the vertical resolution at 500 nm improves when using additional LOS at 89° and 91°. Analysis of the retrieval errors in Fig. 7.13f confirms the improvement of the resolution at 500 nm due to the smaller retrieval error compared to scenario 2. However, in real applications, the pointing accuracy needed for these LOS is difficult to achieve because of the intrinsic pitch and roll of an aircraft in flight.

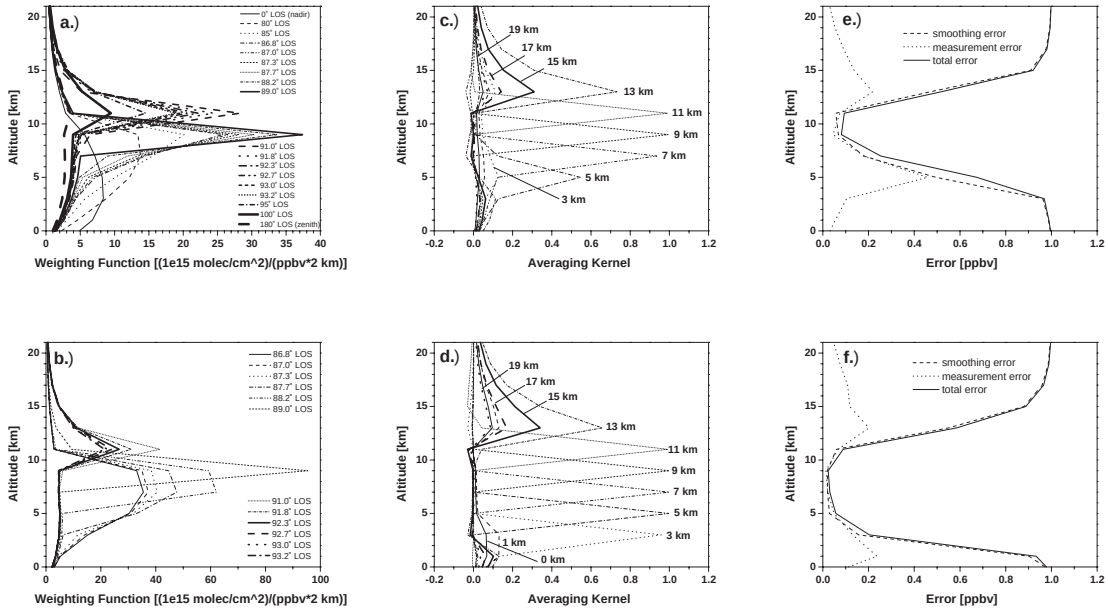

Figure 7.14: The weighting functions for the investigation dealing with the limb twelve LOS setup are shown for 350 nm in plot a and for 500 nm in plot b, the corresponding averaging kernels are shown in plots c and d, and the retrieval errors are shown in plots e and f.

7.6.4 Limb Setup: Twelve LOS

This investigation was done to test the influence of the AMAXDOAS measurements done in limb mode on the retrieval. As discussed above the LOS used were selected by transforming the retrieval grid into tangent heights. The tangent heights were translated into LOS as discussed in section 4.4 'Measurement Geometry'.

At 350 nm, the peak values of the 3 km and 5 km averaging kernels are decreased significantly as can bee seen in Fig 7.14c compared to Fig. 7.1c. This is a result of the limited visibility in the UV, since the distances between tangent points and aircraft for the lower tangent heights are large (over 330 km for a tangent height of 1 km). This LOS setup is not sensitive to the lower troposphere in the UV. This is confirmed by taking a look at the weighting functions (see Fig. 7.14a) and the retrieval errors (see Fig. 7.14e), because these plots show small values in weighting functions and large retrieval errors below 5 km altitude compared to small retrieval errors between 7 and 11 km altitude.

At 500 nm, the averaging kernels for 3 km and 5 km are much larger compared to those at 350 nm (see Fig. 7.14c and d). Therefore the sensitivity to the lower troposphere is much larger, too. This is confirmed by the retrieval errors in Fig. 7.14f. But the 0 km and 1 km averaging kernels are still very small indicating a low sensitivity below 1 km altitude. This sensitivity study shows that profile retrieval from airborne DOAS measurements needs more LOS in addition to the limb viewing LOS.

It is worth mentioning that this LOS setup will cause problems in practice if the aircraft is not flying with a steady pitch and roll or the recording of the pitch and roll in the

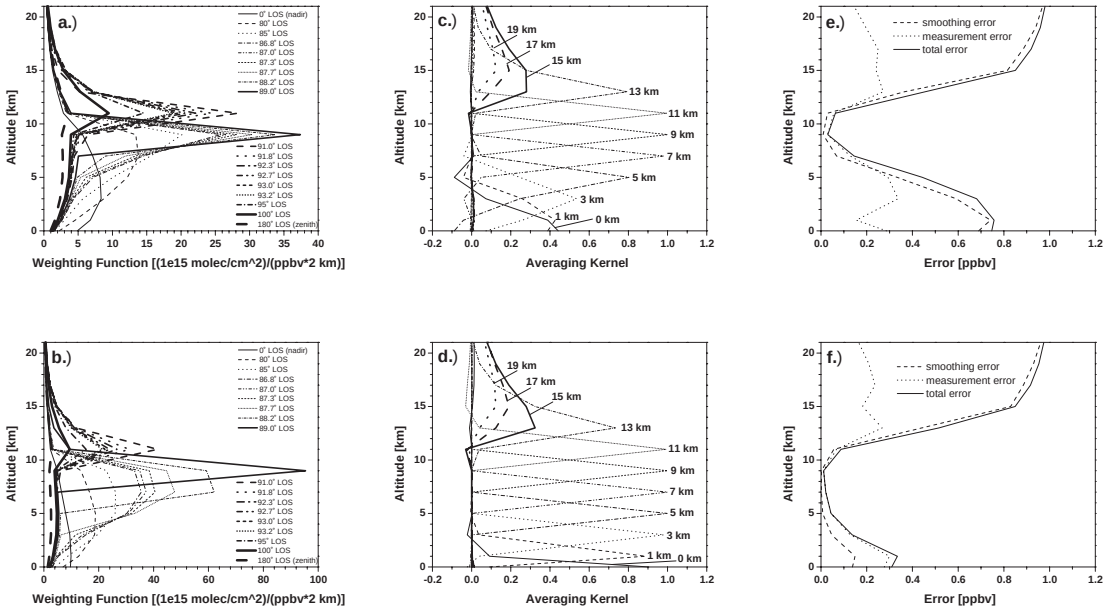

Figure 7.15: The weighting functions for the investigation dealing with the enhanced limb 18 LOS setup are shown for 350 nm in plot a and for 500 nm in plot b, the corresponding averaging kernels are shown in plots c and d, and the retrieval errors are shown in plots e and f.

flight data has an error larger than 0.1° (see chapter 6 'Error Analysis').

7.6.5 Enhanced Limb Setup: 18 LOS

The last section dealing with the twelve LOS limb setup has shown that taking into account only limb measurements does not yield any profile information for the lower troposphere near the surface in the UV and visible wavelength regions. To improve the ability to retrieve profile information near the surface, LOS from the nadir mode and LOS pointing more to the stratosphere will be included in this setup in addition to the twelve limb LOS: 0°, 80°, 85°, 95°, 100°, and 180°.
At 350 m, this setup is improving the ability to retrieve profile information in the lower troposphere below 5 km altitude as can be seen in Fig: 7.15c. The peak values of the 3 km and the 5 km averaging kernels are much larger compared to scenario 27 (see Fig. 7.14c).
At 500 nm there is also an improvement in the 0 km and 1 km averaging kernels, because in this scenario those averaging kernels have much larger values (see Fig. 7.14d) compared to scenario 28.

7.6.6 Downsized Enhanced Limb setup: Twelve LOS

As discussed above the approach using twelve limb LOS in not very useful in practice because the required pointing accuracy of 0.2° is difficult to realize. Therefore a downsized version of this approach was also tested. Instead of 18 LOS required for all

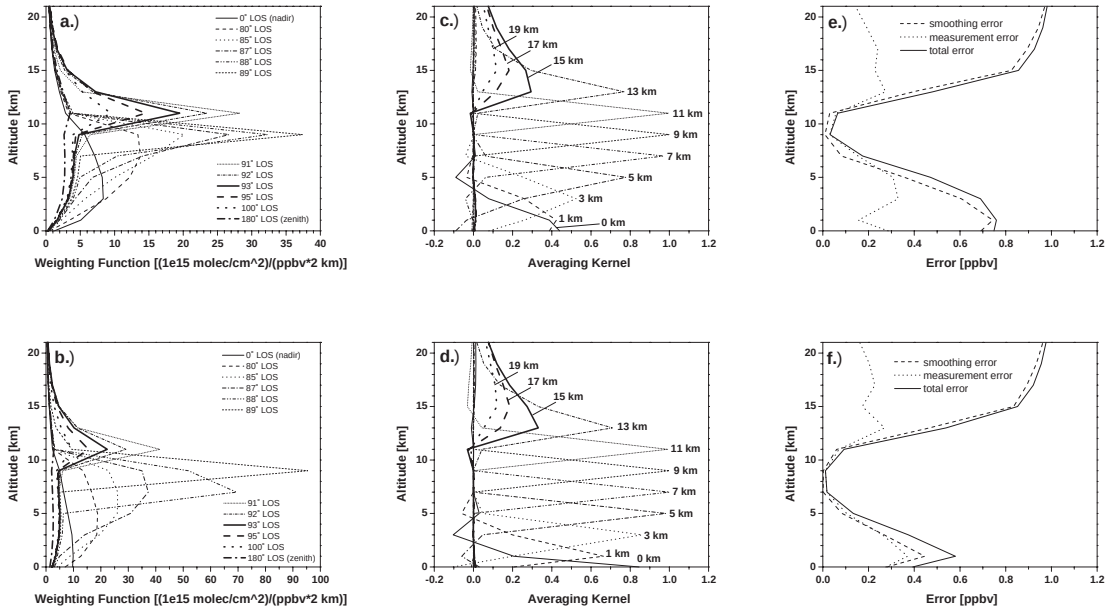

Figure 7.16: The weighting functions for the investigation dealing with the downsized enhanced limb twelve LOS setup are shown for 350 nm in plot a and for 500 nm in plot b, the corresponding averaging kernels are shown in plots c and d, and the retrieval errors are shown in plots e and f.

tangent heights from 0 to 9 km only twelve LOS were used. This scenario is realized by using the LOS 0°, 80°, 85°, 88°, 89°, 91°, 92°, 95°, 100°, and 180° plus the LOS 87° and 93°. The comparison of the 18 LOS study to this downsized enhanced twelve limb LOS study (see Fig: 7.15) reveals a difference in averaging kernel peak values of less than 10%. This is a small change compared to the 60% increase in the 3 km averaging kernel peak value between the additional LOS (scenario 26) and the downsized enhanced twelve limb LOS study (scenario 32) at 500 nm (see Fig. 7.13d and Fig. 7.16d). From this we conclude, that no further information is gathered in going from twelve to 18 LOS. At 350 nm there is practically no difference between the ten LOS setup and this twelve LOS setup (see Fig. 7.13c and Fig. 7.16c). At 350 nm, the ten LOS setup is already the LOS setup with the best performance. For 500 nm the LOS setup with the best performance is the setup with 18 LOS, but for practical reasons the twelve LOS setup is as good as the 18 LOS setup. The retrieval error for the twelve LOS study at 500 nm (see. Fig. 7.16f) supports the good performance of the twelve LOS.

7.6.7 The Best LOS Setup!

The best LOS setup depends on the task laying ahead. When designing a new instrument one is free to choose the LOS to get the best LOS setup possible. In case a new instrument can be designed the sensitivity studies have shown that the best LOS setup is definitely the enhanced limb 18 LOS setup assuming the field of view of the instrument is small enough. The field of view of the telescope(s) has to be small in order to guarantee all LOS to be separated considering the small differences of the limb viewing

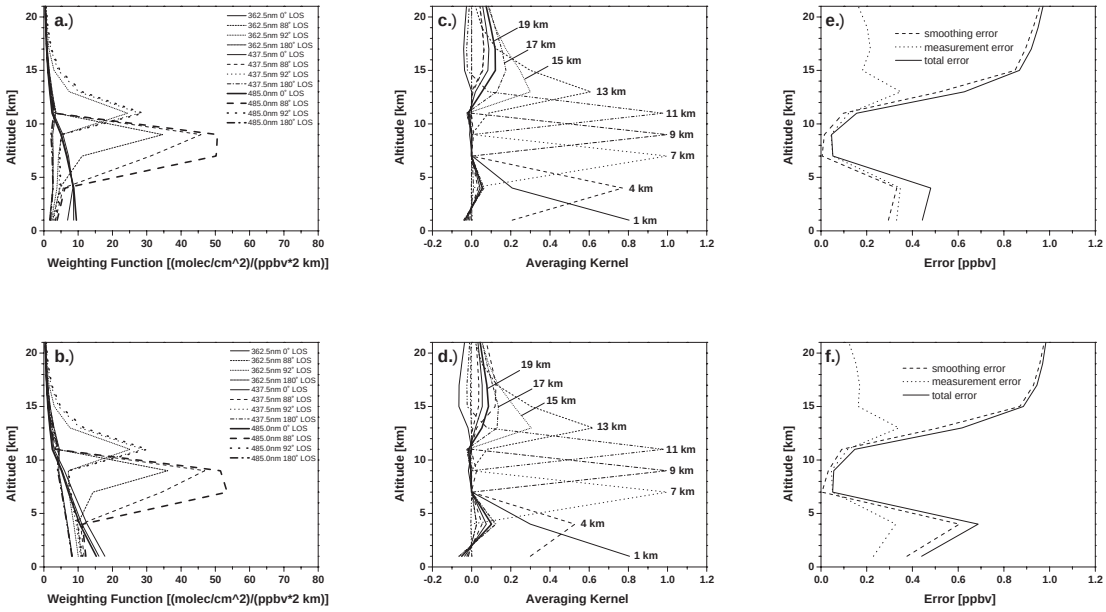

Figure 7.17: The weighting functions for the investigation dealing with the combination of four LOS and three wavelengths are shown for an albedo of 0.1 in plot a and for an albedo of 0.9 in plot b, the corresponding averaging kernels are shown in plots c and d, and the retrieval errors are shown in plots e and f.

LOS in the enhanced limb 18 LOS setup. Another limit is the detector area, it has to be large enough to fit 18 different spectra on one chip in case one telescope is used per LOS. If only one telescope is used detectors have to be sensitive enough to guarantee very short integration times. Short integration times are necessary when acquiring one spectra for each LOS. To fulfill the requirement of quasi-simultaneous measurements the time period between the measurement of the first LOS and the measurement of the last LOS must not be too large. Otherwise the assumption of the homogeneity of the atmosphere may not be correct due to the high velocity of the aircraft. If one or more of those requirements mentioned above cannot be achieved the second best LOS setup is the downsized enhanced limb twelve LOS setup. This setup is more practical due to the reduced number of LOS and the larger differences in angles of the LOS.
The best LOS setup for the AMAXDOAS instrument is a different one than discussed above. Due to several reasons the AMAXDOAS LOS setup was reduced to four LOS after the second test flight of the AMAXDOAS instrument as discussed in the chapter 4 'The Experimental Setup'. The main reason for the reduction to four LOS is the increase in signal-to-noise ratio because more lines of the CCD chip are assigned to each LOS. The increased signal-to-noise ratio results in smaller retrieval errors. For four LOS the best LOS setup is a combination of four LOS and three wavelengths (4-3 setup). Fig. 7.17 shows the results of a profile retrieval using the 4-3 setup. Compared to scenarios 21 and 22 (Fig. 7.11) taking into account four LOS at three wavelengths separately, the 4-3 setup presents a profile retrieval with a significantly increased vertical resolution. The retrieved profiles from the four LOS setup have

FWHM values of 4.0 to 7.8 km whereas the 4-3 setup produces profiles with a vertical resolution of 2.0 to 4.0 km below 10 km altitude. The best resolution of 2.0 km is achieved near flight altitude, and the poorer resolution is achieved near the surface. During fine tuning the profile retrieval using the 4-3 setup a different retrieval grid had to be used as in the previous sensitivity studies. In the 4-3 setup the retrieval grid was changed to a grid with points at 1 km, 4 km, 7 km, 9 km, 11 km, ..., 39 km.

7.7 Influence of the Retrieval Grid on the Retrieval

Up to now only one retrieval grid (0 km, 1 km, 3 km, ..., 39 km) has been used with the exception of the flight altitude study and the 4-3 setup of the previous section. By using only one retrieval grid it is possible to investigate the influences of other parameters on the retrieval. This section deals with the influence of the choice of the grid on the retrieval. The scenarios presented here will be compared to different scenarios acting as reference scenario. This approach is used to take into account the potential maximum vertical resolution of different LOS setups meaning a LOS setup including more limb viewing LOS is able to retrieve profiles with a higher vertical resolution than a LOS setup with less limb viewing LOS.
The choice of the retrieval grid is a trade off between vertical resolution and retrieval errors meaning a good vertical resolution comes along with large retrieval errors and vice versa. The task is to find a fair compromise: a vertical resolution with retrieval errors one can accept.

7.7.1 Retrieval Grid with 1 km step size

This section is dealing with the retrieval grid using 1 km step size and will be compared to scenarios 29 and 30 acting as reference scenarios. These scenarios using 18 LOS were chosen as reference because they promise the best retrieved profiles considering a vertical resolution of up to 2 km. This investigation is supposed to detect the ability of the 18 LOS setup to retrieve profiles with an achieved vertical resolution of 1 km. The 18 LOS setup seems to be the most promising setup among all setups discussed above, because scenario 30 is the only one able to provide a vertical resolution of up to 2 km from the surface up to an altitude of about 12 or 13 km. A good retrieval with 2 km vertical resolution is a necessary precondition when trying to retrieve profiles using a grid with 1 km step size. Fig. 7.18c shows the averaging kernels of the enhanced limb 18 LOS setup (scenario 33) calculated on a retrieval grid with 1 km step size at 350 nm. Apparently at 350 nm this retrieval is able to retrieve profile information with 1 km vertical resolution considering the 8-km, 9-km, and 10-km averaging kernels. These averaging kernels have FWHM values of 1.1 to 1.2 km. Below 8 km the FWHM values increase rapidly to values of 2.9 to 5.3 km. Also the peak values of the averaging kernels below 8 km decrease rapidly leading to large retrieval error values as can be seen in Fig. 7.18e. At 500 nm (scenario 34) the results look quite different but are only a little bit more promising. The maximum value of the FWHM below 10 km altitude is 2.8 km at 1 km altitude, and the minimum values of the FWHM are 1.1 km and 1.0 km at 4 km and 9 km altitude respectively (see Fig. 7.20a). At 500 nm the vertical resolution

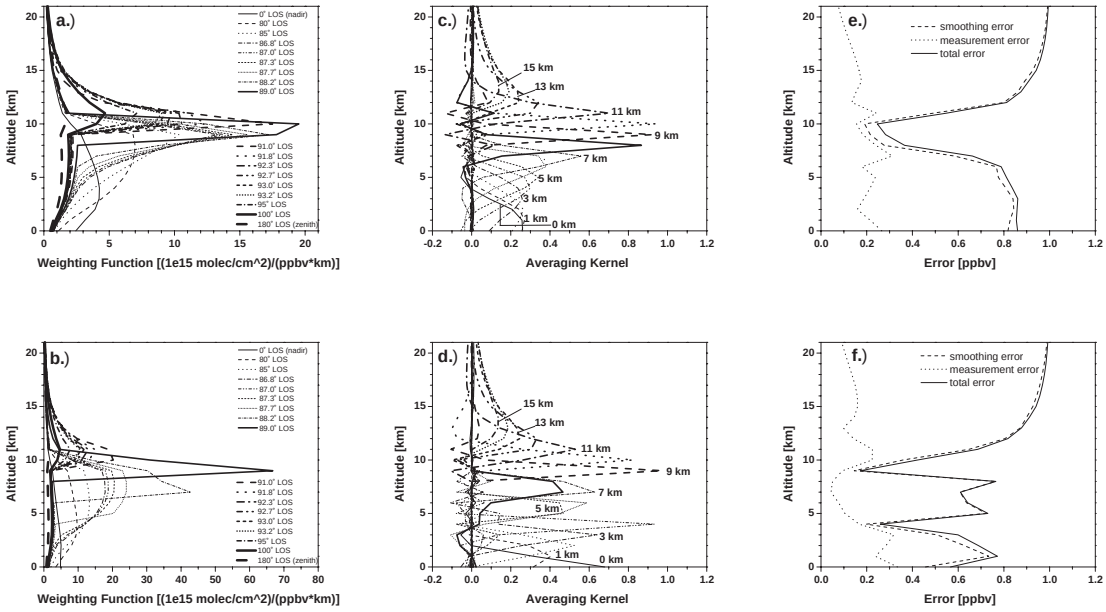

Figure 7.18: The weighting functions for the investigation dealing with the retrieval grid using 1 km step size are shown for 350 nm wavelength in plot a and for 500 nm wavelength in plot b, the corresponding averaging kernels are shown in plots c and d, and the retrieval errors are shown in plots e and f.

is much better in the lower troposphere below 5 km altitude therefore the vertical resolution at 8 km altitude is much worse. Considering the results of the previous sections where three wavelengths were combined in one retrieval, this concept might be very promising here as well in order to increase the vertical resolution to values below 2.0 km. Compared to scenarios 29 and 30 the quality of the profile retrieval has not increased when using a retrieval grid with 1 km step size in the enhanced limb 18 LOS setup.

7.7.2 Retrieval Grid with 3 km step size

The scenarios presented in this section dealing with the retrieval grid using 3 km step size (0 km, 3 km, ..., 39 km) will be compared to scenarios 25 and 26. This approach was chosen because these scenarios resulted in quite promising retrieved profiles. As the sensitivity studies dealing with different LOS setups have shown the retrieval process can be optimized by using different LOS setup leaving the retrieval grid untouched. In this study the LOS setup will not be altered showing how the retrieval grid has to be altered to get the best retrieval using the same LOS setup. Fig. 7.19c shows the averaging kernels of the profile retrieval using a retrieval grid with 3 km step size at 350 nm. The minimum FWHM value (best vertical resolution) below 15 km altitude is 3.0 km and therefore larger than compared to the best vertical resolution of 2.0 km in scenario 25 (see Fig. 7.20b). The advantage of the results of this investigation is the increase of the worst vertical resolution near the surface from 5.0 km at 1 km

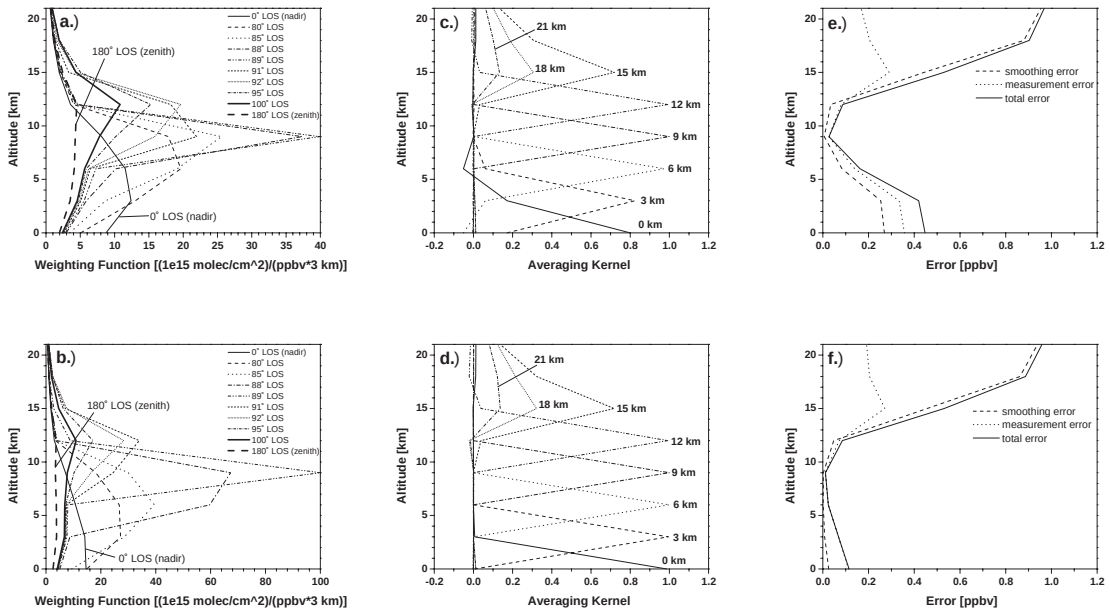

Figure 7.19: The weighting functions for the investigation dealing with the retrieval grid using 3 km step size are shown for 350 nm wavelength in plot a and for 500 nm wavelength in plot b, the corresponding averaging kernels are shown in plots c and d, and the retrieval errors are shown in plots e and f.

altitude (scenario 25) to 3.8 km at 0 km altitude (scenario 35). At 500 nm the result is virtually the same. The worst vertical resolution is increased from 4.2 km at 3 km altitude (scenario 26) to 3.0 km between 0 km and 9 km altitude (scenario 36). On the other hand the best vertical resolution is decreased from 2.0 km (scenario 26) to 3.0 km (scenario 36). The increase in quality of the retrieval can be seen in Fig. 7.19e and f as well. The retrieval errors are much smaller compared to those of scenarios 25 and 26.

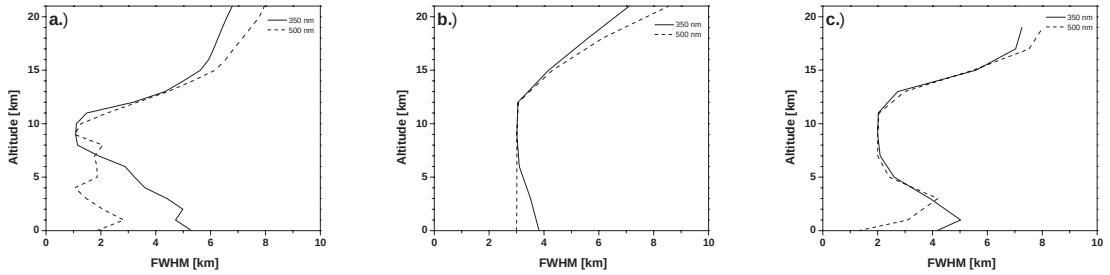

Figure 7.20: Vertical Resolution (FWHM) of a scenarios 33/34, b scenarios 35/36, and c scenarios 25/26 .

7.8 Summary

This chapter presenting the sensitivity studies for APROVAL has shown that:

- The variation of wavelength in the profile retrieval demonstrates the wavelength dependent vertical resolution of the profile retrieval with different vertical resolutions in different altitudes. At 350 nm, the best vertical resolution is achieved near flight altitude whereas at 500 nm a better vertical resolution is achieved in the lower troposphere.
- The variation of albedo in the profile retrieval indicates an increased sensitivity of the profile retrieval at 350 nm in case of an increased albedo.
- At 350 nm, there is no change in the sensitivity of the profile retrieval when varying the aerosol concentration. On the other hand the profile retrieval is sensitive to different aerosol concentrations at 500 nm. No aerosol in the atmosphere reduces the quality of the profile retrieval in the lower troposphere. With increasing aerosol concentration the sensitivity at 3 and 9 km altitude is increasing.
- Flying at 2 km altitude instead of 10 km altitude is reducing the quality of the profile retrieval dramatically. APROVAL is not suitable for analyzing measurements at these low flight altitudes.
- The influence of the SZA on the profile retrieval is insignificant for SZA $< 90°$ at 350 nm. On the other hand at 500 nm and for SZA larger than 80° the sensitivity at 9 km altitude is increasing on the cost of the sensitivity at the altitudes below 9 km.
- The best LOS setup is the enhanced limb 18 LOS setup with one limb LOS per retrieval grid point meaning the altitude of each retrieval grid point is translated into the corresponding limb viewing LOS. For practical reasons the downsized enhanced limb twelve LOS setup is nearly as good as the enhanced limb 18 LOS setup. For the AMAXDOAS instrument the 4-3 LOS (four LOS at three wavelengths) proved to be the best LOS setup.
- The choice of the retrieval grid is a trade off between vertical resolution of the retrieved profiles and the total retrieval errors. For most of the sensitivity studies a retrieval grid with 2 km step size and 1 km step size at surface (0 km, 1 km, 3 km, 5 km, 7 km, $\cdots$, 39 km) was found to be the ideal retrieval grid. For the AMAXDOAS instrument and 4-3 LOS setup a slightly different retrieval grid (1 km, 4 km, 7 km, 9 km, $\cdots$, 39 km) with a larger step size in the lower troposphere proved to be the best.

Chapter 8

Profile Retrieval using Simulated Data

In this chapter profiles will be retrieved from simulated slant columns for both the AMAXDOAS and SCIAMACHY instruments. The main purpose of this investigation is to confirm the results of the previous chapter for the AMAXDOAS instrument. Another purpose is to demonstrate the extension of APROVAL for space-based instruments.

8.1 AMAXDOAS

To sustain the conclusions of the sensitivity studies, a consistency study is performed as well as an investigation on the sensitivity of the profile retrieval on different tropospheric NO_2 profiles. Last but not least the sensitivity of the stratospheric vertical NO_2 column on the profile retrieval is investigated.
Unless stated otherwise the assumptions made in this investigation are the same to those made in the previous chapter. The chosen LOS setup is discussed in section 8.1 'Consistency Study'. The albedo was set to 0.1, the flight altitude is 10 km altitude, and the SZA is again 51.6°.

8.1.1 Consistency Study

The aim of the consistency study is to demonstrate the potential of APROVAL. This potential is investigated by retrieving a profile from simulated data. The advantage of using simulated slant columns in this study is the knowledge of the 'true' atmospheric NO_2 profile, because the NO_2 profile in the simulated slant columns is known. This investigation uses the 4-3 setup introduced in the previous chapter because the profile retrieval using real AMAXDOAS data (see next chapter) is based on the 4-3 setup too. The simulated slant columns used in this chapter are calculated using eq. 5.2. The forward model calculates the weighting functions $\mathbf{K}$, and $\mathbf{x}$ is the 'true' profile of NO_2 as mentioned above. Fig. 8.1 shows the retrieved profile is numerically equal to the a priori profile as one would expect, since the profile information contained in the slant column is identical with the a priori profile information. This study verifies in theory the feasibility of the retrieval of profiles from slant column measurements.

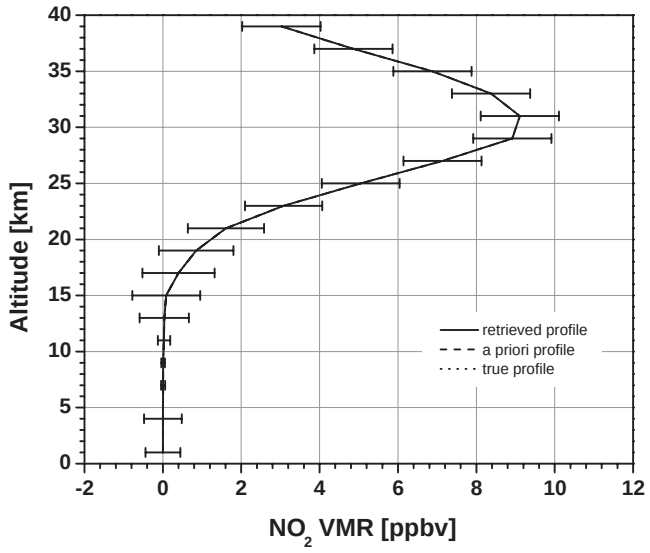

Figure 8.1: The consistency study for the 4-3 setup. This plot represents the retrieved profile using eq. 5.2 to calculate the simulated slant columns.

8.1.2 Sensitivity to different profile layers

This section presents an analysis of retrieved profiles studying the sensitivity to profile perturbations in different tropospheric layers. The aim of this study is to show the response of the retrieval algorithm to simulated data including tropospheric NO_2 abundance in different layers. Thus the ability of the retrieval algorithm to retrieve profile information in the troposphere is demonstrated. It should be noted that this study is of theoretical character because the peak NO_2 values are coinciding with the grid points of the retrieval grid. This investigation is performed for two LOS setups: the 4-3 setup and the enhanced limb 18 LOS setup at 500 nm.

4-3 Setup

The 4-3 setup was chosen in this study because this specific setup will be used to retrieve profile information using real AMAXDOAS measurements in the next chapter. Fig. 8.2 shows the retrieved profiles for simulated data including perturbations of 1 ppbv in the profile at every grid point from 1 to 17 km altitude. It can be seen in Fig. 8.2a and b the perturbation at 1 and 4 km altitude are not precisely reproduced. This is due to the reduced quality of the averaging kernels in this altitude region and the increased retrieval error as discussed in chapters 5 'The Retrieval Method', 6 'The Error Analysis', and 7 'Sensitivity Study'. It was argued that increased values in resolution and retrieval errors are a measure of poor quality of the retrieved profiles.
In contrast the perturbations from 7 to 11 km are reproduced very good by the retrieved profiles. This result is sustained by the argument used above as can be seen

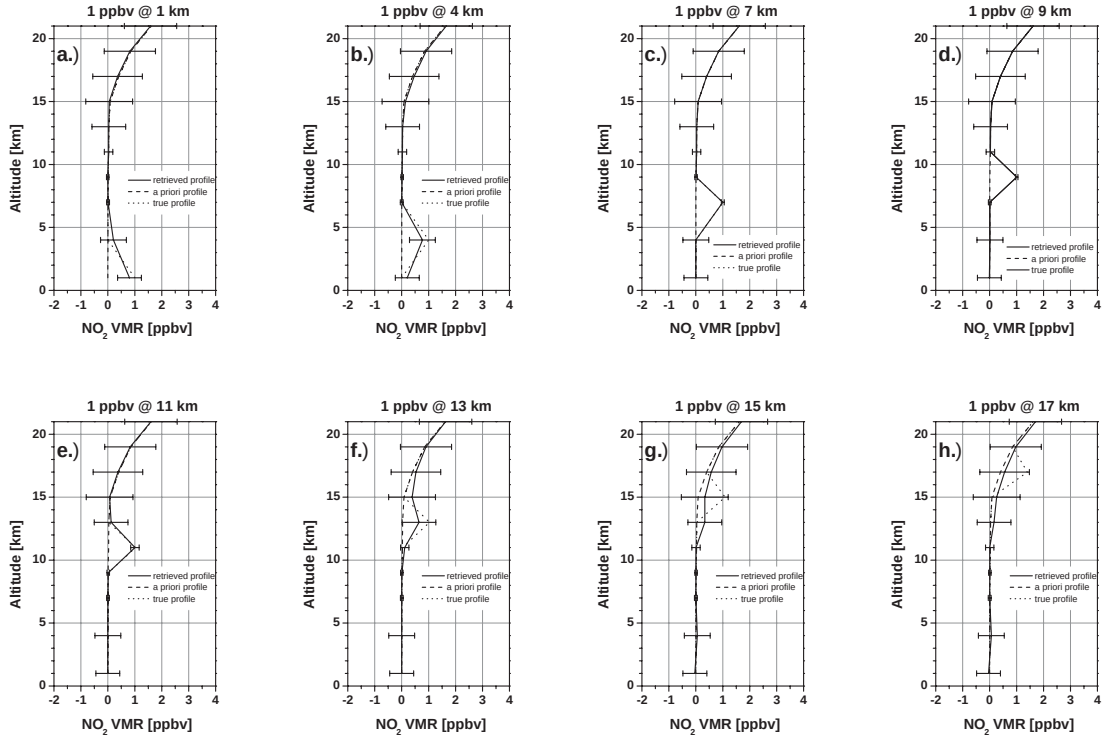

Figure 8.2: The study was performed for the 4-3 setup. This plot represents the retrieved profiles for simulated data including perturbation in the profile at different altitudes.

in Fig. 8.2c to e. Between 13 and 17 km altitude the perturbed peaks could not be precisely reproduced as shown in Fig. 8.2f to h. The peaks in the retrieved profiles are significantly broadened compared to the peaks in the 'true' profiles. Again this is caused by the broad averaging kernels of these altitudes. This characteristic of the retrieval algorithm will be discussed in more detail in section 8.1.3 'Sensitivity to the Stratospheric Column'.
The error bars are the total retrieval errors as discussed in chapter 6 'Error Analysis'. It is demonstrated by Fig. 8.2 that small errors result in a high retrieval quality, since the true profile is reproduced very good by the retrieved profiles. On the other hand large errors result in poor retrieval quality because in areas with large errors the true profile is not reproduced very good by the retrieved profiles.

Enhanced LIMB 18 LOS Setup

In this analysis the enhanced limb 18 LOS setup at 500 nm was chosen to demonstrate the ability of the retrieval algorithm to retrieve profile information in the troposphere. The setup was chosen in comparison to the 4-3 setup used for real data analysis in the next chapter. The aim of this investigation is to demonstrate the ability of the enhanced limb 18 LOS setup at 500 nm which proved to be the most promising setup for profile retrieval in chapter 7 'The Sensitivity Study'.
Fig. 8.3a and b present the retrieved profiles for simulated data modeled for profiles per-

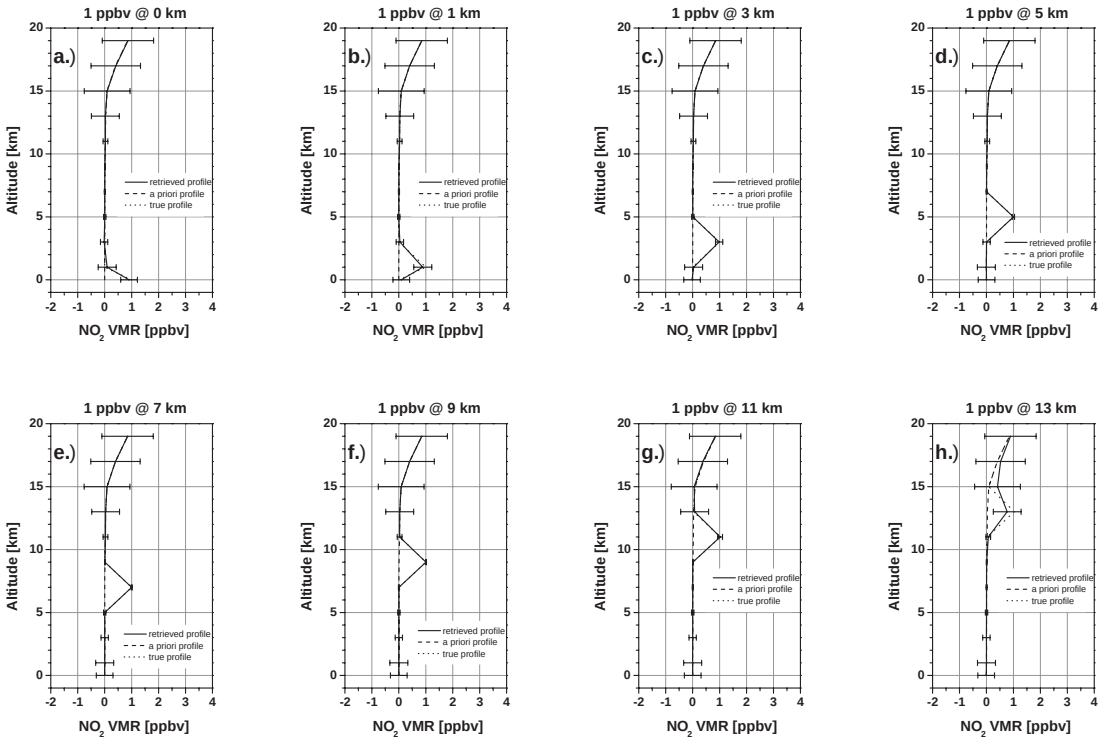

Figure 8.3: The study was performed for the enhanced limb 18 LOS setup. This plot represents the retrieved profiles for simulated data including perturbation in the profile at different altitudes.

turbed at 0 and 1 km altitude. The retrieved profiles reproduce the perturbed profiles very good in comparison to the retrieved profiles of the two lower most perturbation levels of the 4-3 setup. This increased quality is due to the increased number of LOS and the choice of the specific LOS as discussed in chapter 7 'The Sensitivity Study'. The quality of the retrieved profiles is enhanced by the increased peak values of the averaging kernels near the surface, the improved focusing of the averaging kernels on the peak altitude, and the decreased retrieval errors. The retrieved profile for perturbations between 3 and 11 km altitude (Fig. 8.3c to g) are reproduced equally well as the retrieved profiles with perturbation between 7 and 11 km altitude of the 4-3 setup are indicating. Above 11 km the enhanced limb 18 LOS setup at 500 nm has the same problems as the 4-3 setup even though only retrieved profiles for perturbations up to 13 km altitude are shown (Fig. 8.3h). As already mentioned the explanation of this characteristic is discussed in section 8.1.3 'Sensitivity to the Stratospheric Column'.

8.1.3 Sensitivity to the Stratospheric Column

This investigation deals with the response of the retrieval algorithm to changing stratospheric columns. The result of this analysis is crucial to the profile retrieval using real AMAXDOAS data because APROVAL is not sensitive to the stratosphere as the sensitivity studies have shown. Fig. 8.4 shows retrieved profiles calculated from simulated

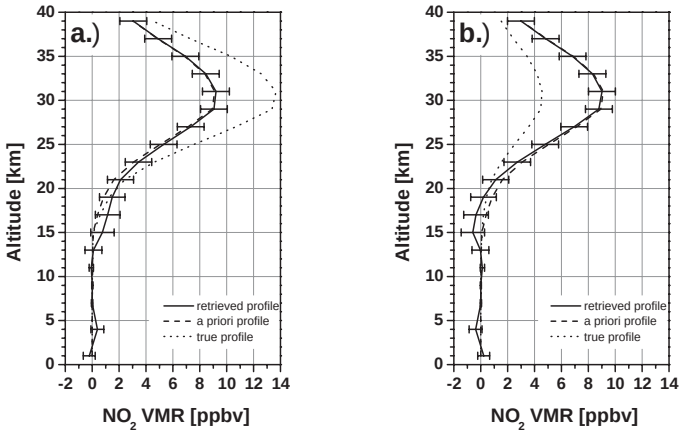

Figure 8.4: The study was performed for the 4-3 LOS setup. This plot represents the retrieved profiles for simulated data including increased stratospheric columns by +50% plot a and -50% plot b.

slant columns with changes of ±50% compared to the a priori profile. Meaning the 'true' profile used to calculate the simulated slant column differs by ±50% from the a priori profile. Fig. 8.4a deals with the first case of the a priori profile + 50% as 'true' profile. In this case the retrieval algorithm expects 50% more stratospheric NO_2 as suggested by the a priori profile. Due to the insensitivity of the retrieval algorithm to the stratosphere the algorithm is forced to retrieve the values of the a priori profile in the stratosphere. Since the measured data suggest more NO_2 in the stratosphere as retrieved, the algorithm puts the surplus NO_2 in the region with the smallest averaging kernel peak values where the averaging kernels still have distinct peaks - this is the altitude region above 13 km and below 20 km. As can be seen in Fig. 8.4a too, the troposphere is not influenced by the surplus NO_2 except for layers 1 km and 4 km, and the influence in these layers is well within error bars.

Fig. 8.4b presents the second case where the 'true' profile is 50% less of the a priori profile. In this case the effect is exactly vice versa. The measured slant column suggest less stratospheric NO_2 than retrieved by the retrieval algorithm. Thus the difference is compensated by negative NO_2 values in the retrieved profile. Again the retrieval algorithm puts the negative values in the altitude region with the smallest averaging kernel peak values where the averaging kernels still have distinctive peaks. In this case the influence on the troposphere is restricted to the lowest layers, too and well within the error bars. But it has to be noted that an uncertainty of the stratospheric column results in an additional error in the lower two layers of the retrieval grid. In the profile retrieval using real AMAXDOAS data the stratospheric column is measured using the zenith LOS to correct for the uncertainty in the stratospheric column as discussed in the next paragraph.

This characteristic of the retrieval algorithm can be used to correct for differences in the measured stratospheric slant column and the stratospheric slant column of the used

a priori profile. The AMAXDOAS measurements contain this information, since the zenith viewing LOS is measuring almost exclusively the stratospheric NO_2 slant column as discussed in section 4.4 'The measurement Geometry'. The retrieval algorithm developed in this work interprets the difference of the retrieved profile to the a priori profile at 17 km altitude as correction parameter to account for varying stratospheric slant columns.
This characteristic of the retrieval algorithm already showed up in chapter 6 'The Error Analysis' while discussing the forward model error. In this investigation the largest errors occurred mainly at 15 km altitude. Now it can be understood why. For example, in the study concerning the forward model error component due to a changing pressure profile an increase of 10% in pressure increases the NO_2 abundance slightly as well, since the NO_2 is given in volume mixing ratio. This additional NO_2 is missing in the a priori profile. So the retrieval algorithm adds that amount to layers above 13 km altitude. This explanation is valid for all forward model error components as described in chapter 6 'Error Analysis'.

8.2 SCIAMACHY

This section deals with the investigation of the profile retrieval using simulated SCIAMACHY slant columns. The purpose of this study is to demonstrate the potential of APROVAL. Even though no real SCIAMACHY data will be analyzed with APROVAL, a sensitivity study presenting the expected theoretical vertical resolution and the expected theoretical total retrieval error is shown.
Since there are some profound differences compared to the profile retrieval using simulated AMAXDOAS slant columns, these differences have to be discussed. The key difference of this profile retrieval is the difference in viewing geometry. As already discussed in chapter 4 'The Experimental Setup' the SCIAMACHY instrument in limb mode is scanning the atmosphere from the lower altitudes towards the higher altitudes. The parameter for the SCIAMACHY LOS in limb mode is the tangent height with a step size of about 3.3 km. Fig. 8.5 presents profile retrieval characteristics for simulated SCIAMACHY slant columns. Plot a shows the weighting functions of this profile retrieval, and it can be seen that these weighting functions are quite different compared to the AMAXDOAS weighting functions of chapter 7 'The Sensitivity Study'. The profile retrieval using AMAXDOAS data proved to be most sensitive near flight altitude whereas according to Fig. 8.5 the profile retrieval using SCIAMACHY data is very sensitive in the altitudes between 10 and 30 km. This difference is due to the larger altitude range covered by the limb viewing LOS. This result is backed up by the plots c and d of Fig. 8.5, because the vertical resolution is the best in this specific altitude range and the retrieval error is the smallest. Another difference compared to the AMAXDOAS profile retrieval is the retrieval grid. In the SCIAMACHY profile retrieval the retrieval grid was set to the grid of the tangent heights. The weighting functions of the SCIAMACHY profile retrieval are not calculated on the fine grid with 100 m step size as in the AMAXDOAS profile retrieval (see chapter 5 'The Retrieval Method'), since the SCIAMACHY profile retrieval does not retrieve values near the earth's surface.

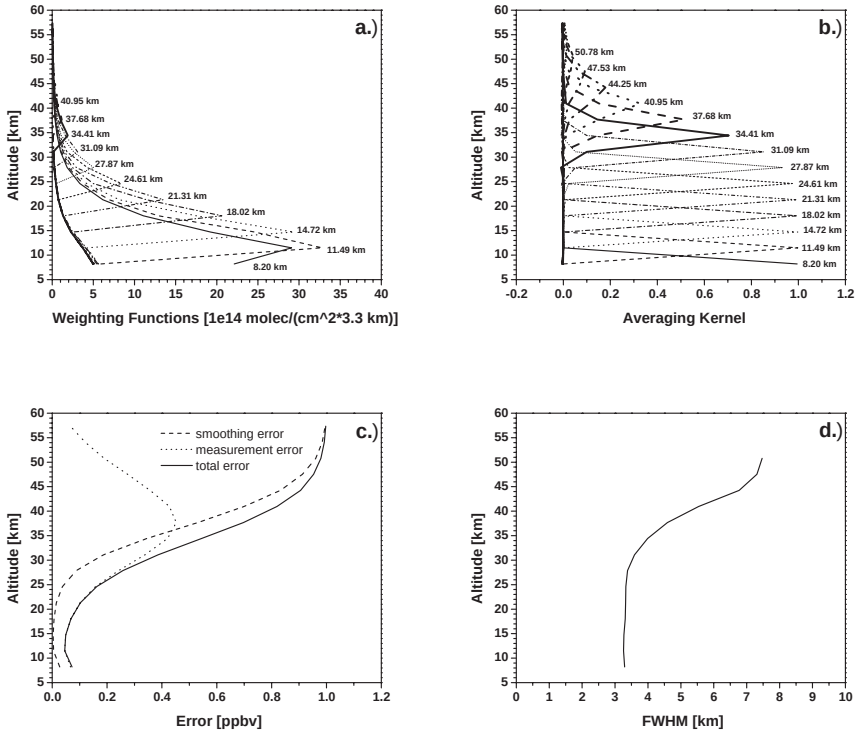

Figure 8.5: The weighting functions for the profile retrieval using the SCIAMACHY simulated data are shown in plot a, the corresponding averaging kernels are shown in plots b, the retrieval errors are shown in plots c, and the resolution (FWHM) of the profile retrieval is shown in plot d.

8.2.1 Consistency Study

The aim of this investigation is the same as that of the consistency study of the profile retrieval using AMAXDOAS simulated data. This study is supposed to demonstrate the potential of APROVAL for SCIAMACHY data. The simulated slant columns used in this section are calculated using eq. 5.2, too. The forward model calculates the weighting functions $\mathbf{K}$ and $\mathbf{x}$ is the 'true' profile of NO_2 as mentioned above. Fig. 8.6 shows the retrieved profile is numerically equal to the a priori profile as one would expect, since the profile information contained in the slant column is identical with the a priori profile information. This study verifies the feasibility of the retrieval of profiles from slant columns measured by the SCIAMACHY instrument.

8.2.2 Sensitivity to different profiles

This investigation is a combination of the two studies 'Sensitivity to different profile layers', and 'Sensitivity to stratospheric columns' conducted for the AMAXDOAS profile retrieval. These two studies are combined for the SCIAMACHY profile retrieval because the response of the AMAXDOAS profile retrieval to tropospheric NO_2 abundance is completely different than to stratospheric NO_2 abundance. This is not the

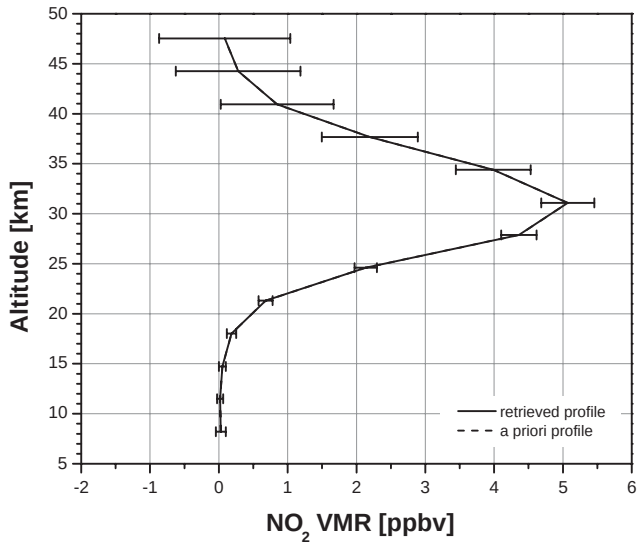

Figure 8.6: The consistency study for the SCIAMACHY instrument. This plot represents the retrieved profile using eq. 5.2 to calculate the simulated slant columns.

case concerning the SCIAMACHY profile retrieval, because this retrieval is sensitive to the entire altitude range containing significant NO_2 abundance.
Fig. 8.7 is presenting the retrieved profiles resulting from simulated slant columns calculated with profiles varying significantly from the a priori profile. These profiles have an increase of almost 100% in stratospheric NO_2 in addition to perturbations of 3 ppbv in different altitudes. The true profile used to simulate the slant columns from which the profile of Fig. 8.7a is retrieved has a perturbation of 3 ppbv at 11.5 km altitude. As can be seen APROVAL can reproduce the true profile very good. This is expected considering the high retrieval quality observed in that altitude range (see

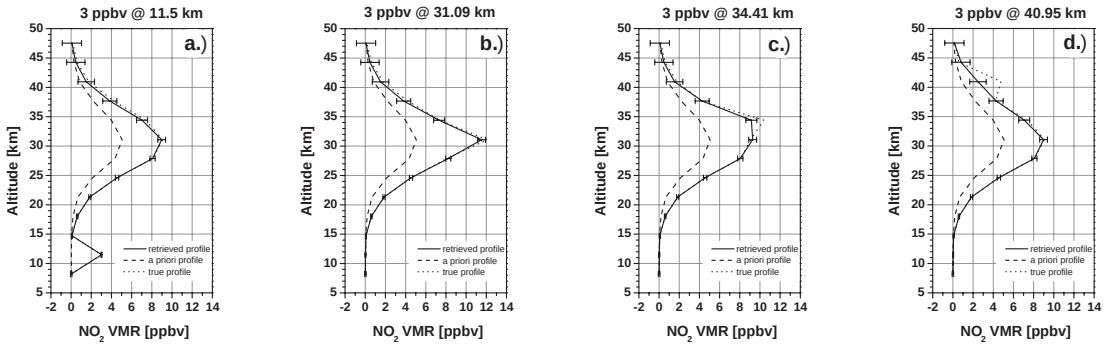

Figure 8.7: Sensitivity of the SCIAMACHY profile retrieval to different layers.

Fig. 8.5). The SCIAMACHY profile retrieval being able to retrieve unexpected features in the profile does not change up to an altitude of 31 km as shown in Fig. 8.7b. Starting at 34.4 km altitude the SCIAMACHY profile retrieval is losing the ability to distinguish peaked features in the profile. This can be seen in Fig. 8.7c where the true profile has a distinct feature at 34.4 km altitude, but the profile retrieval is not able to reproduce it. This gets worse for higher altitudes (see Fig. 8.7d).

8.3 Summary

The results of the profile retrieval using simulated data is summarized have shown that:

- The consistency study involving the 4-3 LOS setup has shown a consistent profile being retrieved from simulated slant columns which are calculated using specific atmospheric temperature, pressure, and trace gas concentration profiles. The latter acted as a priori information during the retrieval process.
- The investigation dealing with the sensitivity to different profile layers has shown for the 4-3 LOS setup that APROVAL is able to retrieve profile information with a very small uncertainty ($\leq$ 0.15 ppbv) from the altitudes near flight altitude and with an acceptable uncertainty ($<$ 0.5 ppbv) from altitudes in the lower troposphere. The uncertainties on the retrieved profiles for the enhanced limb 18 LOS setup near flight altitude ($<$ 0.1 ppbv) and in the lower troposphere (0.3 ppbv) are even smaller than those of the 4-3 LOS setup.
- The variation of the stratospheric column in the retrieval process using the 4-3 LOS setup induces uncertainties at altitudes between 15 and 19 km altitude. Fortunately the AMAXDOAS instrument measurements include the measurement of the stratospheric column, so the a priori information can be adjusted to the measured stratospheric column.
- This investigation could prove that APROVAL is applicable to satellite limb measurements from the SCIAMACHY experiment. A trace gas profile can be retrieved from 12 to 35 km altitude.

Chapter 9

Profile Retrieval using Real AMAXDOAS Data

In this chapter the results from the profile retrieval using real data from the AMAXDOAS instrument will be presented. First a brief description of the SCIAMACHY VALidation and Utilization Experiment (SCIA-VALUE) campaigns will be given followed by a study to find the optimum of the measurement error and the a priori error compared to the sensitivity studies. Finally the results of selected flights will presented.

9.1 The SCIA-VALUE Campaigns 2002/2003

This section is a brief overview of the SCIA-VALUE activities in 2002/2003 [Fix *et al.*, 2004]. The meteorological research aircraft FALCON 20 from the German Aerospace Center (DLR) in Oberpfaffenhoffen near Munich was chosen as instrument platform. Besides the AMAXDOAS instrument two other instruments for atmospheric remote sensing were installed: The first instrument is the Ozone lidar experiment (OLEX) operated by the DLR and the second instrument is the airborne submillimeter radiometer (ASUR) operated by the Institute of Environmental Physics of the University of Bremen. The OLEX system measures the atmospheric backscatter at four wavelengths 308, 355, 532, and 1064 nm. The 308 nm radiation is generated by a XeCl eximer LASER, and the radiation of the other three wavelengths is generated by a Q-switched Nd:YAG LASER [Wirth and Renger, 1998]. The receiver system uses a 35-cm Cassegrainian telescope. The received light is split into four channels, one for each wavelength. The backscattered light at 1064 nm is detected by means of a silicon avalanche photodiode (APD), whereas the light at the shorter wavelengths is measured by photo-multiplier tubes (PMT). OLEX is zenith viewing and its measurement range extends from about 2 km above flight altitude to about 30 km. The system provides high resolution two-dimensional cross sections of ozone number densities, aerosol extinction, color ratio and particle depolarization. In addition, cirrus or polar stratospheric cloud (PSC) cover information is determined.
ASUR is a passive heterodyne sensor operating in the frequency range 604 - 662 GHz [Küllmann *et al.*, 2001]. The sensor is characterized by a superconductive low noise mixer, a tunable local oscillator, and two spectrometers: an acousto-optical spectrom-

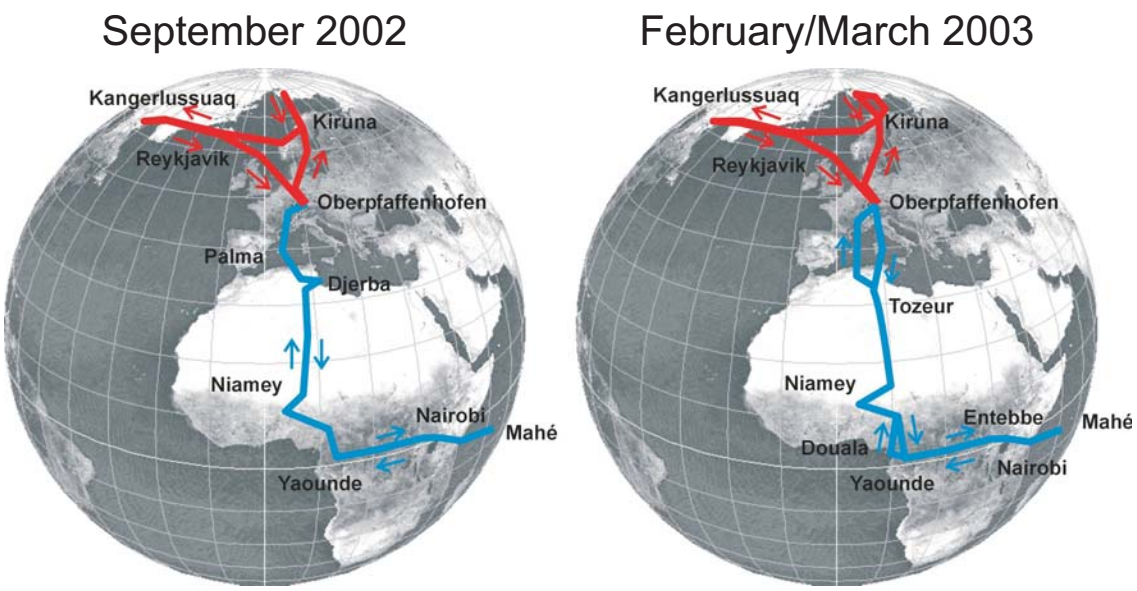

Figure 9.1: Flight Routes for the SCIA-VALUE Campaigns in September 2002 and February/March 2003 [Fix *et al.*, 2004].

eter with a bandwidth of 1.5 GHz and a resolution of 1.5 MHz, and a chirp-transform spectrometer with a bandwidth of 178 MHZ and a resolution of 278 kHz. It allows for the spectral detection of stratospheric trace gases like O_3, N_2O, ClO, HCl, HNO_3, CH_3Cl, HO_2, H_2O, NO, and BrO. Vertical profiles from 15 to over 50 km altitude can be retrieved for most of the species with a vertical resolution of typically 6 km in the lower and 12 km in the upper stratosphere.

Two major campaigns have been performed in fall 2002 and spring 2003 as a German contribution to the validation of the SCIAMACHY onboard Europe's remote sensing satellite ENVISAT (see Fig. 9.1). These two campaign took place six and twelve months after the launch of ENVISAT on Feb. 28, 2002. Fig. 9.1 shows the flight routes across the globe. These flight patterns have been selected to cover large meridional and latitudinal cross sections. The first campaign consisted of a northern and a southern part. The northern part led from Oberpfaffenhofen near Munich to Kiruna (Sweden), Sprizbergen, Iceland, and Greenland and then back to Oberpfaffenhofen via Iceland. The southern part started in Oberpfaffenhofen and led to Palma de Mallorca, Djerba (Tunesia), Yaounde (Cameroon), Nairobi (Kenya), and to the Seychelles and back. During this campaign data of a total of 54 flight hours over a period of 25 days have been recorded crossing 18 ENVISAT orbits.

The second campaign in spring 2003 had flight routes very similar to those of the first campaign, but the sequence of the northern and southern parts were exchanged. The second campaign started with the southern and ended with the northern part. During the second campaign data of a total of 59 flight hours over a period of 28 days have been recorded crossing ten ENVISAT orbits.

9.2 Optimum Measurement Error and A Priori Error

The measurement errors and a priori errors assumed in the sensitivity studies had only theoretical character. To improve the quality of the profile retrieval these errors have to be adapted to reality.
The relation between the measurement error and the a priori error proved to be a sensitive one, since a change in ratio of the measurement error and the a priori error influences the quality of the retrieved profile significantly. The relation between these two errors has the meaning of a weight of information. In case the measurement errors are small and the a priori errors are larger the profile retrieval weights the information in favor of the information contained in the measurements and vice versa. In case the measurement error is too small compared to the a priori error the retrieved profiles begin to oscillate. A good example for such an oscillation due to the relation of the two errors can be seen in Fig. 9.2a (black curve). The goal of the following investigation is to reduce these oscillations. The proposed solution to this problem is to adjust the ratio of the measurement error and a priori error.

9.2.1 Measurement Error

The first error component to be considered is the measurement error. As already described in chapter 6 'Error Analysis' errors are treated as covariance matrices in this retrieval algorithm meaning the square root of the diagonal elements of the covariance matrix create the vector containing the errors. Fig. 9.2a shows the reaction of the retrieval to increasing measurement errors. The increasing measurement error is

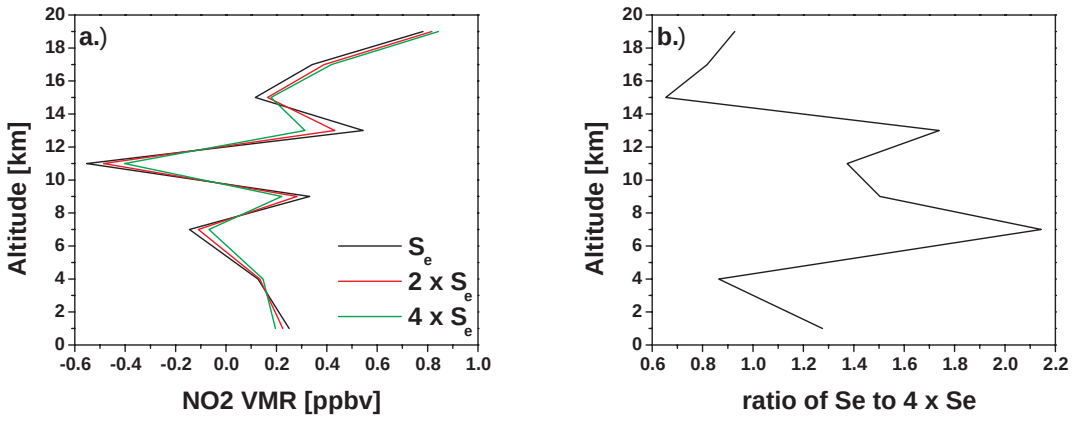

Figure 9.2: The Quality of the retrieval is depending on the magnitude of the measurement error. S_e is the covariance matrix of the measurement error of chapter 6 'Error Analysis'. In plot a the profile retrieval is compared to ones with two times and four times the measurement error covariance matrix. In plot b the ratio (ratio of the absolute values) of the retrieved profiles of plot a using S_e and four times S_e as measurement errors is shown.

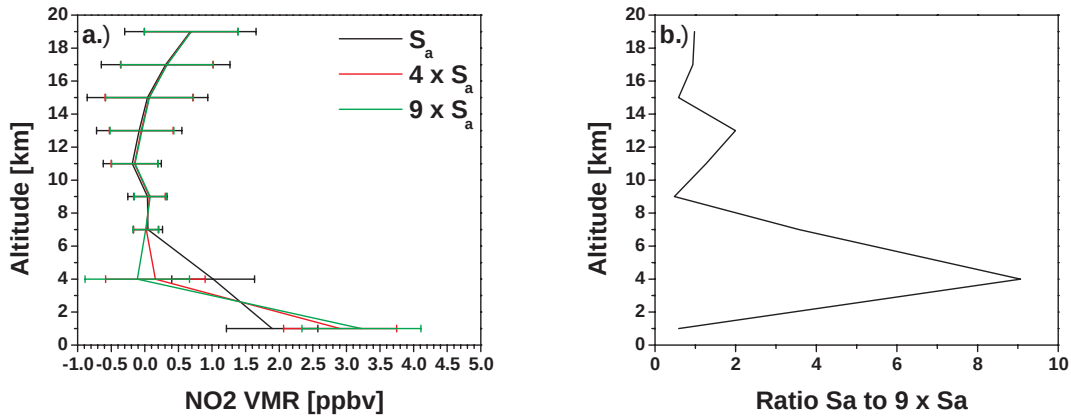

Figure 9.3: The Quality of the retrieval is depending on the magnitude of the a priori error. S_a is the covariance matrix of the a priori error of chapter 6 'Error Analysis'. In plot a a study is shown where the a priori was assumed to be altitude dependant. The factors given in the plot consider the lowest level (1 km altitude) only. The second level (4 km altitude) was multiplied by one and all other levels were multiplied by 0.5. In plot b the ratio (ratio of the absolute values) of the retrievals S_a and nine times S_a is presented.

significantly reducing the artificial oscillations which sometimes occur in the profile retrieval. In Fig. 9.2b the ratio of measurement errors of the model runs using measurement errors S_e and four times S_e are shown. It can be seen that the magnitude of the harmonic behavior can be reduced by a factor of 2.1 in some altitudes when the measurement error covariance matrix is increased by a factor of four (the single errors are increased by a factor of 2).
The suggested increase of the measurement error shown in Fig. 9.2 is physically reasonable, because the measurement errors used in the profile retrieval are the fitting errors of the nonlinear least square fit of the slant columns in the DOAS data analysis. These values could only be a guideline for the real errors of the measured slant columns because the methodical error due to the DOAS data analysis are not included in the fitting errors. The methodical error includes error components due to errors in the absorption cross sections and uncertainties in the choice of the fitting window.

9.2.2 A Priori Error

The second error to be adapted in comparison to the sensitivity studies is the a priori error. This error represents the assumed variability in the atmosphere due to missing information, since the a priori profile represents climatological information only. In the sensitivity studies an altitude independent error of the a priori profile was used suggesting an uncertainty being the same over the entire altitude range. Since the a priori profile does not contain any tropospheric NO_2, this assumption is not very useful, because large differences in the abundance of tropospheric NO_2 are to be expected. Thus 1 ppbv error in the a priori seems to be too small for the retrieval level closest to

the surface (1 km). On the other hand since APROVAL is not sensitive to stratospheric NO_2 an error of 1 ppbv seems to be too large for the stratosphere. Thus three different error profiles for the a priori profile have been tested. The first error profile contains error values of 1 ppbv over the entire altitude range. The second error profile contains an error of 2 ppbv at 1 km altitude, an error of 1 ppbv at 4 km altitude, and 0.7 ppbv from 7 to 39 km altitude. The last error profile looks like the error profile just described except that the error at 1 km altitude is 3 ppbv.

Fig. 9.3a shows the reaction of the retrieval towards increased a priori errors at 1 km altitude. It can be seen that retrieved NO_2 values at 1 km are increased significantly in case the a priori error is increased from 1 to 3 ppbv at the same altitude. The retrieved NO_2 value at 4 km altitude has decreased significantly confining the tropospheric NO_2 closer to the surface. This is perfectly reasonable, since the tropospheric NO_2 is expected to be mainly in the boundary layer. The increased a priori error at 1 km altitude allows the retrieval algorithm to retrieve higher NO_2 values, since the total retrieval errors are not as small as the sensitivity studies have shown. In case the total retrieval errors are increased the retrieval tends towards the a priori profile when a priori errors are small and the a priori profile contains no tropospheric NO_2.

Fig. 9.3b shows the ratio of the profile retrieval using the 1 ppbv a priori error to the retrieval using the 3 ppbv a priori error at 1 km altitude. As can be seen the NO_2 values at 1 km altitude are increased by 70 % when using an a priori error of 3 ppbv at 1 km altitude. At 4 km altitude the NO_2 values are smaller by a factor of nine when using an a priori error of 3 ppbv at 1 km altitude.

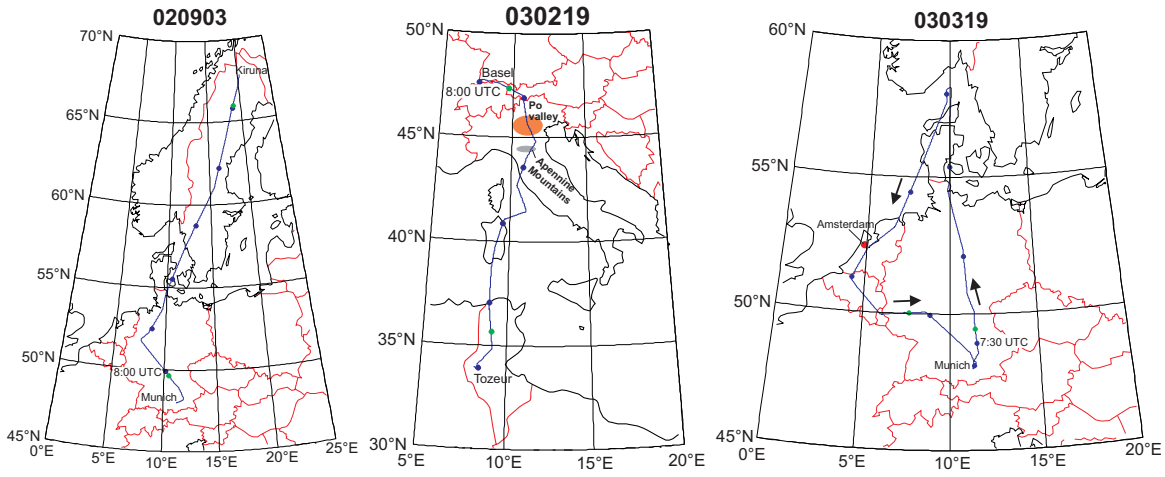

Figure 9.4: Flight tracks of the flights 020903, 030219, and 030319. The blue dots on the flight tracks mark half and full hours. The first blue dot of each flight track is marked by the corresponding time. The flight tracks between the green dots mark flight altitudes ≥ 10 km. The time intervals between the green dots are plotted in Figures 9.9 - 9.14.

9.3 Results

In this section the results from the profile retrieval using real AMAXDOAS data will be presented. Three flights have been selected from all flights described above. The flights presented here were selected because of the presence of tropospheric NO_2. Fig. 9.4 shows the flight tracks of the three selected flights. The first flight on Sep. 3, 2002 shown in the left plot is from the first campaign in September 2002. It is the beginning of the northern part of the campaign from Munich to Kiruna (Sweden). The second flight on Feb. 19, 2003 (plot in the middle of Fig. 9.4) is from the second campaign in February 2003. It is the beginning of the southern part of the campaign from Basel to Tozeur (Tunesia). The last flight on Mar. 19, 2003 shown in the right plot of Fig. 9.4 is from the second campaign as well. It is a supplement for the last flight of the northern part of the second campaign because SCIAMACHY was switched off due to a malfunction. This supplemental flight was a round trip over Germany, Denmark, The Netherlands, and Belgium.
Fig. 9.5 shows the differential slant columns (lower panel) of the 425 to 450 nm fitting window in comparison to the retrieved profiles (upper panel). The differential slant columns are shown as an example for the data input used by APROVAL. The slant

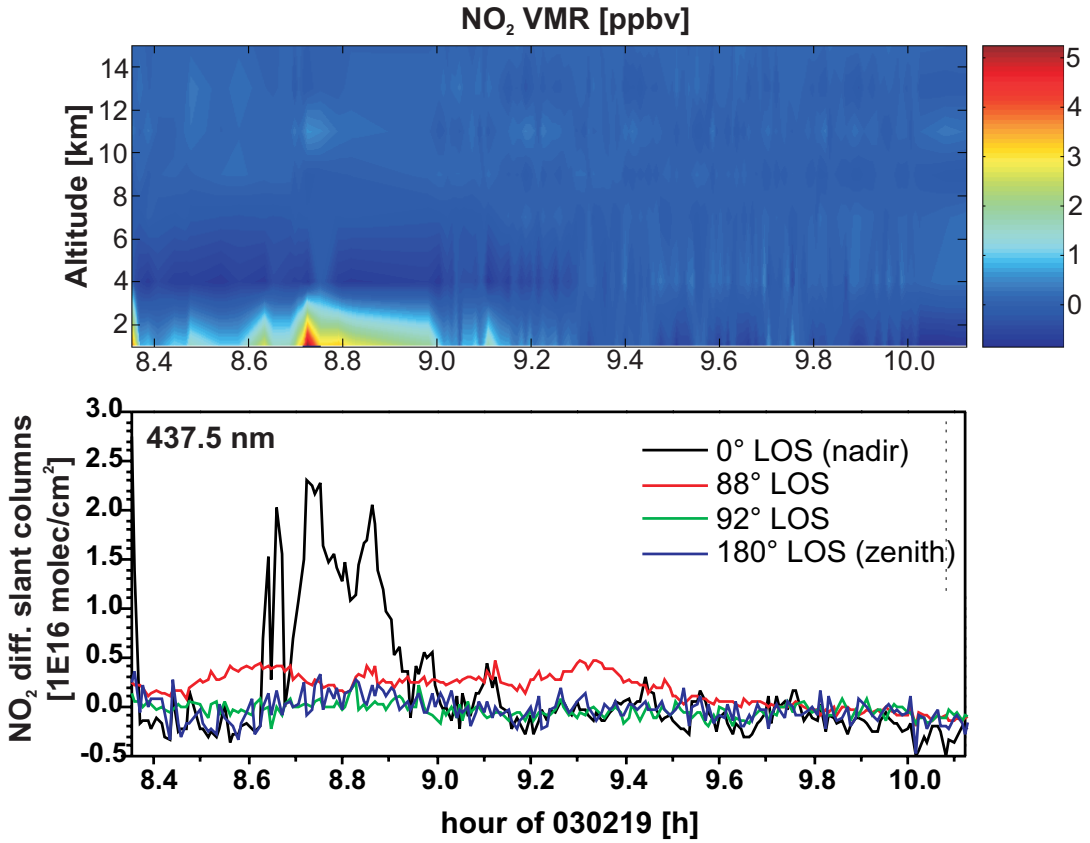

Figure 9.5: Differential slant columns compared (lower panel) [Wang, 2004] to the retrieved profiles (upper panel) of flight 030219. The slant columns for all three wavelengths are shown in appendix B.

column data are the result of the DOAS analysis of the measured spectra using the AMAXDOAS instrument performed by Wang [2004]. The background spectrum is always a spectrum with one of smallest SZA which was taken from the same LOS (see Tab. 9.1). The fitting errors (multiplied by a factor of two as described in section 9.2.1 'Measurement Error') of the DOAS analysis act as measurement errors in the retrieval process and the a priori errors are those described in section 9.2.2 'A priori Error' (see above).

Flight 020903

This flight was chosen due to enhanced NO_2 slant column values in the nadir direction. Fig. 9.6 presents profiles for interesting features showing up in the contour plots (see Fig. 9.9 and 9.10). The plots in Fig. 9.6 depict the profiles from 1 to 15 km altitude only, since APROVAL is insensitive for the stratosphere as shown in chapter 7 'Sensitivity

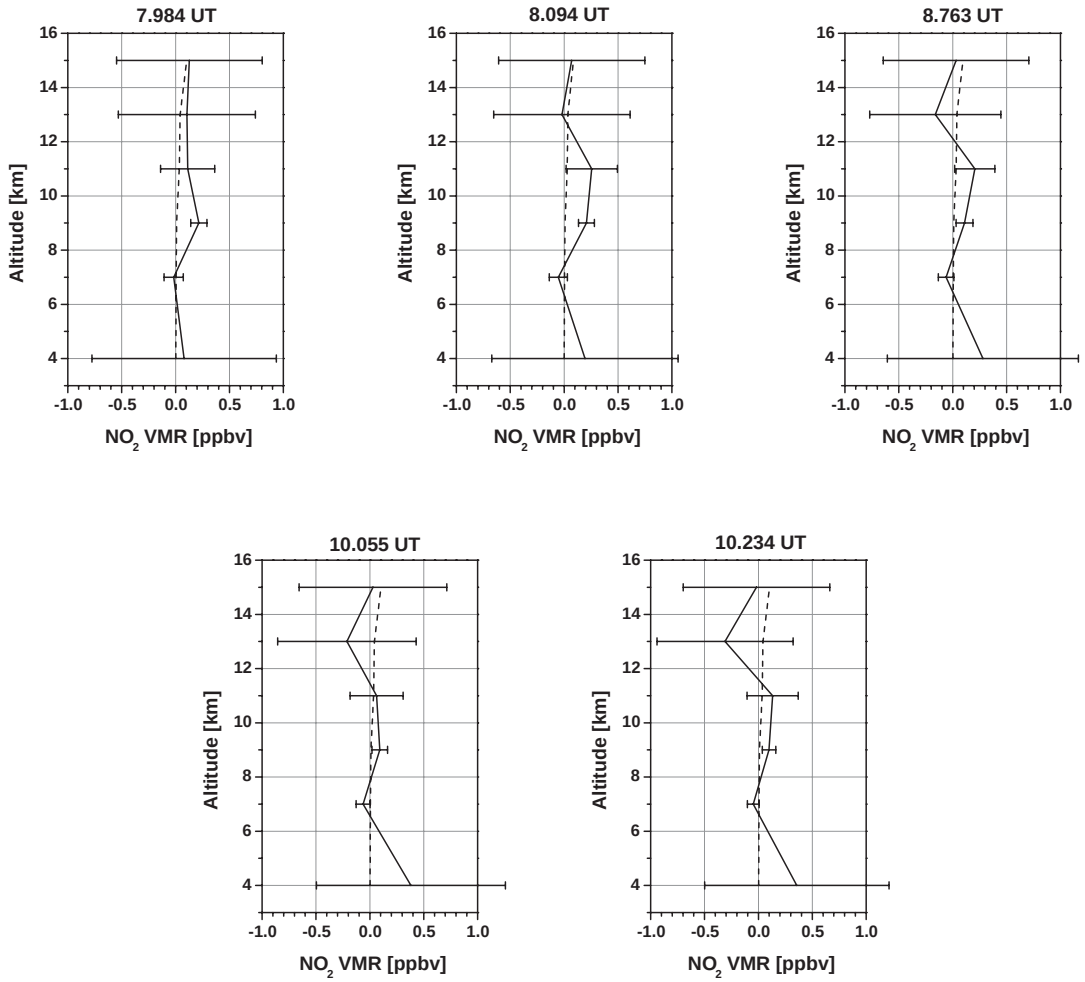

Figure 9.6: Selected profiles of interesting areas of flight 020903. Solid lines with error bars represent the retrieved profiles and the dashed lines represent the a priori profiles.

Table 9.1: Parameters for DOAS analysis of the three flights.

date	fitting window [nm]	LOS [°]	SZA of background spectrum [°]	LOS of background spectrum [°]
020903	344.97 ... 379.95	0	55.33	0
020903	345.07 ... 380.05	88	55.33	88
020903	345.02 ... 380.08	92	55.33	92
020903	344.96 ... 380.03	180	55.33	180
020903	425.04 ... 449.99	0	55.46	0
020903	425.07 ... 449.98	88	55.31	88
020903	425.08 ... 450.01	92	55.31	92
020903	424.94 ... 449.95	180	55.35	180
020903	471.89 ... 497.04	0	55.35	0
020903	471.93 ... 497.04	88	55.31	88
020903	471.91 ... 496.98	92	55.35	92
020903	471.91 ... 496.97	180	55.39	180
030219	345.00 ... 379.99	0	56.49	0
030219	345.00 ... 379.98	88	56.49	88
030219	344.99 ... 379.96	92	56.49	92
030219	344.96 ... 379.94	180	56.49	180
030219	424.90 ... 449.91	0	56.6	0
030219	425.02 ... 449.95	88	56.6	88
030219	424.97 ... 449.92	92	56.6	92
030219	424.88 ... 449.84	180	56.49	180
030219	471.89 ... 496.93	0	56.6	0
030219	471.89 ... 496.93	88	56.6	88
030219	471.91 ... 496.97	92	56.6	92
030219	471.80 ... 496.90	180	56.6	180
030319	345.06 ... 380.06	0	61.56	0
030319	345.07 ... 380.05	88	61.56	88
030319	345.06 ... 380.04	92	61.56	92
030319	345.04 ... 380.02	180	61.56	180
030319	409.93 ... 455.86	0	61.55	0
030319	409.96 ... 455.93	88	61.55	88
030319	409.94 ... 455.90	92	61.55	92
030319	409.94 ... 455.90	180	61.55	180
030319	472.11 ... 496.91	0	61.55	0
030319	471.89 ... 496.96	88	61.55	88
030319	471.89 ... 496.96	92	61.55	92
030319	471.88 ... 496.96	180	61.55	180

Studies'. The profiles presented in this figure are the basis for the interpretation of the retrieved profiles in the next chapter.

Fig. 9.9 shows the contour plots of the retrieved profiles using only data with flight altitudes of 10 km and above. This figure also illustrate retrieved profiles with 'profile

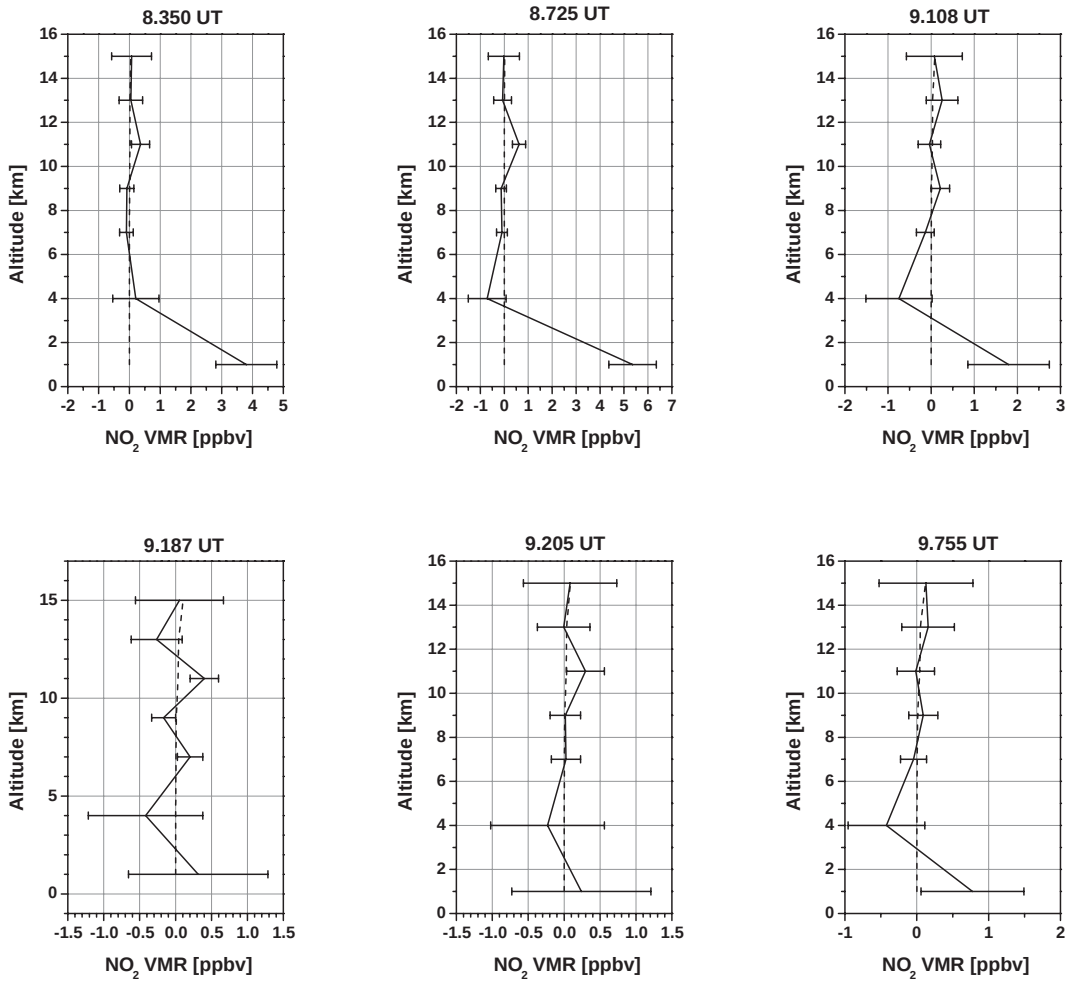

Figure 9.7: Selected profiles of interesting areas of flight 030219. Solid lines with error bars represent the retrieved profiles and the dashed lines represent the a priori profiles.

value(h) + error(h) > 0'[1] meaning retrieved profiles (with absolute values larger than the error) are not considered in the results.

Fig. 9.10 shows real signals only meaning 'profile value(h) - error(h) > 0' has to be true. Only profile values larger than the corresponding error are considered as real, because profile values with error bars crossing the zero line are considered to be below detection limit of the AMAXDOAS instrument. This method of data representation is very useful to decide whether a feature in the contour plot is real or below the detection limit. This figure shows that small amounts of NO_2 were detected at 9 km altitude. The interpretation of these amounts of NO_2 will be done in chapter 10 dealing with the interpretation of the data.

[1]h is referring to the altitude and error is referring to the total retrieval error of the profile retrieval

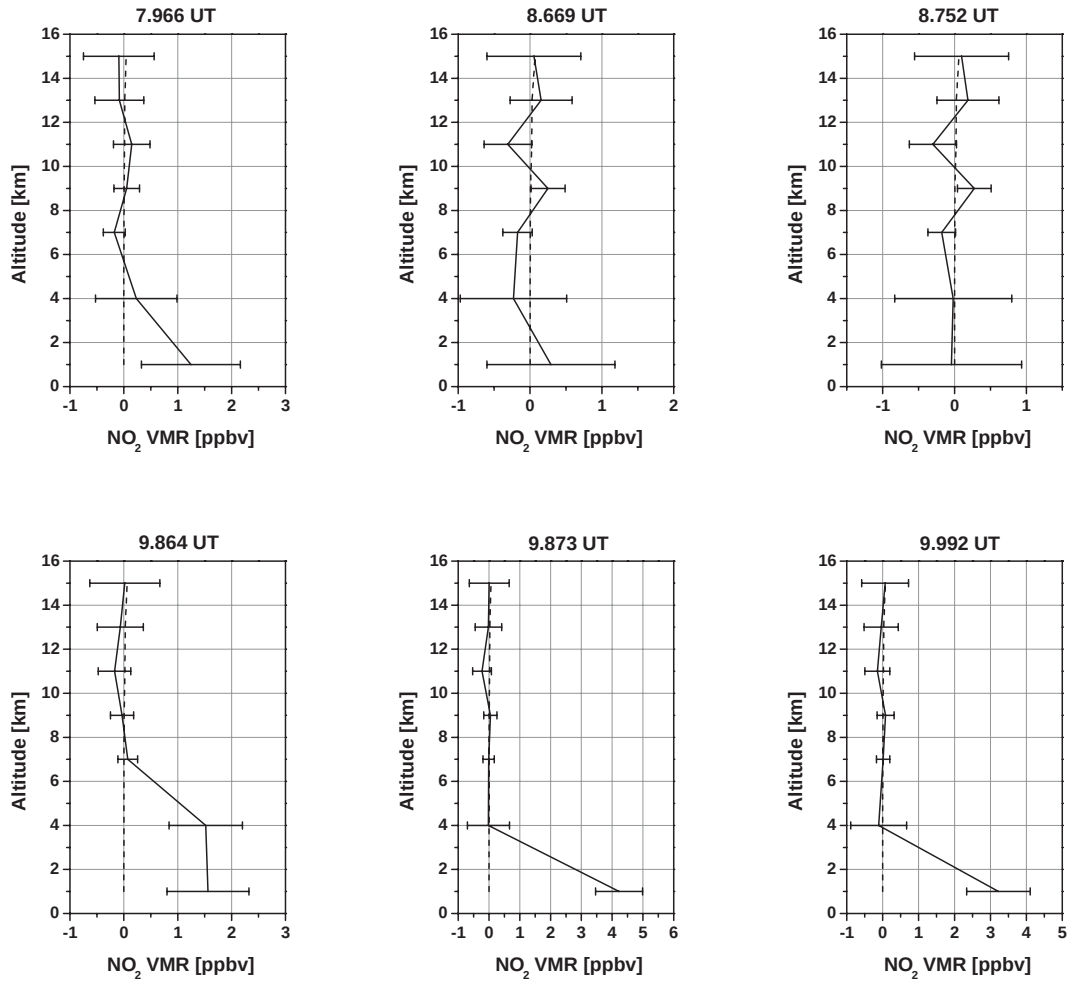

Figure 9.8: Selected profiles of interesting areas of flight 030319. Solid lines with error bars represent the retrieved profiles and the dashed lines represent the a priori profiles.

Flight 030219

This flight was chosen because enhanced NO_2 slant columns were observed in the beginning of the flight in nadir direction. Fig. 9.7 shows profiles for interesting features showing up in the contour plots (see Fig. 9.11 and 9.12). Again the plots in Fig. 9.7 show the profiles from 1 to 15 km altitude only, since APROVAL is insensitive for the stratosphere as shown in chapter 7 'Sensitivity Studies'. The profiles presented in this figure will be analyzed in chapter 10 dealing with the interpretation of the retrieved profiles. This plot shows that the AMAXDOAS instrument is able to detect tropospheric NO_2.

Fig. 9.11 shows the contour plots of the retrieved profiles using again only data with flight altitudes of 10 km and above. As already described for flight 020903 the figure shows retrieved profiles with 'profile value(h) + error(h) > 0' only.

Fig. 9.12 shows real signals only with the definition of 'real signal' being the same

as described above in 'Flight 020903'. Compared to flight 020903 tropospheric NO_2 was detected during this flight. The amounts and geographical locations as well as the meteorological situation will be analyzed in the next chapter. Further there was NO_2 detected at 11 km altitude in several occasions. Again the interpretation of these findings will be done in the next chapter.

Flight 030319

This flight was chosen because enhanced NO_2 slant columns were observed in the beginning of the flight in nadir direction. Fig. 9.8 shows profiles for interesting features showing up in the contour plots (see Fig. 9.13 and 9.14). Again the plots in Fig. 9.8 show the profiles from 1 to 15 km altitude only due to the insensitivity of the profile retrieval to the stratosphere. As mentioned earlier the analysis of the profiles is discussed in the next chapter.
Fig. 9.13 shows the contour plots of the retrieved profiles using again only data with flight altitudes of 10 km and above. As already described for flight 020903 the figure shows retrieved profiles with 'profile value(h) + error(h) > 0' only.
Fig. 9.14 shows real signals only with the definition of 'real signal' being the same as described above in 'Flight 020903'. Compared to flight 020903 tropospheric NO_2 was again detected during this flight. The amounts and geographical locations as well as the meteorological situation will be analyzed in the next chapter.

9.4 Summary

The results of the profile retrieval using real AMAXDOAS data have shown that:

- Three flights of the two SCIA-VALUE campaigns in 2002 and 2003 were analyzed.
- In this chapter it has been proved that slant column measurements from the AMAXDOAS instrument do contain NO_2 profile information up to an altitude of 13 km.
- Only four LOS [0° (nadir), 88°, 92°, and 180° (zenith)] at three wavelengths (362.5 nm, 437.5 nm, and 485.0 nm) are necessary to retrieve profile information at a good vertical resolution of 2.1 to 4.0 km.
- APROVAL was able to retrieve large amounts of NO_2 of up to 5.4 ppbv in the boundary layer in several occasions.
- APROVAL was able to retrieve significant amounts of NO_2 as low as 0.1 ppbv in the UTLS region in several occasions.

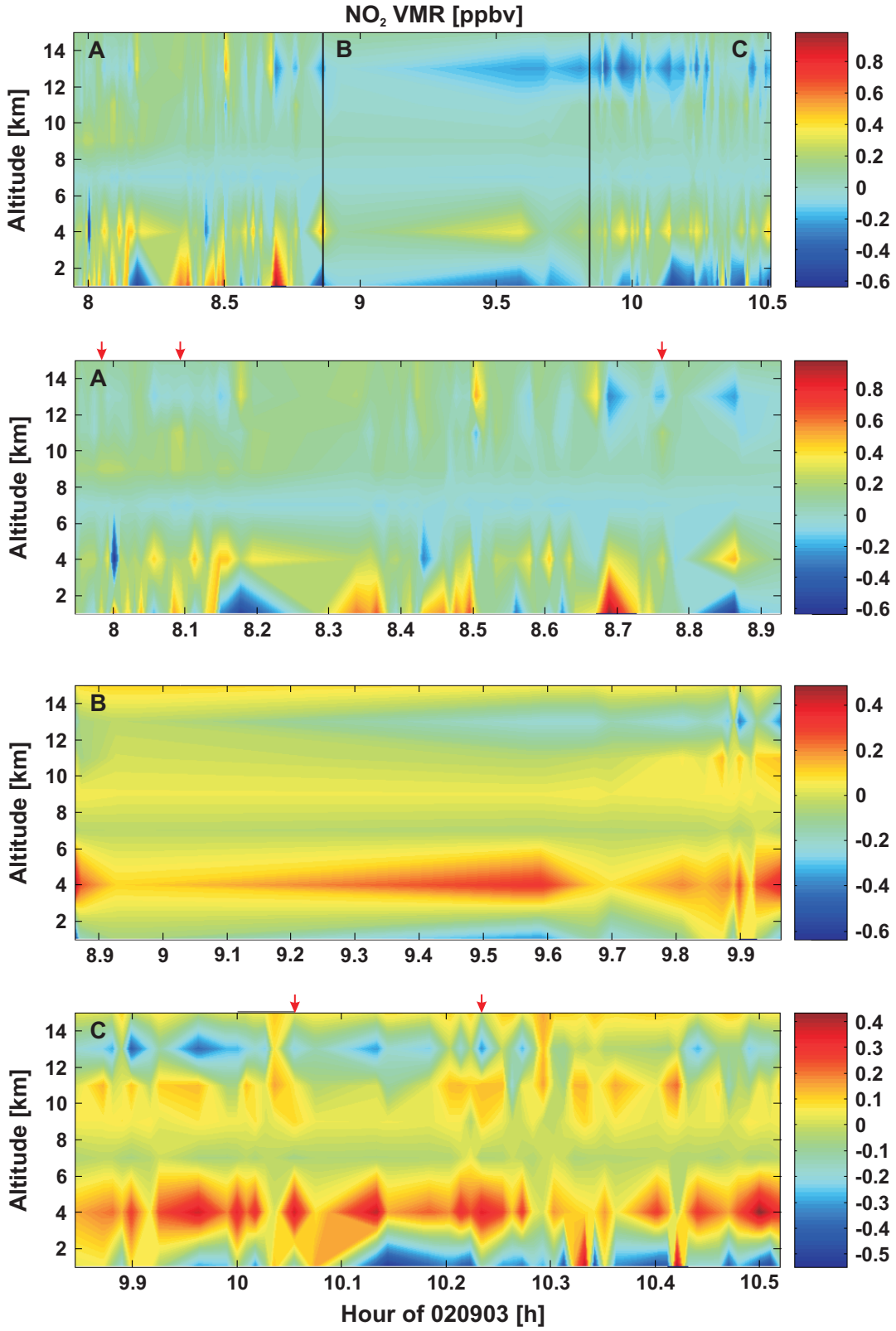

Figure 9.9: Contour plot of the retrieved profiles of flight 020903. The time is given in UTC. The upper panel is an overview over the entire flight and the lower three panels (A, B, and C) are zoomed into the regions of further interest. The red arrows mark the profiles shown in Fig. 9.6.

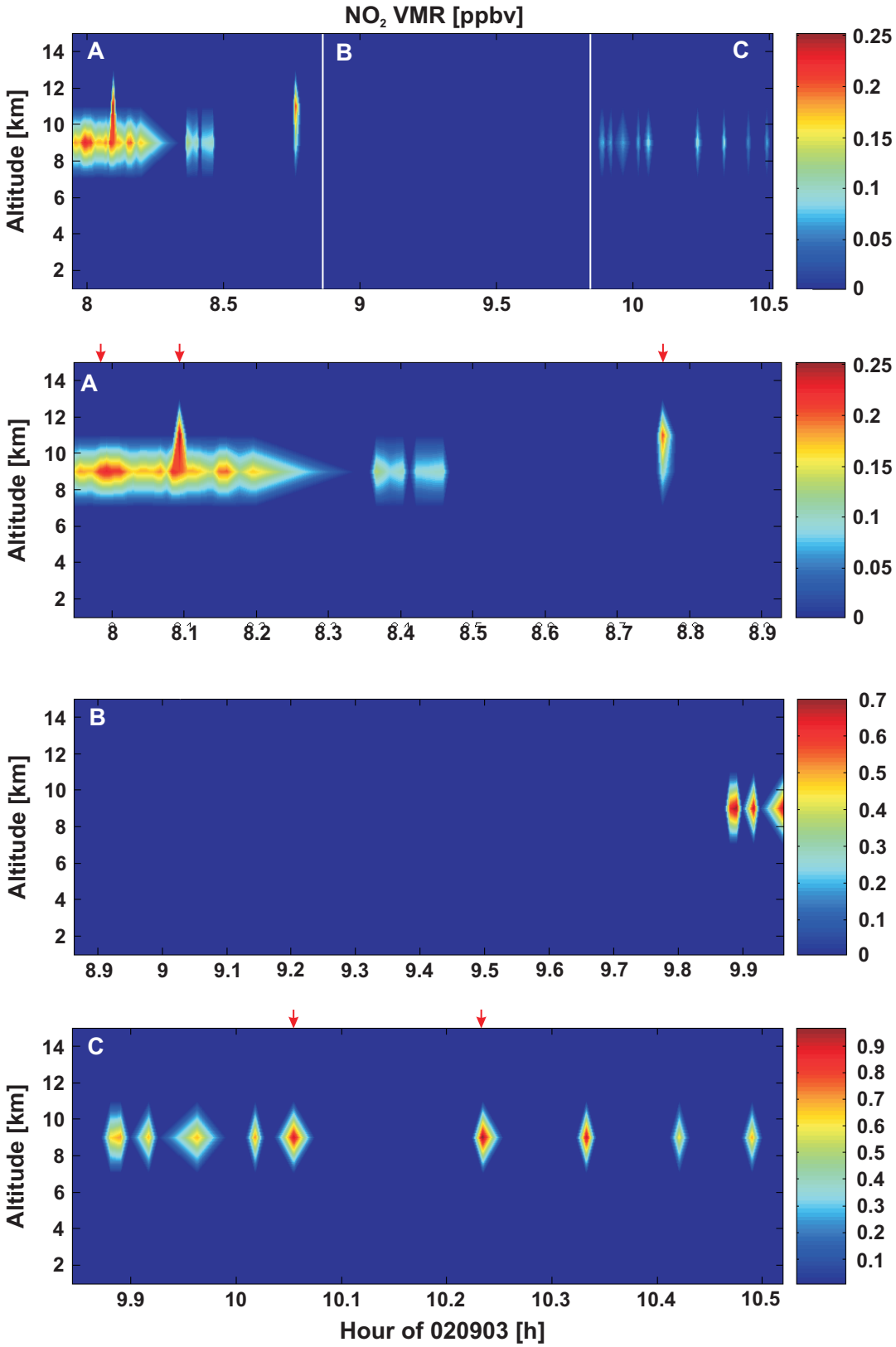

Figure 9.10: Contour plot of the retrieved profiles of flight 020903 showing data larger than the error bars meaning that after the error is subtracted from the data the value is still larger than zero. The time is given in UTC. The upper panel is an overview over the entire flight and the lower three panels (A, B, and C) are zoomed into the regions of further interest. The red arrows mark the profiles shown in Fig. 9.6.

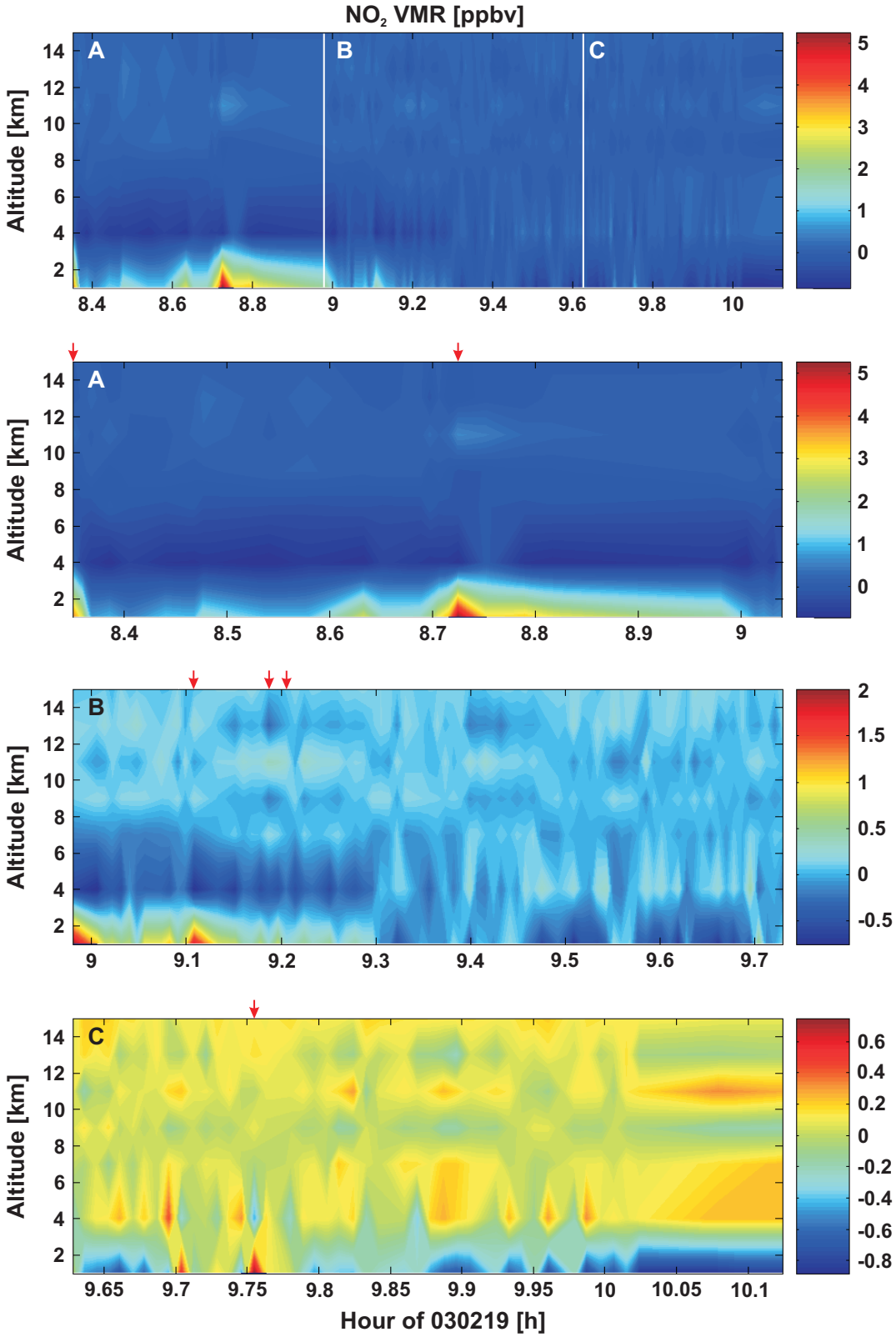

Figure 9.11: Contour plot of the retrieved profiles of flight 030219. The time is given in UTC. The upper panel is an overview over the entire flight and the lower three panels (A, B, and C) are zoomed into the regions of further interest. The red arrows mark the profiles shown in Fig. 9.7.

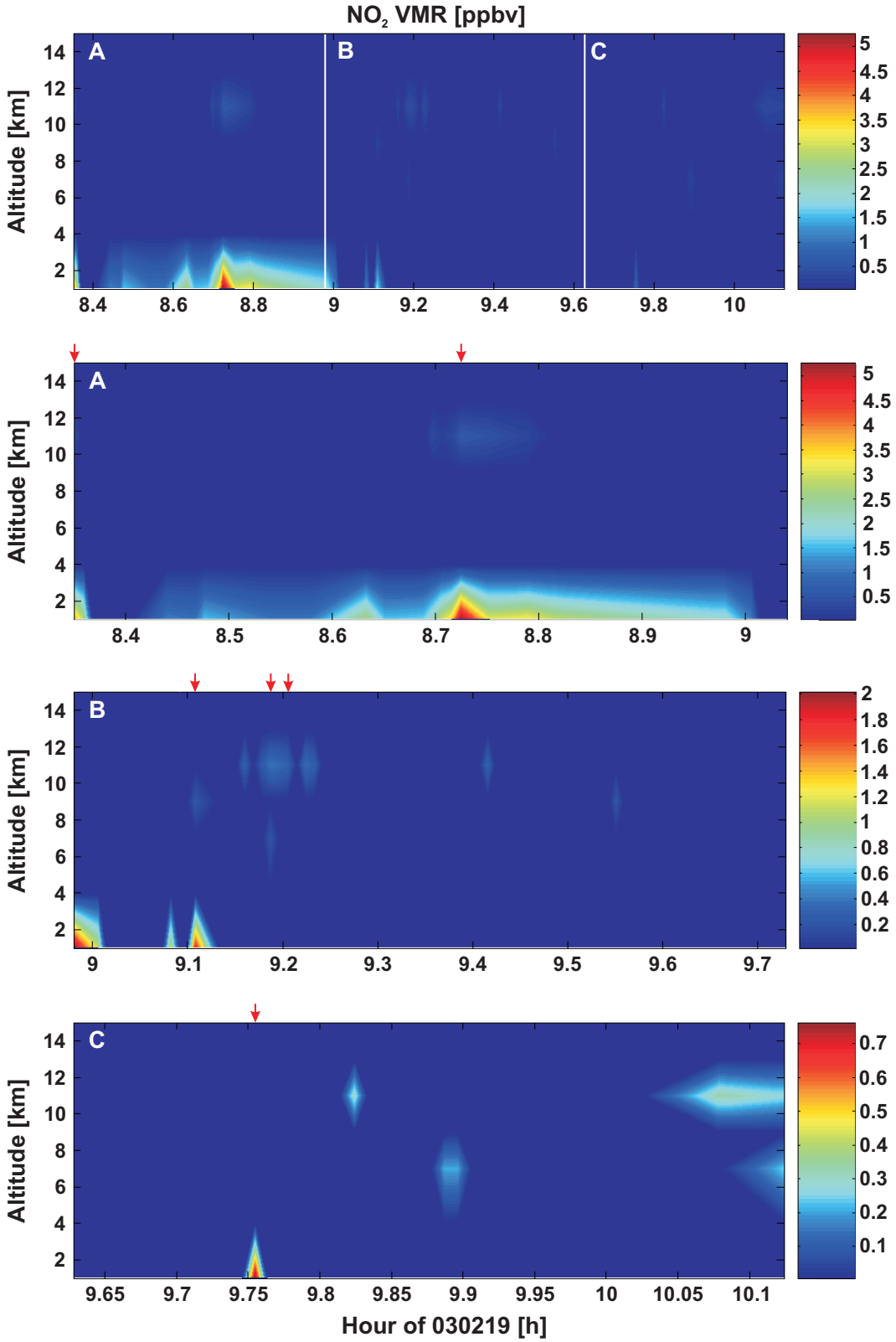

Figure 9.12: Contour plot of the retrieved profiles of flight 030219 showing data larger than the error bars meaning that after the error is subtracted from the data the value is still larger than zero. The time is given in UTC. The upper panel is an overview over the entire flight and the lower three panels (A, B, and C) are zoomed into the regions of further interest. The red arrows mark the profiles shown in Fig. 9.7.

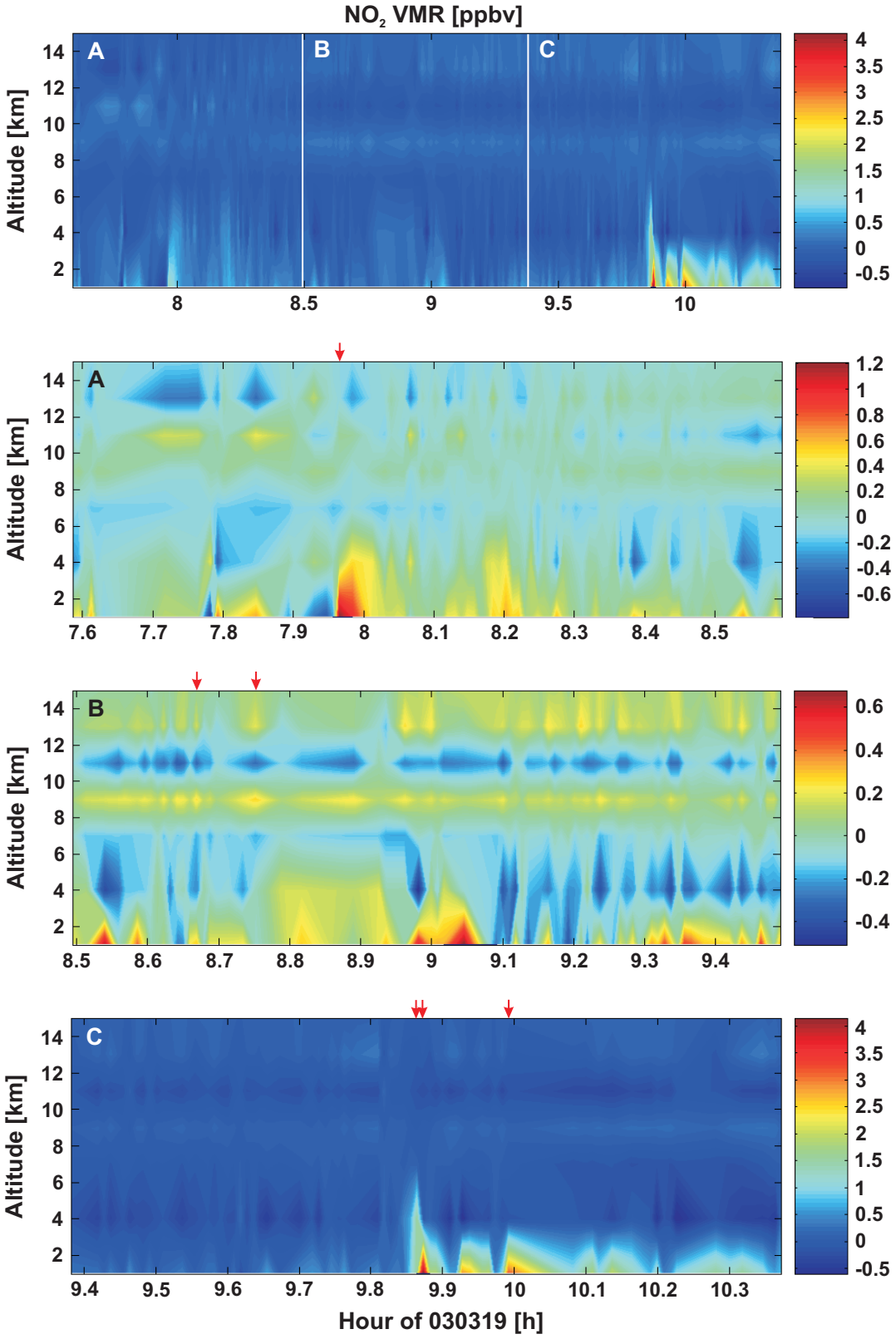

Figure 9.13: Contour plot of the retrieved profiles of flight 030319. The time is given in UTC. The upper panel is an overview over the entire flight and the lower three panels (A, B, and C) are zoomed into the regions of further interest. The red arrows mark the profiles shown in Fig. 9.8.

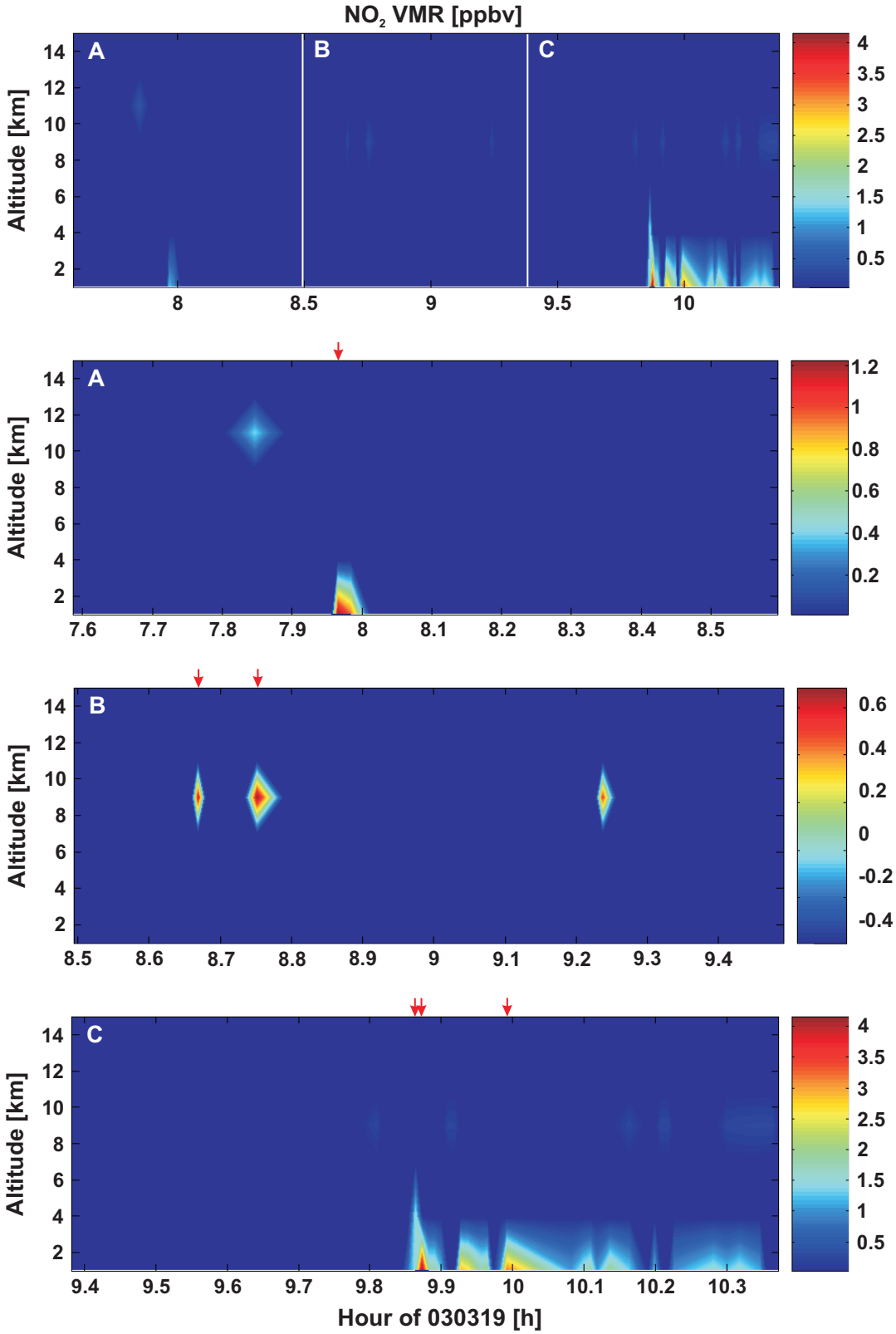

Figure 9.14: Contour plot of the retrieved profiles of flight 030319 showing data larger than the error bars meaning that after the error is subtracted from the data the value is still larger than zero. The time is given in UTC. The upper panel is an overview over the entire flight and the lower three panels (A, B, and C) are zoomed into the regions of further interest. The red arrows mark the profiles shown in Fig. 9.8.

Chapter 10

Interpretation and Discussion

In this chapter the interpretation of the retrieved profiles presented in the previous chapter will be discussed. The interpretation is based on literature that was already introduced in chapter 3 dealing with NO_2 chemistry, satellite images showing clouds, and maps. This chapter is divided into two main parts. The first part is dealing with tropospheric boundary layer pollution, which is caused by high NO_x emissions as can be seen later. The second topic is the emission of NO_x in the UTLS region caused by

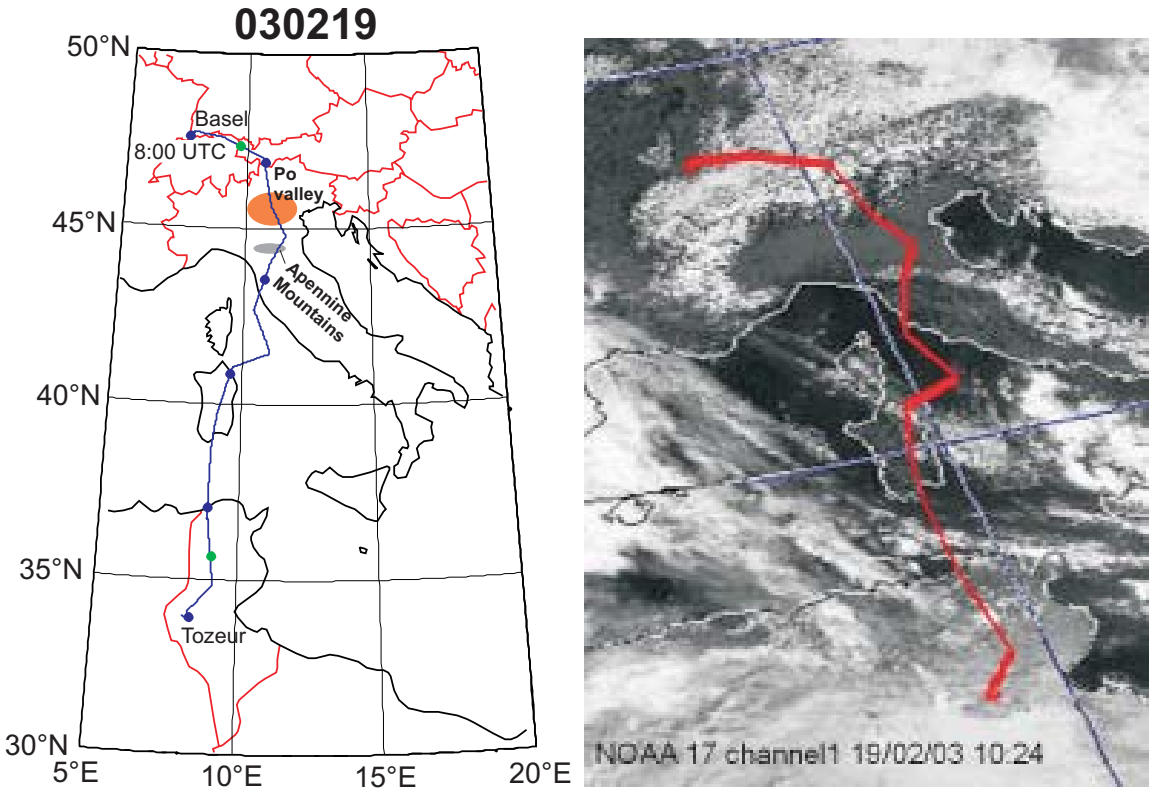

Figure 10.1: Flight track for Feb. 19, 2003 and NOAA satellite image of Feb. 19, 2003 at 10:24 UTC. The blue dots on the flight track mark full and half hours. The first blue dot near Basel marks 8:00 UTC the next marks 8:30 UTC and so on. The flight track between the green dots marks flight altitudes $\geq$ 10 km.

Figure 10.2: Geographical location of tropospheric NO_2 south of Lake Constance. The colored bars indicate the AMAXDOAS footprint of a measurement. The orange bar represents the measurement at 8.350 UTC (8:21:00 UTC) and the blue bar represents the next measurement at 8.359 UTC (8:21:32 UTC).

air traffic.

10.1 Tropospheric Boundary Layer Pollution

In this section two flights (030219 and 030319) will be presented because on these flights tropospheric boundary layer pollution could be detected.

10.1.1 Flight 030219

This flight started in Basel, Switzerland as already described in the previous chapter. Fig. 10.1 shows the flight track as well as a satellite image from the NOAA-17 satellite for the same day at 10:24 UTC that is 15 minutes before touch down (10:35 UTC) in Tozeur, Tunesia. It is hard to distinguish from the right plot of Fig. 10.1 if the first part of the flight was over clouds or snow cover. According to the logbook the Alps were covered with snow and no clouds were present. Some clouds were reported for the Po valley (area marked in orange in Fig. 10.1), but the ground was reported to be visible so that the clouds must be very small - too small for the pixel size of

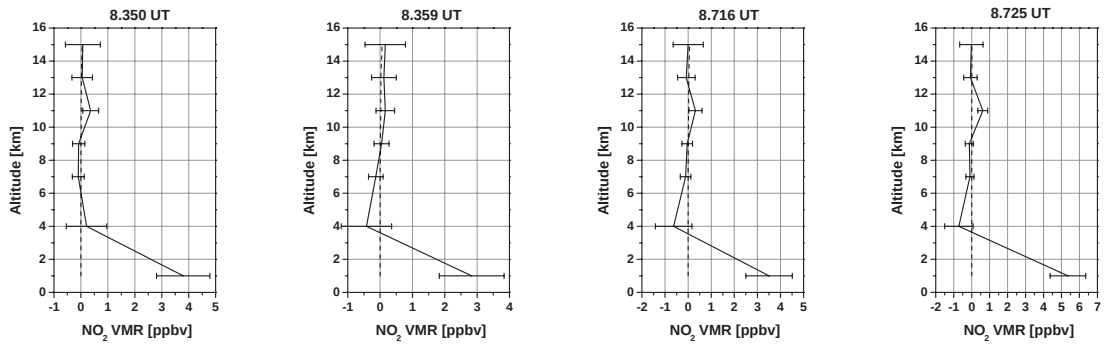

Figure 10.3: Retrieved profiles of the tropospheric NO_2 south of Lake Constance (8.350 UTC and 8.359 UTC) and near Verona, Italy (8.716 UTC and 8.725 UTC). Solid lines represent the retrieved profile and the dashed lines represent the a priori profile.

the detector of the NOAA-17 satellite, since there are no clouds visible in the satellite

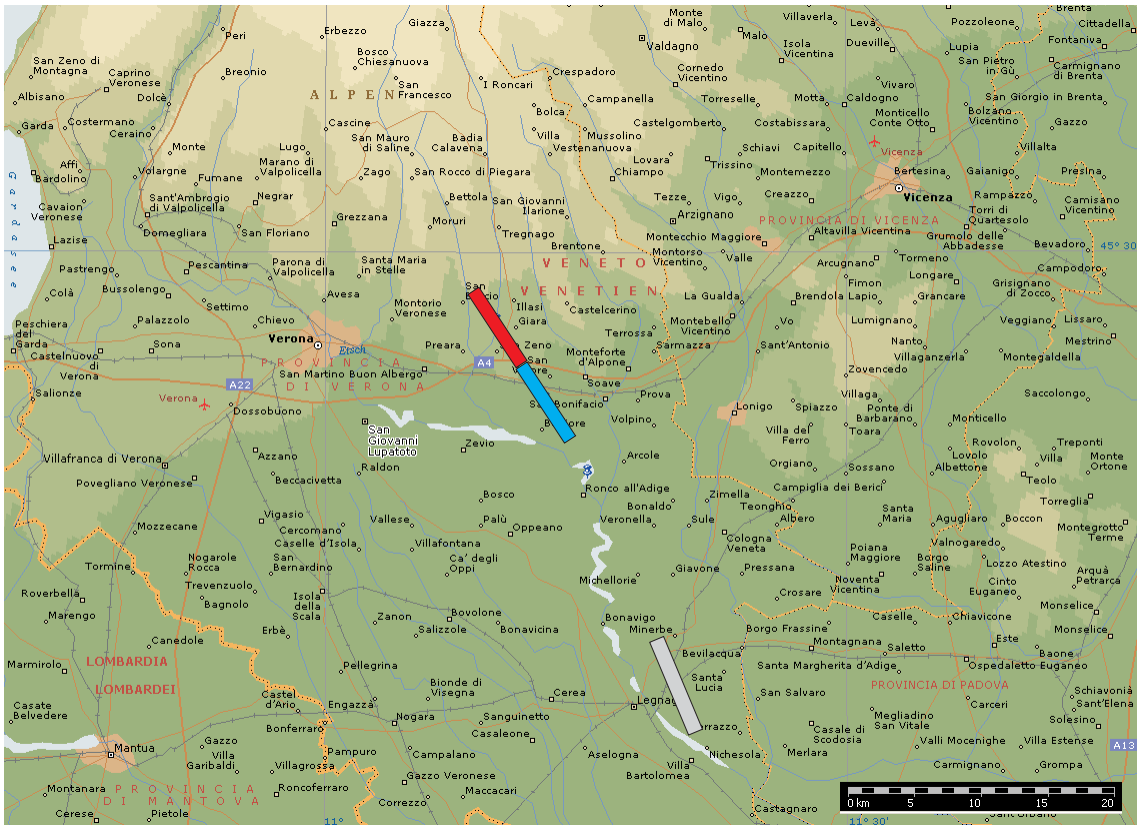

Figure 10.4: Geographical location of tropospheric NO_2 near Verona (Italy). The colored bars indicate the AMAXDOAS footprint of a measurement. The orange bar represents the measurement at 8.716 UTC (8:42:58 UTC), the blue bar represents the next measurement at 8.725 UTC (8:43:30 UTC), and the gray bar represents the measurement at 8.752 UTC (8:45:07 UTC).

Figure 10.5: Geographical location of tropospheric NO_2 near the island of Elba (Italy). The colored bars indicate the AMAXDOAS footprint of a measurement. The orange bar represents the measurement at 9.099 UTC (9:05:56 UTC) and the blue bar represents the next measurement at 9.108 UTC (9:06:29 UTC).

image over the Po valley. The aircraft was crossing the Apennine Mountains (area marked in gray in Fig. 10.1) which were snow covered according to the logbook. The clouds over northern Sardinia and the Mediterranean Sea south of Sardinia are not important, since no tropospheric NO_2 was observed in these areas.

Fig. 9.12 shows tropospheric NO_2 in four occasions. A comparison of the measured slant columns from the AMAXDOAS instrument and the SCIAMACHY instrument was done by Heue *et al.* [2004]. The first tropospheric NO_2 plume occurs at 8.350 UTC (8:21:00 UTC). The following events are at 8.725 UTC (8:43:30 UTC), 9.108 UTC (9:06:29 UTC), and 9.755 UTC (9:45:18 UTC). The first observation of tropospheric NO_2 is still north of the Alps and south of Lake Constance (see Fig. 10.2). The footprint of the first measurement (8.350 UTC) is covering part of the Rhine valley containing two major Highways - the Swiss N13 and the Austrian A14. The daily averaged volume of traffic on the Swiss Highway N13 is 23625 [ASTRA, 2003] vehicles for February 2003 on weekdays (Feb. 19, 2003 is a Wednesday). The time of crossing the Rhine valley and the Swiss highway N13 was 8:21:00 UTC (9:21:00 local time) shortly after the morning rush hour. Thus the NO_x of the morning rush hour accumulated in the valley. Fig. 10.3 shows the plots of the measurements at 8.350 UTC and 8.359 UTC. It can

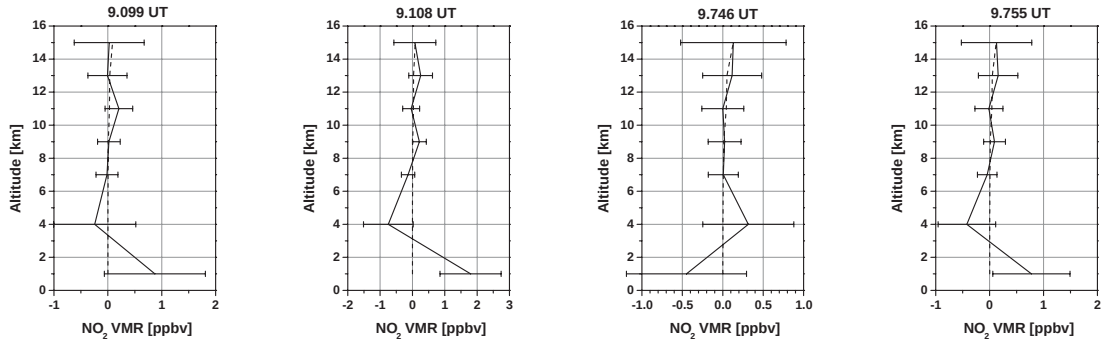

Figure 10.6: Retrieved profiles of the tropospheric NO_2 over the island of Elba (9.099 UTC and 9.108 UTC) and southern Sardinia (9.746 UTC and 9.755 UTC). Solid lines represent the retrieved profile and the dashed lines represent the a priori profile.

be seen that the maximum of the tropospheric NO_2 is at 8.350 UTC coinciding with crossing the Rhine valley and the Swiss highway N13.

The second observation of tropospheric NO_2 is just south of the Alps near the city of Verona (Italy, population: 252,000[1]) (see Fig. 10.4). It can be seen that in this incident the footprints of the two measurements shown in this figure are again very close to the Italian highway A4. It was not possible to find any statistical data on traffic for highway A4. The next valid measurement due to the selection process of the results described in the previous chapter is at 8.752 UTC (8:45:07 UTC). This measurement indicates 3.1 ppbv of NO_2 at the lowest level compared to 5.4 ppbv of NO_2 at the same level at 8.725 UTC (8.43:30 UTC). Fig. 10.3 shows the retrieved profiles for the measurements at 8.716 UTC and 8.725 UTC.

The third incident of tropospheric NO_2 was observed over the coast of the island of Elba (see Fig. 10.5). The retrieved profiles for the footprints shown in this plot can be found in Fig. 10.6. These plots show no tropospheric NO_2 for the orange colored footprint and 1.8 ppbv NO_2 in lowest level for the blue footprint. The island Elba is a major destination of tourists even though the island is a national park. This could explain the increased tropospheric NO_2 value. The largest settlement on the island is Portoferraio on the north shore of the island which is the main port for ferry traffic to the mainland (Piombino). The footprint of the measurement containing the enhanced tropospheric NO_2 is not crossing the major ferry route.

A fourth observation of tropospheric NO_2 was made over southern Sardinia (see Fig. 10.7). The retrieved profiles for the footprints shown in this plot can be found in Fig. 10.6 as well. These plots show no tropospheric NO_2 for the orange footprint and only a slightly enhanced value of tropospheric NO_2 for the blue footprint of 0.8 ppbv, which is only 0.1 ppbv above the detection limit defined by the total retrieval error of 0.7 ppbv for this measurement. The only possible source in the map is the city of Cagliari with a population of 180,000[2]. The footprint of the measurement with the

[1]source: http://www.aberhallo.de/lexikon/index.php/Hauptseite
[2]source: http://www.aberhallo.de/lexikon/index.php/Hauptseite

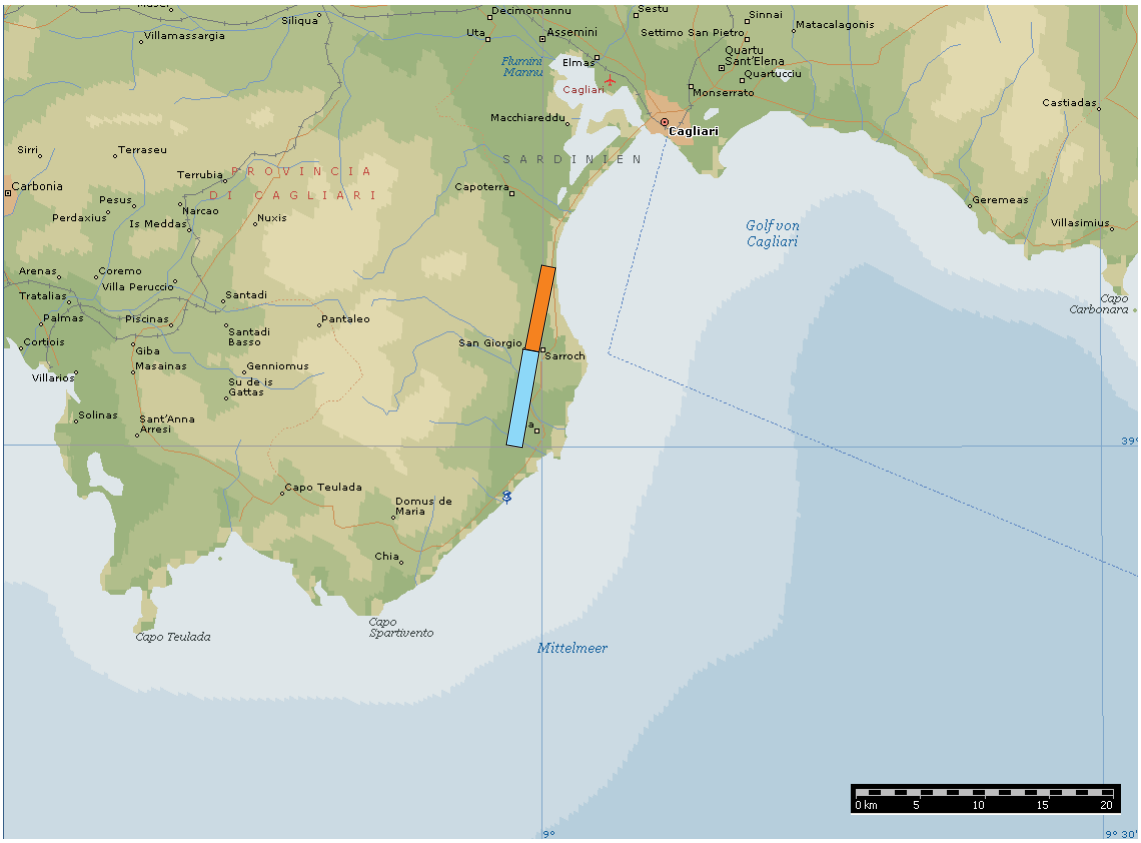

Figure 10.7: Geographical location of tropospheric NO_2 over southern Sardinia (Italy). The colored bars indicate the AMAXDOAS footprint of a measurement. The orange bar represents the measurement at 9.746 UTC (9:44:46 UTC) and the blue bar represents the next measurement at 9.755 UTC (9:45:18 UTC).

slightly enhanced tropospheric NO_2 is only 20 km south east of Cagliari.

10.1.2 Flight 030319

This flight started in Oberpfaffenhofen near Munich as a round trip, and it is a substitute for a SCIAMACHY validation flight on March 17, 2003 due to a malfunction of ENVISAT on that day. Fig. 10.8 shows the flight track as well as a satellite image from the Meteosat satellite for the same day at 10:00 UTC, which is a little bit over an hour before touchdown at 11:02 UTC in Oberpfaffenhofen. It should be noted that the first and the last part of the flight were over cloudless regions.

Fig. 9.14 presents tropospheric NO_2 in four occasions. The first tropospheric NO_2 plume is observed at 7.966 UTC (7:57:58 UTC). Fig.10.9 sketches the geographic area where the tropospheric NO_2 was observed. The retrieved profiles associated with the footprints of Fig. 10.9 can be seen in Fig. 10.10. These plots show the maximum of the tropospheric NO_2 in the second (blue) footprint of Fig. 10.9. A tropospheric NO_2 value of 1.2 ppbv NO_2 was observed 10 km to the north-east of the town Wernigerode

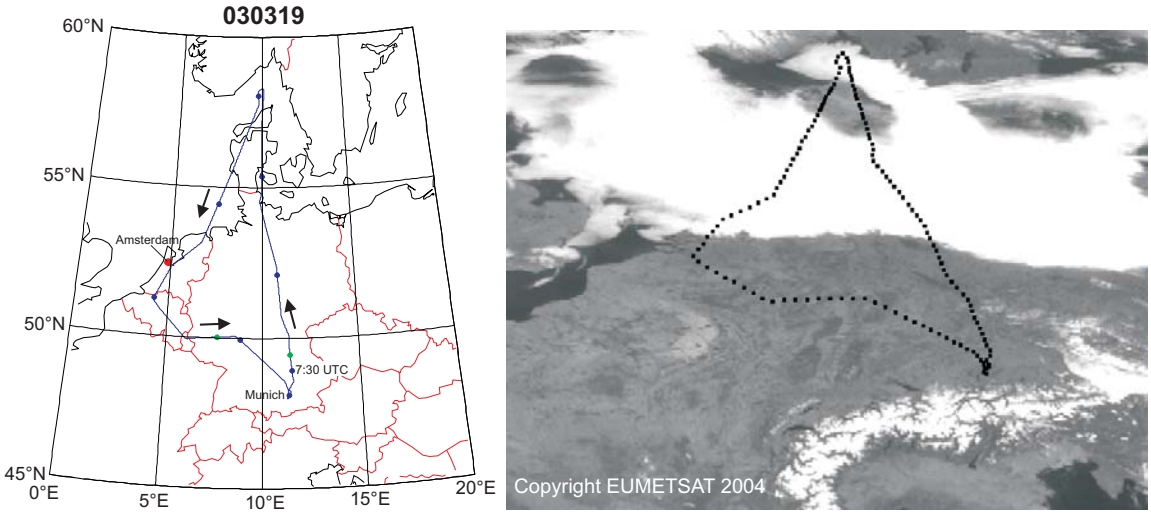

Figure 10.8: Flight track for Mar. 19, 2003 and METEOSAT satellite image of Mar. 19, 2003 10:00UTC. The blue dots on the flight track mark full and half hours. The first blue dot marks 7:30 UTC the next marks 8:00 UTC and so on. The flight track between the green dots marks flight altitudes $\geq$ 10 km.

with a population of 35,000[3]. Although 1.2 ppbv of tropospheric NO_2 is not very high compared to other NO_2 values observed in the troposphere with AMAXDOAS, the map shown in Fig 10.9 does not indicate another plausible source of the tropospheric NO_x. In this case the only explanation is transport of tropospheric NO_2. To investigate the origin of the tropospheric NO_2 tropospheric trajectory models have to be used, but it is doubted that such small scale events as seen at 7.966 UTC can be reproduced correctly.

According to the logbook of this flight the edge of the cloud cover was crossed at 7:57 UTC. Fig. 10.11 demonstrates the cloud cover at 8:00 UTC recorded by the Meteosat 7 satellite. The left plot shows the actual satellite image of the area with the position of the aircraft being right on the edge of the cloud cover at 7.966 UTC when the tropospheric NO_2 was observed in the retrieved profile. To get a closer look on the situation the pixel intensity was plotted against time in the right plot. The observed edge of the cloud cover from the aircraft was marked as vertical line in the right plot. It should be noted that it is hard to tell for the operator[4] onboard the aircraft when the aircraft is directly over the cloud edge. Fig. 10.11 leads to the conclusion that the operator was a little overhasty in the observation of crossing the edge of the cloud cover. The pixel intensities represent the crossing of the cloud cover edge more objectively because the measurement at 7.966 UTC (red circle) is situated on a pixel not being totally cloudless but as well not totally cloud covered. It is an important issue whether the measurement was done over a clouded or cloudless surface due to the fact that APROVAL does not account for clouds and the retrieval of NO_2 over a clouded surface is not working properly due to multiple scattering and reflected photons. Thus the NO_2 will be overestimated.

[3]source: http://www.aberhallo.de/lexikon/index.php/Hauptseite

[4]It should be noted that the operator of flight 030319 and the author are the same person

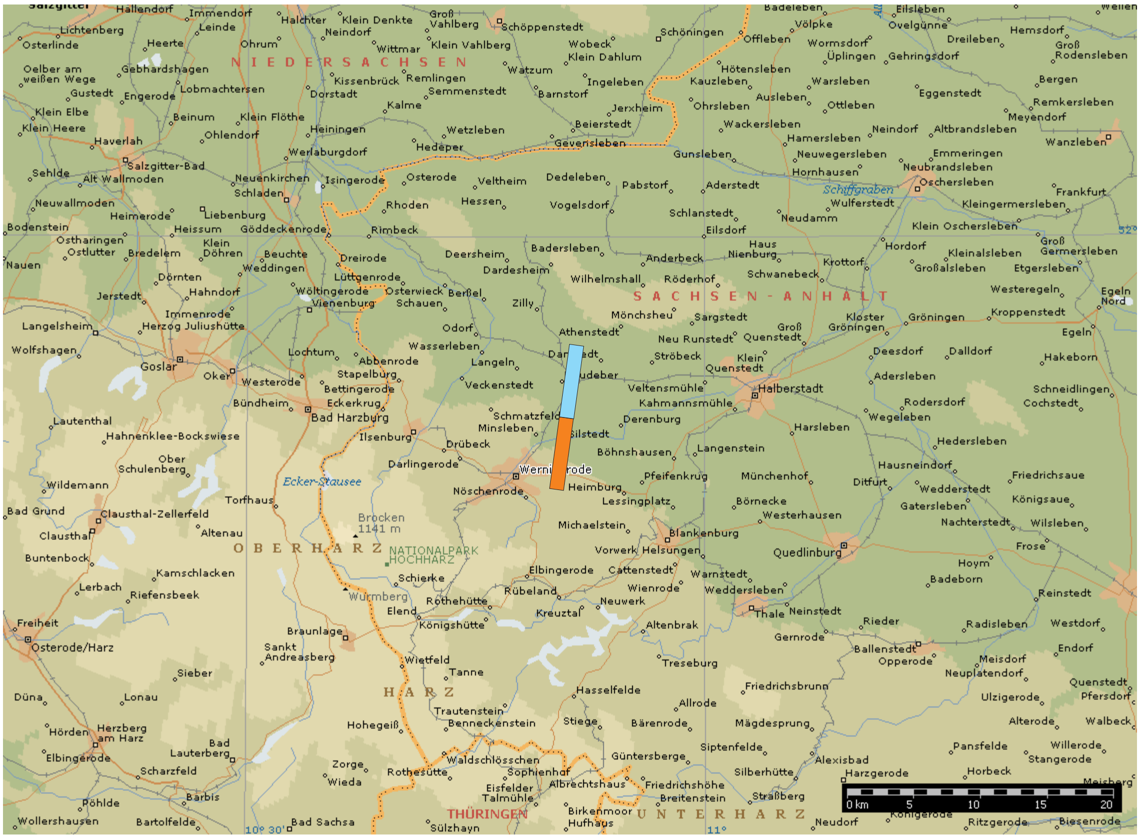

Figure 10.9: Geographical location of tropospheric NO_2 over central Germany. The colored bars indicate the AMAXDOAS footprint of a measurement. The orange bar represents the measurement at 7.957 UTC (7:57:25 UTC) and the blue bar represents the next measurement at 7.966 UTC (7:57:58 UTC).

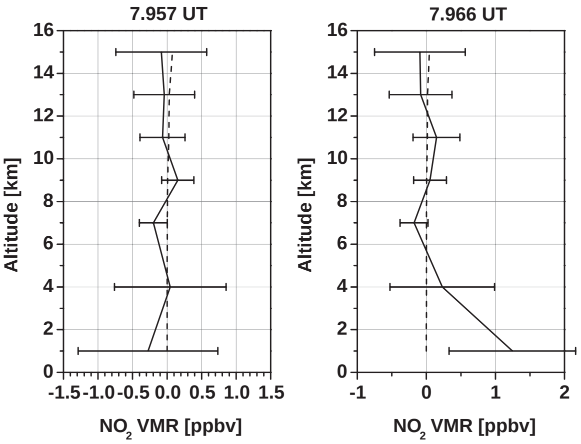

Figure 10.10: Retrieved profiles of the tropospheric NO_2 in central Germany (7.957 UTC and 7.966 UTC). Solid lines represent the retrieved profile and the dashed lines represent the a priori profile.

The second tropospheric NO_2 event on March 19, 2003 was observed at 9.873 UTC. Fig. 10.12 shows the geographic location of that event. This NO_2 plume was observed 20 km south of the large city of Amsterdam (population: 720,000 [city], 1,100,000 [metropolitan area][5]) and 10 km north-west of the city of Utrecht (population: 260,000[6]). The footprint of the measurement taken at 9.864 UTC also crossed the highway A2 connecting the cities of Amsterdam and Utrecht. Fig. 10.13 shows the data of the radiosonde sounding in DeBilt (5 km east of Utrecht and 20 km east of the observed NO_2 plume. According to the data in these plots the wind at the surface comes from northerly directions.
Unfortunately Fig. 10.14 shows that these measurements were done over clouded areas. This was also reported by [Wang *et al.*, 2004]. APROVAL cannot deal with cloudy situations because the version of the radiative transfer model SCIATRAN used in the retrieval algorithm does not support the calculation of weighting functions for cloudy situations. In a sensitivity study (not shown) clouds are approximated simply by a surface albedo of 0.9, but the result is rather poor. Here the profile retrieval of the data at 9.864 UTC and 9.873 UTC is not working due to an dramatic overestimation of tropospheric NO_2 in the lowest two levels and an underestimation of the stratospheric NO_2. This leads to the conclusion that the retrieved profiles at 9.864 UTC and 9.873 UTC have to be considered with care regarding the quantity of tropospheric NO_2.
The third tropospheric NO_2 plume is observed at 9.928 UTC (9:55:41 UTC). Fig. 10.15 illistrates the geographic location of the NO_2 plume and Fig. 10.16 shows the retrieved profiles associated with the footprints of Fig. 10.15. This plume is situated 20 to 50 km south of the city of Rotterdam (population: 530,000[7]). The last three footprints are

[5]source: http://www.aberhallo.de/lexikon/index.php/Hauptseite
[6]source: http://www.aberhallo.de/lexikon/index.php/Hauptseite
[7]source: http://www.aberhallo.de/lexikon/index.php/Hauptseite

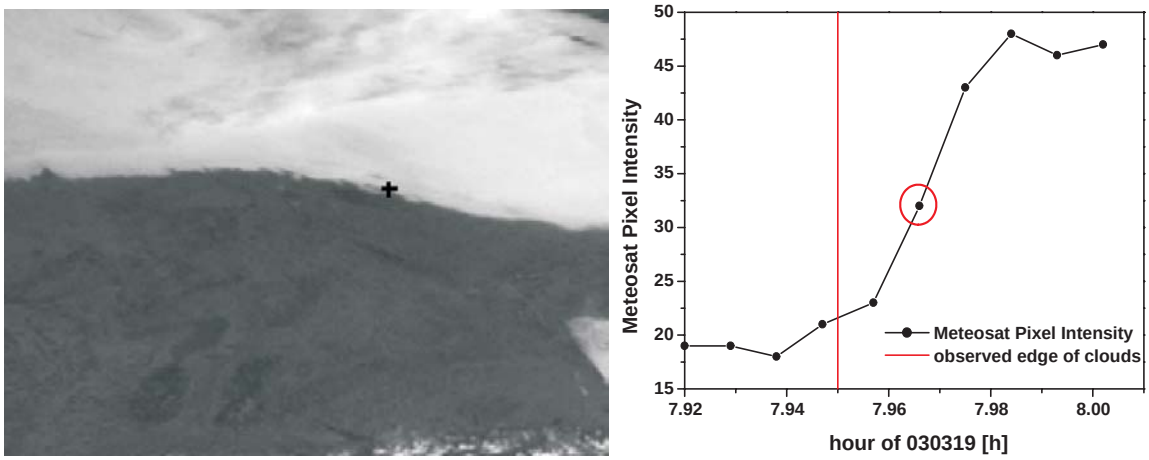

Figure 10.11: Cloud cover at 7.966 UTC on Mar. 19, 2003. The right plot shows the position (cross) of the aircraft at 7.966 UTC on the 8:00 UTC Meteosat image. The left plot shows the observed edge of the cloud cover from the aircraft in comparison to the pixel intensities of the pixels crossed by the aircraft from 7.920 UTC to 8.002 UTC. The red circle marks the time the tropospheric NO_2 was observed.

Figure 10.12: Geographical location of tropospheric NO_2 near Amsterdam (The Netherlands). The colored bars indicate the AMAXDOAS footprint of a measurement. The orange bar represents the measurement at 9.864 UTC (9:51:50 UTC) and the blue bar represents the next measurement at 9.873 UTC (9:52:23 UTC).

right on top of the highway A58. Since the distance from Utrecht to Rotterdam is only 50 km, the wind data from the radiosonde can be used to interpret the measurements south of Rotterdam as well. The first two footprints are exactly downwind of the city of the Rotterdam (see Fig. 10.13) considering a wind direction of 340° to 0°. It has to be noted that the measurement of 9.946 UTC is not included in the data shown in Fig. 9.13 and Fig. 9.14 due to the fact that the retrieved profile at 9.946 UTC has a large negative value at 11 km altitude. As described in chapter 9 'Profile Retrieval using real AMAXDOAS data' profiles with negative values having an absolute value larger than the corresponding error are not considered. In this case the retrieved profile is plotted due to the fact that the negative value is at 11 km altitude and therefore far away from the value of interest (tropospheric value at 1 km altitude). But still this profile has to be considered with care. The reason this profile is included in this series of measurements is to demonstrate that the spatial distribution of the plume observed between 9.928 UTC and 9.964 UTC is quite large.

The last large tropospheric NO_2 event is observed at 9.992 UTC (9:58:31 UTC). Fig. 10.17 shows the retrieved profiles of the measurements taken at 9.983 and 9.992 UTC and Fig. 10.18 shows the geographic location of the NO_2 plume. It is located

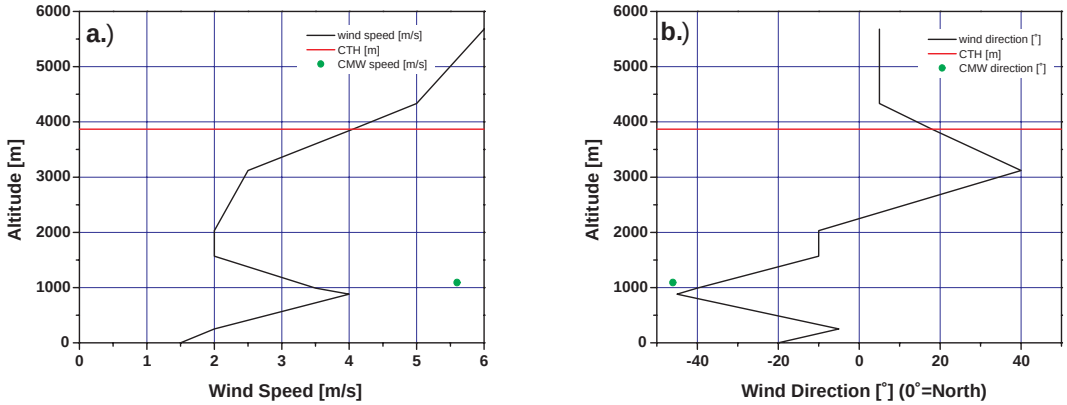

Figure 10.13: Radiosonde data from DeBilt near Amsterdam for Mar. 19, 2003, 12UTC. The radiosonde data are compared to Meteosat data of the cloud motion wind analysis (CMW) and the cloud analysis (CA). Plot a shows the wind speed and plot b shows the wind direction. The solid red line represents the cloud top hight from the CA.

10 km to the north-west of the city of Antwerp (population: 476,000[8]). The retrieved profile of the first footprint specifies a tropospheric NO_2 value of 1 ppbv and the retrieved profile of the second footprint states a tropospheric NO_2 value of 3.2 ppbv. The first footprint is situated directly across highway A12 connecting Antwerp and Rotterdam. The second footprint is right beside another highway (R2) which acts as

[8]source: http://www.aberhallo.de/lexikon/index.php/Hauptseite

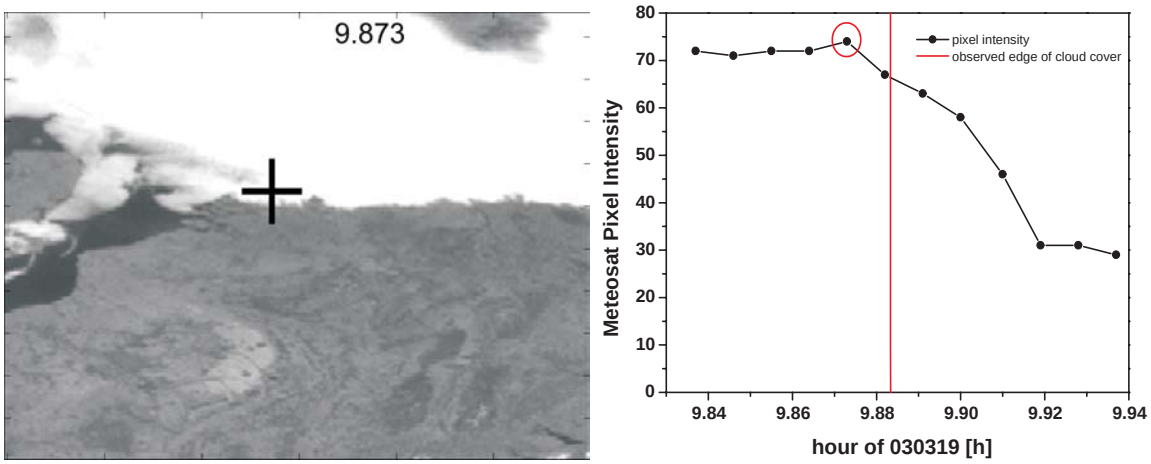

Figure 10.14: Cloud cover at 9.873 UTC on Mar. 19, 2003. The right plot shows the position (cross) of the aircraft at 9.873 UTC on the 10:00 UTC Meteosat image. The left plot shows the observed edge of the cloud cover from the aircraft in comparison to the pixel intensities of the pixels crossed by the aircraft from 9.837 UTC to 9.937 UTC. The red circle marks the time the tropospheric NO_2 was observed.

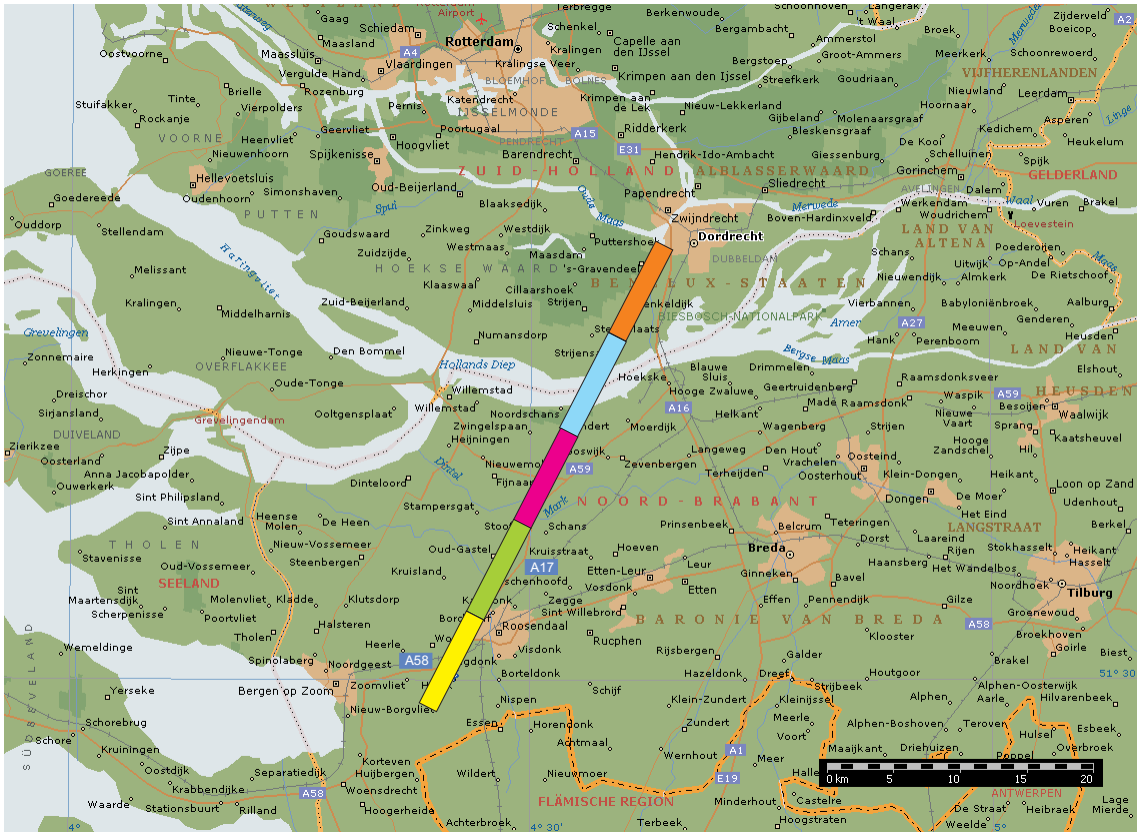

Figure 10.15: Geographical location of tropospheric NO_2 south of Rotterdam (The Netherlands). The colored bars indicate the AMAXDOAS footprint of a measurement. The orange bar represents the measurement at 9.928 UTC (9:55:41 UTC), the blue bar represents the next measurement at 9.937 UTC (9:56:13 UTC), the purple bar represents the measurement after that at 9.946 UTC (9:56:46 UTC), the green bar represents the next measurement at 9.955 UTC (9:57:18 UTC), and the yellow bar represents the following measurement at 9.964 UTC (9:57:50 UTC).

periphery of Antwerp. The distance between the footprint of the 9.992 UTC measurement and DeBilt (the location of the radiosonde launch station) is only 100 km. Due to this small distance - considering the density of radiosonde launch sites - the radiosonde data can be applied for the interpretation of this last NO_2 plume as well. The wind direction according to Fig. 10.13 is 340° to 0°. In this case the highway R2 is located downwind regarding the position of the 9.992 UTC measurement. But there is another highway A58 going from east to west about 12 km in upwind direction.

Unfortunately the next measurement at 10.002 UTC is useless due to the fact that APROVAL was not working properly because of a roll value of over 20° of the aircraft during that measurement. This profile shows a very high tropospheric NO_2 value at 1 km altitude and a large overshooting at the 4 km level casting doubt on this profile.

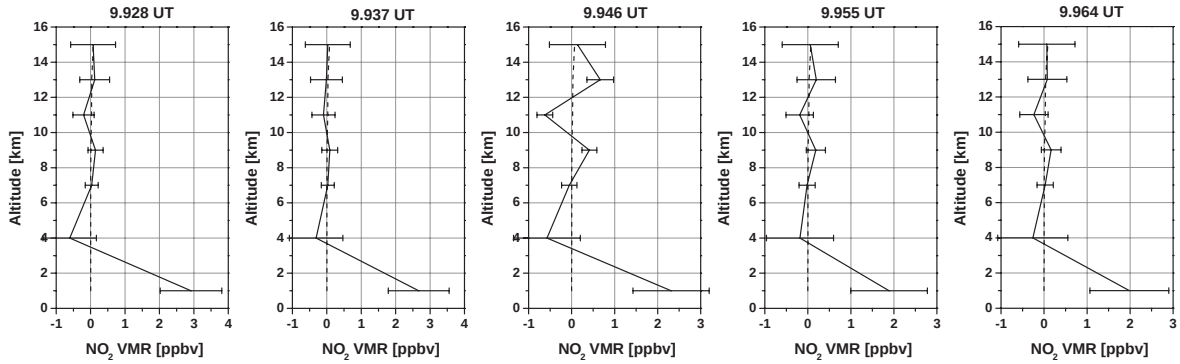

Figure 10.16: Retrieved profiles of the tropospheric NO_2 south of Rotter (The Netherlands) (9.928 UTC to 9.964 UTC). Solid lines represent the retrieved profile and the dashed lines represent the a priori profile.

10.2 Aircraft Emissions

In this section three flights (030219, 020903, and 030319) will be presented because on these flights NO_2 in the UTLS region could be observed. The discussion of the flights will not be in chronological order because the interpretation of flight 020903 uses arguments of the discussion of flight 030219.

10.2.1 Flight 030219

Fig. 9.12 shows some signals in 11 km altitude. The altitude range from 5 to 15 km is referred to as the Upper Troposphere/Lower Stratosphere (UTLS). Enhanced NO_2 values in this region can be interpreted as NO_2 from air traffic. In the following these NO_2 values will be compared to measurements of known aircraft sources. The problem with accidental measurements of air traffic NO_2 is the lack of information about the

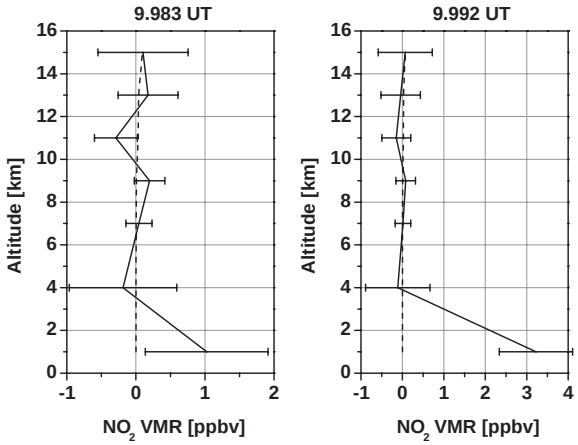

Figure 10.17: Retrieved profiles of the tropospheric NO_2 near Antwerp (Belgium) (9.983 UTC and 9.992 UTC). Solid lines represent the retrieved profile and the dashed lines represent the a priori profile.

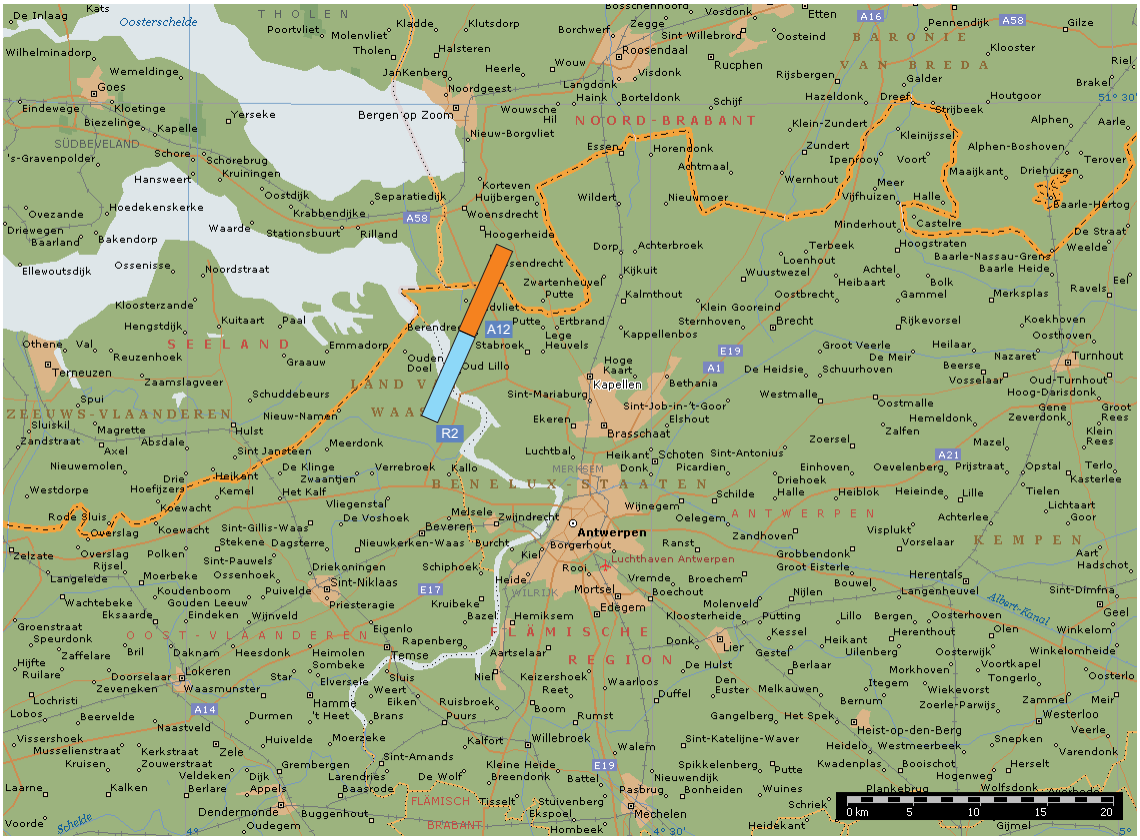

Figure 10.18: Geographical location of tropospheric NO_2 near Antwerpen (Belgium). The colored bars indicate the AMAXDOAS footprint of a measurement. The orange bar represents the measurement at 9.983 UTC (9:58:59 UTC) and the blue bar represents the next measurement at 9.992 UTC (9:59:31 UTC).

flight pattern of the measuring aircraft relative to the measured aircraft. In chapter 3 about the NO_2 chemistry the measurements of known aircraft sources were already introduced. Arnold *et al.* used the meteorological research aircraft FALCON of the German Aerospace Center (DLR) to trail a commercial airliner DC-9 in about 2 km distance at 9.4 km altitude. Considering the velocity of the aircrafts this distance translates to 9 seconds difference in time. In other words they measured 150 ppbv of NO_2 9 seconds after emission.

Fahey *et al.* used the NASA's high flying research aircraft ER-2. They flew loops in the same altitude to encounter the ER-2's own exhaust plume about 10 minutes after emission. They measured 0.8 ppbv NO_2 above the background value.

Schumann *et al.* used the FALCON research aircraft as well to measure exhaust plumes of different commercial airliners. The correlation of plume and aircraft was done by using the video records from the air traffic control radar display of the flight control station at Prestwick. Unfortunately the plume ages do not exceed 100 minutes. Fig. 10.19 shows the NO measurements of plumes of different ages. The NO_2 was converted using NO/NO_x ratios calculated from NO and NO_x measurements presented in [Ziereis

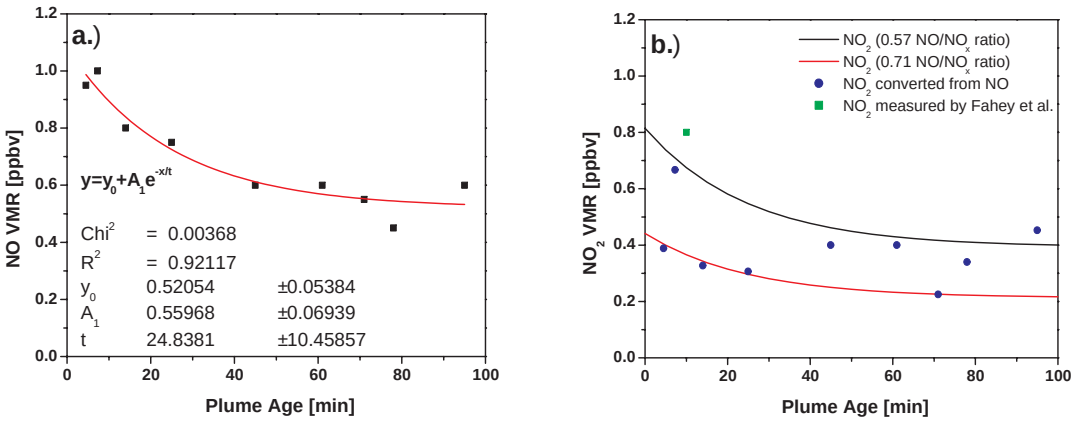

Figure 10.19: VMR of NO (a) and NO_2 (b) in plumes of different ages [Schumann *et al.*, 1995]. The NO_2 VMR was calculated using the NO/NO_x ratios of [Ziereis *et al.*, 2000] for different altitudes. The solid lines represent the exponential decay for NO_2 calculated with the maximum and minimum values of the NO/NO_x ratios in altitudes between 9.4 and 11.2 km.

et al., 2000]. According to these NO measurements[9] the first order exponential decay that was fitted to the data shows an offset of 0.52 ppbv. Even though only the excess NO (NO above the background value) was plotted in Fig. 10.19 the excess NO would always be 0.52 ppbv and would not decrease to 0. This is curious because only the excess NO_2 caused by aircrafts was plotted. The learning from this series of measurements is that considering only plume ages below 100 minutes is insufficient to draw conclusions for plumes being a couple of hours old. For the converted NO_2 values a range is given because according to [Ziereis *et al.*, 2000] the NO/NO_x ratios vary at different altitudes. The value measured by [Fahey *et al.*, 1995] is fitting into the results represented by [Ziereis *et al.*, 2000] even though the value by Fahey *et al.* is exceeding the maximum (black line of Fig. 10.19b) of [Schumann *et al.*, 1995].
What kind of conclusions can be drawn from the measurements presented above considering the NO_2 values observed in 11 km in retrieved profiles from this work? The first conclusion is the AMAXDOAS instrument was not following another aircraft directly, since the NO_2 values in all incidents are much too small compared to the measurements presented in [Arnold *et al.*, 1992]. Fig 10.20 shows the incidents of enhanced NO_2 in 11 km altitude as they were observed in Fig. 9.12. The incidents at 8.350 UTC, 8.725 UTC, 8.752 UTC, 9.160 UTC, and 9.205 UTC can be interpreted as enhanced NO_2 due to air traffic, since all incidents occurred between the Alps and 150 km northwest of Rome. The air traffic in this area is very dense considering the fuel consumption of aircraft over Europe (see Appendix A). Whereas the incidences at 9.108 UTC, 9.187 UTC, and 9.824 UTC are questionable due to the problem of occurring oscillations in the retrieved profiles described in the previous chapter. Therefore the last three incidents will not be considered as air traffic NO_2 observations. From the remaining three

[9]Note: one NO value of 2.4 ppbv was omitted due to the fact that it exceeded the adjacent values by almost 1.5 ppbv. Thus it is considered to be a maverick.

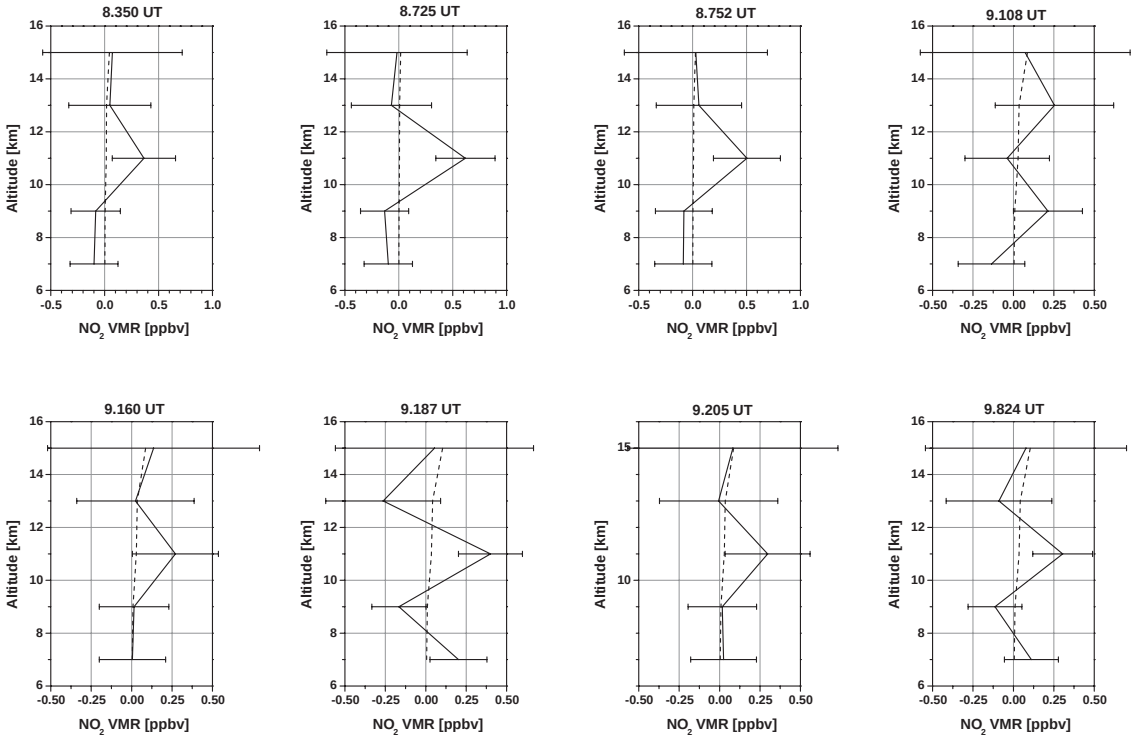

Figure 10.20: Examples of retrieved profiles with air traffic NO_2 in 11 km altitude on Feb. 19, 2003. Solid lines represent the retrieved profile and the dashed lines represent the a priori profile.

incidents considered as air traffic NO_2: Two incidents show a strong signal which is significantly above the detection limit (8.725 UTC and 8.752 UTC), and one is showing a good signal above the detection limit (8.350 UTC).
Comparing the retrieved NO_2 values in 11 km altitude at 8.725 UTC (0.6 ppbv) and 8.752 UTC (0.5 ppbv) to the results presented in [Fahey *et al.*, 1995; Schumann *et al.*, 1995] it is evident that plumes containing such air traffic NO_2 values two of these incidents are at least 20 to 30 minutes old (see Fig. 10.19). The third incident at 8.350 UTC is observed 0.4 ppbv NO_2 in 11 km altitude. According to Fig. 10.19 a plume containing this amount of NO_2 can be between five and 100 minutes old. So for this amount of air traffic NO_2 Fig. 10.19 is not very useful due to the large uncertainty in the NO/NO_x ratio. In case the altitude the NO_2 is observed in (11 km) is considered the NO/NO_x is fixed to 0.71 according to [Ziereis *et al.*, 2000]. This proposes the use of the NO_2 decay marked by the red curve in Fig. 10.19 and results in a plume age of smaller than ten minutes. The task of determining the age of the plumes observed by AMAXDOAS measurements is a difficult one and is not solved to total satisfaction. But, what the measurements of [Fahey *et al.*, 1995; Schumann *et al.*, 1995] are telling is that the amounts of NO_2 observed in 11 km altitude by the AMAXDOAS instrument are definitely in the range of NO_2 amounts contained in plumes emitted by aircraft less than 100 minutes ago.
The interpretation of the NO_2 values in this altitude range is facing another problem.

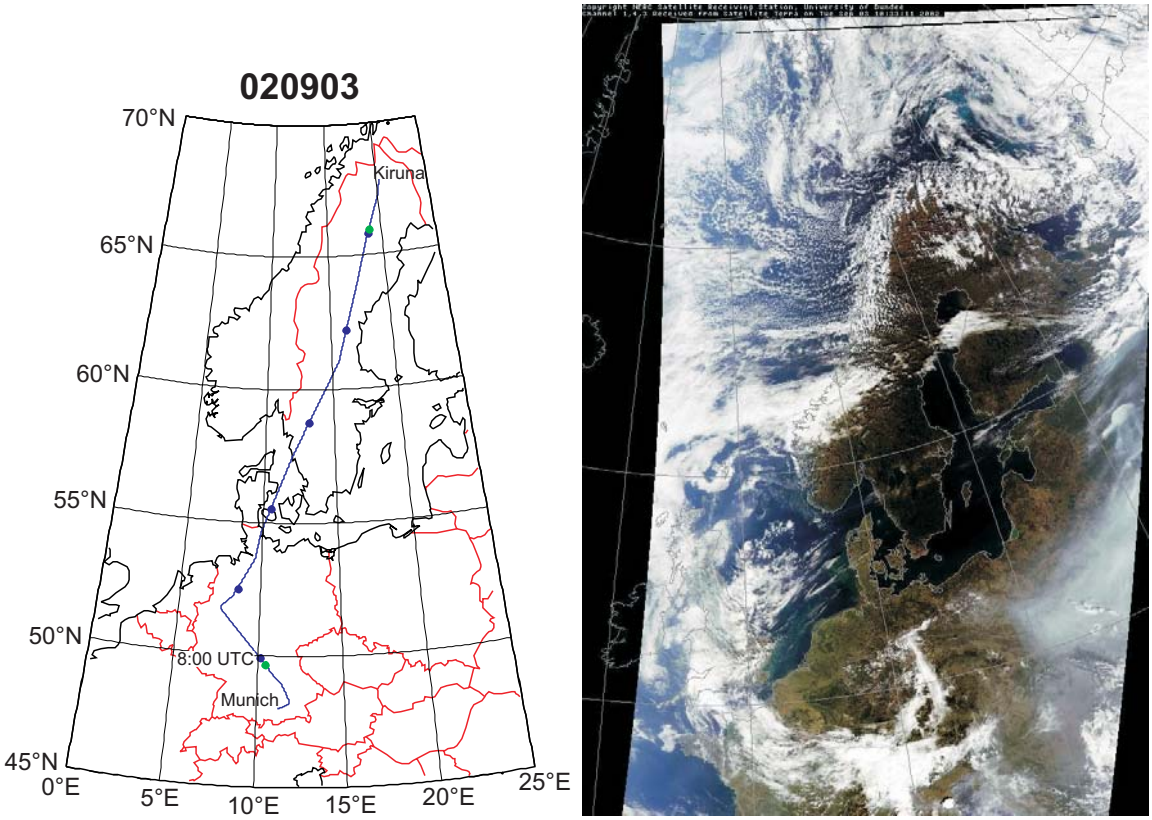

Figure 10.21: Flight track for Sep. 3, 2002 and MODIS satellite image of Sep. 3, 2002 10:33UTC. The blue dots on the flight track mark full and half hours. The first blue dot near Munich marks 8:00 UTC the next marks 8:30 UTC and so on. The flight track between the green dots marks flight altitudes $\geq$ 10 km.

It has to be kept in mind that the times it takes to complete one single AMAXDOAS measurement is 30 sec. During this period of time the FALCON travels 6 km. For the observed NO_2 values one has to assume that the NO_2 is uniformly distributed over 6 km. But this might not be the case, as we have seen in the plume dimensions observed by Fahey *et al.* [1995]. A narrower plume would lead to an underestimation of the NO_2 VMR by the AMAXDOAS instrument due to averaging over a larger area. So the conclusion of this paragraph is that the observed NO_2 values are a lower limit of the actual NO_2 values at best due to the missing information regarding dimension and geometry of the flight pattern in relation to the observed plume.

10.2.2 Flight 020903

This flight started near Munich as already mentioned in the previous chapter. Fig. 10.21 shows the flight track as well as a satellite image from the MODIS satellite for the same day at 10:33 UTC, which is almost exactly the same time the aircraft touched down (10:31 UTC) in Kiruna, Sweden. It can be seen that this flight started with a cloud cover over southern Germany, but there are no clouds visible for the entire flight except some scattered clouds in northern Sweden near Kiruna. The logbook of the

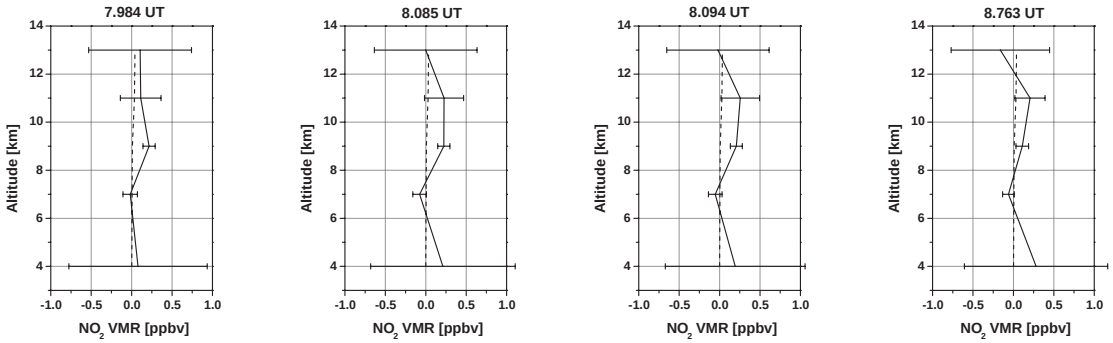

Figure 10.22: Examples of retrieved profiles with enhanced NO_2 in 9 km altitude on Sep. 9, 2002. Solid lines represent the retrieved profile and the dashed lines represent the a priori profile.

flight reported some clouds also in areas where no clouds are visible in the satellite image. Those clouds must be very scattered and considerably smaller than the pixel size of the MODIS detector. The cloud situation is not very important on this flight because no enhanced tropospheric NO_2 values were observed. This can be seen in Fig. 9.10 since no tropospheric signals occur in these plots. Comparing with Fig. 9.9 the tropospheric NO_2 values are smaller than the total retrieval errors, resulting in the omission of those signals in Fig. 9.10 as already discussed in the previous chapter.
Fig. 9.10 is indicating several signals in 9 km altitude. Some are shown in Fig. 10.22 in more detail. The profile retrieval of these data illustrates an exceptionally small total retrieval error in 7 and 9 km altitude compared to the profile retrieval of the other data on Sep. 3, 2002 and Mar. 19, 2003. The small total retrieval error is due to the small error components of the smoothing error and the measurement error for this profile retrieval. Thus exceptionally small amounts of NO_2 in 9 km altitude can be detected. In three incidents at 7.984 UTC, 8.085 UTC, and 8.094 UTC an amount of 0.2 ppbv NO_2 was retrieved in 9 km altitude. The fourth incident at 8.763 UTC only 0.1 ppbv NO_2 was retrieved, which is only slightly over the detection limit of 0.07 ppbv determined by the total retrieval error.
Comparing the NO_2 amounts of 0.1 to 0.2 ppbv in 9 km altitude with the results of [Fahey *et al.*, 1995; Schumann *et al.*, 1995] in Fig. 10.19 it has to be declared that these NO_2 amounts are below the amounts of NO_2 found in plumes by [Schumann *et al.*, 1995]. It could be proposed that 0.1 to 0.2 ppbv of NO_2 in 9 km altitude belongs to plumes much older than those analyzed by Schumann *et al.*. Even though the NO_2 found in 9 km altitude is quite small (0.1 to 0.2 ppbv) it has to be considered air traffic NO_2, since these incidents occurred over Germany where the air traffic is dense (see Appendix A).

10.2.3 Flight 030319

In Fig. 9.14 seven occasions of NO_2 in the UTLS region can be found. Unfortunately, on the second glance on Fig. 10.23 (showing a few examples of NO_2 in the UTLS region)

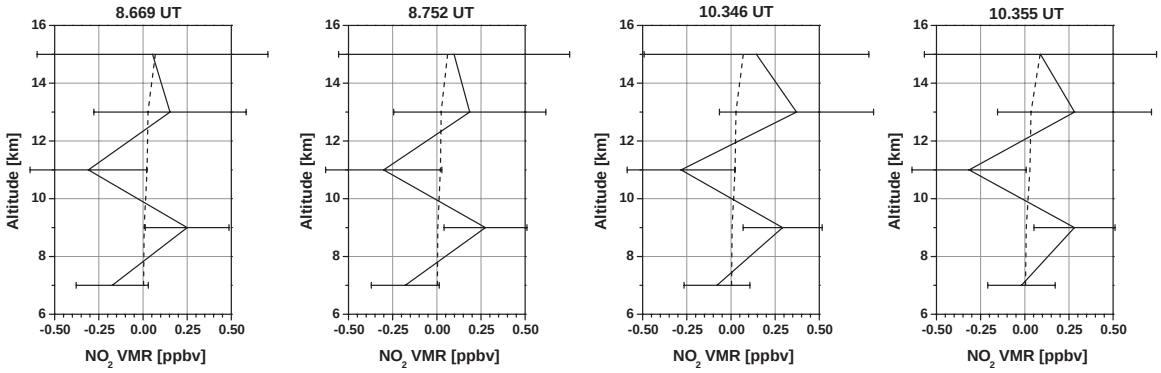

Figure 10.23: Examples of retrieved profiles with enhanced NO_2 in the UTLS region on Mar. 19, 2003. Solid lines represent the retrieved profile and the dashed lines represent the a priori profile.

the retrieved profiles possess some artificial structures already described in chapter 9 'Profile Retrieval using real AMAXDOAS data'. It was concluded that the oscillating in behavior was caused by too small measurement errors in relation to the a priori errors therefore the measurement error covariance matrix was increased. This increase was justified by the fact the measurement errors used are based on the fitting errors of the DOAS data analysis, but neglecting other error sources in the data analysis. A further increase in the measurement errors is not desirable, since with increasing measurement error the total retrieval is increasing. An increasing total retrieval error is reducing the averaging kernels and the retrieval quality.
The conclusion that has to be drawn for NO_2 in the UTLS region on flight 030319 is that no NO_2 in the UTLS region could be observed on this flight.

10.3 Summary

In this chapter it was shown that:

- APROVAL is able to detect boundary layer NO_2. On the three days analyzed at least eight occasions have been reported.
- The profile retrieval was able to detect boundary layer NO_2 values between 0.8 and 5.4 ppbv.
- APROVAL is able to detect NO_2 in the UTLS region. This NO_2 was interpreted as NO_2 from aircraft emissions. On the three days analyzed at least eight occasions have been reported.
- The profile retrieval was able to retrieve NO_2 values in the UTLS region between 0.1 and 0.6 ppbv.

Chapter 11

Summary and Outlook

This work deals with the analysis of data from the Airborne Multiaxis Differential Optical Absorption Spectrometer (AMAXDOAS). The development of the AMAXDOAS instrument is a joint venture of the University of Bremen and the University of Heidelberg, in which the author was actively involved.
The most important conclusion from this work is that the AMAXDOAS instrument is a success. It has been flown successfully in two airborne campaigns (SCIA-VALUE) in 2002 and 2003. In this work it could be proved that the AMAXDOAS Profile retrieval Algorithm (APROVAL) using multiaxis skylight measurements is possible and provide relevant new data.
Within this work APROVAL was developed based on the well known Optimal Estimation Method, and it was tested extensively in sensitivity studies, which demonstrate the behavior of the algorithm regarding different wavelengths and different lines of sight (LOS) to name just a few. The key conclusion of the sensitivity studies is that the ideal LOS setup for the AMAXDOAS instrument includes four LOS (0° [nadir], 88°, 92°, and 180° [zenith]) and using three wavelength regions (center wavelengths at 362.5 nm, 437.5 nm, and 485.0 nm). Virtually this 4-3 LOS setup consists of twelve LOS.
Finally APROVAL was used to analyze real AMAXDOAS measurements gathered during two major airborne campaigns in 2002 and 2003. The main conclusion of the profile retrieval using real AMAXDOAS data is: APROVAL was able to detect boundary layer NO_2 in several occasions with values of up to 5.4 ppbv and NO_2 in upper tropopshere/lower stratosphere (UTLS) region with values up to 0.6 ppbv. The latter was interpreted as NO_4 from air traffic emissions.
In the following sections the results of the chapters 'Error Analysis', 'Sensitivity Study', 'Profile Retrieval using simulated data', 'Profile Retrieval using real AMAXDOAS data', and 'Interpretation and Discussion' will be summarized separately. At the end an outlook for future work is given that could improve the AMAXDOAS instrument and APROVAL.

11.1 Error Analysis

The error analysis was done to estimate the uncertainty introduced by the forward model influencing the profile retrieval process. The main conclusions of the error anal-

ysis are:

- The uncertainty of the total forward model error due to variation of the forward model parameters adds up to 0.6 ppbv at 350 nm at 0 km altitude and to 0.7 ppbv at 500 nm at the same altitude. Fortunately this total forward model error is a worst case scenario as discussed in the section of each forward model parameter. Thus this error is not taken into account in APROVAL.

- The largest contribution to the total forward model error is the variation of ±50% (±0.15 absolute) in surface albedo, which results in uncertainties of 0.3 ppbv at 350 nm at 0 km altitude and 0.5 ppbv at 500 nm at 1 km altitude. It has to be noted that an absolute change of 0.15 in surface albedo is very large and does not occur over land or ocean except at boundaries to snow covered regions. Large changes in albedo (from 0.1 to 0.9) are subject to a study of its own.

- An accurate pointing of the LOS proved to be very important for the profile retrieval, since a variation of -1° in LOS results in uncertainties of up to 0.9 ppbv in the retrieved profile in some altitudes at 500 nm. Fortunately this is not an issue considering the AMAXDOAS instrument, since the recording of the flight data has an uncertainty of 0.01° regarding the pitch and roll of the aircraft.

11.2 Sensitivity Study

Sensitivity studies have been performed to determine the amount of profile information contained in airborne UV/vis skylight absorption measurements. The key conclusions to be drawn from these studies are:

- A profile retrieval at different wavelengths results in retrieved profiles with different vertical resolutions in different altitudes. At 350 nm, the best vertical resolution of 2.1 km is achieved near flight altitude. On the other hand the best vertical resolution at 500 nm is achieved in the lower troposphere. This feature is important for APROVAL.

- The best LOS setup is the enhanced limb 18 LOS setup with one limb LOS per retrieval grid point meaning the altitude of the retrieval grid point corresponds to the tangent height of the specific limb LOS. For practical reasons the downsized limb twelve LOS setup is as good as the enhanced limb 18 LOS setup. Only four LOS (0° [nadir], 88°, 92°, and 180° [zenith]) result in a limited quality of the retrieved profiles with a limited vertical resolution.

- The combination of four LOS (0° [nadir], 88°, 92°, and 180° [zenith]) at three different wavelengths (center wavelengths at: 362.5 nm, 437.5 nm, and 485.0 nm) lead to the ideal LOS setup for the AMAXDOAS instrument. This LOS setup was implemented in APROVAL.

- The choice of the optimum retrieval grid for a specific LOS setup is a trade off between vertical resolution of the retrieved profiles and the total retrieval error.

A small vertical resolution is accompanied by a large total retrieval error and vice versa. For most sensitivity studies the retrieval grid with points at 0 km, 1 km, 3 km, 5 km, $\cdots$, 39 km is the ideal choice. For the AMAXDOAS instrument using the 4-3 LOS setup a retrieval grid with points at 1 km, 4 km, 7 km, 9 km, $\cdots$, 39 km is the best choice.

11.3 Profile Retrieval using simulated data

The profile retrieval using simulated AMAXDOAS data include sensitivity studies which test APROVAL under well known conditions. The key results are:

- Considering the 4-3 LOS setup the sensitivity of the profile retrieval to different altitudes was investigated resulting in very small uncertainties (≤ 0.15 ppbv) of the retrieved profile at altitudes near flight altitude. The uncertainties of the retrieved profiles in the lower troposphere are larger but still acceptable (< 0.5 ppbv). The uncertainties for the enhanced limb 18 LOS setup are even smaller at altitudes near flight altitude (< 0.1 ppbv) and in the lower troposphere (0.3 ppbv).

- Variations of the stratospheric column result in uncertainties of the retrieved profiles at altitudes between 15 and 19 km. Fortunately information on the stratospheric column is included in the AMAXDOAS data, so these uncertainties due to incorrect a priori information can be corrected.

- A modified APROVAL can be applied to limb viewing satellite measurements (SCIAMACHY) as well. A trace gas profile can be retrieved from 12 to 35 km altitude.

11.4 Profile Retrieval using real AMAXDOAS data

The profile retrieval using APROVAL and real AMAXDOAS data has shown that:

- Three flights of the SCIA-VALUE campaigns in 2002 and 2003 were analyzed.

- Slant columns measurements of the AMAXDOAS instrument do contain profile information. The retrieved profile information reaches from the boundary layer up to an altitude of 13 km.

- Only four LOS [0° (nadir), 88°, 92°, and 180° (zenith)] at three wavelengths (362.5 nm, 437.5 nm, and 485.0 nm) are necessary to retrieve profile information with a good vertical resolution of 2.1 to 4.0 km.

- APROVAL is able to retrieve amounts as large as 5.4 ppbv of NO_2 in the boundary layer.

- APROVAL is able to retrieve amounts as small as 0.1 ppbv of NO_2 in UTLS region.

11.5 Interpretation and Discussion

The interpretation and discussion of the retrieved profiles of the three flights have shown that:

- APROVAL using real AMAXDOAS data is able to detect boundary layer NO_2. At least eight occasions have been reported on the three days that have been analyzed.
- Boundary layer NO_2 with a VMR between 0.8 and 5.4 ppbv has been reported.
- APROVAL using real AMAXDOAS data is able to detect NO_2 in the UTLS region. The NO_2 in this region was interpreted as emissions from aircrafts. At least eight occasions have been reported on the three days that have been analyzed.
- NO_2 in the UTLS regions with a VMR as low as 0.1 ppbv and up to 0.6 ppbv was detected.

11.6 Outlook

APROVAL was tested using three days of data only. So more testing and validation is necessary. The only problem is the limited availability of tropospheric NO_2 profile data. It is proposed by the author to analyze the existing AMAXDOAS data to retrieve Ozone and BrO profiles from these data because Ozone profiles can be validated using Ozone sonde data, which have a higher availability.
According to the sensitivity studies the 4-3 LOS setup of the current AMAXDOAS instrument is not the ideal LOS setup to retrieve profile information. It would be interesting to use different limb LOS in order to improve the total retrieval error and the vertical resolution of the retrieved profiles. Unfortunately there are many modifications of the AMAXDOAS telescopes and the two domes necessary to accomplish this target. The author proposes to design a dome containing one telescope per spectrometer only. This design would include a movable telescope to be able to realize every desirable LOS. With this modification different LOS setup could to be tested to validate the performances of those LOS setups predicted by the sensitivity studies.
Another interesting modification of the AMAXDOAS instrument is the stabilization of the temperature of the spectrometers. Using a thermostat that is able to cool and heat the spectrometers would improve the quality of the DOAS fit due to reduced wavelength drifts of the measured spectra.
A camera in nadir direction recording the cloud situation below the aircraft can help to interpret the retrieved profiles because cloud free scenarios can be identified more precisely. This will improve the quality of the retrieved profile because the uncertainties due to albedo changes can be eliminated significantly.

Appendix A

Air Traffic Fuel Consumption

Fig. A.1 shows the distribution of fuel burned as calculated in 1 month (May) of the 1992 NASA inventory. The most heavily trafficked areas are clearly visible (United States, Europe, North Atlantic, North Asia) [Ellis *et al.*, 1999]. The report by [Ellis *et al.*, 1999] also predicts an increase in global fuel consumption by air traffic from 129.4 - 139.4 Tg in the year 1992 to 285.0 - 308.6 Tg in 2015 (the margins of the estimates

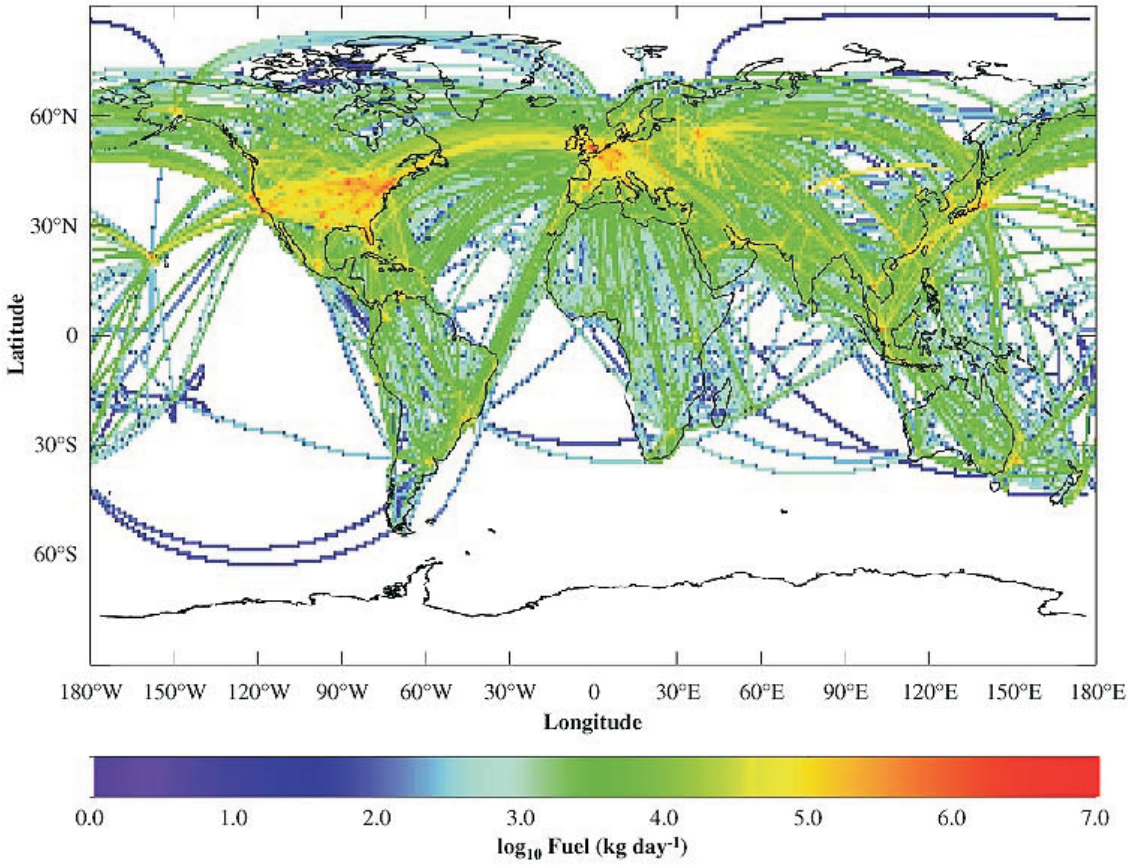

Figure A.1: Geographical distribution of fuel burned by civil aviation in one month (May 1992) [Ellis *et al.*, 1999].

depend on the study (NASA, ANCAT, and DLR) chosen). This is an increase of a factor larger than two in 23 years.

Appendix B

Measured Slant Columns

Here all measured differential slant columns used in this work are presented and compared to the profiles retrieved with APROVAL.
Fig. B.1 to Fig. B.3 show the measured slant columns for Sep. 3 2002, Feb. 19 2003, and Mar. 19 2003 respectively in comparison to the profiles retrieved from these data. The SZA of the background spectra used in the DOAS analysis for each LOS of each flight can be found in Tab. 9.1.
The slightly enhanced NO_2 values (0.25 ppbv) in the beginning of flight 020903 at 9 km altitude are caused by the slightly enhanced slant column values of the 88° LOS at 362.5 nm as can be seen in Fig. B.1. The large NO_2 values (5.4 ppbv) in the boundary layer observed on flight 030219 are caused by the large NO_2 slant columns at 0° LOS and 485 nm. The fact that these NO_2 values are located in the boundary layer is supported by the much smaller NO_2 slant columns observed at 362.5 nm in the same LOS (0°) because at 362.5 nm the larger part of the photons is scattered significantly above the boundary layer. At 485 nm the situation is different because most photons are scattered within the boundary layer. This can be explained by the wavelength dependent Rayleigh scattering.
The enhanced NO_2 values in the boundary layer of flight 030319 can be explained in the same way.

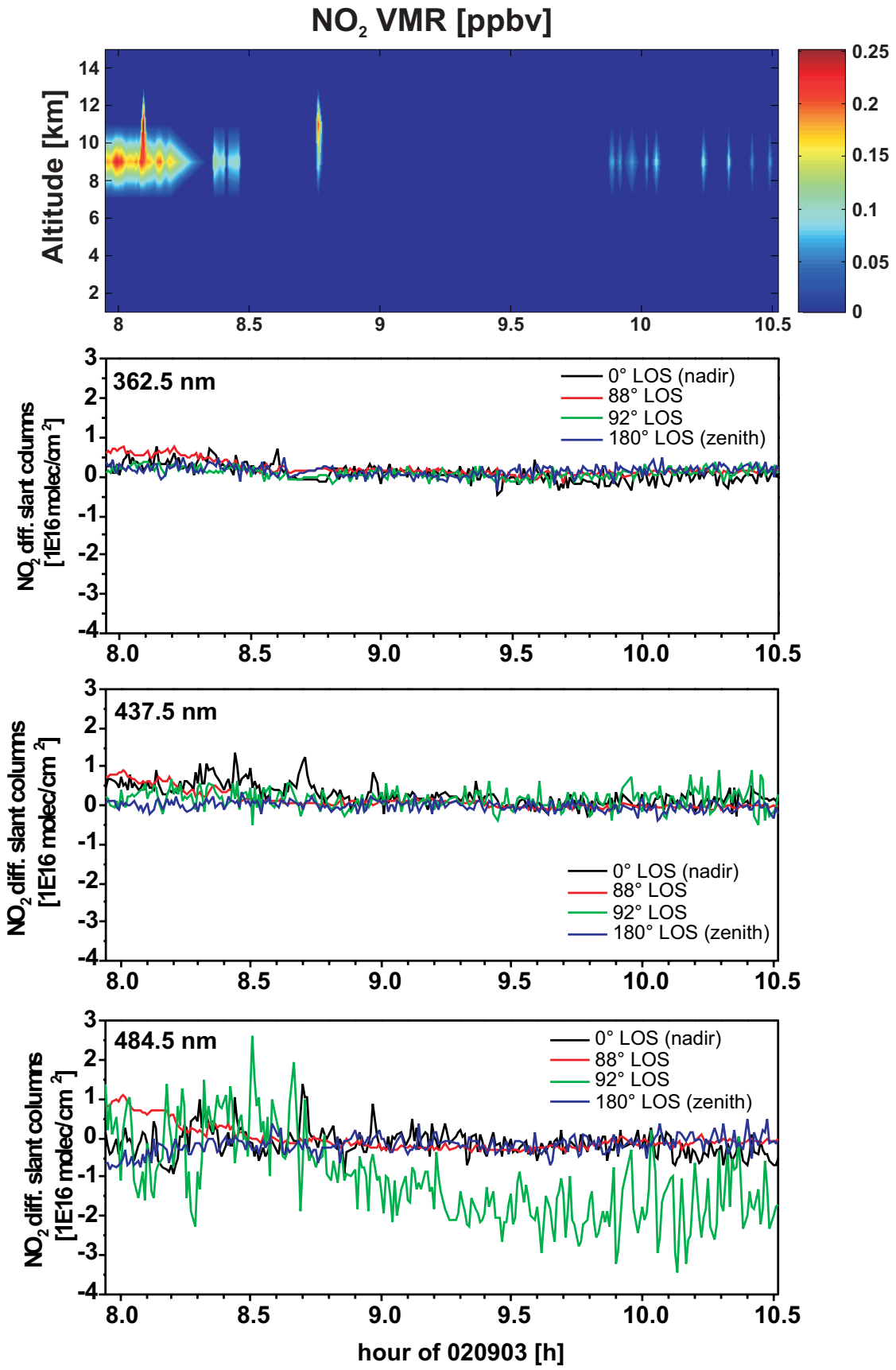

Figure B.1: Comparison of measured slant columns and retrieved profiles for Sep. 3 2002.

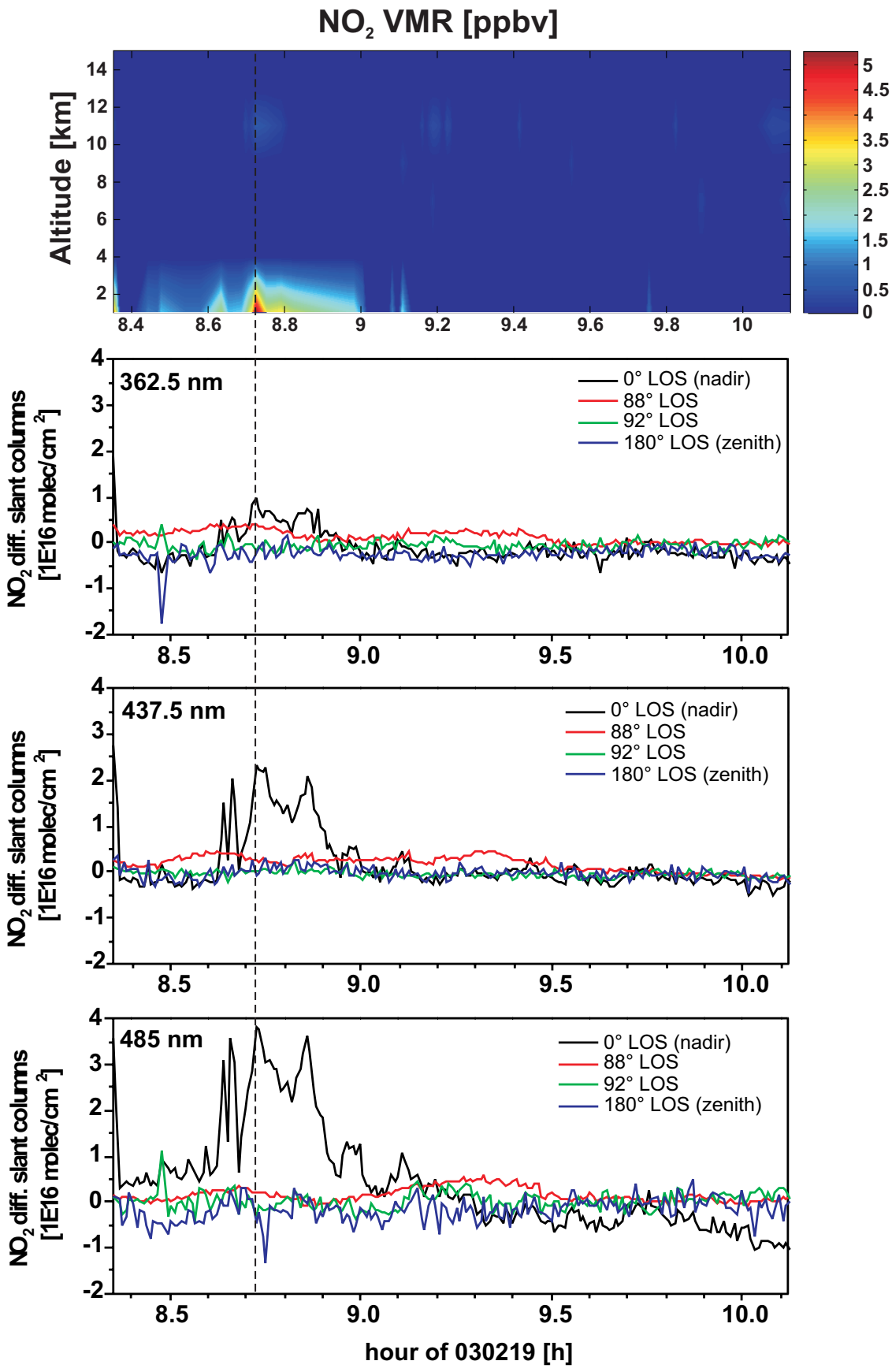

Figure B.2: Comparison of measured slant columns and retrieved profiles for Feb. 19 2003.

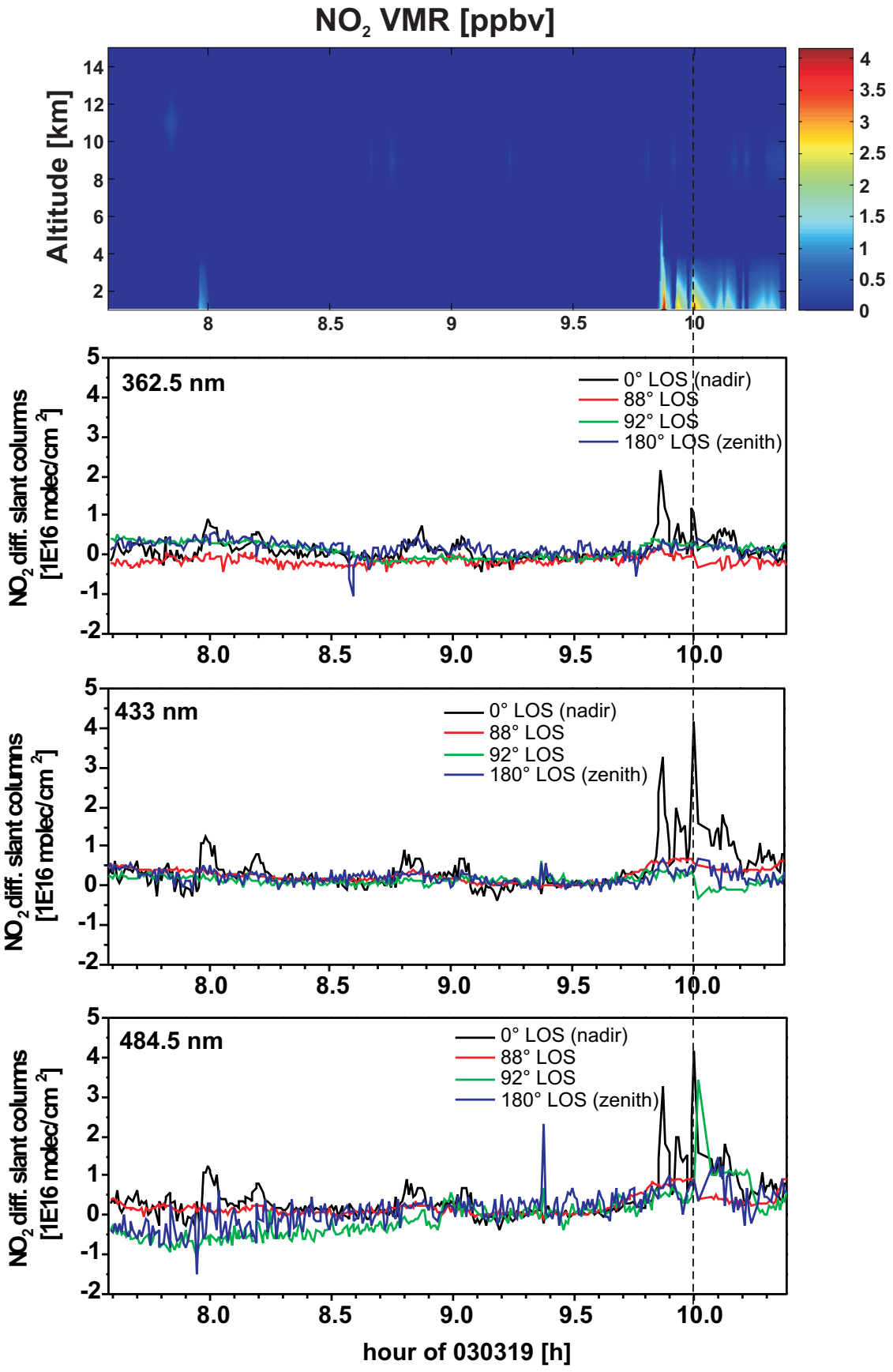

Figure B.3: Comparison of measured slant columns and retrieved profiles for Mar. 19 2003.

Bibliography

Arnold, F., Scheid, J., Stilp, T., Schlager, H., and Reinhardt, M. E. (1992). Measurements of Jet Aircraft Emissions at Cruise Altitude I:The Odd Nitrogen Gases NO, NO_2, HNO_2 and HNO_3. *Geophys. Res. Let.*, **12**, 2421–2424.

ASTRA (2003). Monatsmittel des 24-stündigen Verkehrs der automatischen Strassenverkehrszählung, Swiss Federal Roads Authority. http://www.verkehrsdaten.ch/e/home.html.

Barrie, L. A., Bottenheim, J. W., Schnell, R. C., Crutzen, P. J., and Rasmussen, R. A. (1988). Ozone destruction and photochemical reactions at polar sunrise in the lower Arctic atmosphere. *Nature*, **334**, 138–141.

Bates, D. and Nicolet, M. (1950). The photochemistry of atmospheric water vapor. *Geophys. Res. Lett.*, **20**, 711.

Bates, D. R. and Hays, P. B. (1967). Atmospheric Nitrous Oxide. *Planet. Space Sci.*, **15**, 189–197.

Blazowski, W. S. and Saywer, R. F. (1975). Fundamentals of pollutant formation in Propulsion Effluents in the Stratosphere. Technical report, Rep. DOT-TST-75-52; pp. (4-1)-(4-52), US Dept. of Trans., Washington, D.C., (Available from the Natl. Tech. Inf. Serv., Springfield, VA).

Bovensmann, H., Burrows, J. P., Buchwitz, M., Frerick, J., Noel, S., and Rozanov, V. V. (1999). SCIAMACHY: Mission Objectives and Measurement Modes. *J. Atmos. Sci.*, **2**, 127–150.

Brandtjen, R., Klüpfel, T., Perner, D., and Knudsen, B. M. (1994). Airborne measurements during the European Arctic Stratospheric Ozone experiment: Observation of OClO. *Geophys. Res. Lett.*, **21**, 1363–1366.

Brasseur, G. and Solomon, S. (1986). *Aeronomy of the middle atmosphere*. D. Reidel Publishing Company.

Brewer, A. W. and Kerr, J. B. (1973). Total ozone measurements in cloudy weather. *PAGEOPH*, **106**, 928–937.

Bruns, M., Buehler, S. A., Burrows, J. P., Heue, K.-P., Platt, U., Pundt, I., Richter, A., Rozanov, A., Wagner, T., and Wang, P. (2004). Retrieval of profile information from airborne multiaxis UV-visible skylight absorption measurements. *Appl. Opt.*, **43 (22)**, 4415–4426.

Burrows, J. P. and Chance, K. V. (1992). SCIAMACHY and GOME: The scientific objectives. *J. Atm. Chem.*, **1715**, 502–511.

Burrows, J. P., Dehn, A., Deters, B., Himmelmann, S., Richter, A., Voigt, S., and Orphal, J. (1998). Atmospheric Remote-Sensing Reference Data from GOME: 1. Temperature-Dependent Absorption Cross Sections of NO_2 in the 231-794 nm Range. *J. Ouant. Spec. Rad. Trans.*, **60**, 1025–1031.

Chandrasekhar, S. (1960). *Radiative Transfer*. Dover, Mineola - N. Y.

Chapman, S. (1930). A theory of upper-atmosphere ozone. *Mem. Roy. Meteorol. Soc.*, **3**, 103.

Chatfield, R. (1994). Anomalous HNO_3/NO_x Ratio of Remote Tropospheric Air: Conversion of Nitric Acid to Formic Acid and NO_x? *Geophys. Res. Lett.*, **21**, 2705–2708.

Chatfield, R. and Crutzen, P. (1984). Sulfur Oxides in Remote Oceanic Air: Cloud Transport of Reactive Precursors. *J. Geophys. Res.*, **89**, 7111–7132.

Chipperfield, M. (1999). Multiannual simulations with a three-dimensional chemical transport model. *J. Geophys. Res.*, **104**, 1781–1805.

Crutzen, P. (1970). The influence of nitrogen oxides on the atmospheric ozone content. *Q. J. R. Meteorol. Soc.*, **96**, 320–325.

Crutzen, P. (1971). Oxygen Production Rates in an Oxygen-Hydrogen-Nitrogen Oxide Atmosphere. *J. Geophys. Res.*, **76**, 7311–7327.

Crutzen, P. (1995). Overview of Tropospheric Chemistry: Developments during the Past Quarter Century and a Look Ahead. *Faraday Discuss.*, **100**, 1–21.

DeMore, W., Sander, S. P., Golden, D. M., Hampson, R. F., Kurylo, M. J., Howard, C. J., Ravishankara, A. R., Kolb, C. E., and Molina, M. L. (1997). Chemical Kinetics and Photochemical data for use in stratospheric modeling. Technical report, JPL Publication 97-4.

Dias-Lalcaca, P., Brunner, D., Imfeld, W., and Staehelin, J. (1998). An Automated System for the Measurements of Nitrogen Oxides and Ozone Concentrations from a Passenger Aircraft: Instrumentation and First Results of the NOXAR Project. *Environ. Sci. Technol.*, **32**, 3228–3236.

Ellis, J., Harris, N., Lister, D., and Penner, J. (1999). Aviation and the Global Atmosphere, IPCC Report on Aviation 1999, fig. 9-10 and tab. 9-8. http://www.grida.no/climate/ipcc/aviation.

Erle, F., A.Grendel, D.Perner, Platt, U., and Pfeilsticker, K. (1998). Evidence of heterogeneous bromine chemistry on cold stratospheric sulphate aerosols. *Geophys. Res. Lett.*, **25**, 4329–4332.

Eumetsat (2000). The meteosat system. Technical report, Eumetsat, EUM TD 05.

Fahey, D. W., Keim, E. R., Woodbridge, R. S., Gao, K. A., Boering, K. A., Daube, B. C., Wofsy, S. C., Lohmann, R. P., Hintsa, E. J., Dessler, A. E., Webster, C. R., May, R. D., Brock, C. A., Wilson, J. C., Miake-Lye, R. C., Brown, R. C., Rodriguez, J. M., Loewenstein, M., Proffitt, M. H., Stimpfle, R. M., Bowen, S. W., and Chan, K. R. (1995). In-situ observations in aircraft exhaust plumes in the lower stratosphere at midlatitudes. *J. Geophys. Res.*, **100**, 3065–3074.

Falk, W. R. (1984). Data reduction from experimental histograms. *Nuclear Instruments and Methods in Physics Research*, **220**, 473–478.

Farman, J. C., Gardiner, B. G., and Shanklin, J. D. (1985). Large losses of total ozone in Antarctica reveal seasonal ClO_x/NO_x interaction. *Nature*, **315**, 207–210.

Finlayson-Pitts, B. J. and Pitts, J. N. (2000). *Chemistry of the Upper and Lower Atmosphere*. Academic Press.

Fix, A., Ehret, G., Flentje, H., Poberaj, G., Finkenzeller, H., Bremer, H., Bruns, M., Burrows, J. P., Kleinböhl, A., Küllman, H., Kuttippurath, J., Richter, A., Wang, P., Heue, K.-P., Platt, U., and Wagner, T. (2004). SCIAMACHY validation by aircraft remote measurements: Design, execution, and first results of the SCIA-VALUE mission. *accepted for publication in Atmos. Chem. Phys. Disscus.*

Grainger, J. F. and Ring, J. (1962). Anomalous Fraunhofer line profiles. *Nature*, **193**, 762.

Greenblatt, G. D. and Ravishankara, A. R. (1990). Laboratory Studies on the Stratospheric NO_x Production Rate. *J. Geophys. Res.*, **95**, 3539–3547.

Hartley, W. N. (1881). On the absorption of solar rays by atmospheric ozone. *J. Chem. Soc.*, **39**, 111.

Hübler, G. e. a. (1988). Airborne measurements of reactive odd nitrogen during NASA's GTE/CITE 2 project. In *Abstracts, Workshop on Tropospheric Ozone, Göttingen, Germany*.

Heue, K.-P. (2004). Construction of the AMAXDOAS telescopes and the AMAXDOAS domes, personal communication.

Heue, K.-P., Richter, A., Wagner, T., Bruns, M., Burrows, J. P., v. Friedeburg, C., ee, W.-D., Platt, U., Pundt, I., and Wang, P. (2004). Validation of SCIAMACHY tropospheric NO_2-columns with AMAXDOAS measurements. *accepted for publication in Atmos. Chem. Phys. Disscus.*

Hidalgo, H. and Crutzen, P. J. (1977). The tropospheric and stratospheric composition perturbed by NO_x emissions of high-altitude aircraft. *J. Geophys. Res.*, **82**, 5833–5866.

Hilberg, D. (1989). Akima-Interpolation. *ct*, **6**, 206–214.

Hönninger, G. and Platt, U. (2002). The role of BrO and its vertical distribution during surface ozone depletion at alert. *Atmos. Environ.*, **36**, 2481–2489.

Houghton, J. T. (1986). *The Physics of Atmospheres*. Cambridge University Press.

Jaegle, L., Jacob, D. J., Wang, Y., Weinheimer, A. J., Ridley, B. A., Campos, T. J., Sachse, G. W., and Hagen, D. E. (1998). Sources and Chemistry of NO_x in the Upper Troposhere over the United States. *Geophys. Res. Lett.*, **25**, 1705–1708.

Johnston, H. (1971). Reduction of stratospheric ozone by nitrogen oxide catalysts from supersonic transport exhaust. *Science*, **173**, 517.

Johnston, H., Kinnison, D. E., and Wuebbles, D. J. (1989). Nitrogen Oxides From High-Altitude Aircraft: An Update of Potential Effects on Ozone. *J Geophys. Res.*, **94**, 16351–16363.

Kauss, J. (1998). *Aerosol Parametrisierung für Strahlungstransport-Simulationen im ultratvioletten bis nahinfraroten Spektralbereich*. Master's thesis, Universität Bremen.

Küllmann, H., Bremer, H., Kleinböhl, A., von König, M., and Künzi, K. (2001). The Airborne Submillimeter Radiometer (ASUR) as a tool for stratospheric sensing. In *International Symposium on Sub-Millimeter Wave Earth Observations from Space - III (S. Buehler (Ed.)), Logos Verlag Berlin, pp. 15-24*.

Kneizys, F. X., Shettle, E. P., Abreu, L. W., Chetwynd, J. H., Anderson, G. P., Gallery, W. O., Selby, J. E. A., and Clough, S. A. (1986). Users Guide to LOWTRAN 7. Technical report, AFGL-TR-88-0177, (NTIS AD A206773), Air Force Geophysics Laboratory AFGL, Hanscom AFB, MA.

Kurosu, T., Rozanov, V., and Burrows, J. (1997). Parameterization Schemes for Terrestrial Water Clouds in the Radiative Transfer Model GOMETRAN. *J. Geophys. Res.*, **102 (D18)**, 21809–21824.

Lee, M., Heikes, B. G., and Jacob, D. J. (1998). Enhancements of Hydroperoxides and Formaldehydes in Biomass Burning Impacted Air and Their Effect on Atmospheric Oxidant Cycles. *J. Geophys. Res.*, **103**, 13201–13212.

McElroy, C. T., McLinden, C. A., and McConnell, J. C. (1999). Evidence for bromine monoxide in the free troposphere during the arctic polar sunrise. *Nature*, **397**, 338–341.

McInnes, G. and Walker, C. (1992). The global distribution of aircraft air pollutant emissions. Technical report, LR 872 (AP), ISBN 0 85624 731 6, Warren Spring Lab., Hertfordshire, Eng.

McKeen, S. A., Gierczak, T., Burkholder, J. B., Wennberg, P. O., Hanisco, T. F., Keim, E. R., Gao, R.-S., Liu, S. C., Ravishankara, A. R., and Fahey, D. W. (1997). The photochemistry of Acetone in the Upper Troposphere: A Source of Odd-Hydrogen Radicals. *Geophys. Res. Lett.*, **24**, 3177–3180.

McKenzie, R. L. and Johnston, P. V. (1982). Seasonal variations in stratospheric NO_2 at 45°S. *Geophys. Res. Lett.*, **9**, 1255–1258.

McKenzie, R. L., Johnston, P. V., McElroy, C. T., Kerr, J. B., and Solomon, S. (1991). Altitude distributions of stratospheric constituents from ground-based measurements at twilight. *J. Geophys. Res.*, **96**, 15499–15511.

Melamed, M. L., Solomon, S., Daniel, J. S., Langford, A. O., Portmann, R. W., Ryerson, T. B., Nicks, D. K., and McKeen, S. A. (2003). Measuring reactive nitrogen emissions from point sources using visible spectroscopy from aircraft. *J. Environ. Monit.*, **5**, 29–34.

Molina, J. M. and Rowland, F. S. (1974). Stratospheric sink for chlorofluoromethanes: chlorine atom-catalysed destruction of ozone. *Nature*, **249**, 810–812.

Molina, L. T. and Molina, M. J. (1987). Production of Cl_2O_2 from the self-reaction of the ClO radical. *J. Phys. Chem.*, **91**, 433–436.

Noel, S., Bovensmann, H., Wuttke, M. W., Burows, J. P., Gottwald, M., Krieg, E., Goede, A. H. P., and Mager, R. (2000). SCIAMACHY nomial operations and special features. In *Proc. ERS-ENVISAT symposium Gothenburg, 10–16 Oct. 2000, CD-ROM (SP-461)*.

Noxon, J. F. (1975). Nitrogen dioxide in the stratosphere and troposphere measured by ground-based absorption spectroscopy. *Science*, **189**, 547–549.

Noxon, J. F. (1979). Stratospheric NO_2. 2. Global behaviour. *J. Geophys. Res.*, **84**, 5067–5076.

Perliski, L. M. and Solomon, S. (1993). On the evaluation of air mass factors for atmospheric near-ultraviolet and visible absorption spectroscopy. *J. Geophys. Res.*, **98**, 10363–10374.

Perner, D. and Platt, U. (1979). Detection of nitrous acid in the atmosphere by differential optical absorption. *Geophys. Res. Lett.*, **6**, 917–920.

Petritoli, A., Ravegnani, F., Giovanelli, G., Bortoli, D., Bonaf, U., Kostadinov, I., and Oulanovsky, A. (2002). Off-axis measurements of atmospheric trace gases by use of an airborne ultraviolet-visible spectrometer. *Applied Optics*, **27**, 5593–5599.

Pfanhauser, W. (2004). Technical notes on roper scientific ccd cameras, roper scientific gmbh, http://www.roperscientific.de/theory.html.

Pfeilsticker, K. and Platt, U. (1994). Airborne measurements during the Arctic Stratospheric Experiment: Observation of O_3 and NO_2. *Geophys. Res. Lett.*, **21**, 1375–1378.

Platt, U. and Hausmann, M. (1994). Spectroscopic meausrements of the free radicals NO_3, BrO, IO, and OH in the troposphere. *Res. chem. Intermed.*, **20**, 557–578.

Platt, U. and Perner, D. (1980). Direct measurements of atmospheric CH_2O, HNO_2, O_3, NO_2 and SO_2 by differential absorption in the near UV. *J. Geophys. Res.*, **85**, 7453–7458.

Pommereau, J.-P. and Goutail, F. (1988). Stratospheric O_3 and NO_2 observations at the southern polar circle in summer and fall 1988. *Geophys. Res. Lett.*, **15**, 895–897.

Prather, M. J. and Jacob, D. J. (1997). A Persistent Imbalance in HO_x and NO_x Photochemistry of the Upper Troposphere Driven by Deep Tropical Convection. *Geophys. Res. Lett.*, **24**, 3189–3192.

Press, W. H., Flannery, B. P., Teukolsky, S., and Vetterling, W. T. (1989). *Numerical recipes in PASCAL.* Cambridge University Press.

Preston, K. E. (1995). *The Retrieval of NO_2 vertical profiles from ground-based Twilight UV-visible measurements*. Ph.D. thesis, Pembroke College, Cambridge.

Preston, K. E., Jones, R. L., and Roscoe, H. K. (1997). The retrieval of NO_2 vertical profiles from ground-based twilight UV-visible measurements. *J. Geophys. Res.*, **102**, 19089–19097.

Pundt, I., Heue, K.-P., Wang, P., Richter, A., Bruns, M., v. Friedeburg, C., Laepple, T., Platt, U., Burrows, J. P., and Wagner, T. (2004a). Airborne Multi Axis-DOAS measurements of formaldehyde of the photochemical plume of Milan city. in preperation, 2004.

Pundt, I., Heue, K.-P., Song, B. C., Richter, A., Wang, P., Platt, U., Burrows, J. P., and Wagner, T. (2004b). Airborne Tomographic Measurements of NO_2 Plumes from Point sources using the AMAXDOAS instrument. in preperation, 2004.

Richter, A. (1997). *Absorptionsspektroskopische Messungen Stratosphärischer Spurengase über Bremen.* Ph.D. thesis, Universität Bremen, in German.

Richter, A. (2003a). AMAXOMA Manual, version 4.9. Technical report, Universität Bremen.

Richter, A. (2003b). How to use Weighting Functions for DOAS. Technical report, Universität Bremen.

Richter, A., Wittrock, F., Eisinger, M., and Burrows, J. P. (1998). GOME Observations of Tropospheric BrO in Northern Hemispheric Spring and Summer 1997. *Geophys. Res. Lett.*, **25**, 2683–2686.

Rodgers, C. D. (1976). Retrieval of atmospheric temperature and composition from remote measurements of thermal radiation. *Rev. Geophys.*, **14**, 609–624.

Rodgers, C. D. (1990). Characterization and error analysis of profiles retrieved from remote sounding measurements. *J. Geophys. Res.*, **95**, 5587–5595.

Rodgers, C. D. (2000). *Inverse Methods for atmospheric sounding: Theory and Practice, Series on Atmospheric, Oceanic and Planetary Physics, Vol. 2*. Academic Press.

Roedel, W. (1992). *Physik unserer Umwelt: Die Atmosphäre*. Springer Verlag.

Rozanov, A., Rozanov, V., and Burrows, J. P. (2000). Combined differential-integral approach for the radiation field computation in a spherical shell atmosphere: Non-limb geometry. *J. Geophys. Res.*, **105**, 22937–22942.

Rozanov, A., Rozanov, V., and Burrows, J. P. (2001). A numerical radiative transfer model for a spherical planetary atmosphere: combined differential integral approach involving the Picard iterative approximation. *J. Quant. Spectrosc. Radiat. Transfer*, **69**, 491–512.

Rozanov, A., Rozanov, V., and Burrows, J. P. (2002). Evaluation of the Combined Differential-Integral Approach for Limb Viewing Geometry. *Adv. Space Res.*, **29**, 1843–1848.

Rozanov, V., Diebel, D., Spurr, R. J. D., and Burrows, J. P. (1997). GOMETRAN: A radiative transfer model for the satellite project GOME - the plane-parallel version. *J. Geophys. Res.*, **102**, 16683–16695.

Rozanov, V., Kurosu, T., and Burrows, J. (1998). Retrieval of atmospheric constituents in the UV-visible: A new quasi-analytical approach for the calculation of weighting functions. *J. Quant. Spectrosc. Radiat. Transfer*, **60**, 277–299.

Russell, A. G., Winner, D. A., Harley, R. A., McCue, K. F., and Cass, G. R. (1993). Mathematical Modelling and Control of the Dry Deposition Flux of Nitrogen-Containing Air Pollutants. *Einviron. Sci. Technol.*, **27**, 2772–2782.

Schiller, C., Wahner, A., Platt, U., Dorn, H., Callies, J., and Ehalt, D. H. (1990). Near UV atmospheric absorption measurements of column abundances during Airborne Arctic Stratospheric Expedition, January-February 1989: 2. OClO observations. *Geophys. Res. Lett.*, **17**, 501–504.

Schoeberl, M. R. and Hartmann, D. L. (1991). The dynamics of the stratospheric polar vortex and its relation to springtime ozone depletions. *Science*, **251**, 46–52.

Schulte, P., Schlager, H., Ziereis, H., Schumann, U., Baughcum, S. L., and Deidewig, F. (1997). NO_x Emissions Indices of Subsonic Long-Range Jet Aircraft at Cruise Altitude: In-Situ Measurements and Predictions. *J. Geophys. Res.*, **102**, 21431–21442.

Schumann, U., Konopka, P., Baumann, R., Busen, R., Gerz, T., Schlager, H., Schulte, P., and Volkert, H. (1995). Estimate of diffussion parameters of aircraft exhaust plumes near the tropopause from nitric oxide and turbulence measurements. *J. Geophys. Res.*, **100**, 14147–14162.

Shettle, E. P. and Fenn, R. W. (1979). Models of the aerosols of the lower atmosphere and the effects of humidity variations on their optical properties. Technical report, AFGL-TR-79-0214, Project 7670, Air Force Geoph. Lab., Hanscom AFB, MA.

Singh, H. B., Kanakidou, M., Crutzen, P. J., and Jacobs, D. J. (1995). High concentrations and photochemical fate of oxygenated hydrocarbons in the global troposphere. *Nature*, **378**, 50–54.

Solomon, S., Schmeltekopf, A. L., and Sanders, W. R. (1987a). On the interpretation of zenith sky absorption measurements. *J. Geophys. Res.*, **92**, 8311–8319.

Solomon, S., Mount, G. H., Sanders, R. W., and Schmeltekopf, A. L. (1987b). Visible spectroscopy at McMurdo Station, Antarctica. 2. Observations of OClO. *J. Geophys. Res.*, **92**, 8329–8338.

SOST (2004). Sciamachy operations support, operation concepts. http://atmos.af.op.dlr.de/projects/scops/.

Stolarski, R. and Cicerone, R. (1974). Stratospheric chlorine: a possible sink for ozone. *Can. J. Chem.*, **52**, 1610.

Suhre, K., Cammas, J.-P., Nedelec, P., Rosset, R., Marenco, A., and Smit, H. G. J. (1997). Ozone -Rich Transient in the Upper Equatorial Atlantic Troposphere. *Nature*, **388**, 661–663.

Tsai, F., Sun, W.-S., and Chen, J.-P. (2001). A Composite Study of Civil Aircraft Impacts on Ozone and Sulfate over the Taiwan Area. *TAO*, **12**, 109–135.

Vountas, M., Rozanov, V., and Burrows, J. P. (1998). Ring Effect: Impact of Rotational Raman Scattering on Radiative Transfer in Earth's Atmosphere. *J. Quant. Spectrosc. Radiat. Transfer*, **60**, 943–961.

Wagner, T. and Platt, U. (1998). Satellite mapping of enhanced BrO concentrations in the troposphere. *Nature*, **395**, 486–490.

Wagner, T., Bruns, M., Burrows, J., Fietkau, S., Finocchi, F., Heue, K.-P., Hönninger, G., Platt, U., Pundt, I., Richter, A., Rollenbeck, R., von Friedeburg, C., Wittrock, F., and Xie, P. (2001). The AMAXDOAS instrument and its application for SCIAMACHY validation. In *Proceedings of the 15th ESA Symposium on European Rocket and Balloon Programmes and Related Research (ESA SP-471, August 2001), Biarritz, France*.

Wahner, A., Jakoubek, R. O., Mount, G. H., Ravishankara, A. R., and Schmeltekopf, A. L. (1989a). Remote sensing observations of daytime column NO_2 during the airborne Antarctic ozone experiment, August 22 to October 2, 1987. *J. Geophys. Res.*, **94**, 16619–16632.

Wahner, A., Jakoubek, R. O., Mount, G. H., Ravishankara, A. R., and Schmeltekopf, A. L. (1989b). Remote sensing observations of nighttime OClO column during the Airborne Antarctic Ozone Experiment, September 8, 1987. *J. Geophys. Res.*, **94**, 11405–11411.

Wahner, A., Callies, J., Dorn, H., Platt, U., and Schiller, C. (1990a). Near UV atmospheric absorption measurements of column abundances during airborne arctic stratospheric expedition, January-February 1989: 3. BrO observations. *Geophys. Res. Lett.*, **17**, 517–520.

Wahner, A., Callies, J., Dorn, H., Platt, U., and Schiller, C. (1990b). Near UV atmospheric absorption measurements of column abundances during Airborne Arctic Stratospheric Expedition, January-February 1989:1. Technique and NO_2 observations. *Geophys. Res. Lett.*, **17**, 497–500.

Wahner, A., Mentel, T. F., and Sohn, M. (1998). Gas-Phase Reaction of N_2O_5 with Water Vapor: Importance of Heterogeneous Hydrolysis of N_2O_5 and Surface Desorption of HNO_3 in a Large Teflon Chamber. *Geophys. Res. Lett.*, **25**, 2169–2172.

Wang, P. (2004). Data analysis of the AMAXDOAS data, 2004. Personal Commumication.

Wang, P., Richter, A., Bruns, M., Rozanov, V. V., Burrows, J. P., Heue, K.-P., Wagner, T., Pundt, I., and Platt, U. (2004). Measurements of tropospheric NO_2 with an airborne multi-axis DOAS instrument. *accepted for publication in Atmos. Chem. Phys. Disscus.*

Wayne, R. (1991). *Chemistry of Atmospheres*. Oxford Science Publications.

Wennberg, P. O., Hanisco, T. F., Jaegle, L., Jacob, D. J., Hintsa, E. J., Lanzendorf, E. J., Anderson, J. G., Gao, R., Keim, E. R., Donnelly, S. G., Del Negro, L. A., Fahey, D. W., McKeen, S. A., Salawitch, R. J., and Webster, C. R. (1998). Hydrogen Radicals, Nitrogen Radicals, and the Productions of O_3 in the Upper Troposphere. *Science*, **279**, 49–53.

Wirth, M. and Renger, W. (1998). Evidence of Large Scale Ozone Depletion Within the Artic Polar Vortex 94/95 Based on Airborne Lidar Measurements. *Geophys. Res. Lett.*, **23**, 813–816.

Wittrock, F., Oetjen, H., Richter, A., Rozanov, A., and Burrows, J. (2004). MAX-DOAS measurements of atmospheric trace gases in Ny ålesund. *Atmos. Chem. Phys.*, **4**, 955–966.

Yung, Y. L., Pinto, J. P., Watson, R. T., and Sander, S. P. (1980). Atmospheric Bromine and Ozone Perturbations in the Lower Stratosphere. *J. Atmos. Sci.*, **37**, 339–353.

Ziereis, H., Schlager, H., Schulte, P., van Velthofen, P. F. J., and Slemr, F. (2000). Distributions of NO, NO_x, and NO_y in the upper troposphere and lower stratosphere between 28° and 61°N during POLINAT 2. *J. Geophys. Res.*, **105**, 3653–3664.

Index

List of Tables

List of Figures

Danksagung

Zum Schluß möchte ich mich für die viele Unterstützung bedanken, die ich während dieser Arbeit erhalten habe und ohne die es mir nicht möglich gewesen wäre, die Arbeit zu Ende zu bringen:

- Prof. Dr. John P. Burrows danke ich das interessante Thema.
- Dann möchte ich natürlich dem AMAXDOAS team danken: Dr. Andreas Richter danke für ich für die vorbildliche Betreuung meiner Arbeit, Dr. Ping Wang danke ich für die Auswerung der AMAXDOAS-Daten, ohne die diese Arbeit nicht möglich gewesen wäre. Dann wären da selbstverständlich noch Klaus-Peter Heue und Dr. Thomas Wagner aus Heidelberg, die für den Heidelberger Teil des AMAXDOAS Instruments verantwortlich waren. Ein 'halbes' AMAXDOAS fliegt eben nicht.
- Für ein sehr gutes Arbeitklima möchte ich der DOAS-Gruppe (Dr. Andreas Richter, Folkard Wittrock, Dr. Silvia Schlieter, Hilke Oetjen, Sixten Fietkau, Thomas Medeke, Hendrik Nüss, Dr. Ping Wang, Dr. Bernd Sierk, Yemi Afe, Dr. Annette Ladstädter-Weissenmayer, Andreas Heckel und Tibi Tarsu) danken.
- Dr. Alexej Rozanov danke ich sehr für seine Unterstüzung bei Problemen und Fragen zum SCIATRAN Model.
- Dr. Stefan Bühler danke ich für seine Hilfestellungen bei der Optimal Estimation Methode.
- Ein großer Dank gilt auch dem Flugbetrieb des DLR, der für die Planung und Durchführung der Flugzeugmesskampagnen verantworlich war.
- Bedanken möchte ich mich auch bei den beiden Sektretärinnen Sabine Packeiser und Birgit Teuchert des IUP, die mir so manche Wege durch die Universitätsbürokratie gezeigt und so viele bürokratische Tätigkeit abgenommen haben.
- Hilke Oetjen und Dr. Andreas Richter danke ich sehr auch dafür, daß sie diese Arbeit Korrektur gelesen haben, und damit diese Arbeit lesbarer gemacht haben.
- Ich danke meinen Eltern für die geduldige Unterstützung während meiner Doktorandenzeit.
- Nadja verdient großen Dank dafür, daß sie mich jedes Wochenende vom alltäglichen Leben eines Doktoranden abgelenkt und mich auf andere Gedanken gebracht hat.